Final Report

Transformational SOFC Technology

DE-FE0027584

January 30, 2022

PI: Hossein Ghezel-Ayagh, PhD

Prepared by:

FuelCell Energy Corporation
3 Great Pasture Road
Danbury, CT 06810

FuelCell Energy

Prepared for:

National Energy Technology Laboratory (NETL)
U.S. Department of Energy

DISCLAIMER

This Final Technical Progress Report was prepared with the support of the U.S. Department of Energy, under Award No. DE-FE0027584. However, any opinions, findings, conclusions, or recommendations expressed herein are those of the author(s) and do not necessarily reflect the views of the DOE.

TABLE OF CONTENTS

LIST OF FIGURES

LIST OF TABLES

EXECUTIVE SUMMARY

This project was conducted under the Co-operative Agreement No. DE-FE0027584 with the US Department Energy to developed advanced Solid Oxide Fuel Cell (SOFC) Technologies. The overall objective of this project was to advance SOFC technology at the cell and stack level to enhance cell robustness and durability, increase performance, and reduce balance-of-plant (BOP) requirements. By reducing system complexity combined with the increases in power density and efficiency, the ultimate goal of the project was to increased reliability and to reduce capital and operating costs of installed systems.

The project was focused on pathways that will reduce the cost of the SOFC cell and stack, including the following areas:

- Robust, redox tolerant cell technology
- Lower cost cell manufacturing through advances in cell design, which will reduce the amount of material, energy and time used in the fabrication of SOFCs
- High performance, low temperature electrolyte based on improvement of established materials
- Innovative SOFC stack architecture which truly integrates Balance of Plant functionality into the stack level design
- Thermal management of the fuel cell stack for increased durability and expanded window of operation
- Novel stack design amenable for use in sub-MW to multi-MW-scale power plants and having low replacement cost

The incorporation of balance-of-plant (BOP) equipment into the stack platform increased the economic viability of smaller scale systems. The project objectives were met by a multi-prong approach, including new cell design complemented with modifications to existing cell technology, as well as a new stack design incorporating components typically included in the BOP, such as heat exchangers, oxidizer, fuel reformers, and recycle systems.

The project culminated with demonstration of a stack test validating the viability of the cell and stack improvements. A cost model was also developed to estimate costs for the advanced stack technology at high volume manufacturing levels.

The net outcome of the project is SOFC cell and stack technology with costs significantly below current DOE targets without compromising and, in some cases, improving on the performance and degradation rate demonstrated with the current state-of-the-art stack design. The results of this project advanced the reliability, robustness, and endurance of low-cost SOFC technology that ultimately are ready to be deployed in coal power systems with greater than 60 percent efficiency (based on higher heating value of fuel) and the capability for ≥97% CO_2 capture at a cost-of-electricity that is approximately 40 percent below presently available Integrated Gasification Combined Cycle systems.

1 Introduction

Solid Oxide Fuel Cell (SOFC) technology represents an important opportunity to utilize fossil fuels in an efficient and environmentally-friendly manner. SOFCs are scalable, efficient and produce negligible emissions compared to combustion-based electrical power generation technologies. SOFC systems are modular and amenable to be configured for a range of applications, from small distributed generation to larger utility-scale baseload generation. Additionally, the high operating temperature of SOFCs allows for ultra-efficient generation of electric power from a variety of fossil fuels including natural gas and coal, while offering the remainder of fuel energy as useful heat.

In recent years, great strides have been made in increasing SOFC steady state performance and endurance, while reducing the cost of cells, stacks, and systems. Albeit the bane of SOFC commercialization has been higher than desired system cost and greater performance degradation rate as a result of operational upsets and transients. Although projected SOFC system cost at volume production is approaching the commercialization cost targets, they still remain high as compared to the exiting mature technologies such as gas turbines. The lack of robustness of the SOFC technology to ride through the inevitable system dynamics (such as sudden power outages) would make an SOFC system more prone to accelerated degradation and shorter useful life, which also translates to a higher system maintenance cost because of the increased frequency of fuel cell stack replacements.

This project had several objectives including a reduction in system cost as well as an increase in the longevity of SOFC performance in order to circumvent the obstacles to commercialization of the technology. The main purpose of the project was to reduce SOFC system capital cost and to increase the fuel cell useful life by developing a gamut of innovative concepts. The approach was bottoms-up; it initiated by development of radically new and novel concept in fuel cell structure and fabrication processes and moved up to integration of essential balance-of-plant components into a transformational stack architecture. The specific goals of the project were to enhance the robustness of the SOFC technology to mitigate the effects of system operational dynamics, to increase the redox capability of the fuel cell anode, and to lower the overall system cost by integrating the functionality of many balance of plant components within the SOFC stack.

The scope of work was designed to focus on SOFC cell and stack improvements that enable low-cost SOFC systems with vastly simplified BOP systems and containment modules. In support of these goals, the following activities were conducted during this project:

- Developed single-stage sintered cells to reduce manufacturing cost and enhance cell durability.
- Enhanced redox stability of existing cell technology.
- Adapted manufacturing process for improved cell technology.
- Investigated incorporation of heat exchanger and oxidizer into stack-level assembly.
- Investigated anode recycle solutions at the stack level, utilizing incoming fuel pressure as the motive power.
- Optimized flow field geometry of cell layers for full utilization of incorporated stack structures.
- Designed, fabricated, and tested a stack prototype for ≥1000 hours to demonstrate effectiveness of stack design improvements.

- Estimated factory cost of advanced SOFC cell and stack technologies, based on anticipated operating conditions of a commercial SOFC product and high-volume manufacturing.

2 Cell Technology & Manufacturing Development

The objectives of this task were to identify and prioritize the areas of cost reduction in cell materials and manufacturing processes that can be implemented in fabrication of the state-of-the-art SOFC cells. Validation testing of the proposed solutions were conducted, leading to refinements of the cell materials set and manufacturing processes. The new cell technology and manufacturing process was utilized to deliver cells for a 5-kW stack validation test.

2.1 Innovative Cell Architecture

This effort incorporated a dual-focused approach to increasing SOFC durability, particularly during redox cycling. The two approaches comprised both a novel cell architecture, focused on single-step sintering, and the microstructure optimization of established (TSC III) cell technology.

2.1.1 Single Stage Sintered Cell Process

Objective:

The objective of this activity was to develop transformational materials and processes to enable single-stage sintering of cells, implying the fabrication and co-sintering of the mechanical support, anode functional layer (AFL) scaffold, bi-layer electrolyte (SDC/YSZ) and cathode functional layer (CFL) scaffold performed in one step.

Approach:

Materials selection and manufacturing processes were developed for each cell layer to enable single-step sintering. The mechanical YSZ-based support and AFL were optimized for porosity to enable infiltration of electrocatalyst and fast gas diffusion. Additives to the support/AFL were investigated with the goal of increasing electrical conductivity and reducing the electrocatalyst loading requirement. A bi-layer (SDC/YSZ) based electrolyte was developed to enable reduced sintering temperatures while also improving electrolyte density. CFL development was focused on optimization of the pore structure and investigation of additives to increase electrical conductivity and reduce the electrocatalyst loading requirement. Atomic layer deposition technologies were also investigated as a means to improve performance and stability. Accelerated cell life testing was performed at high temperatures to characterize the stability and performance of developed material sets and processes. Post-test analysis were performed to observe the extent of microstructural changes. Previously-developed coarsening/electrochemical models were utilized to predict long-term performance based on test observations.

Results & Discussion:

This activity of the project was primarily performed at Northwestern University centered on development of new processing approaches that enable new cell designs that can operate at lower temperature than current state of the art SOFCs. The project work aimed to develop an SOFC with 1) infiltrated fuel and oxygen electrodes; 2) good stability after multiple redox cycles; and 3) reasonably small resistance and hence high power density at 600°C, all based on industrially-scalable processing utilizing tape casting and reduced-temperature sintering. The target cell design to incorporate these requirements consisted of 1) a bi-layer electrolyte

consisting of a very thin YSZ layer on the fuel side and a GDC layer on the oxygen side; 2) 8YSZ support layer; and 3) an ionically-conducting or two-phase oxygen electrode scaffold. In order to enable the production of high-quality GDC/YSZ bi-layers with high density and without substantial interdiffusion, low-temperature co-firing (1200-1250°C) was utilized in preparation of the anode-supported cells, by using Fe dopant as sintering aids in the electrolyte layers.

The approach to achieve next-generation low-temperature (≤ 600°C) SOFCs employed was a bi-layer GDC/YSZ electrolyte (GDC = $Gd_{0.1}Ce_{0.9}O_{1.95}$; YSZ = $Y_{0.16}Zr_{0.92}O_{2-\delta}$).[1] Very thin (~ 1 μm) YSZ electrolytes can be used in low-T SOFCs (Figure 2.1-1), but there were concerns regarding the gas tightness and long-term stability of such thin electrolytes. Many low-temperature SOFCs have employed doped ceria electrolytes[2] instead of YSZ because of their higher conductivity, as shown in Figure 2.1-1. However, cells with single doped ceria layers (e.g. GDC) generally yield low open-circuit voltage (OCV) due to significant electronic conduction,[3] and there may be mechanical stability issues due to the volume expansion of highly reduced ceria. The addition of a thin fuel-side YSZ layer with a thicker GDC layer is useful for achieving near-theoretical OCV,[4] but processing presents significant challenges; when fired together at temperatures typically used to form dense electrolytes, ~1400°C, high electrolyte resistance results due to formation of a low conductivity zirconia/ceria interdiffused interfacial layer.[5,6,7,8,9] However, the Northwestern project team has previously developed a method for obtaining yttria-stabilized zirconia YSZ/GDC bi-layers with minimal interdiffusion, enabled by a novel method for reducing the firing temperature to 1250°C.[10,11,12] In this prior work, the electrolytes had thick YSZ layers with thin GDC protective layers. For the current project work, the same processing approach is being adapted for making low-T SOFCs, *i.e.,* a thin-film GDC electrolytes with a very thin protective YSZ layer on the fuel side.

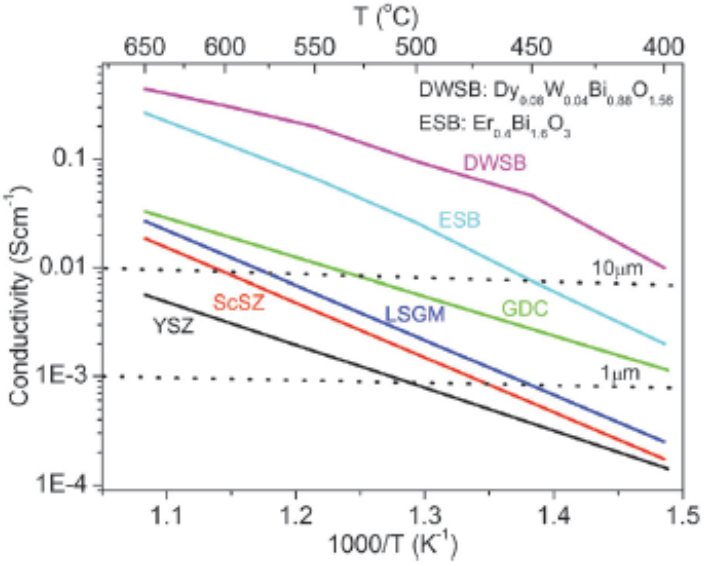

Figure 2.1-1 Target conductivity values of SOFC electrolyte yielding ASR of 0.1 Ωcm^2

The Ni-YSZ composite fuel electrode also requires improvements to provide good performance at reduced operating temperature. The reduced-temperature firing scheme employed here has been shown to result in increased TPB density in Ni-YSZ, improving performance.[10,11,12] In addition, pure YSZ or low-Ni-content Ni-YSZ would be infiltrated with Ni, and potentially modified with infiltrated GDC, in order to introduce a higher TPB density and hence enhance low-temperature performance. Also, it is hypothesized that an infiltrated fuel electrode would be more

resistant to redox events than a typical composite electrode since the Ni/NiO can have a lower volume fraction in the fuel electrode support, and so irreversible structural changes that occur during redox events would cause less stress that can damage the device integrity. Materials to be used for the infiltrated cathodes, selected based on prior work and literature information,[1] are $Sm_{0.5}Sr_{0.5}CoO_3$ (SSC), LSCF, LNO, and PLNO. The use of Sr-free nickelates (LNO and PLNO) may avoid or mitigate issues with Sr segregation and reactions with the YSZ electrolyte. These materials would be infiltrated into ionically-conducting scaffolds such as GDC or LSGM, or, alternatively into LSCF-GDC composite electrodes.

Bi-Layer Electrolyte Cell Fabrication

Methods have been successfully developed to tape cast dense YSZ layers as thin as 2-3 μm, via alterations in the tape casting slurry formulation. However, initial attempts to co-sinter the YSZ and GDC layers in a bi-layer electrolyte cell resulted in partial delamination of the GDC layer due to poor shrinkage match. While work was ongoing to adjust the processing to resolve this issue, another path to a solution was also investigated. In this case, the YSZ layer is directly tape casted on the carrier film, and then laminating with the anode functional layer and anode support tapes. The resulting structure is co-fired at 1250°C to form a thin dense YSZ electrolyte layer on the anode support. A thin GDC barrier layer is then applied by screen printing and fired at a lower temperature, 1200°C for 2 h. Figure 2.1-2 shows a fracture cross sectional SEM view of the cell structure, after application of LSCF-GDC cathode functional layer and LSCF current collector layer. The YSZ layer appears to be fully dense. While the GDC barrier in this case is not fully dense, this does not appear to be a major issue as porous GDC is widely used as a barrier layer in SOFCs with LSCF cathodes.

Figure 2.1-3 shows the performance of this type of cell at different temperatures. Power density values are reasonable, but substantially less than for cells of this type with thicker electrolytes.[10] The reason for the lower power density can be seen in the impedance spectra in Figure 2.1-4. While the ohmic (electrolyte) resistance appears to be smaller than that seen in prior cells,[10] the difference is not enough to make a large difference in power density. The main features, responses at ~ 2 and 2000 Hz, are similar to those seen in prior cells, but the low frequency response is much larger than in prior cells. This response is mainly related to gas diffusion in the anode. Thus, it seems likely that the anode supports in these cells were too dense, yielding substantial concentration polarization. This may well be due to the different characteristics of the new NiO powder used in making the cells, necessitated since the previous supplier is no longer selling NiO. Thus, it's expected that the performance of the cells can be substantially improved with some adjustments to processing and formulation, e.g., increasing the pore former in the support.

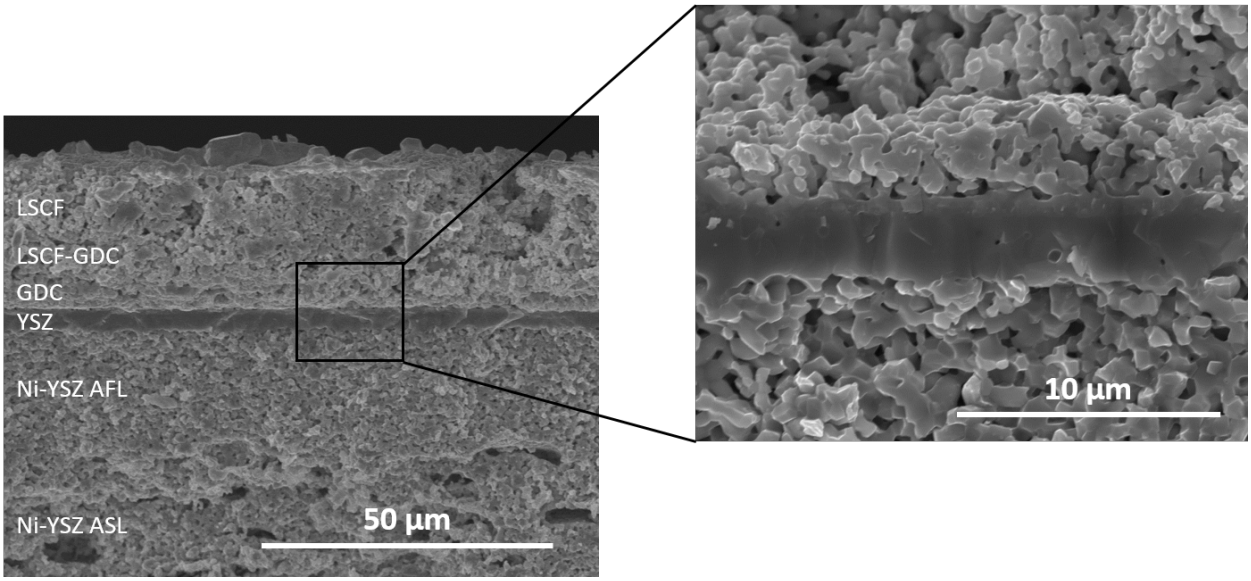

Figure 2.1-2 SEM images of the anode-supported cell with tape casted Ni-YSZ ASL, Ni-YSZ AFL, YSZ electrolyte and screen printed GDC barrier layer, LSCF-GDC cathode functional layer and LSCF cathode current collector.

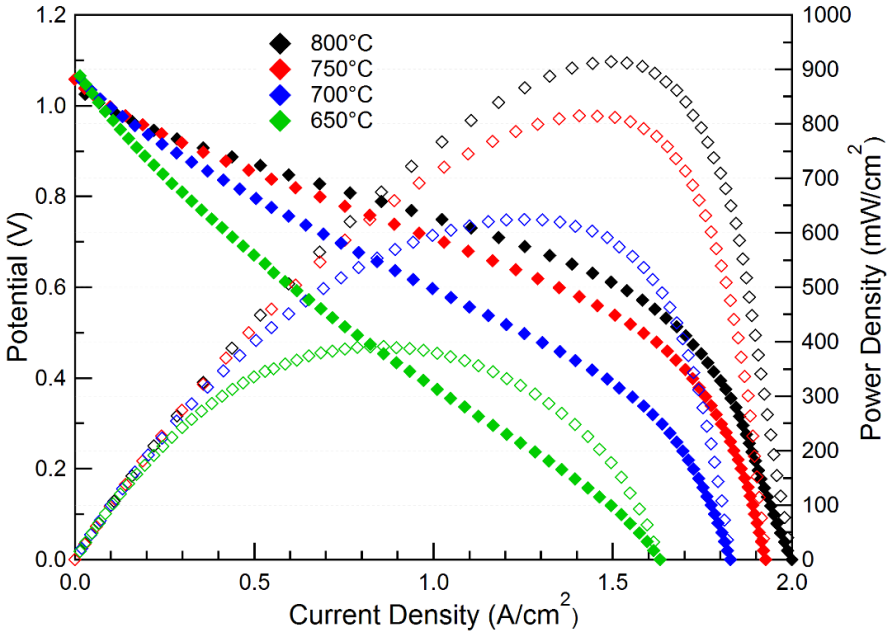

Figure 2.1-3 Performance results for a cell of the type shown in Figure 2.1-2, tested in air and humidified hydrogen.

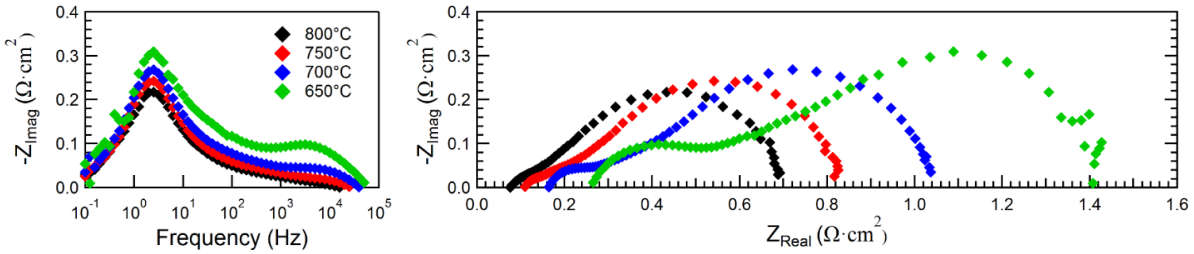

Figure 2.1-4 Impedance spectroscopy results for a cell of the type shown in Figure 2.1-2, tested in air and humidified hydrogen.

Oxygen Electrode Development

Methods were explored for making high-performance cathodes by infiltration into LSCF-GDC composites. The key concept here is to take advantage of the presence of LSCF in the scaffold to provide the electronic conduction needed in the cathode, thereby reducing the number of infiltration steps required. Figure 2.1-5 illustrates the expected structure. In prior work, LSCF and La_2NiO_4 were the infiltrate materials. Here the results of a third infiltrate material, SSC are described. In principle, SSC should be the best of these materials as it has the highest oxygen surface exchange rate,[1] the key attribute needed for an infiltrate in the cathode. Only four infiltration steps were used, substantially less than the number (12) used for infiltration into GDC scaffolds. As before, initial testing is carried out in symmetric cells with GDC electrolytes. All tests were carried out at 650°C in ambient air.

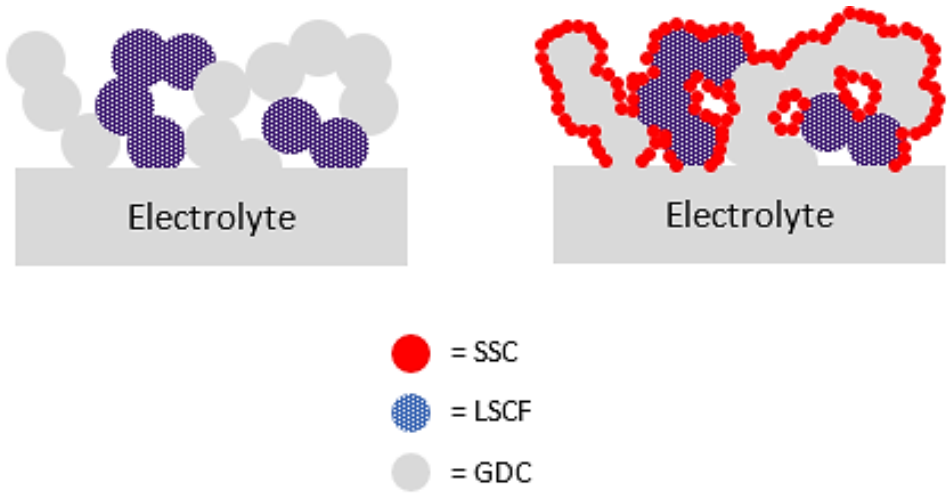

Figure 2.1-5 Schematic illustration of the LSCF-GDC composite electrode before (left) and after (right) infiltration of SSC.

Figure 2.1-6 shows the impedance response from the LSCF-GDC electrode, and Figure 2.1-7 shows the result from the same cell with SSC infiltration. The SSC infiltration was found to reduce the initial cathode resistance from 0.13 to 0.10 Ω cm^2 at 650°C. This was the lowest value of all the cathodes tested thus far.

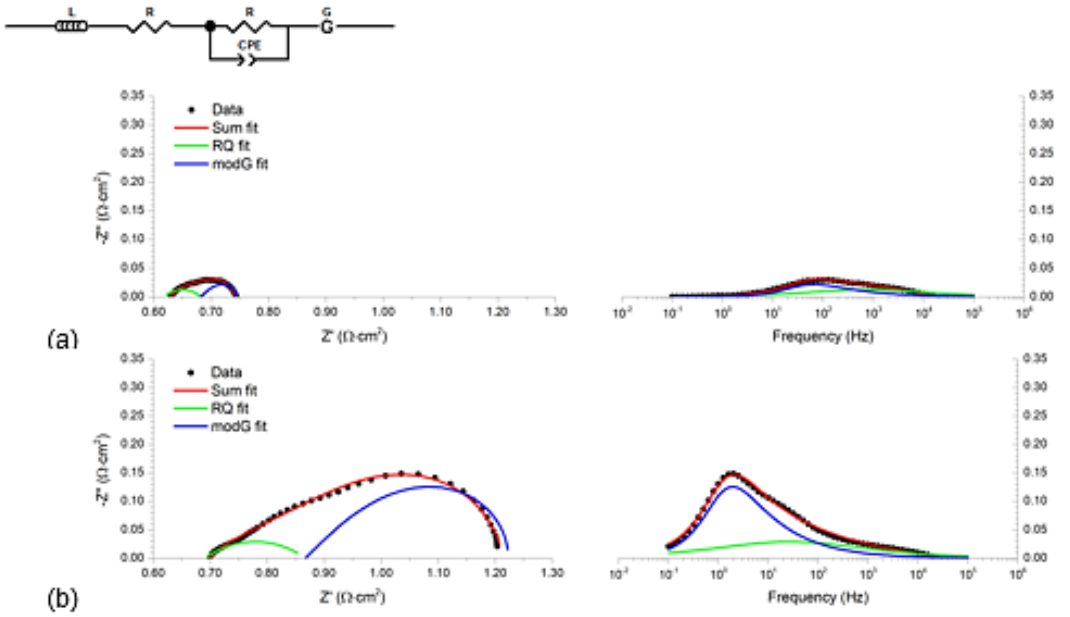

Figure 2.1-6 Nyquist (left) and Bode (right) plots of EIS spectra obtained at 650C in air for an un-infiltrated LSCF-GDC cathode. (a) shows the initial response, and (b) shows the response after ~ 1000 h of testing. The equivalent circuit used to fit the spectra is also shown.

The symmetric cells were life tested in order to observe how the response varies over time. As shown in Figure 2.1-6(b), the impedance response increased substantially over ~ 1000 h for the LSCF-GDC cathode. The increase can also be seen in the plot of polarization resistance versus time given in Figure 2.1-8. The increase is similar to recent observations for LSCF electrodes, where Sr surface segregation is believed to increase the resistance. The fits to the EIS data show two main responses, a Gerischer and an R-Q element. The R-Q element is believed to correspond to charge transfer between the MIEC materials (SSC and LSCF) and GDC, whereas the Gerischer element is related to oxygen surface exchange from the vapor combined with oxygen bulk diffusion. Note that the increase[13] in polarization resistance with time shown in is primarily due to an increase in the Gerischer resistance, which can be explained by the decrease in oxygen surface exchange rate as the Sr surface coverage increases.

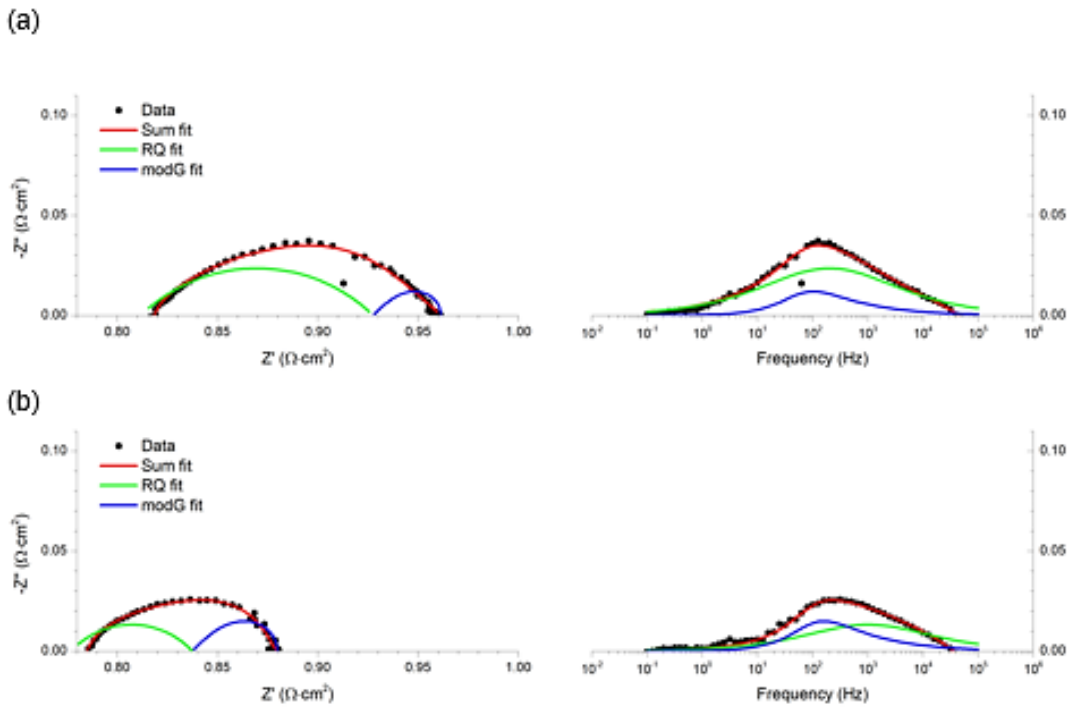

Figure 2.1-7 Nyquist (left) and Bode (right) plots of EIS spectra obtained at 650°C in air for an SSC-infiltrated LSCF-GDC cathode. (a) shows the initial response, and (b) shows the response after ~ 750 h of testing.

Figure 2.1-7 and Figure 2.1-8 show that the resistance increase is much smaller for the SSC-infiltrated LSCF. The reason for this is unclear, but it may suggest that the Sr segregation effect is less important for SSC than for LSCF. In summary, the results show that SSC infiltration is effective for improving both the performance and stability of LSCF-GDC cathodes.

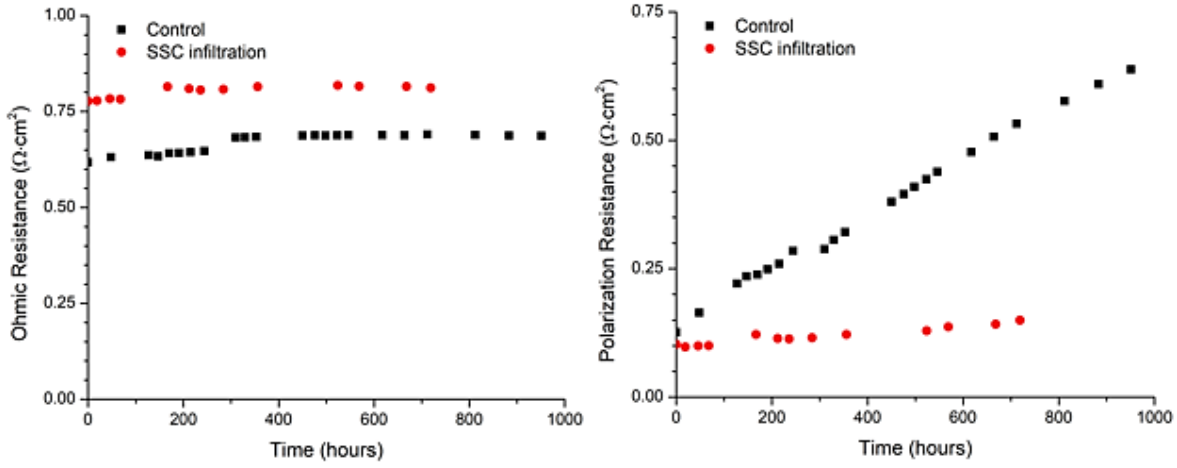

Figure 2.1-8 Ohmic (left) and polarization (right) resistance versus time, taken from fitting the impedance spectroscopy data.

The Ni-YSZ composite fuel electrode also requires improvements to provide good performance at reduced operating temperature. The reduced-temperature firing scheme employed here has been shown to result in increased TPB density in Ni-YSZ, improving performance.[10,11,12] In addition, pure YSZ or low-Ni-content Ni-YSZ infiltrated with Ni, and potentially modified with infiltrated GDC, in order to introduce a higher TPB density and hence enhance low-temperature performance. Also, it is hypothesized that an infiltrated fuel electrode would be more resistant to redox events than a typical composite electrode since the Ni/NiO can have a lower volume fraction in the fuel electrode support, and so irreversible structural changes that occur during redox events would cause less stress that can damage the device integrity. Materials to be used for the infiltrated cathodes, selected based on prior work and literature information,[1] are $Sm_{0.5}Sr_{0.5}CoO_3$ (SSC), LSCF, LNO, and PLNO. Note that the use of Sr-free nickelates (LNO and PLNO) may avoid or mitigate issues with Sr segregation and reactions with the YSZ electrolyte. These materials were infiltrated into ionically-conducting scaffolds such as GDC or LSGM, or, alternatively into LSCF-GDC composite electrodes.

Initial efforts involved tape casting of the Ni-YSZ anode support layer (ASL), Ni-YSZ anode functional layer (AFL) and YSZ electrolyte followed by lamination and firing at 1250°C for 2 h. The GDC barrier layer was then applied in a second step by screen printing and another firing at 1200°C for 2 h, followed by screen printing LSCF-GDC cathode and LSCF current collector and fired at 1100°C for 2 h. Shrinkage matching difficulties made it impossible to produce good bi-layer electrolyte cells by co-firing the GDC and YSZ. Successful preparation of the cells by co-firing. Ni-YSZ ASL, Ni-YSZ AFL and YSZ electrolyte were tape casted as before. After lamination, the anode/electrolyte structure was pre-fired at 1150°C for 3 h. GDC was applied by dip-coating, followed by firing the anode/electrolyte/GDC together at 1250°C for 4 h. The cathode was applied by screen printing and fired at 1050°C for 3 h. SEM images of the cross-sectional surface of the cell are shown in Figure 2.1-9. EDS line scan is shown in Figure 2.1-10 for the line shown in Figure 2.1-9 (right) . Dense YSZ electrolyte and dense GDC barrier layer have been achieved, with the YSZ/GDC bi-layer total thickness being ~ 5 μm.

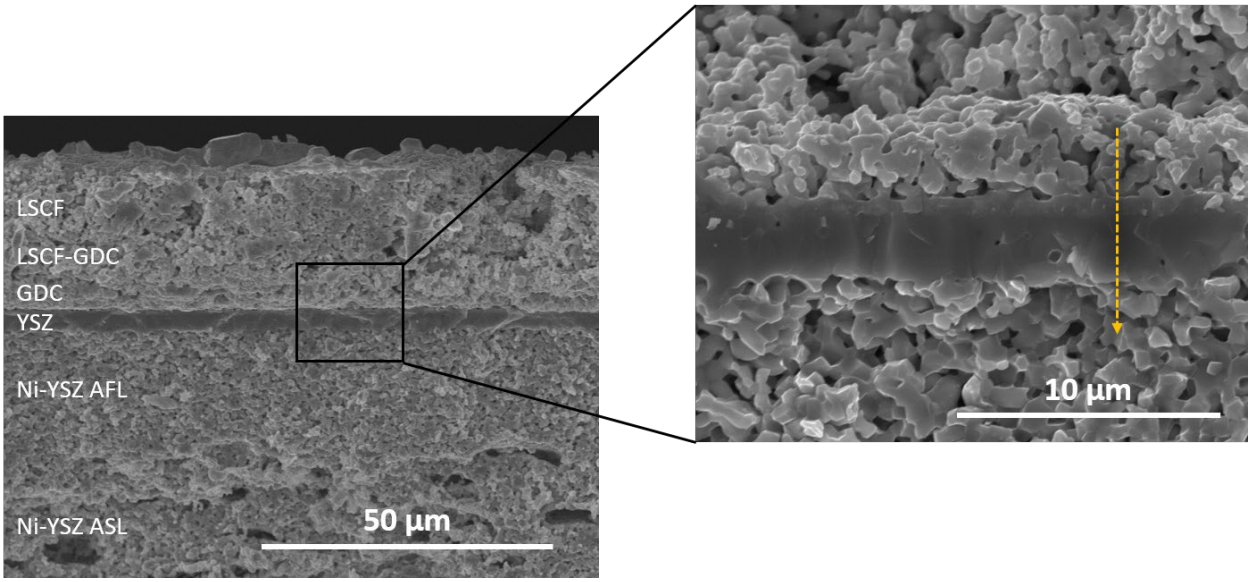

Figure 2.1-9 SEM images of the anode-supported cell with tape casted Ni-YSZ ASL, Ni-YSZ AFL, YSZ electrolyte and screen printed GDC barrier layer, LSCF-GDC cathode functional layer and LSCF cathode current collector.

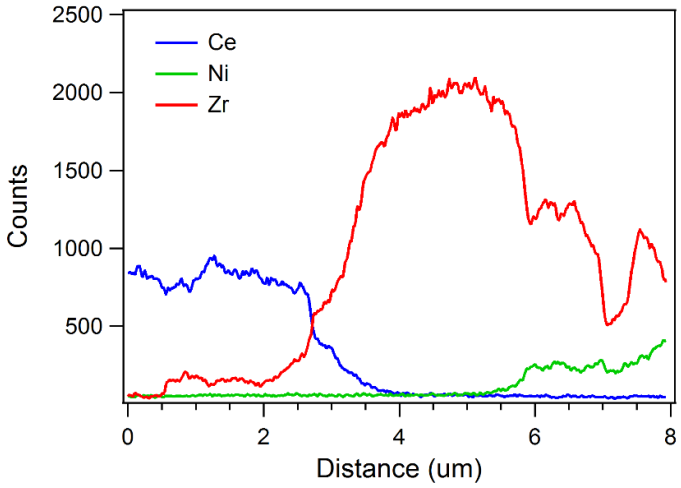

Figure 2.1-10 EDS intensity line scans taken along the line shown in Figure 2.1-9.

Figure 2.1-11 shows the voltage-current characteristics of the cell at varying temperatures. The maximum power density (Pmax) at each temperature was summarized in Table 2.1-1. Significant gas diffusion limitation has been observed, with the limiting current density being ~ 2 A/cm^2 at 800°C. Bode and Nyquist plots of EIS data taken at these temperatures are shown in Figure 2.1-12. The ohmic (RO) and polarization (Rp) resistances are summarized in Table 2.1-2. The dominant low-frequency response is consistent with the diffusion limitation in these cells.

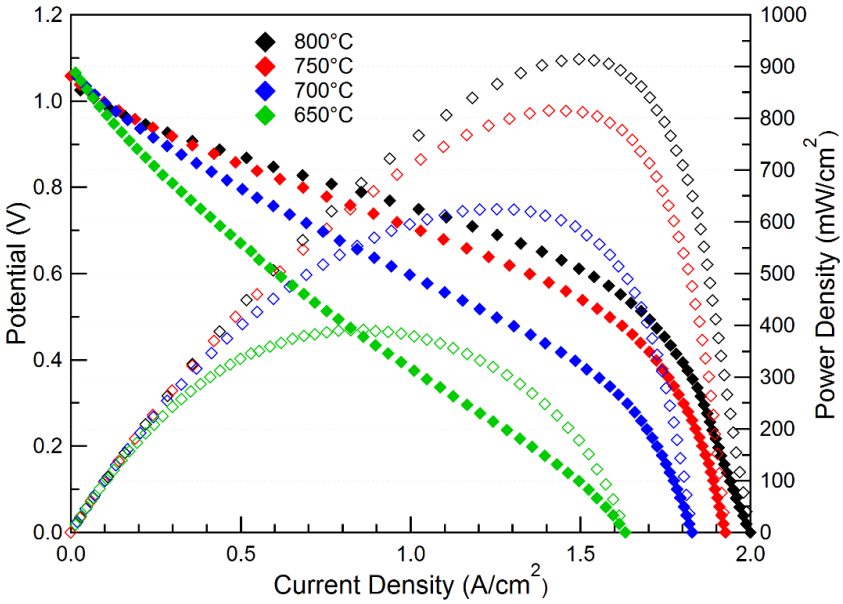

Figure 2.1-11 Performance results for a cell of the type shown in Figure 2.1-9, tested in air and humidified hydrogen.

Table 2.1-1 *Values of P_{max} for different cells*

	Non-infiltrated (mW/cm²)	***LSCF-infiltrated (mW/cm²)***	***SSC-infiltrated (mW/cm²)***
800°C	*914*	*1972*	*2116*
750°C	*815*	*1557*	*1470*
700°C	*625*	*961*	*847*
650°C	*391*	*512*	*433*

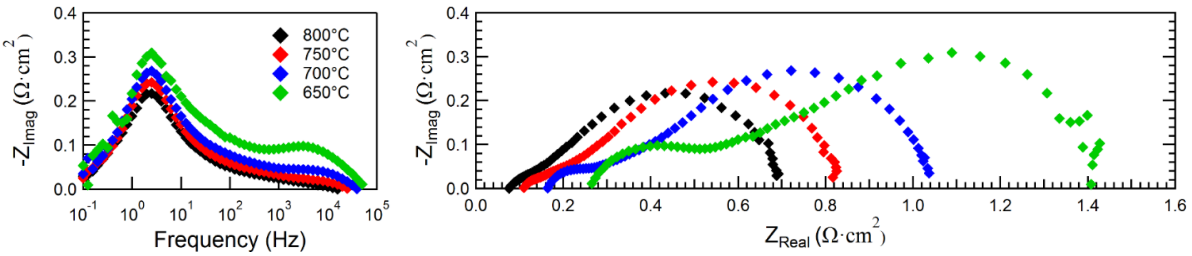

Figure 2.1-12 Impedance spectroscopy results for a cell of the type shown in Figure 2.1-9 tested in air and humidified hydrogen.

In order to enhance the cell performance, especially at lower temperatures, LSCF or $(Sm_{0.5}Sr_{0.5})CoO_3$ (SSC) was infiltrated into the cathode, forming nanoparticles decorating the LSCF-GDC surface. Figure 2.1-13 shows the cell performance of the LSCF-infiltrated and SSC-infiltrated cells. Both showed substantial increase in performance compared to the non-infiltrated cell. The SSC-infiltrated cell has slightly higher Pmax at 800°C, while the LSCF-infiltrated cell yielded higher Pmax at 750, 700 and 650°C.

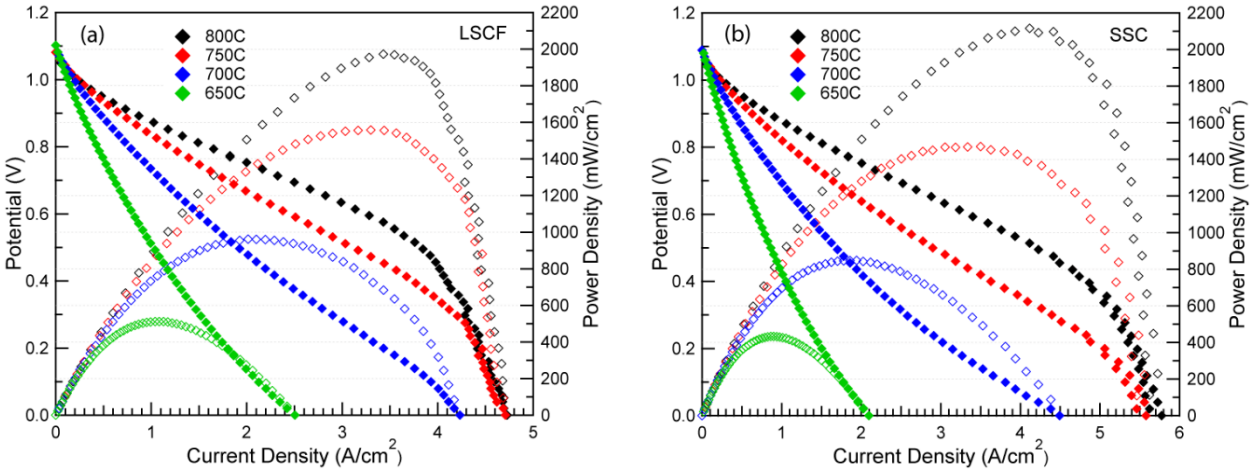

Figure 2.1-13 Voltage and power density versus current density for LSCF-infiltrated (a) and SSC-infiltrated (b) cells tested at different temperatures under humidified H_2 on the anode and flow air on the cathode.

All the Pmax values were summarized in Table 2.1-1 . Figure 2.1-14 and Figure 2.1-15 present the Bode and Nyquist plots of the LSCF and SSC-infiltrated cells, respectively. Compared to the non-infiltrated cell, there is a significant decrease in the low frequency (LF) response centered at 1-10 Hz, whereas the high frequency peak did not change. Whereas the LF peak was temperature dependent without infiltration, for the infiltrated cells it was temperature independent, indicating that it is only associated with gas diffusion. This suggests that the LF response included both the cathode electrochemical process and gas diffusion (presumably associated with the thick anode). Infiltration substantially decreases the cathode response, leaving gas diffusion as the main limiting process. The HF response is not affected by infiltration and is temperature dependent, suggesting that it may be related to interfacial charge transfer resistance, perhaps at the cathode/electrolyte interface.

All ohmic and polarization resistances are listed in Table 2.1-2. Figure 2.1-16 shows the Bode and Nyquist plots of EIS data from LSCF-infiltrated cell measured at 750°C under different hydrogen partial pressures with flow air on the cathode. The LF response grew larger and shifted slightly to lower frequency with decreasing pH_2, consistent with the correlation with anode gas diffusion. There is almost no change in the higher frequencies, as expected for an interfacial process.

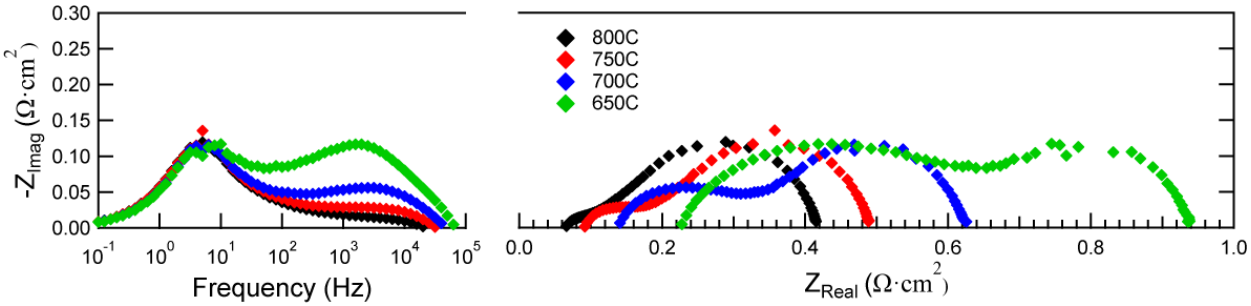

Figure 2.1-14. Bode and Nyquist plots of EIS data from LSCF-infiltrated cell measured at different temperatures under humidified H_2 on the anode and flow air on the cathode.

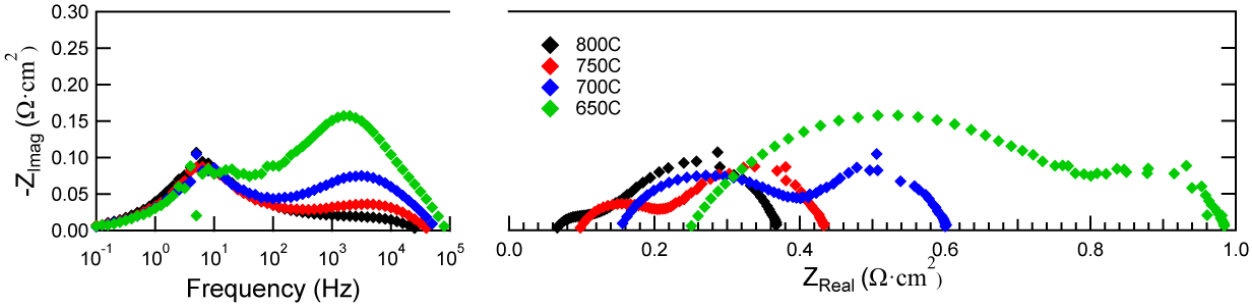

Figure 2.1-15. Bode and Nyquist plots of EIS data from SSC-infiltrated cell measured at different temperatures under humidified H_2 on the anode and flow air on the cathode.

Table 2.1-2 Values of R_o and R_p for different cells.

	***Non-infiltrated* ($\Omega \cdot cm^2$)**		***LSCF-infiltrated* ($\Omega \cdot cm^2$)**		***SSC-infiltrated* ($\Omega \cdot cm^2$)**	
	R_O	R_p	R_O	R_p	R_O	R_p
800°C	*0.08*	*0.61*	*0.06*	*0.35*	*0.06*	*0.31*
750°C	*0.11*	*0.71*	*0.09*	*0.4*	*0.10*	*0.33*
700°C	*0.16*	*0.88*	*0.14*	*0.48*	*0.15*	*0.45*
650°C	*0.26*	*1.15*	*0.23*	*0.71*	*0.25*	*0.73*

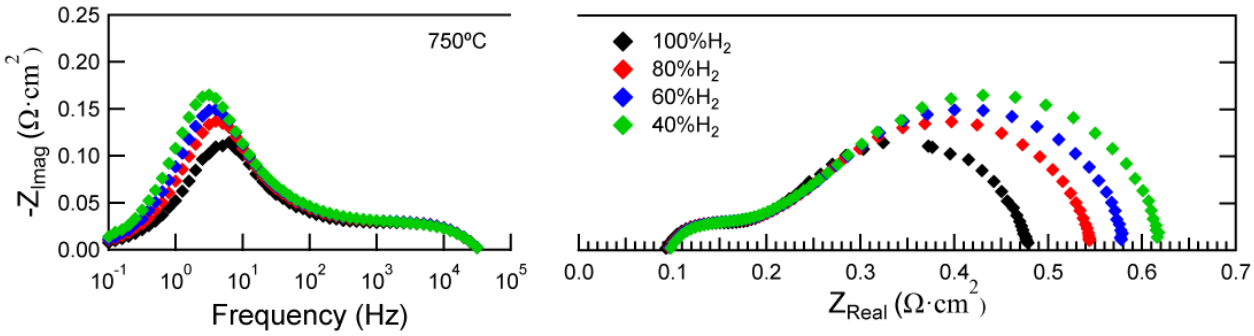

Figure 2.1-16. Bode and Nyquist plots of EIS data from LSCF-infiltrated cell measured at 750°C under different hydrogen partial pressures.

The anode-supported half-cell is produced by tape casting, lamination, and co-sintering, as demonstrated above. For the fabrication of the half-cell with a thin, dense, and adhesive bi-layered electrolyte, the laminate (anode support | anode functional layer (AFL) | 1 mol.% Fe_2O_3-doped $(ZrO_2)_{0.92}(Y_2O_3)_{0.08}$ (YSZ)) was pre-sintered at 1150°C. Then, the 3 mol.% Fe_2O_3-doped $Gd_{0.1}Ce_{0.9}O_{1.95}$ (GDC) layer was coated onto the YSZ layer through a dip-coating process followed by co-sintering at 1250°C. As shown in Figure 2.1-17 (a), the YSZ/GDC electrolyte layer with a thickness of ~2.7 μm was formed on the NiO–YSZ anode functional layer without any sign of crack and/or delamination. The cross-section of the fabricated electrolyte layer was examined through the EDS analysis Figure 2.1-17 (b). The thickness of GDC and YSZ was determined to be ~1 μm and ~1.7 μm, respectively.

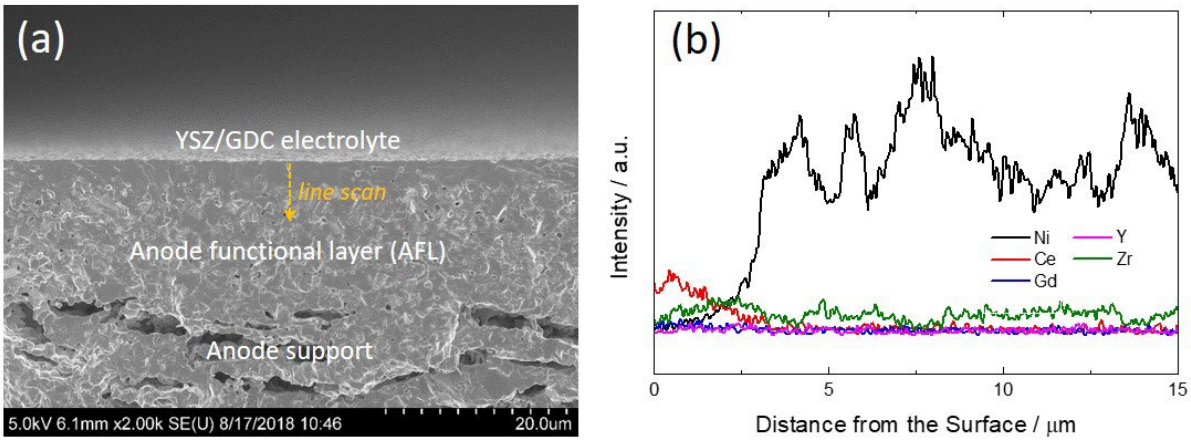

Figure 2.1-17 (a) Cross-sectional SEM micrographs of (b) concentration profiles of Ni, Ce, Gd, Y, and Zr across the anode-supported half-cell.

Anode-supported SOFC have been fabricated using the thin YSZ/GDC electrolyte developed in this work and tested for electrochemical performance under SOFC operating conditions. The typical $La_{0.6}Sr_{0.4}Co_{0.2}Fe_{0.8}O_3$–GDC (LSCF–GDC), was applied on the anode-supported half-cell through a simple screen-printing process. For electrochemical measurements, a silver grid (Heraeus Inc.) was screen-printed onto the cathode to improve current collection. Then, the cell was mounted onto an alumina tube for H_2 supply using Ag sealant (DAD-87, Shanghai Research Institute of Synthetic Resins). During the cell testing, the cathode and the anode were fed with air and H_2 gas humidified with 3 vol.% H_2O, respectively. The electrochemical measurements were carried out using an IM6 Electrochemical Workstation (ZAHNER, Germany). Figure 2.1-18 exhibits the current–voltage (*I*–*V*) curves and the power densities of the cell measured at 600–800°C. The open-circuit voltage (OCV) value was ~1.03 V at 800°C, and increased slightly with decreasing operating temperatures. The maximum power densities at different temperatures for the cell are summarized in Table 2.1-3. The typical ac impedance spectra of the cell is presented in Figure 2.1-19 (a), and the ohmic resistance values, which are represented by the high-frequency intercepts, are summarized as a function of temperature in Figure 2.1-19 (b). Figure 2.1-20 presents the cross-sectional SEM micrograph and the concentration profiles obtained by the EDS analysis for the tested cell. The bi-layered electrolyte composed of ~1 μm-thick GDC and ~1.7 μm-thick YSZ was sandwiched between the AFL and the cathode. The interfaces between the electrolyte and the cathode and/or AFL are quite cohesive. Consequently, the electrochemical and structural analyses presented here prove that a 2.7 μm-thick dense YSZ/GDC electrolyte can be effectively formed in the anode supported SOFC via the methodology proposed.

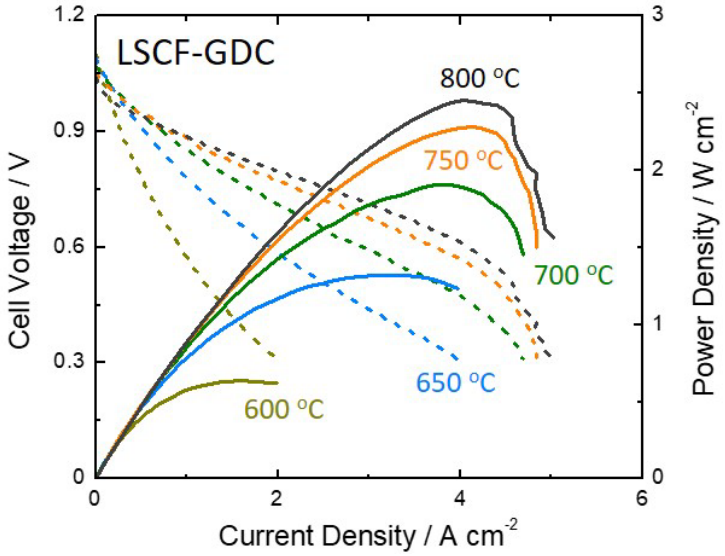

Figure 2.1-18 . *I–V* curves and power densities of the anode-supported SOFC with LSCF–GDC at 600–800°C

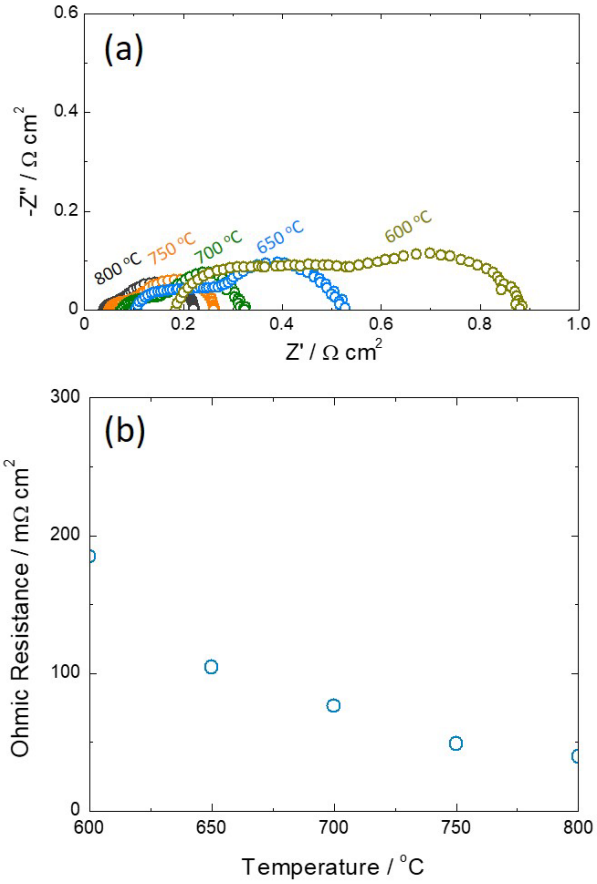

Figure 2.1-19 (a) Nyquist plots of the impedance spectra of the anode-supported SOFC with LSCF–GDC at 600–800°C. (b) The ohmic resistance values of the cell determined from (a).

Table 2.1-3 The maximum power densities of the anode-supported SOFC with LSCF–GDC at 600–800°C.

Temperature (°C)	Cell with LSCF–GDC (W cm^{-2})
800	2.45
750	2.27
700	1.89
650	1.32
600	0.63

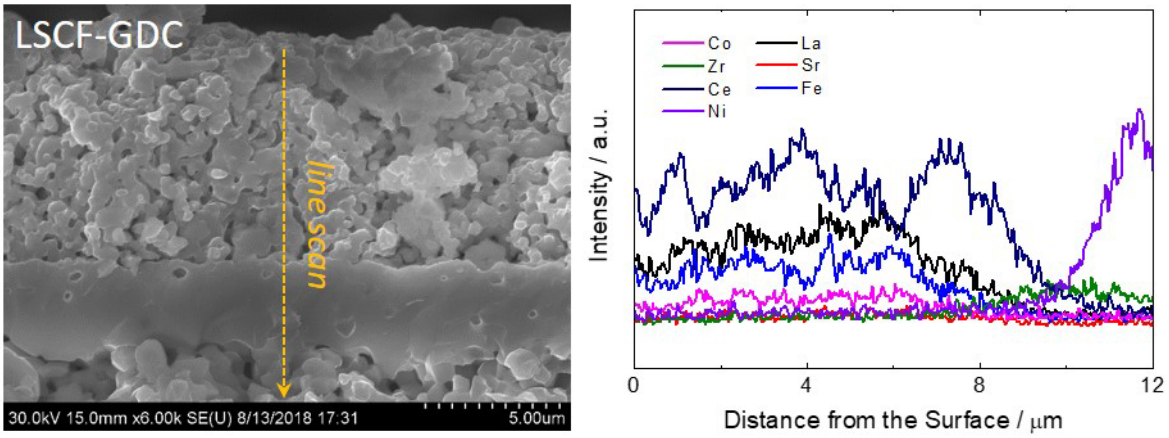

Figure 2.1-20 A cross-sectional SEM micrograph and concentration profiles of Sr, La, Fe, Co, Ni, Ce, and Zr across the anode-supported SOFC with LSCF–GDC.

Improvement in electrochemical performance of the anode is important to obtain desirable power density at low operating temperatures. Among various strategies to enhance electrode performance, one way is the electrode surface modification with nano-sized electrocatalysts. In this work, the Ni–YSZ anode surface was engineered with the $Gd_{0.2}Ce_{0.8}O_2$ (GDC) nano-particles formed via the infiltration technique. The GDC material was chosen as a surface modifier due to its excellent catalytic and mixed ionic/electronic conducting properties in a reducing atmosphere.

In order to make an initial evaluation of the electrochemical performance of enhanced anodes, YSZ-supported symmetric cells with NiO–YSZ electrodes were used. The cells were prepared by tape casting, lamination, and sintering (1250°C for 4 h). Aqueous nitrate solutions of GDC precursors with different concentrations (0.1, 0.5, 1, and 1.5 mol L^{-1}) were prepared by dissolving desirable amounts of $Gd(NO_3)_3{\cdot}6H_2O$ and $Ce(NO_3)_3{\cdot}6H_2O$ in distilled water. Triton X-100 and citric acid were added into the GDC precursor solution as a surfactant and a chelating agent, respectively. Prior to surface tailoring via single-step infiltration, the symmetric cells were heat-

treated in 3 vol.% H_2O-humidified H_2 at 600°C for 6 h to make the scaffold sufficiently porous through reduction of NiO to Ni. Then, 6 μl of SSC solution was infiltrated into a porous anode scaffold. The GDC particles were then obtained by in-situ thermal conversion during the SOFC startup.

The controlled surface tailoring is of great importance to obtain high electrochemical performance of the anode, and thus, the morphology and loading of GDC nanoparticles on the Ni–YSZ anode were controlled by changing the molarity of the GDC solution. Figure 2.1-21 displays the morphological features of GDC on the anode surface. After infiltration with 6 μl of 0.1 M GDC solution, few GDC particles are observed on the porous anode. The loading of GDC nanoparticles increased with increasing molarity of the GDC solution, showing an increased surface coverage. At a 1.5 M GDC infiltration, the anode surface was fully covered with GDC.

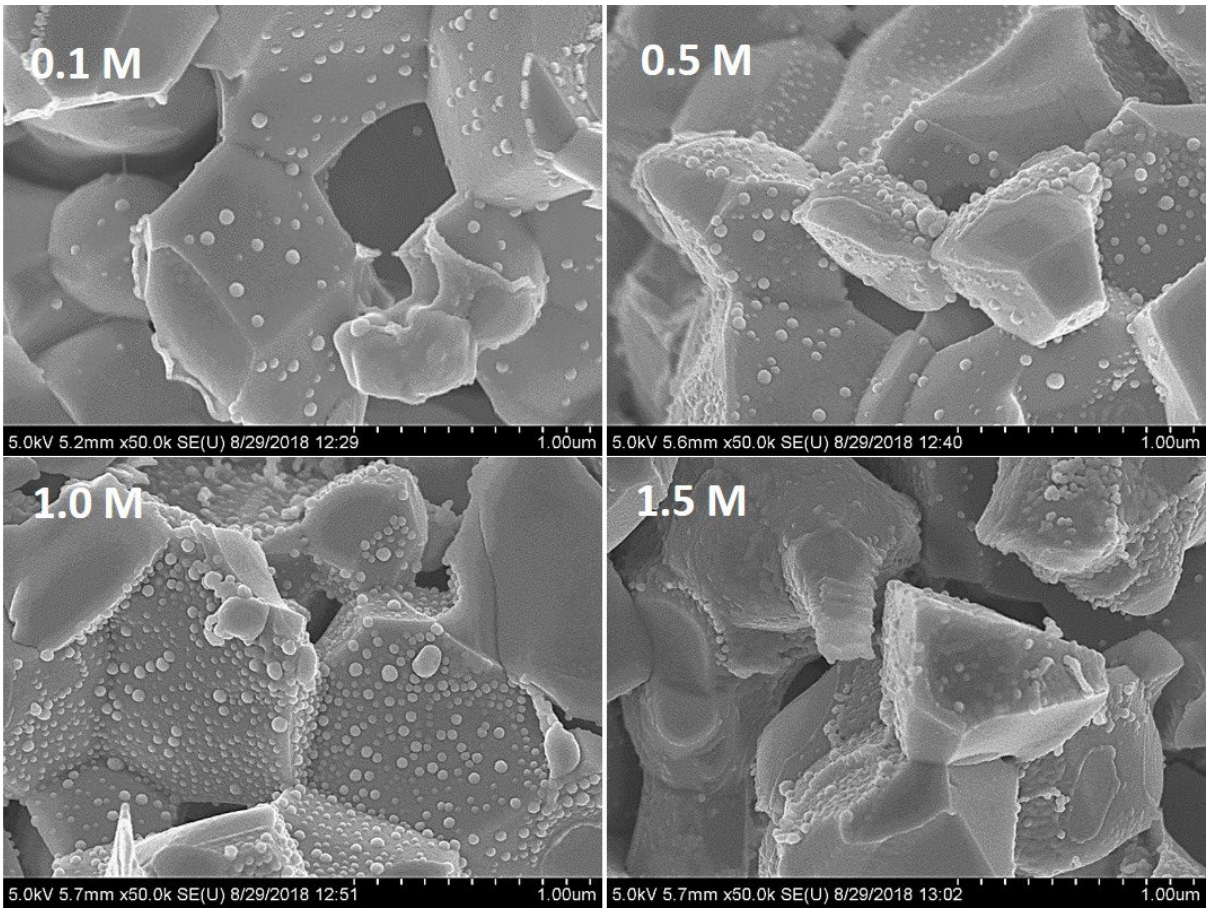

Figure 2.1-21 Cross-sectional SEM images of the Ni–YSZ anodes: after (single) infiltration of 0.1 M GDC; after infiltration of 0.5 M GDC; after infiltration of 1 M GDC; and after infiltration of 1.5 M GDC.

The electrochemical performance of symmetric cell with tailored anodes was evaluated by ac-impedance (EIS) measurements. The EIS measurement was conducted at 600–800°C in 3 vol.% H_2O-humidified H_2, and the Nyquist and Bode plots of the cells at 600, 700, and 800°C are shown in Figure 2.1-22 and Figure 2.1-23. The electrode polarization resistances (R_p) indicative of the electrochemical activity of electrode were determined from the impedance spectra and the results are summarized in Figure 2.1-24(a). Clearly, the R_p value was reduced by the introduction of GDC

nanoparticles, indicating enhanced hydrogen oxidation reaction kinetics. Figure 2.1-24(b) presents the electrode conductance (R_p^{-1}) values determined from the impedance data at temperatures between 600 and 800°C. Also, the activation energy (E_a) values calculated from the linear relationship between $1/T$ and $\ln R_p^{-1}$ are summarized in Figure 2.1-24(b). The activation energy was slightly reduced for low to moderate infiltrant molarities, and significantly reduced for the highest concentration (1.5 M) GDC solution.

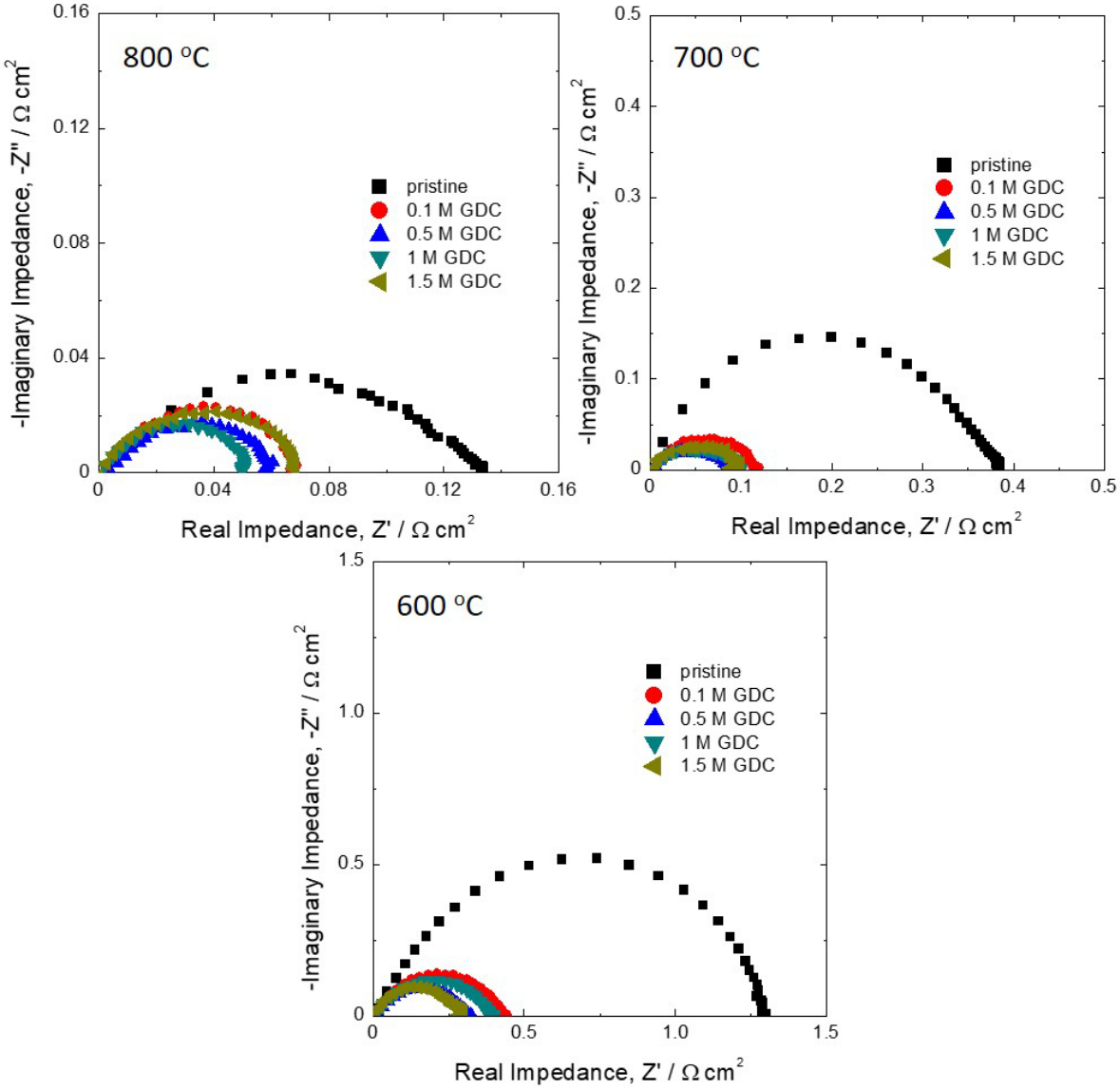

Figure 2.1-22 Nyquist plots of YSZ-supported symmetric cells with tailored Ni–YSZ electrodes measured in 3 vol.% H_2O-humidified H_2 at 800, 700, and 600°C.

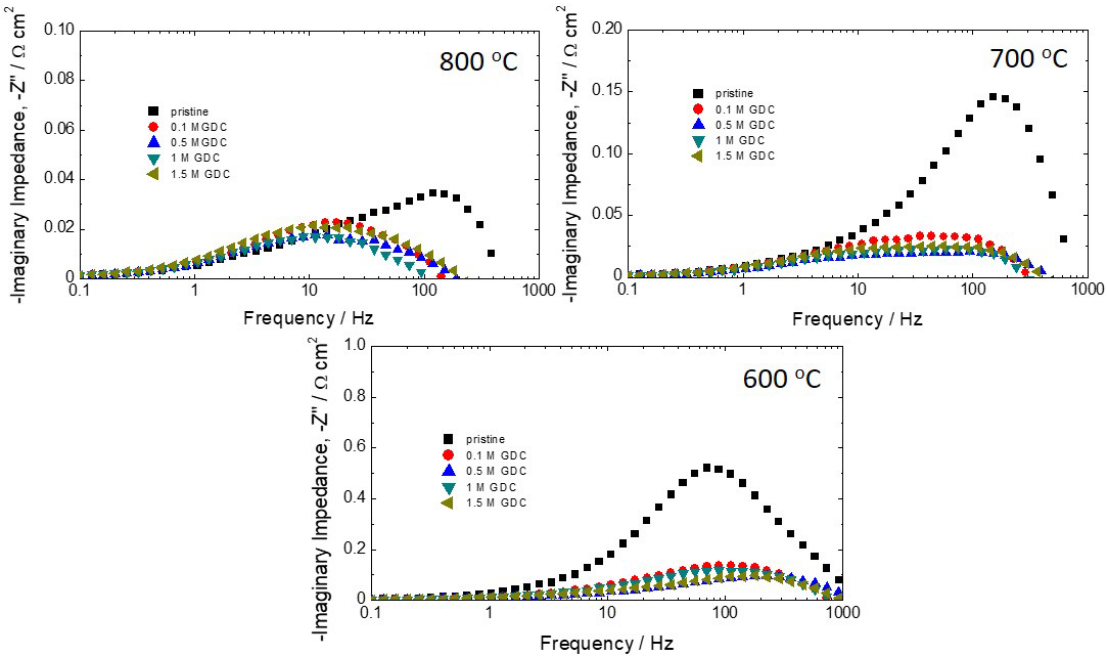

Figure 2.1-23 Bode plots of YSZ-supported symmetric cells with tailored Ni–YSZ electrodes measured in 3 vol.% H_2O-humidified H_2 at 800, 700, and 600°C.

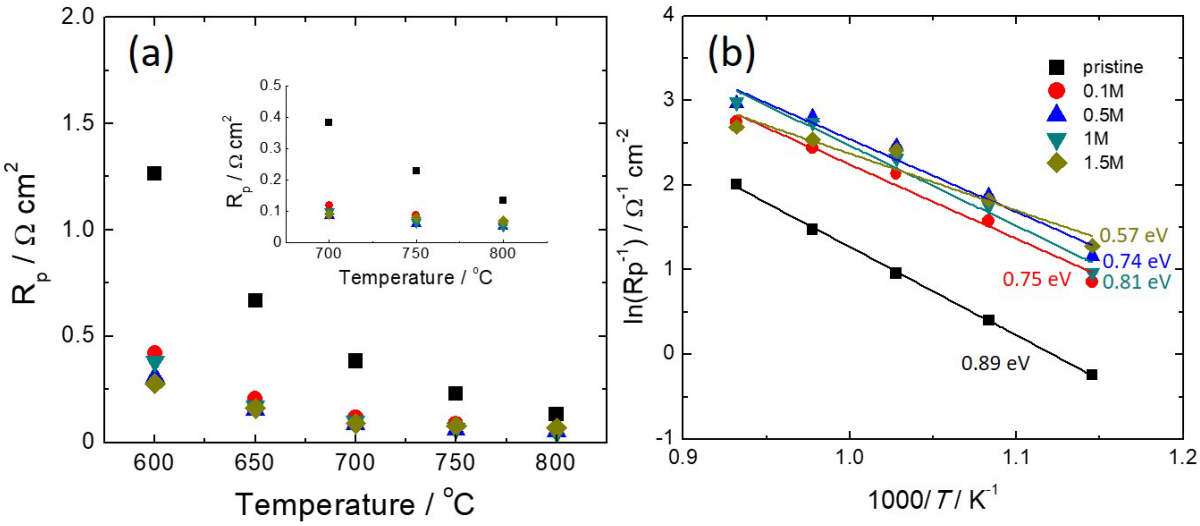

Figure 2.1-24 Temperature dependences of (a) the polarization resistance (Rp) and (b) the electrode conductance (Rp^{-1}) determined from the impedance data.

For the following results, the NiO–YSZ anode-supported SOFC was fabricated through a 3-step process as follows: A laminate composed of NiO–YSZ anode support, anode functional layer (AFL), and 1 mol.% Fe_2O_3-doped $(ZrO_2)_{0.92}(Y_2O_3)_{0.08}$ (YSZ) was sintered at 1250°C for 4 h (step 1). Then, the GDC layer was coated onto the YSZ layer through a screen-printing process followed by sintering at 1250°C for 2 h (step 2). After this half-cell fabrication process, a porous

$La_{0.6}Sr_{0.4}Co_{0.2}Fe_{0.8}O_3$ (LSCF)–GDC composite cathode was screen-printed on the GDC layer and was then sintered at 1100°C for 2 h (step 3).

A silver grid (Heraeus Inc.) was screen-printed onto the LSCF–GDC cathode of full cell constructed here for current collection. Then, the cell was mounted onto an alumina tube for H_2 supply using Ag sealant (DAD-87, Shanghai Research Institute of Synthetic Resins). During the electrochemical characterization of cell, the cathode and the anode were supplied with air and 3 vol.% H_2O-humidified H_2, respectively. The impedance measurements were carried out under open circuit conditions with an IM6 Electrochemical Workstation (ZAHNER, Germany). Figure 2.1-25(a) and (b) exhibit I–V curves and the Nyquist plots of obtained impedance spectra for the cell at different temperatures, respectively. Although overall peak power densities at 600–800°C were lower than those of the full cell with a dense GDC layer shown above, the cell showed better stability. Figure 2.1-26 shows a post-test SEM micrograph of the cell after the electrochemical characterization. The thicknesses of cathode, porous GDC, and YSZ are estimated to be ~10, ~2.5, and ~2 μm. After the performance test, all components still remain cohesive.

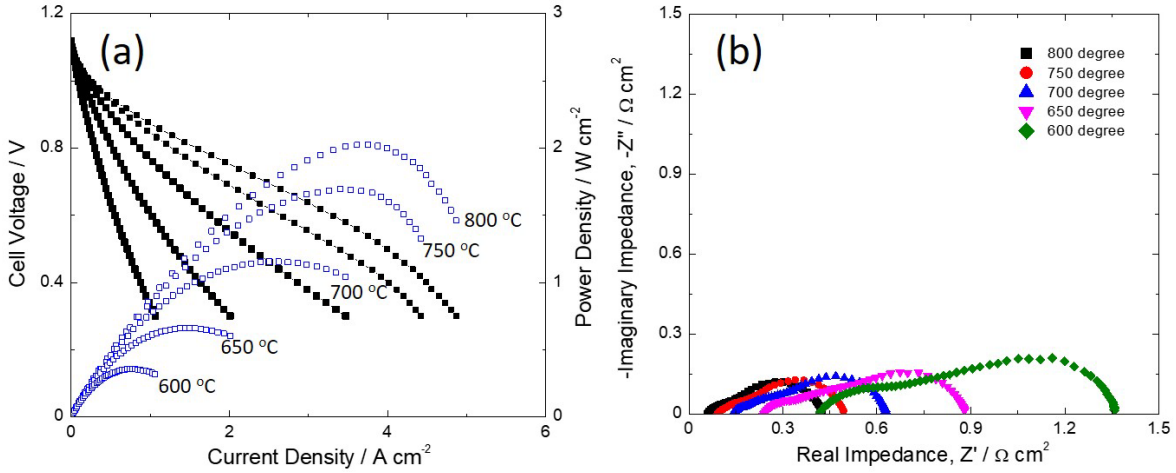

Figure 2.1-25 (a) *I–V* curves and (b) Nyquist plots of the obtained impedance spectra from the Ni–YSZ anode-supported SOFC with LSCF–GDC at 600–800°C.

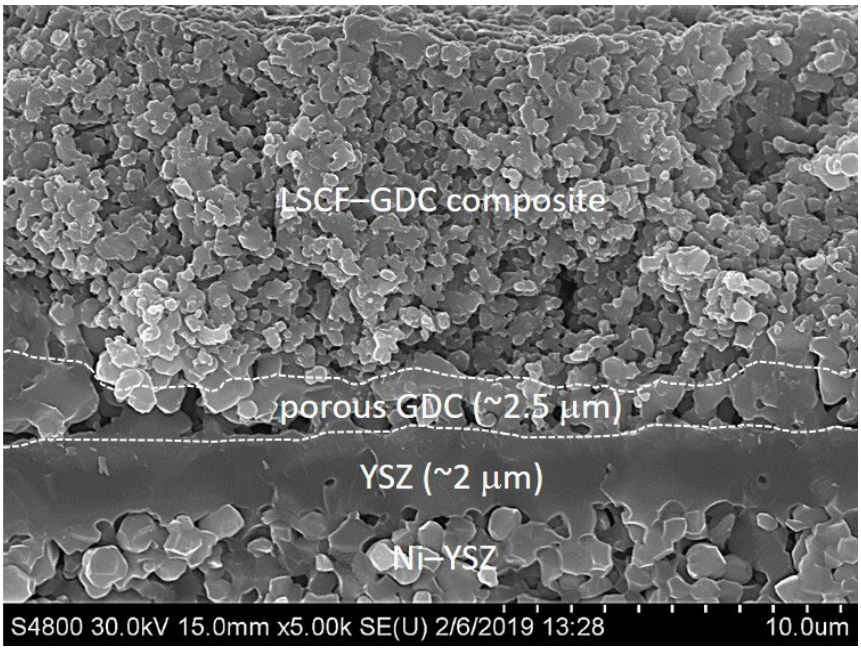

Figure 2.1-26 The post-test SEM micrograph of Ni–YSZ anode-supported SOFC with LSCF–GDC.

2.1.2 TSC III Microstructure Optimization

Objective:

The goal of this effort was to develop cell materials that are tolerant to reduction and oxidation cycling (Redox cycling) which can be expected in real-world system operation.

Approach:

A stiffer ceramic skeleton for the anode substrate and functional layer was developed to resist the expansion resultant from Ni oxidation, thereby lowering stress on the electrolyte. Incorporation of the proper ratios of partially-stabilized zirconia into the AFL and anode substrate was investigated. Grading of the nickel content in the AFL was investigated, with less nickel near the electrolyte. The effect of increased porosity of the anode substrate was studied. A porous barrier layer adjacent to the anode substrate, which oxidizes rapidly to restrict air flow to the anode during a system shutdown, was also be investigated. Pre-oxidation (or controlled redox cycling at lower temperature of 500 to 600°C) was tested on the new cell architecture to further improve the redox tolerance. These developments were incorporated into a cell with thinner electrolyte. The final cell underwent a testing regime with 10 thermal cycles and 10 Redox cycles targeting equivalent or significantly minimized performance loss on redox cycling than that is found with thermal cycling.

Results & Discussion:

Modifications to Test stand 10 (Figure 2.1-27) were completed to allow safe redox testing of 10 cm x 10 cm cells. The test stand modifications and test procedure were required to prevent fuel and air gases mixing at high temperature inside the test furnace (during redox cycles) as well as

in the gas outlet lines in the plant and to prevent electrical shorting when using the standard single-cell current collection arrangement.

Figure 2.1-27 Single-Cell Test Stand 10 After Modifications

A 1 mm thick TSC-II cell was prepared for commissioning of the modified test stand to verify changes to the test stand and compare results with those from previous testing on the same cell type as a baseline. Test methods were updated based on previous testing protocols and taking account of the test stand modifications. In addition, two more cells were prepared for comparison, a 600 µm TSC-III cell using stiffer YSZ skeleton in the anode substrate and a 600 µm cell with higher nickel content (higher porosity when reduced) and stiffer ceramic skeleton in the anode. These tests provided a comparison with previous Redox test results[14,15,16,17] qualifying the new

test stand configuration and also provided a baseline for the 600 µm TSC-III cell that was already used in SOFC stacks, but were tested for Redox tolerance. In addition, the effect of higher porosity and stiffer ceramic skeleton in the anode were evaluated in these early tests with a cell formulation that was developed in the previous SECA Innovative Concepts project.[18]

Figure 2.1-28 shows cell voltage and power density plotted against current density from 800 to 650°C for this test, 102038, prior to Redox cycling.

When kinetic studies of nickel oxidation are considered, as well as the large amount of nickel present in a large anode-supported cell, it becomes clear that it could take a reasonable amount of time and air flow to fully re-oxidize an anode-supported cell in an actual SOFC system. This time frame and amount of air flow may be sufficient that cells do not get fully re-oxidized during a system Redox event, but only partially re-oxidized (a partial redox cycle). With this assumption, in a previous project 10 years ago FuelCell Energy proposed a re-oxidation or redox depth approach in order to determine the length of partial redox cycle times for in-situ testing of the effects of redox cycling on electrochemical performance of planar anode supported cells (ASCs). This analysis uses the amount of nickel within the cell and the flow rate of air to calculate the amount of time it would take to oxidize the cell to a specific redox depth (50% redox depth means that 50% of the nickel in the cell has been re-oxidized and 50% remains as metallic nickel; 100% redox depth represents a complete redox cycle back to a fully oxidized state). The approach assumes all the oxygen in the air feed to the test is used up to oxidize nickel, i.e., fast kinetics. This was confirmed to 60% oxidation depth previously by measuring the length of time taken before oxygen was detected in the outlet gas using gas chromatography. Redox cycles to an oxidation depth of 10%, 20%, 30%, 60%, 120% (excess air flow) and 180% (excess air flow) were performed corresponding to 20, 40, 60, 120, 240 and 360 mins at 120 ml min-1 air flow into the test jig. The reason for the excess air is that as a full redox cycle (100% redox depth) is approached, not all the oxygen is used to oxidize nickel with the test arrangement utilized, so 120% is close to or represents a full redox cycle and 180% is a full redox cycle with almost double the oxygen required to oxidize all nickel in the cell supplied during the test.[14] Baseline electrochemical testing was performed comparing initial current-voltage curves and steady-state degradation testing with tests after redox cycles to varying degrees of oxidation or redox depth. Figure 2.1-29 shows the effect of redox cycles to different oxidation depths on the V-J curves for 102038. Figure 2.1-30 shows the effect on steady-state holds at 750°C, 50% Uf, 25% Uo (air) and 0.5A/cm^2 for the same test, while Figure 2.1-31 shows the same testing as Figure 2.1-28 after all of the Redox cycling.

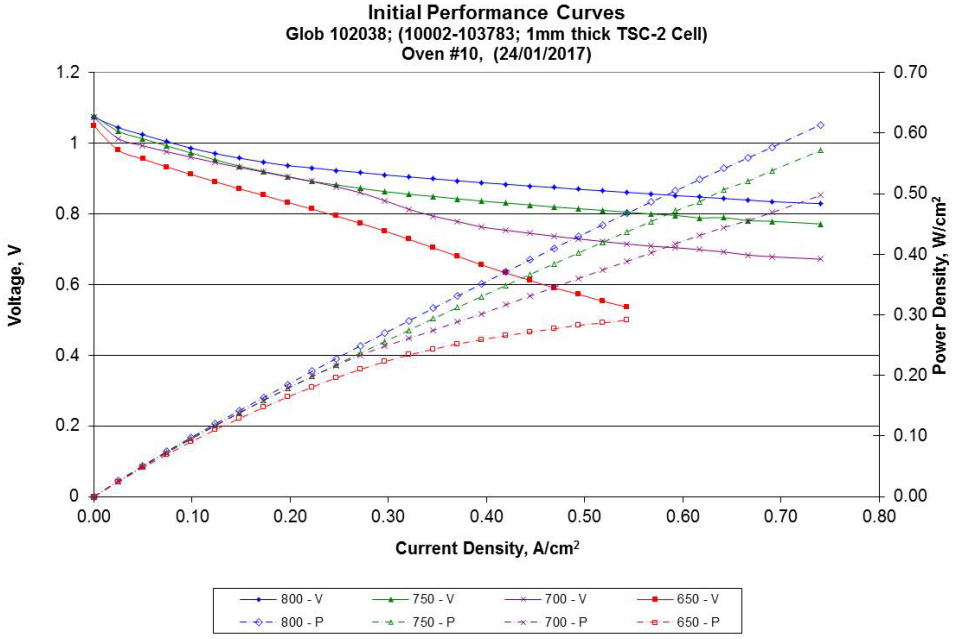

Figure 2.1-28 Test # 102038 Initial Performance Curves 650 – 800°C

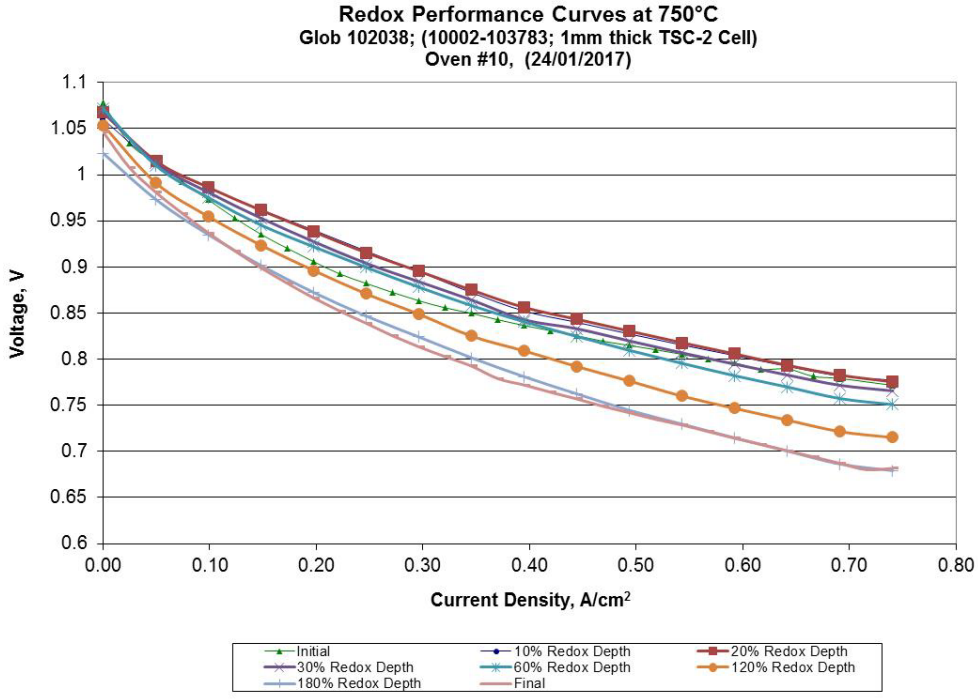

Figure 2.1-29 Test# 102038 Performance Curve Comparison to Various Redox Depths at 750°C

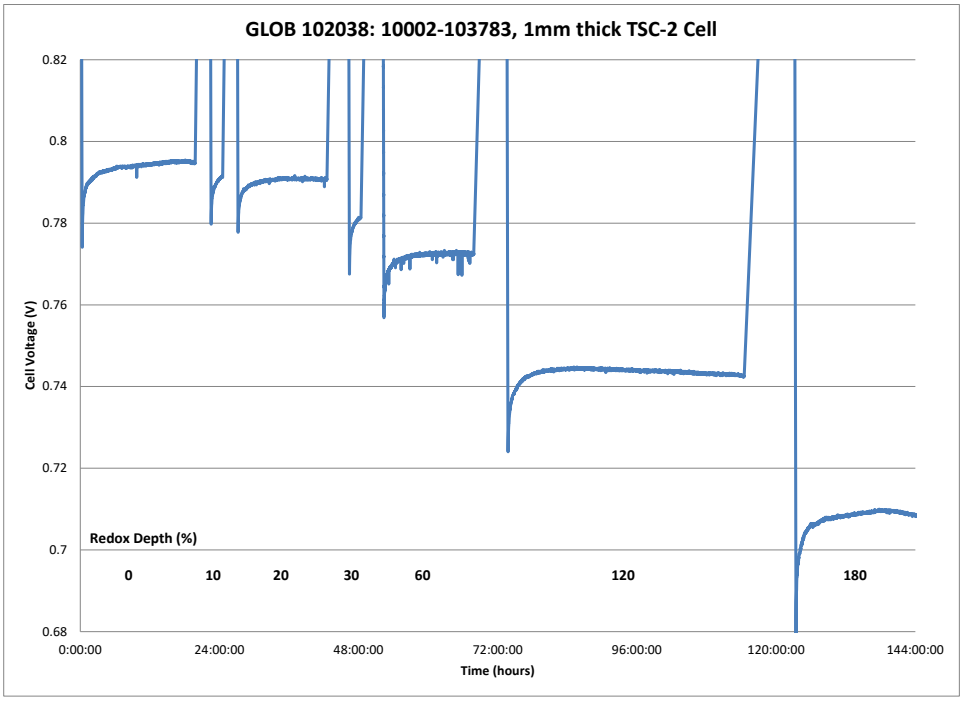

Figure 2.1-30 Test # 102038 Steady State Hold Comparison to Various Redox Depths at 750°C

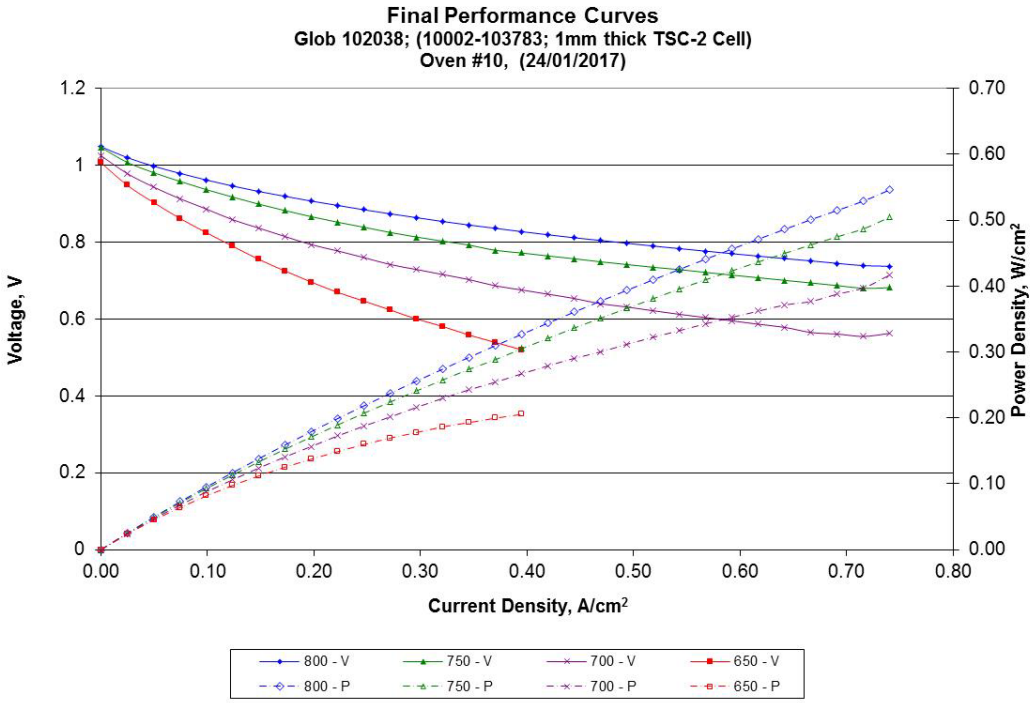

Figure 2.1-31 Test # 102038 Final Performance Curves 650 – 800°C

In a series of tests with adjustments made throughout, a successful redox tolerant cell was developed. Reported below are the 26 cells tested in the effort.

Once the test stand and testing regime were verified it was decided to apply the same methodology to baseline a series of cells that have been developed over the last 10 years with different cell thickness, nickel content and density of the anode substrate layers as well as different functional layers for some of the cells. In each case the time that air was flowing for during each Redox cycle was adjusted to account for the actual amount of nickel in the cell to maintain the same % Redox Depth per cycle irrespective of cell thickness and composition. The Redox Depths are shown clearly in each figure. The cells tested are:

1. Test # 102039, a 600um TSC-3 cell.
2. Test # 102040, a 600um 65/10 cell with increased nickel content in the anode substrate and lower density than the TSC-3 cell;
3. Test # 102041, a 335um 65/10 cell with increased nickel content in the anode substrate and lower density than the TSC-3 cell;
4. Test # 102042, a 400um RSOFC-7 cell with modified composition of the anode substrate;
5. Test # 102043, a 600um TSC-2+ cell.

Figure 2.1-32, Figure 2.1-35, Figure 2.1-39 and Figure 2.1-42 show initial power curves measured from 800 to 650°C for tests 1-4 above respectively. Figure 2.1-33, Figure 2.1-36, Figure 2.1-40 and Figure 2.1-43 show the effects of redox cycles to different oxidation depths on the V-J curves for tests 1-4 above respectively. Figure 2.1-34, Figure 2.1-37, Figure 2.1-41, and Figure 2.1-44 show the effects on steady-state holds at 750°C, 50% Uf, 25% Uo (air) and 0.5A/cm^2 for the same tests. Figure 2.1-38 shows the same testing as Figure 2.1-35 after all of the Redox cycling for test 2 above. The other tests were too damaged during the Redox cycling to perform final power curves over the full temperature range. Table 2.1-4 and Table 2.1-5 show a summary of physical properties and electrochemical performance comparison over Redox cycles for these tests and 101278, a standard TSC-2 cell tested more than 10 years ago in the same way. Clearly the anode modifications and thickness have a large impact on Redox induced degradation. Whilst it appears that thinner cells have more Redox degradation (and it starts at lower Redox Depths), it should be noted that some of these cells developed over a period of 10 years have multiple variations that could affect these results, not just the thickness and nickel content, and so the full data set is required for a comprehensive understanding of these effects.

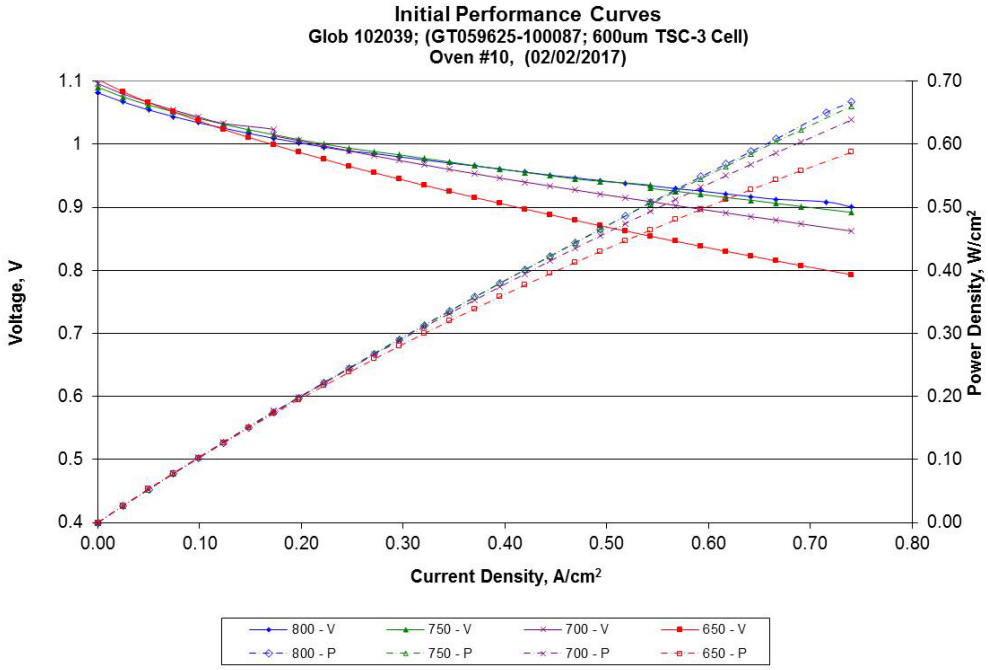

Figure 2.1-32 Test # 102039 Initial Performance Curves 650 – 800°C

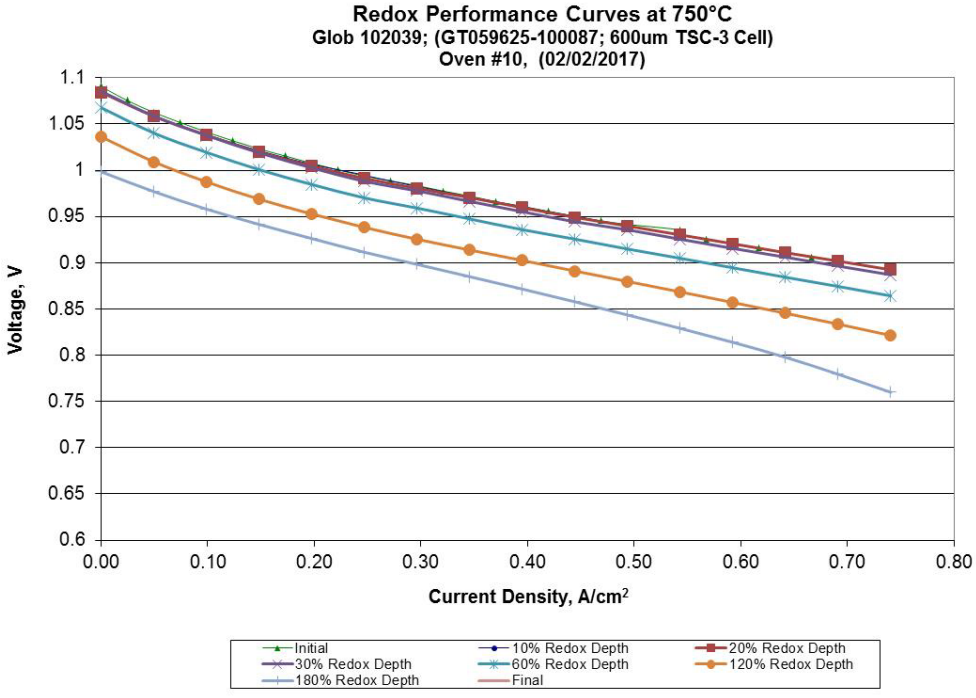

Figure 2.1-33 Test# 102039 Performance Curve Comparison to Various Redox Depths at 750°C

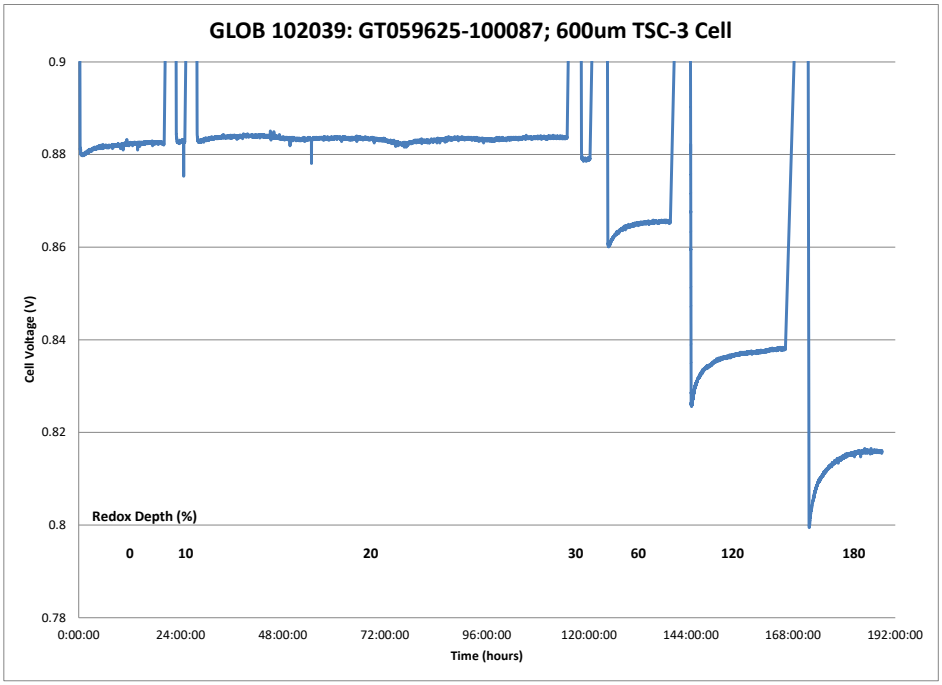

Figure 2.1-34 Test # 102039 Steady State Hold Comparison to Various Redox Depths at 750°C

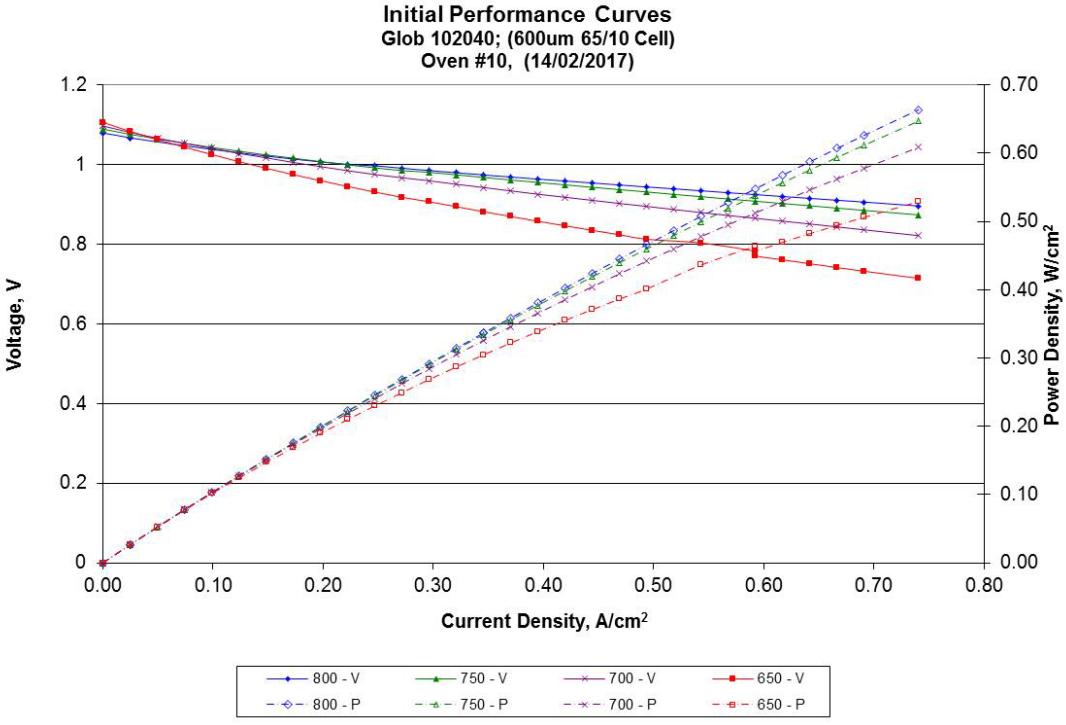

Figure 2.1-35 Test # 102040 Initial Performance Curves 650 – 800°C

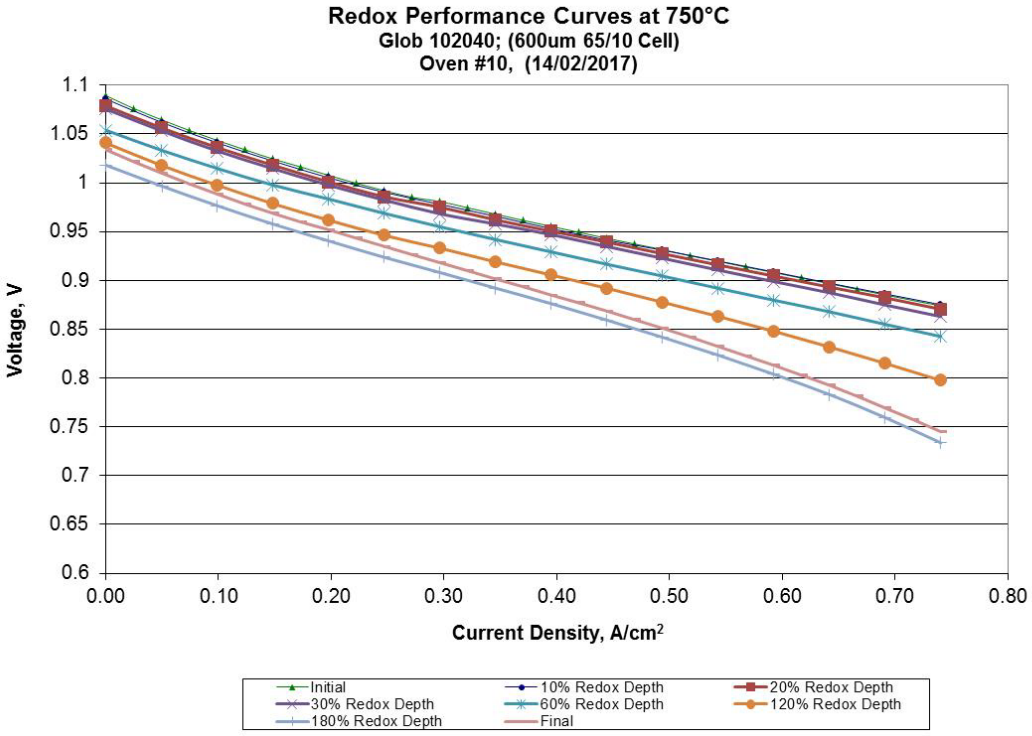

Figure 2.1-36 Test# 102040 Performance Curve Comparison to Various Redox Depths at 750°C

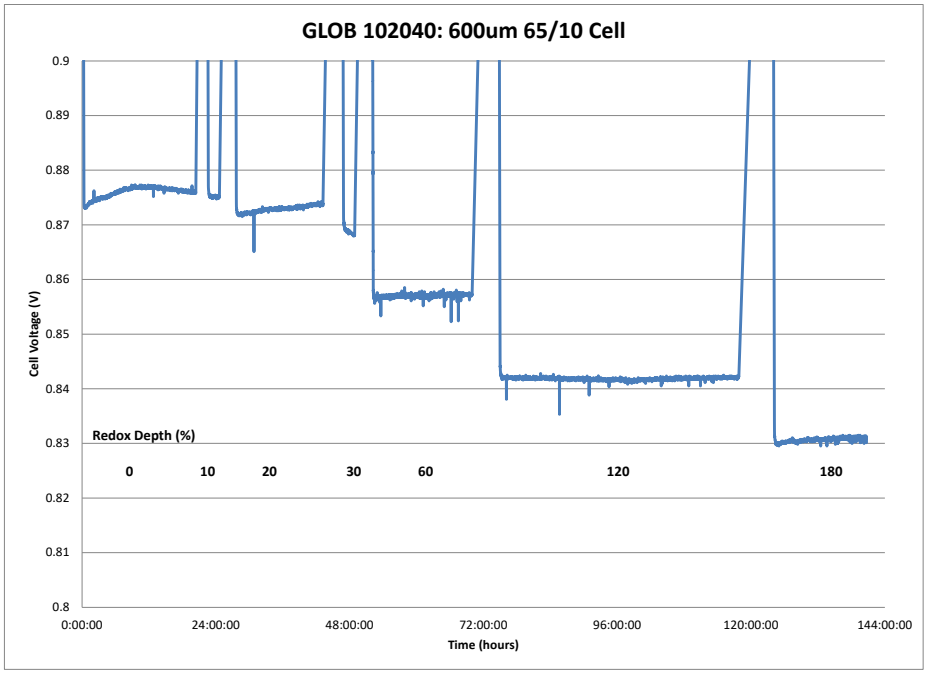

Figure 2.1-37 Test # 102040 Steady State Hold Comparison to Various Redox Depths at 750°C

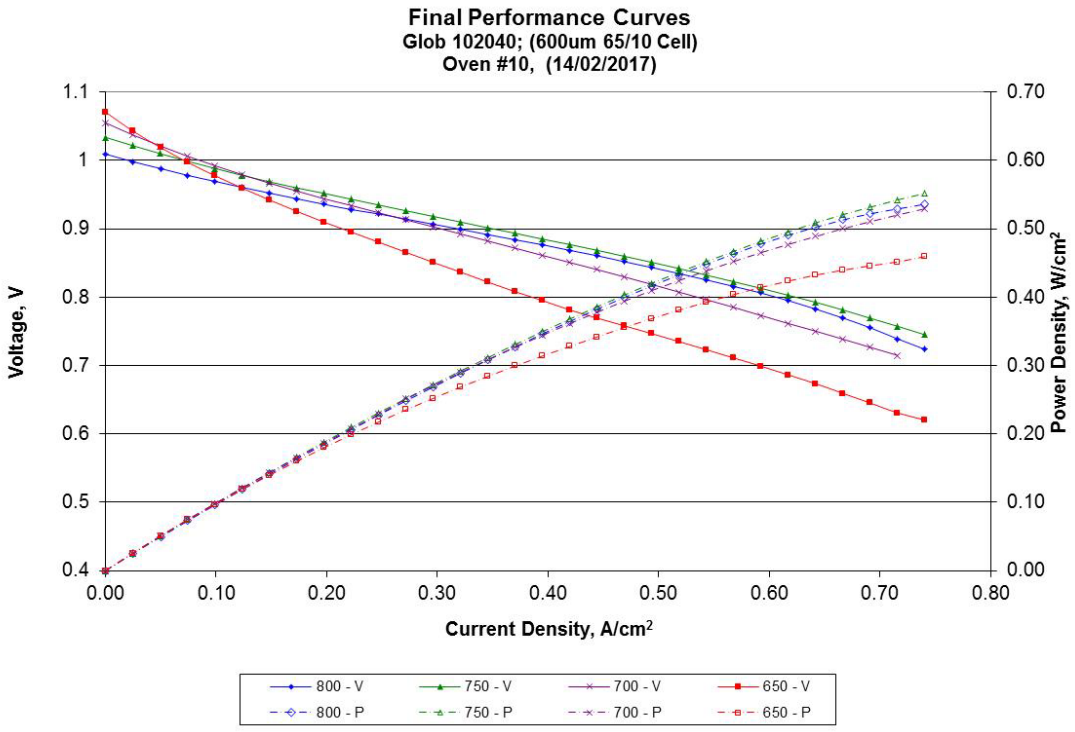

Figure 2.1-38 Test # 102040 Final Performance Curves 650 – 800°C

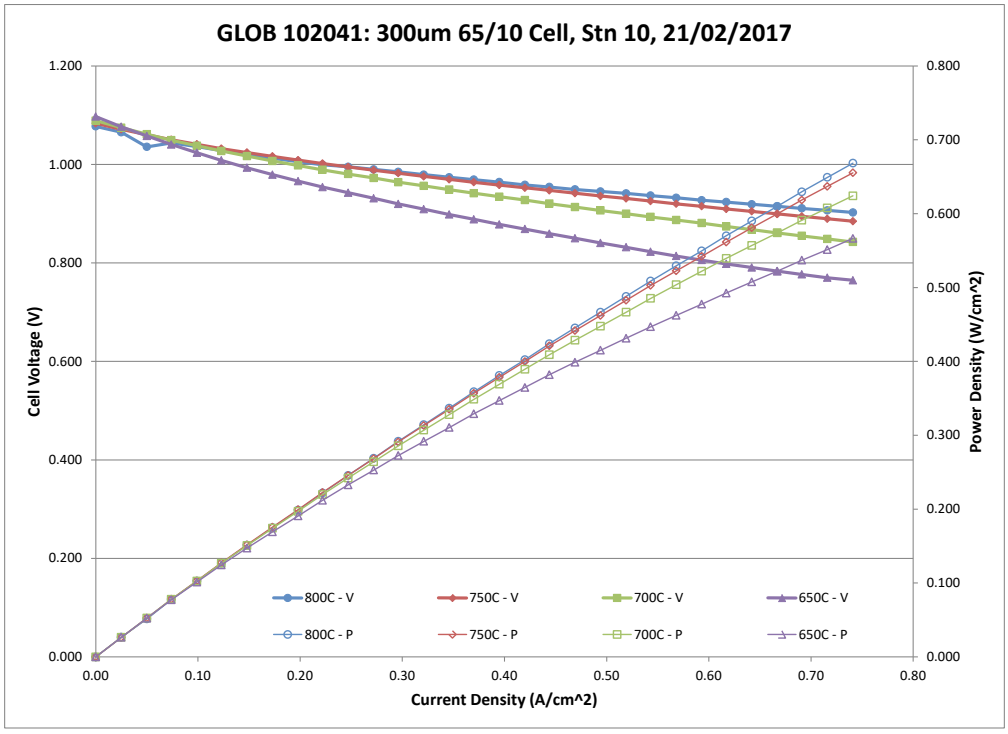

Figure 2.1-39 Test # 102041 Initial Performance Curves 650 – 800°C

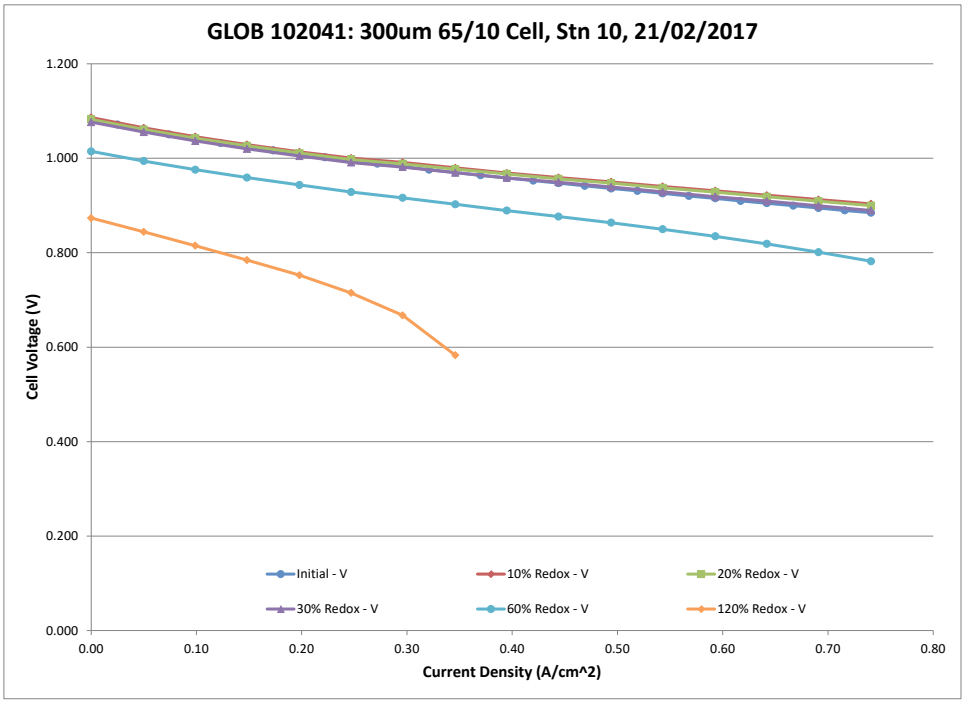

Figure 2.1-40 Test# 102041 Performance Curve Comparison to Various Redox Depths at 750°C

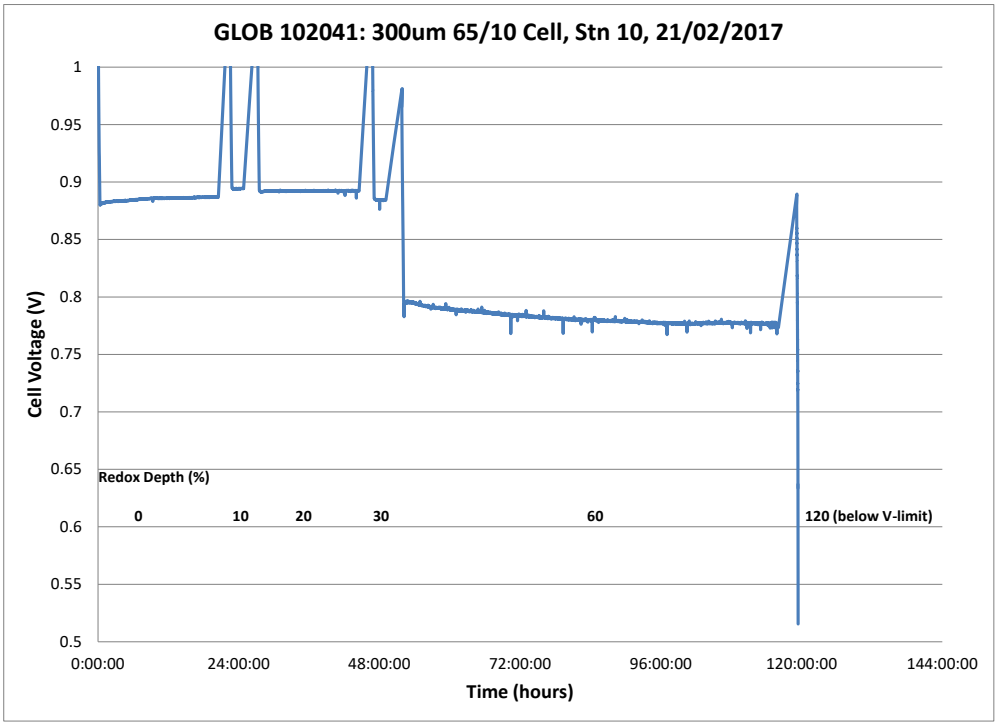

Figure 2.1-41 Test # 102041 Steady State Hold Comparison to Various Redox Depths at 750°C

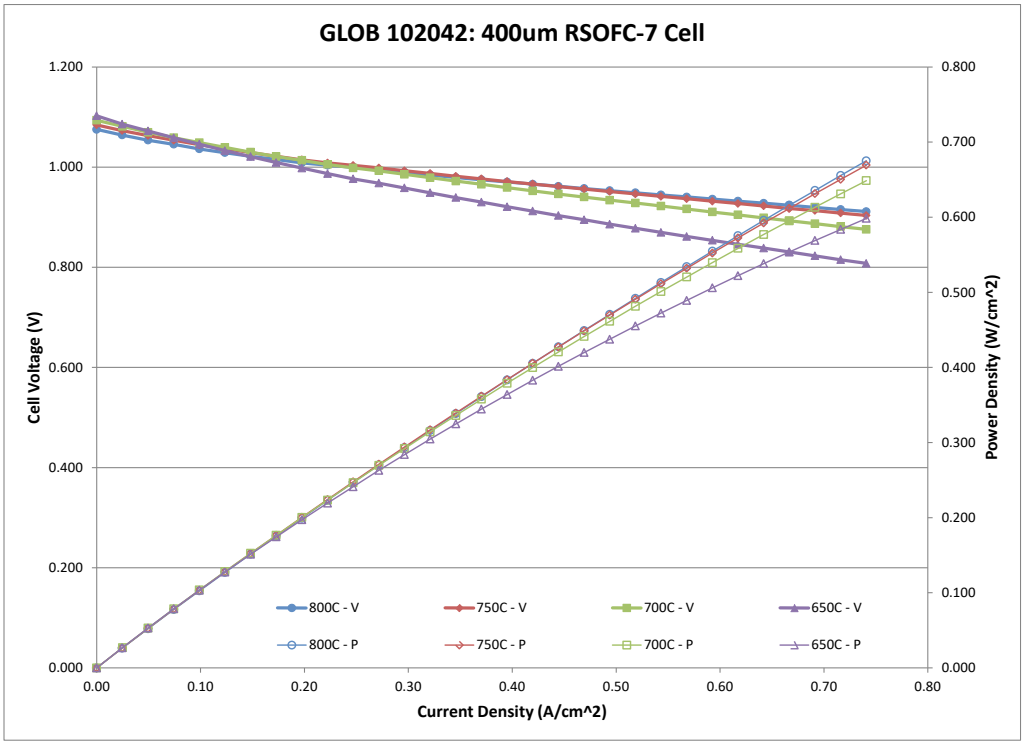

Figure 2.1-42 Test # 102042 Initial Performance Curves 650 – 800°C

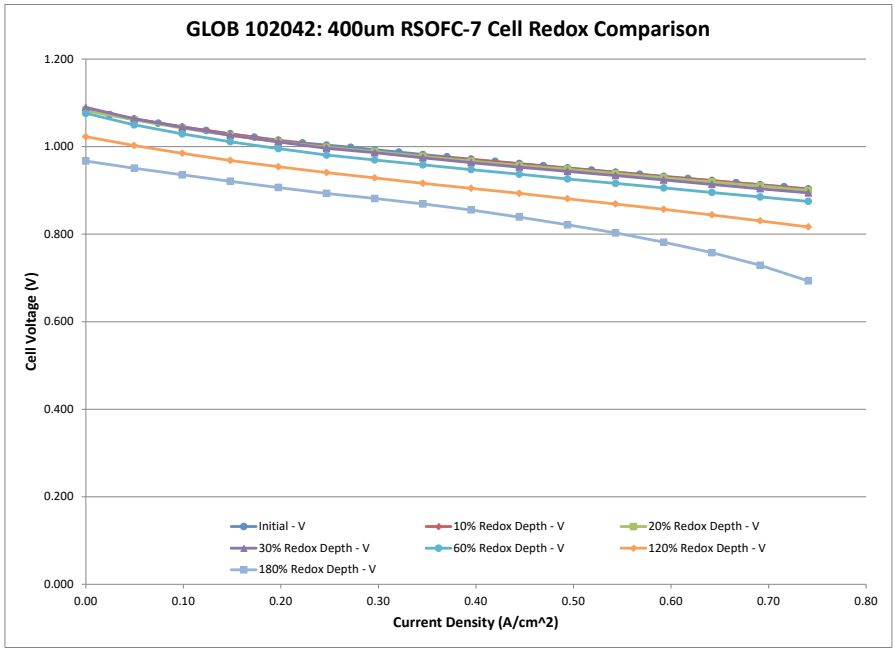

Figure 2.1-43 Test# 102042 Performance Curve Comparison to Various Redox Depths at 750°C

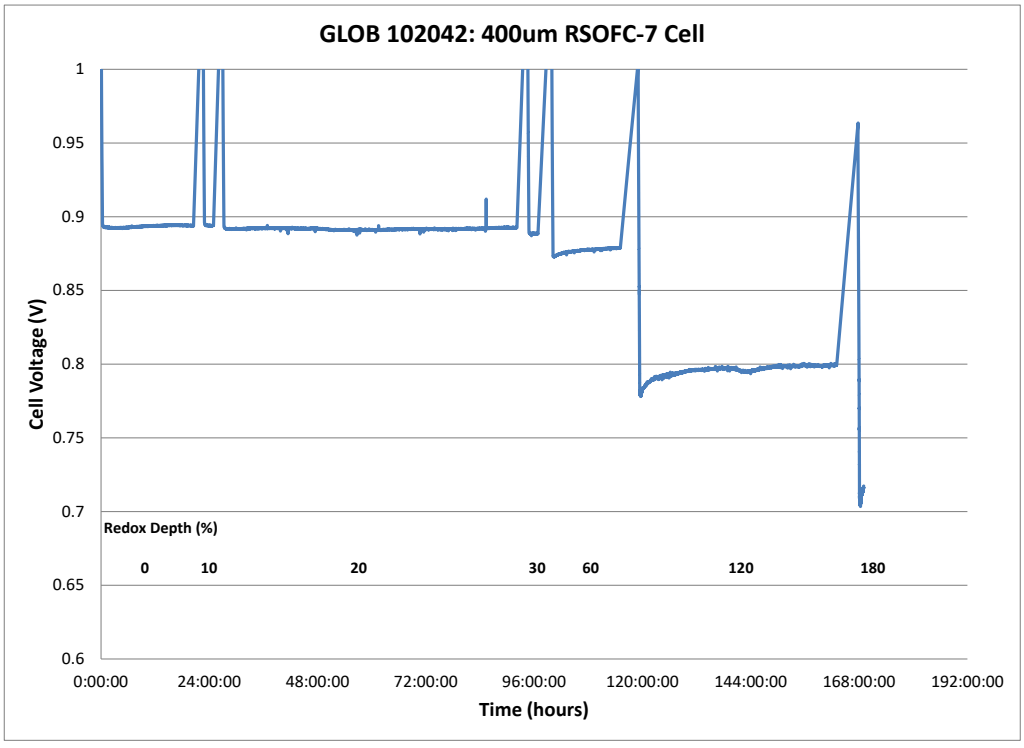

Figure 2.1-44 Test # 102042 Steady State Hold Comparison to Various Redox Depths at 750°C

Figure 2.1-45 shows initial power curves for 102043, the final baseline cell tested, a nominally 600um thick TSC-2+ cell. Figure 2.1-46 shows the effects of redox cycles to different oxidation depths on the V-J curves for this cell and Figure 2.1-47 shows the effects on steady-state holds at 750°C, 50% Uf, 25% Uo (air) and 0.5A/cm^2 for the same test. As can be seen the cell failed at 180% Redox depth, and was not able to run at 50% Uf condition. Autopsy showed the cell was broken.

This same testing methodology was applied to a series of cells based on the nominally 600um thick cells used in large area stacks, but with materials modifications designed to improve Redox tolerance compared with baseline cells. In each case the time that air was flowing for during each Redox cycle was adjusted to account for the actual amount of nickel in the cell to maintain the same % Redox Depth per cycle irrespective of cell thickness and composition.

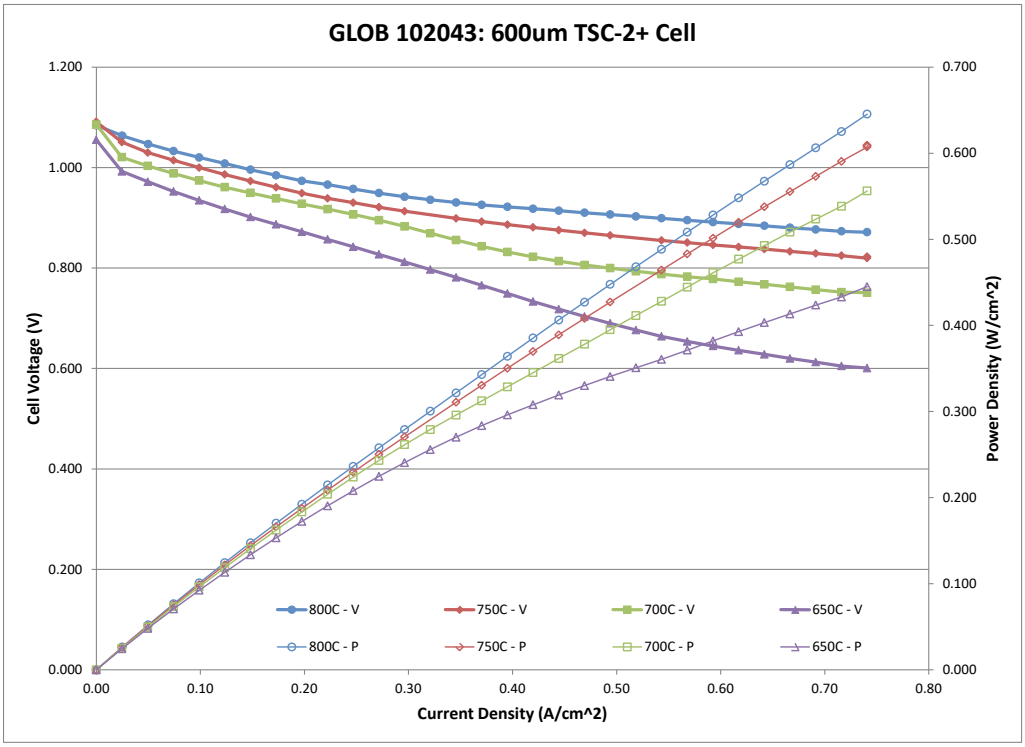

Figure 2.1-45 Test 102043 Initial Performance Curves 650 – 800°C

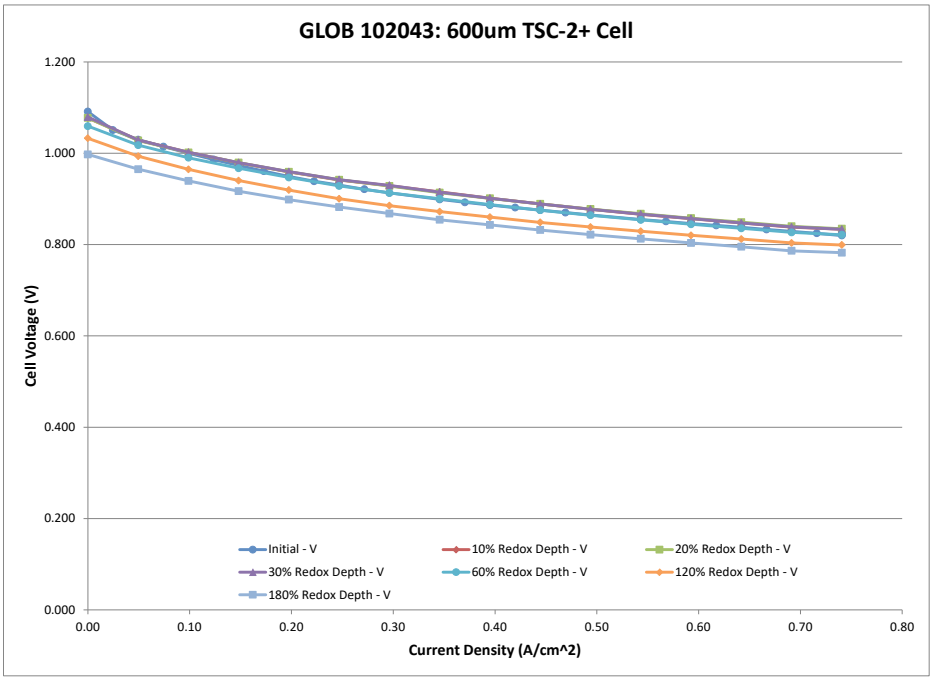

Figure 2.1-46 Test 102043 Performance Curves at Various Redox Depths at 750°C

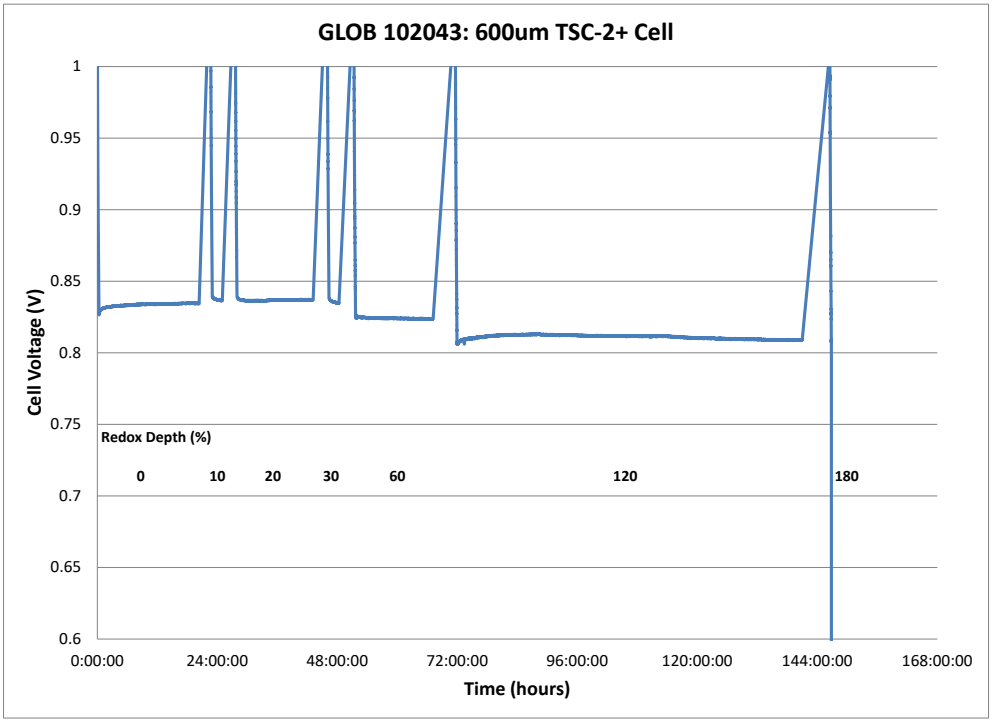

Figure 2.1-47 Test 102043 Steady State Hold Results at Various Redox Depths at 750°C

The redox depths are shown clearly in each figure that follows. Six additional cells were tested (in addition to the final baseline test already described). The cells tested are:

1. Test # 102044, a 600um TSC-3 cell with 5% iron and stronger YSZ skeleton in the anode support, low temperature fired.
2. Test # 102046, a repeat of 102044 to confirm the results;
3. Test # 102048, a repeat of 102039 600um TSC-3 cell as used in stacks to confirm the test stand has no issues after multiple plant power failures and to confirm the baseline for current laser area stack cells Redox tolerance;
4. Test # 102050, a 600um TSC-3 cell with 10% iron replacing some of the Nickel in the AFL;
5. Test # 102053, a 600um TSC-3 cell with oxidation barrier layer and 3-layer graded Nickel content of the AFL layers.
6. Test # 102056, a 600um TSC-3 cell with oxidation barrier layer and 2-layer graded Nickel content of the AFL layers.

Figure 2.1-48, rom 800°C to 650°C for tests 1-6 above respectively. Figure 2.1-49, Figure 2.1-52, Figure 2.1-55, Figure 2.1-58, Figure 2.1-61 and Figure 2.1-64 show the effects of redox cycles to different oxidation depths on the V-J curves for tests 1-Figure 2.1-51, Figure 2.1-54, Figure 2.1-57, Figure 2.1-60 and Figure 2.1-63 show initial power curves measured f 6 above respectively. Figure 2.1-50, Figure 2.1-53, Figure 2.1-56, Figure 2.1-59, Figure 2.1-62 and Figure 2.1-65 show the effects on steady-state holds at 750°C, 50% Uf, 25% Uo (air) and 0.5A/cm^2 for the same tests. Figure 2.1-66 shows the same testing as Figure 2.1-63 after all of the Redox cycling for test 6 above.

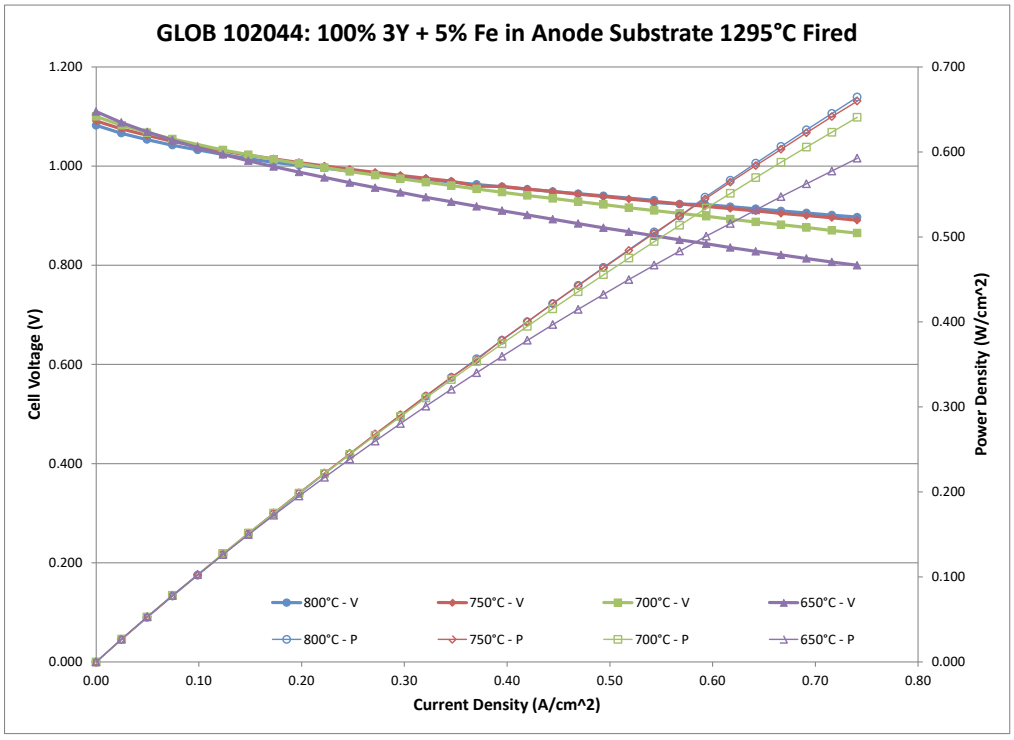

Figure 2.1-48 Test 102044 Initial Performance Curves 650 – 800°C.

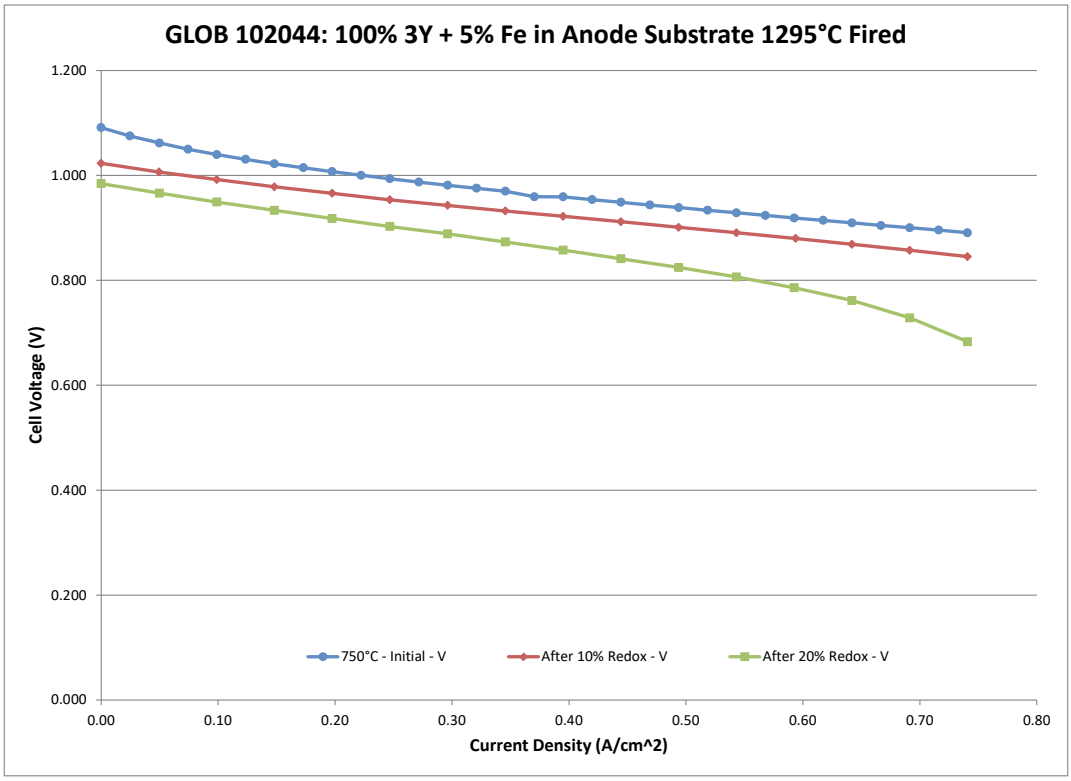

Figure 2.1-49 Test 102044 Performance Curves at Various Redox Depths at 750°C.

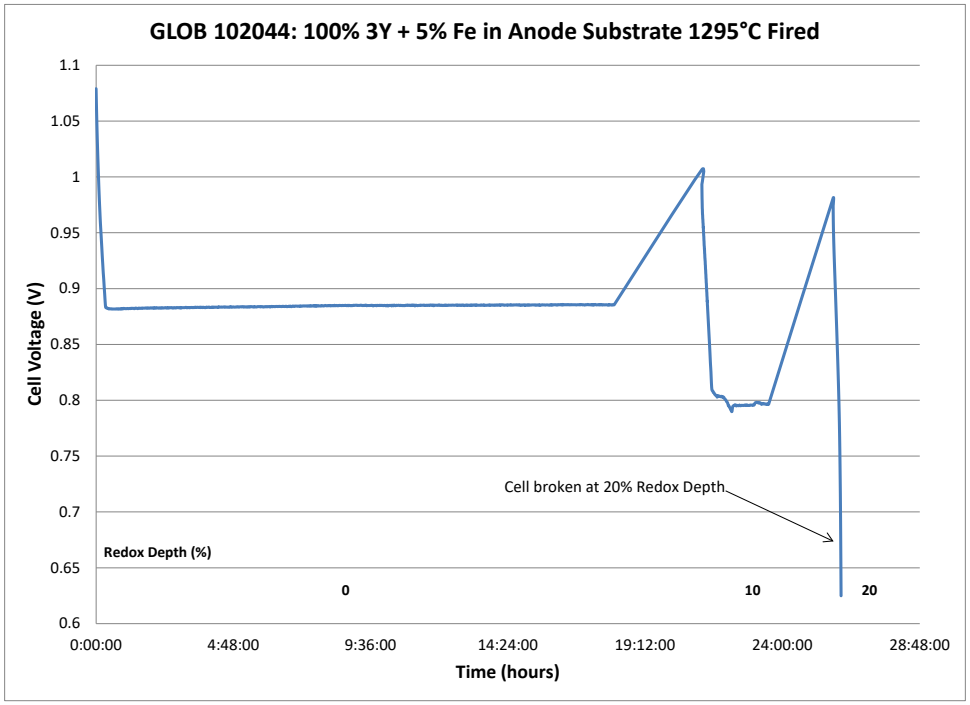

Figure 2.1-50 Test 102044 Steady State Hold Results at Various Redox Depths at 750°C

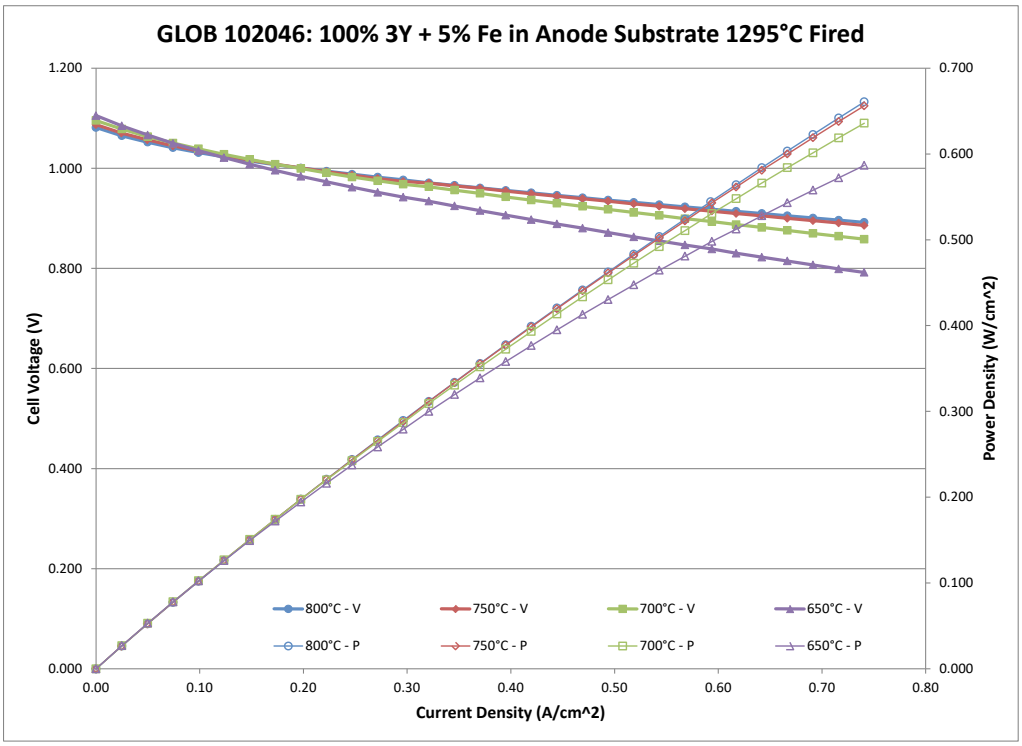

Figure 2.1-51 Test 102046 Initial Performance Curves 650 – 800°C

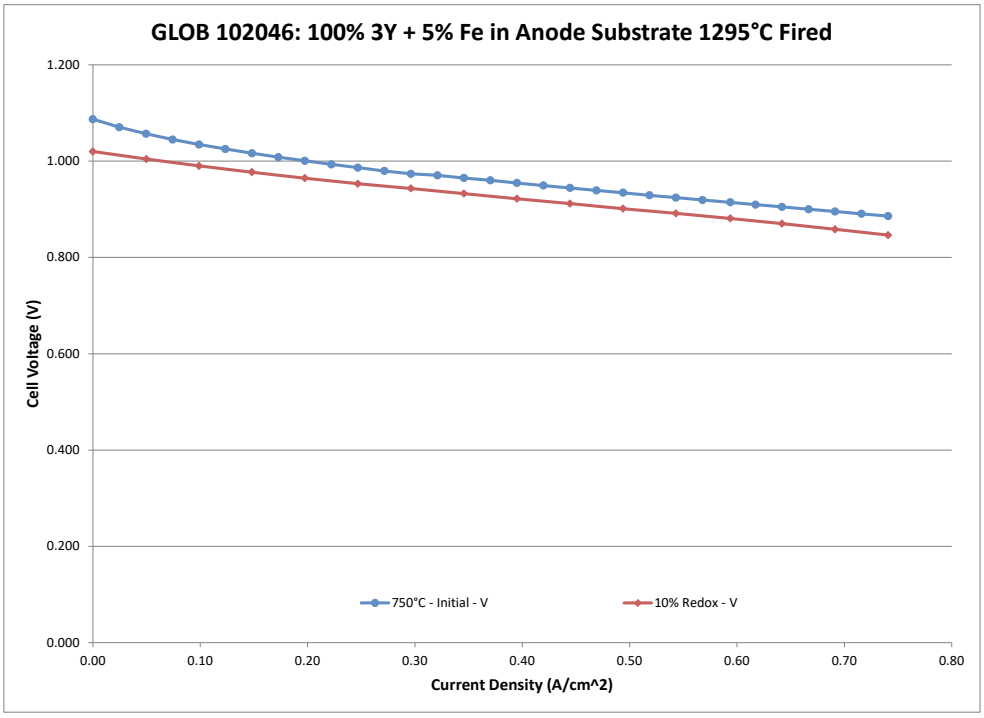

Figure 2.1-52 Test 102043 Performance Curves at Various Redox Depths at 750°C

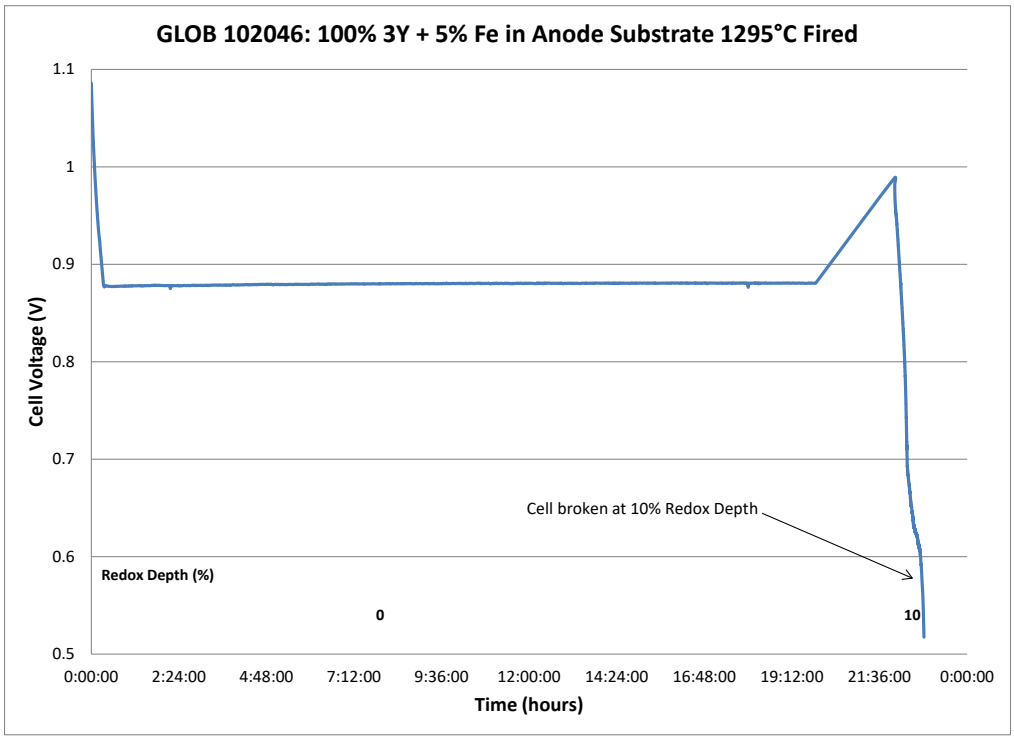

Figure 2.1-53 Test 102046 Steady State Hold Results at Various Redox Depths at 750°C

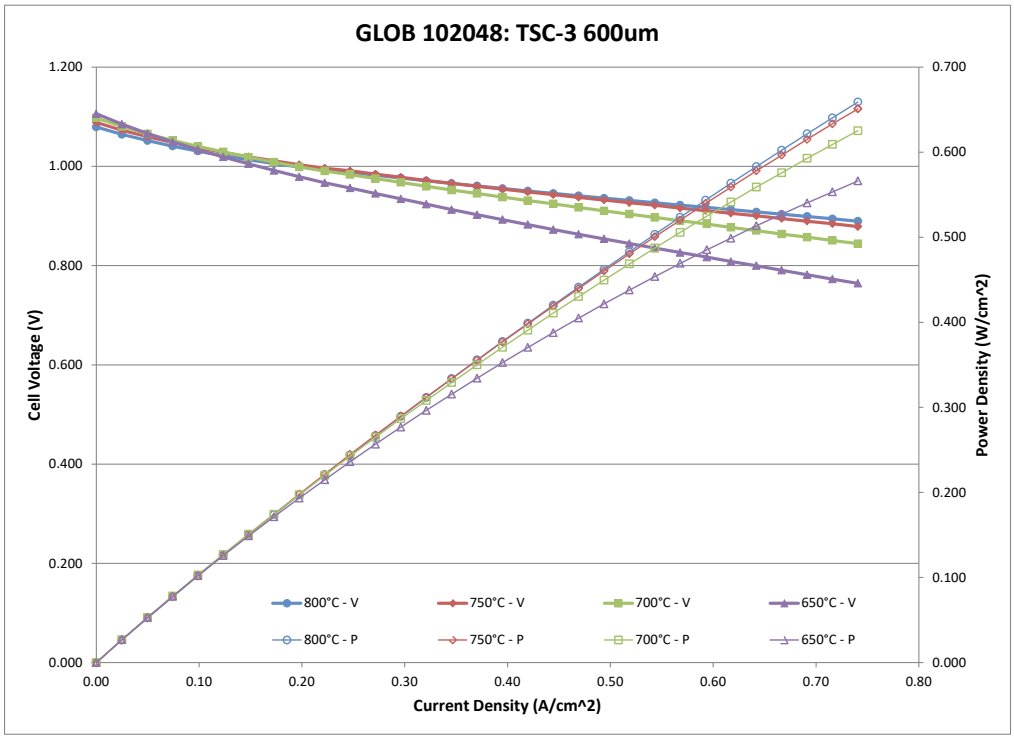

Figure 2.1-54 Test 102048 Initial Performance Curves 650 – 800°C

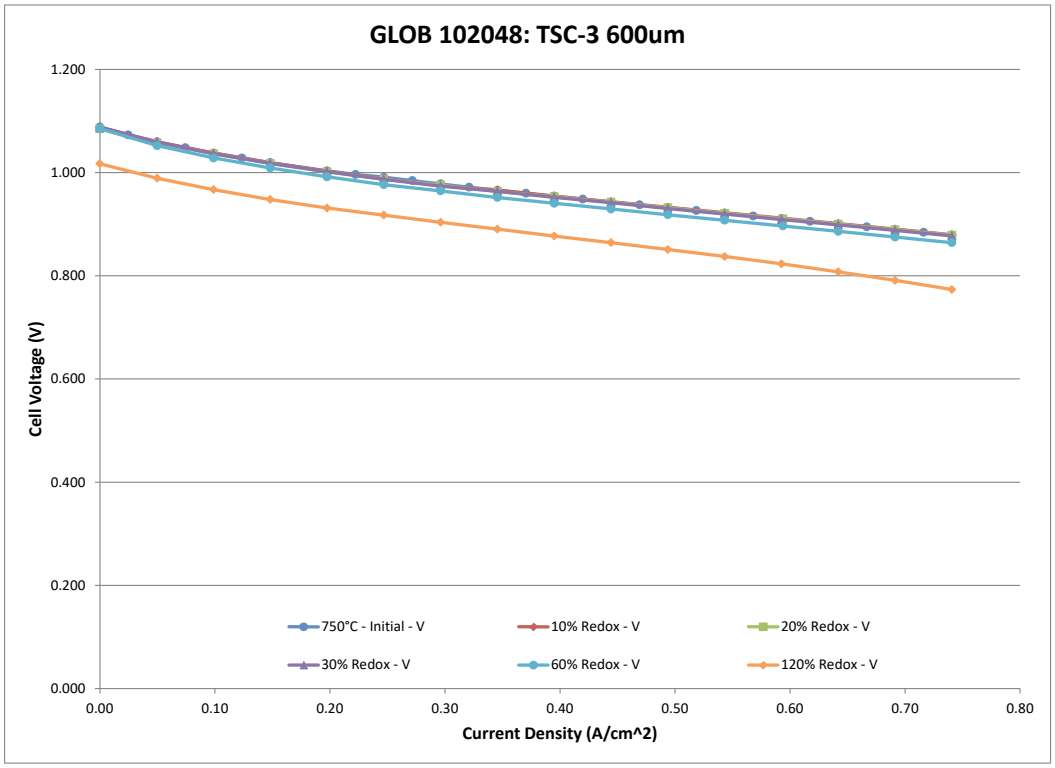

Figure 2.1-55 Test 102048 Performance Curves at Various Redox Depths at 750°C

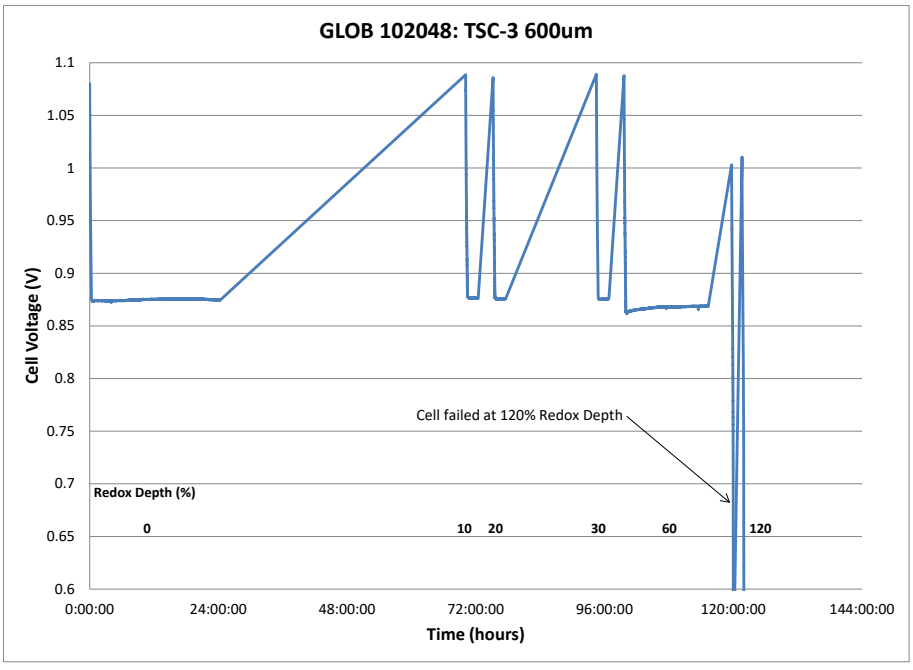

Figure 2.1-56 Test 102048 Steady State Hold to Various Redox Depths at 750°C

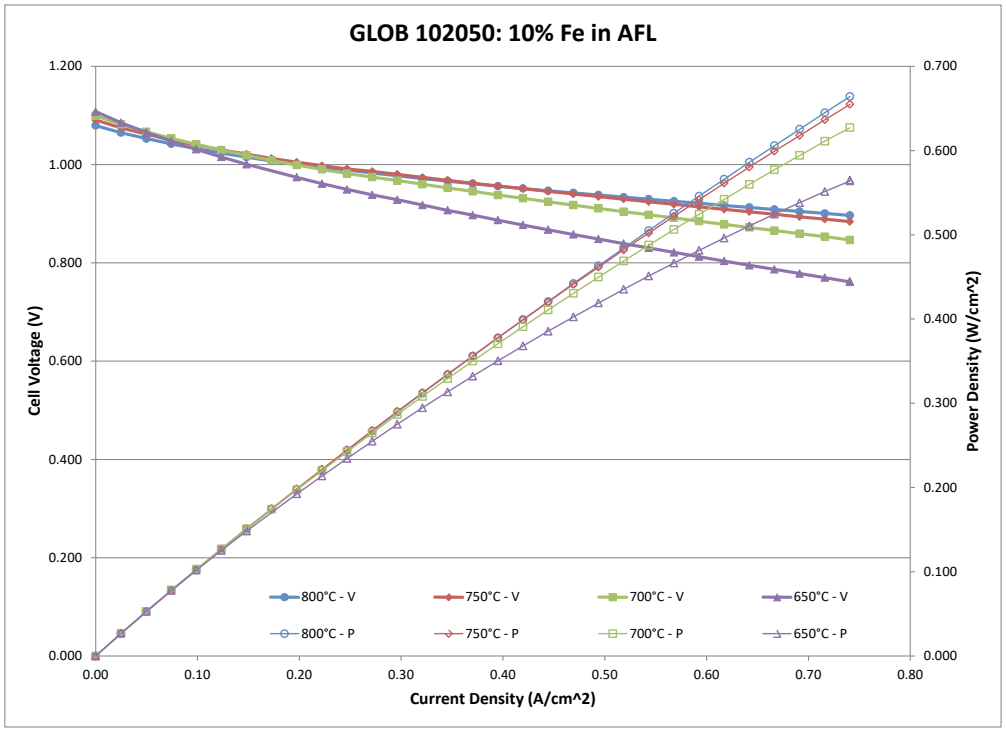

Figure 2.1-57 Test 102050 Initial Performance Curves 650 – 800°C.

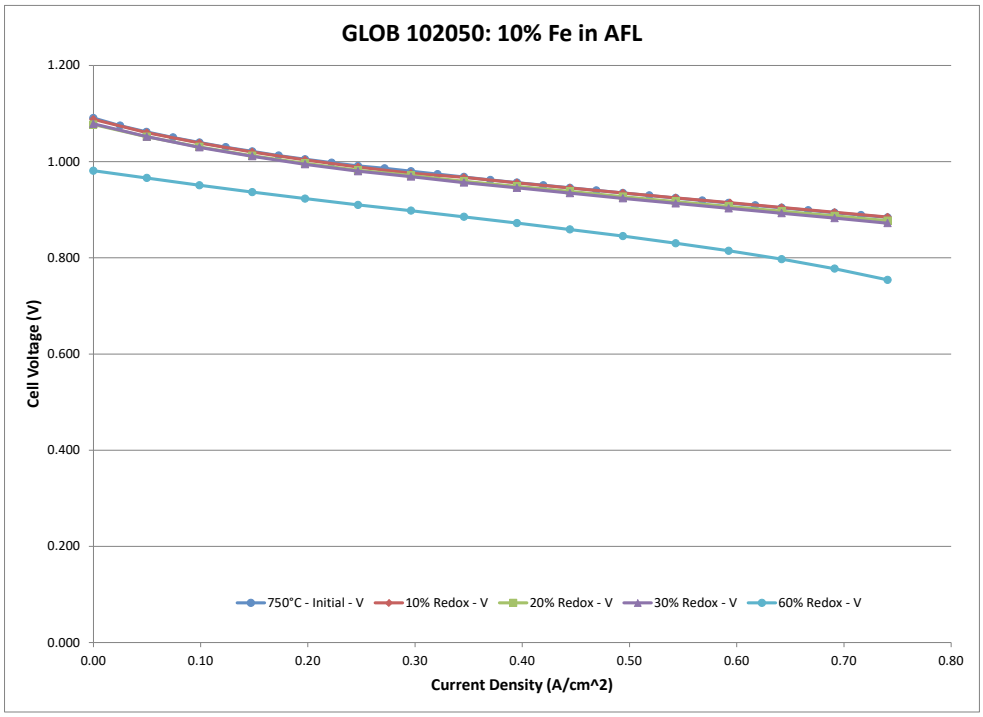

Figure 2.1-58 Test 102050 Performance Curves at Various Redox Depths at 750°C

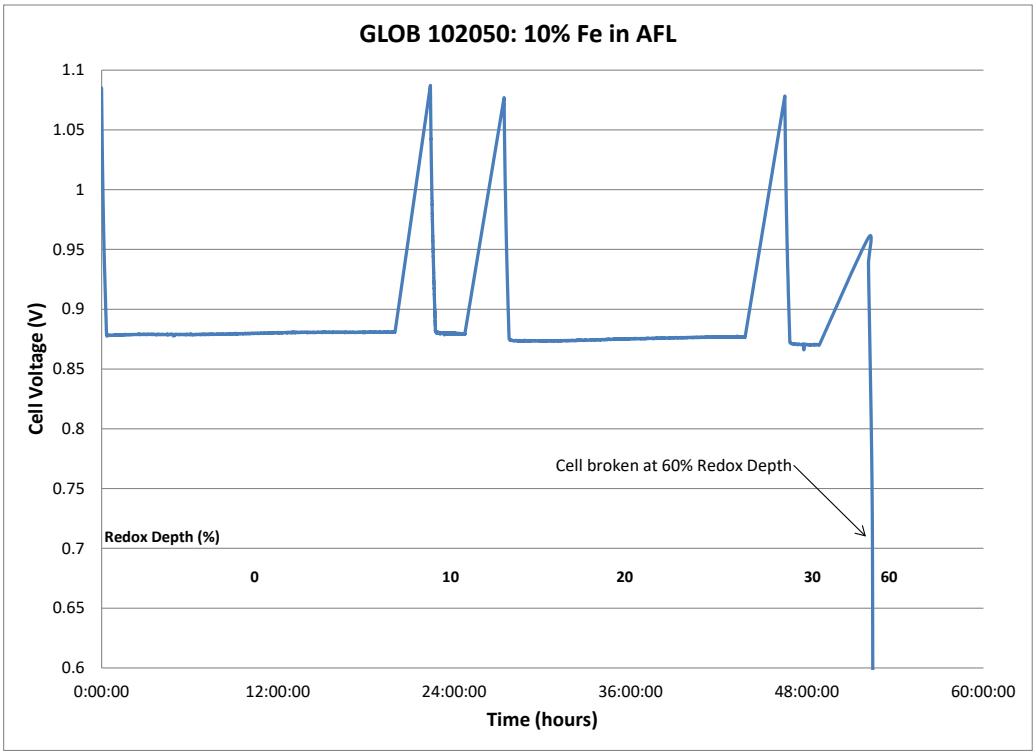

Figure 2.1-59 Test 102050 Steady State Hold Results at Various Redox Depths at 750°C

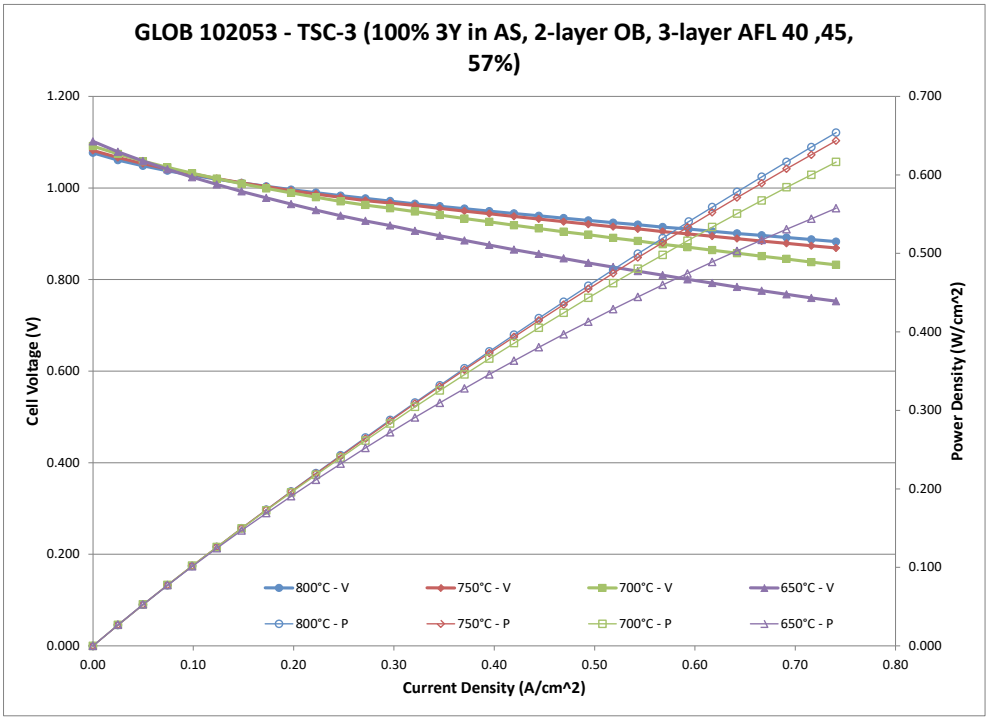

Figure 2.1-60 Test 102053 Initial Performance Curves 650 – 800°C.

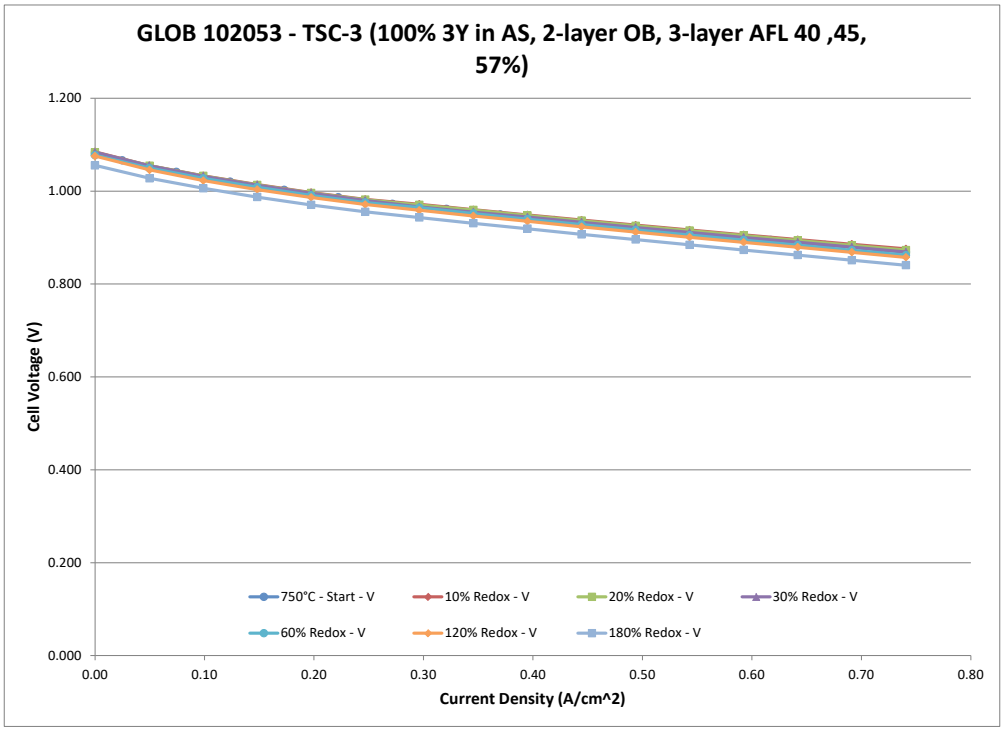

Figure 2.1-61 Test 102053 Performance Curves at Various Redox Depths at 750°C

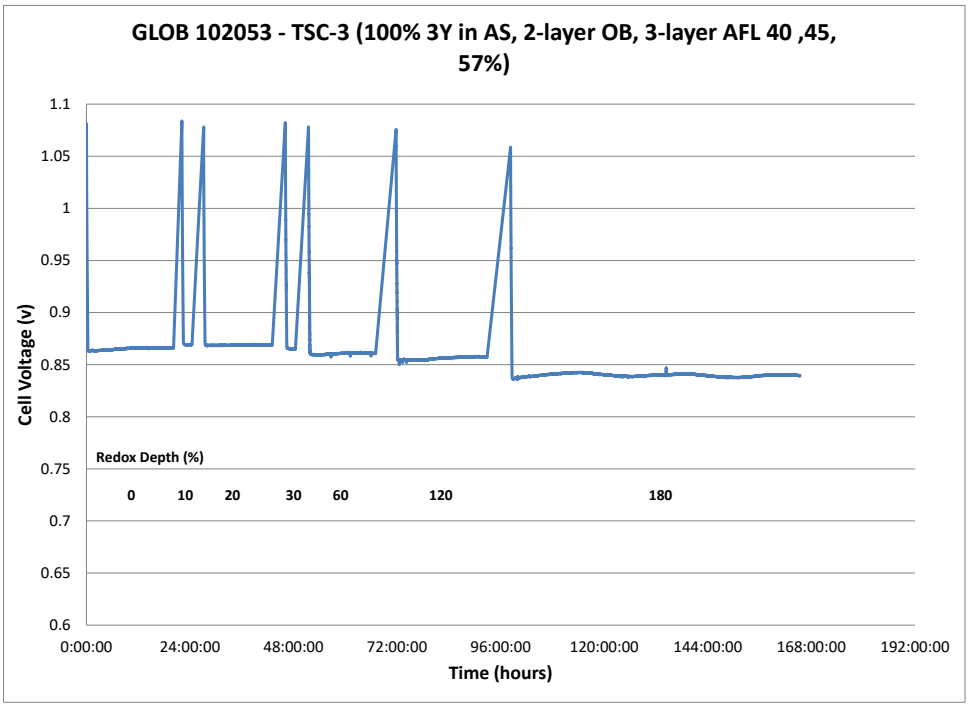

Figure 2.1-62 Test 102053 Steady State Hold Results at Various Redox Depths at 750°C

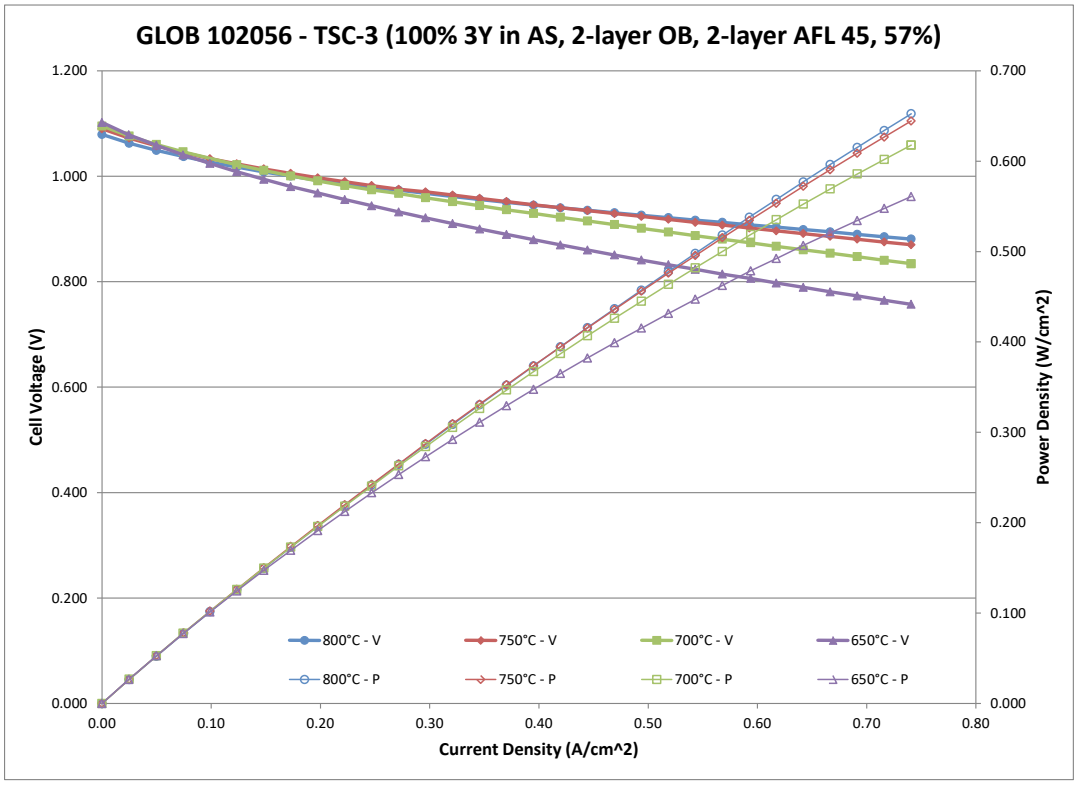

Figure 2.1-63 Test 102056 Initial Performance Curves 650 – 800°C

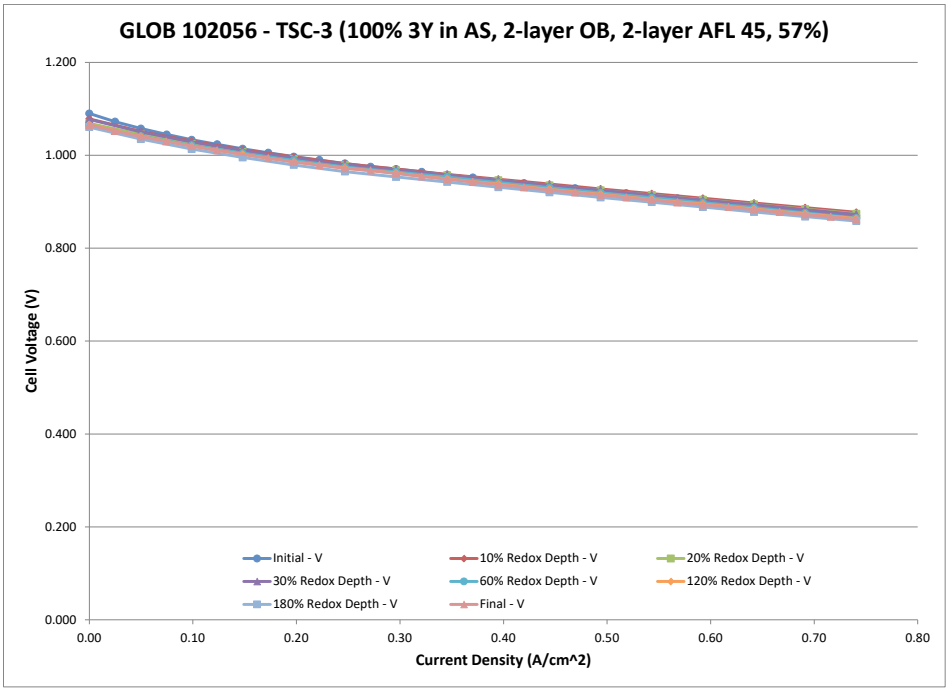

Figure 2.1-64 Test 102056 Performance Curves at Various Redox Depths at 750°C

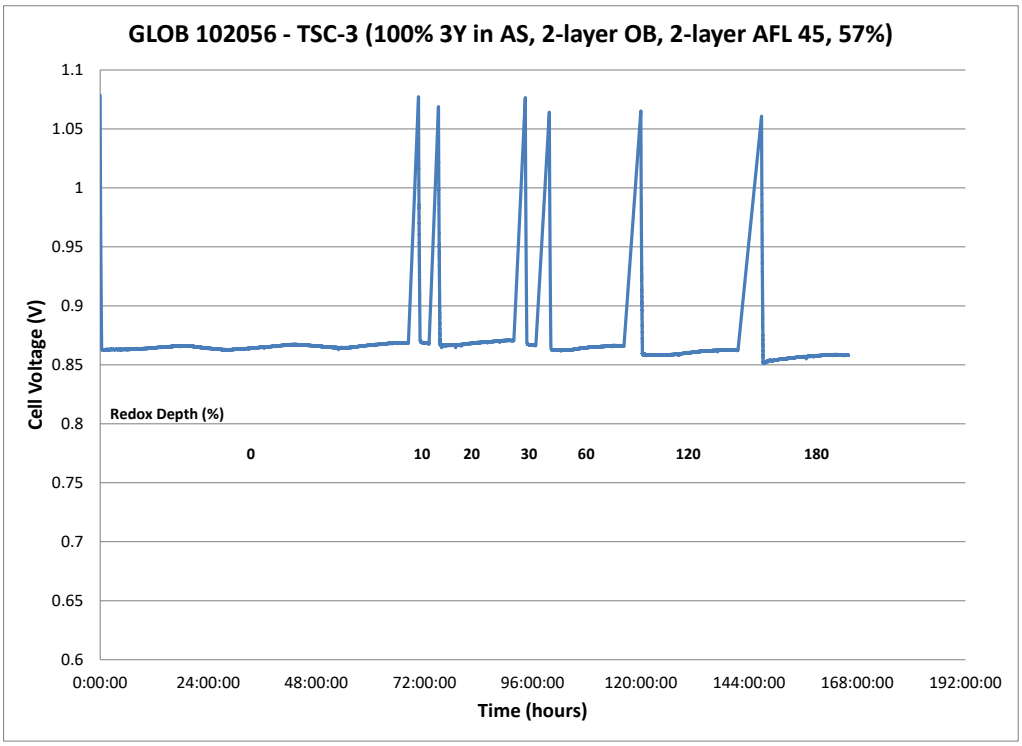

Figure 2.1-65 Test 102056 Steady State Hold Results at Various Redox Depths at 750°C

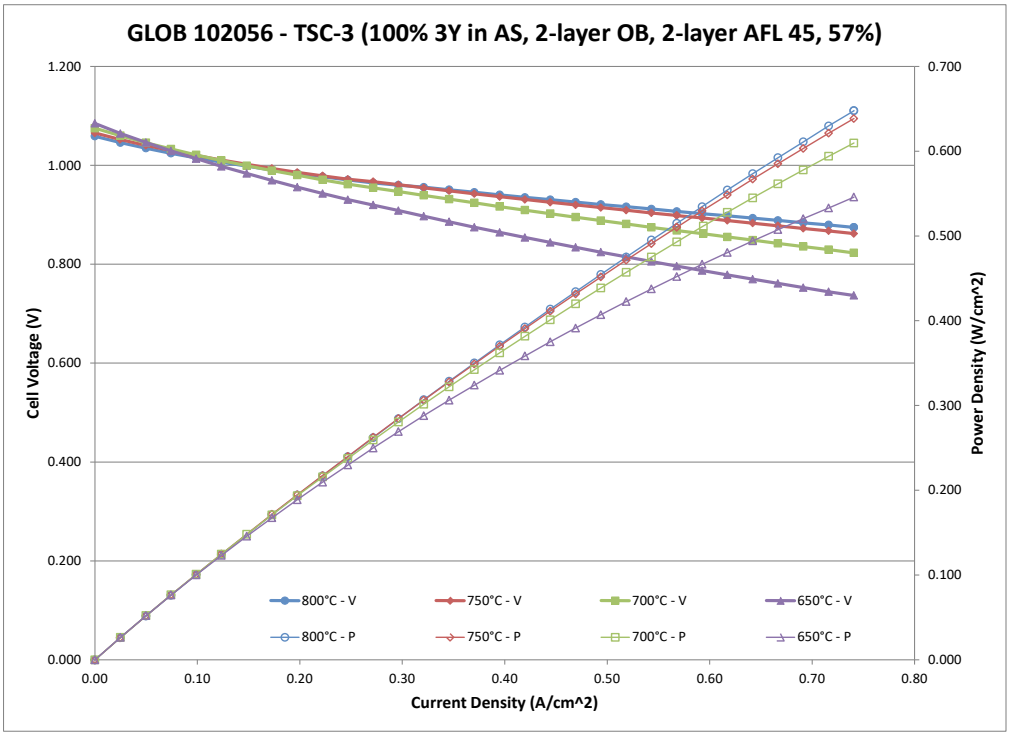

Figure 2.1-66 Test 102056 Final Performance Curves 650 – 800°C

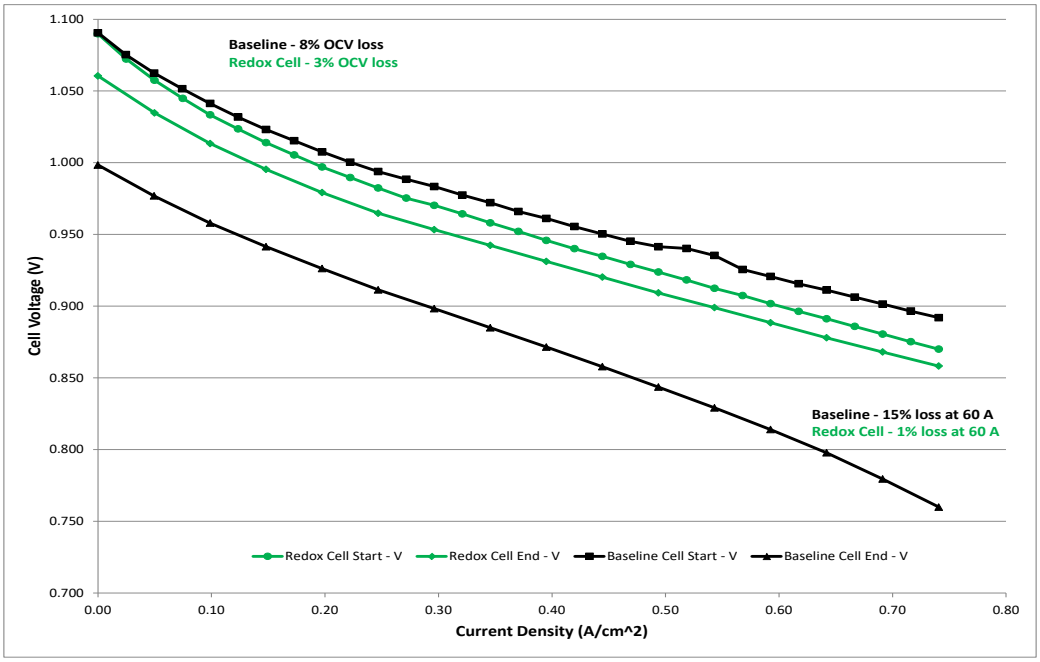

Figure 2.1-67 Initial and Final V-J Curves at 750°C,

Baseline (102039) vs Improved (102056) Redox Cells

While it appears that thinner cells have more Redox degradation (and it starts at lower Redox Depths), it should be noted that some of these cells developed over a period of ten years have multiple variations that could affect these results, not just the thickness and nickel content. The full data set is required for a comprehensive understanding of these effects. In addition, iron addition to the anode substrate for the purpose of lowering sintering temperature clearly has a significant deleterious effect on Redox degradation with cells failing after 10-20% oxidation, unheard of with Nickel based cells that don't contain iron. Iron has a significantly higher volume expansion upon oxidation than nickel and this appears to explain the catastrophic effects of iron addition on Redox tolerance.

Figure 2.1-67 showing the initial and final power curve comparison after cumulative Redox cycles for a baseline cell and 102056 the latest cell developed and tested. OCV degradation has been reduced almost 3-fold while degradation at high current density (0.74 A/cm^2) has been reduced 15-fold compared with the baseline cell currently used in large area stacks.

Figure 2.1-68 shows initial power curves for 102059, a 600um TSC-3 cell with graded 3-layer AFL. Figure 2.1-69 shows the effects of redox cycles to different oxidation depths on the V-J curves for this cell and Figure 2.1-70 shows the effects on steady-state holds at 750°C, 50% Uf, 25% Uo (air) and 0.5A/cm^2 for the same test. As can be seen the cell had the lowest degradation at the time of testing of any cell with the exception of those cells with Oxidation barrier layers.

This same testing methodology was applied to a series of cells based on the nominally 600um thick cells used in large area stacks, but with materials modifications designed to improve Redox tolerance compared with baseline cells. In each case the time that air was flowing for during each Redox cycle was adjusted to account for the actual amount of nickel in the cell to maintain the same % Redox Depth per cycle irrespective of cell thickness and composition.

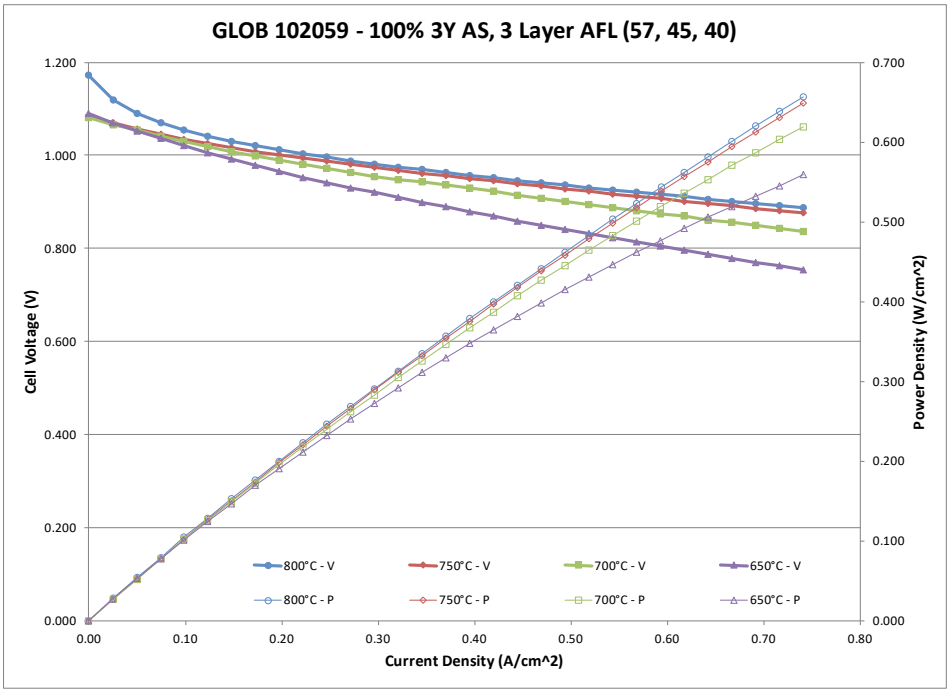

Figure 2.1-68 Test 102059 Initial Performance Curves 650 – 800°C

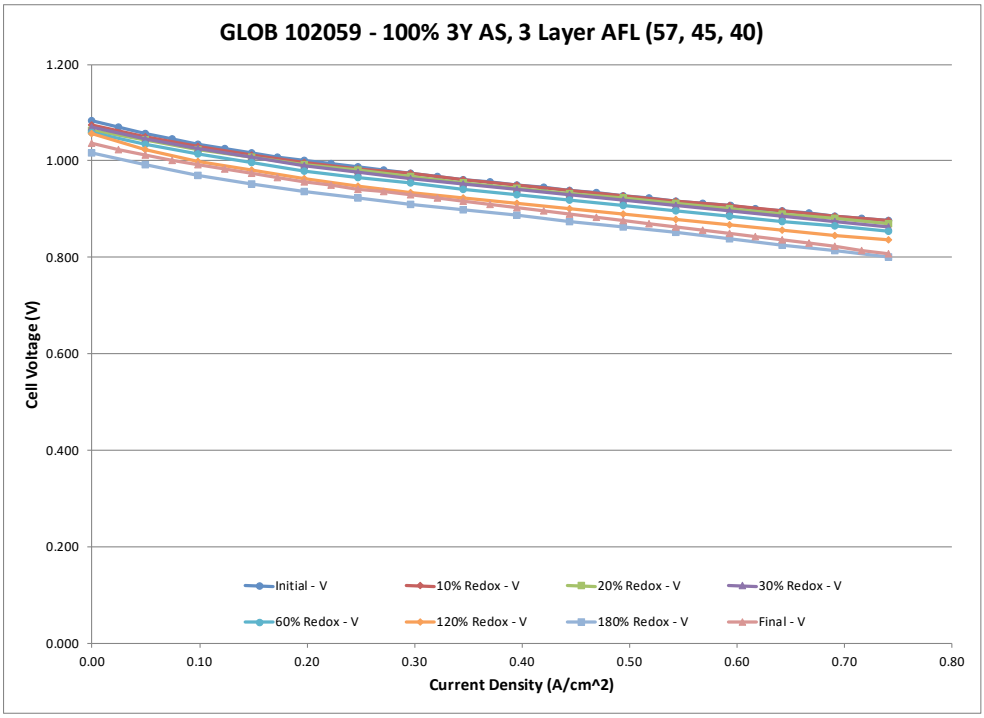

Figure 2.1-69 Test 102059 Performance Curves at Various Redox Depths at 750°C

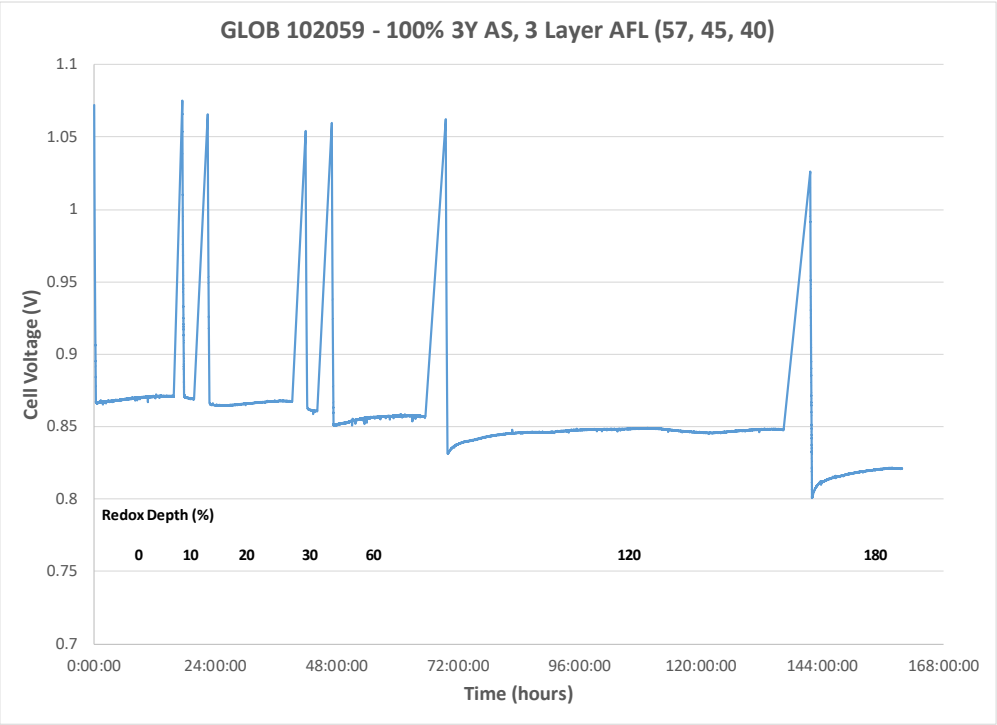

Figure 2.1-70 Test 102059 Steady State Hold Results at Various Redox Depths at 750°C

The cells tested are:

1. Test # 102059, a 600um TSC-3 cell with 3-layer graded Nickel content of the AFL layers;
2. Test # 102062, a 600um TSC-3 cell with 2-layer graded Nickel content of the AFL layers;
3. Test # 102064, a 600um TSC-3 cell with oxidation barrier layer and 2-layer graded Nickel content of the AFL layers;
4. Test # 102067 a 600um TSC-3 cell with 2-layer graded Nickel content of the AFL layers;
5. Test # 102072, a 600um TSC-3 cell with 4 oxidation barrier layers;
6. Test # 102073, a 600um TSC-3 cell with modified composition of oxidation barrier layers (OB-1);
7. Test # 102076, a 600um TSC-3 cell with modified composition of oxidation barrier layers (OB-2).

Figure 2.1-71, Figure 2.1-74, Figure 2.1-77, Figure 2.1-80, and Figure 2.1-83 show initial power curves measured from 800°C to 650°C for tests 2 through 6 above respectively Figure 2.1-72, Figure 2.1-75, Figure 2.1-78,Figure 2.1-81 and Figure 2.1-84 show the effects of redox cycles to different oxidation depths on the V-J curves for tests 2 through 6 above respectively. Figure 2.1-73, Figure 2.1-76, Figure 2.1-79, Figure 2.1-82, and Figure 2.1-85 show the effects on steady-state holds at 750°C, 50% Uf, 25% Uo (air) and 0.5A/cm^2 for the same tests.

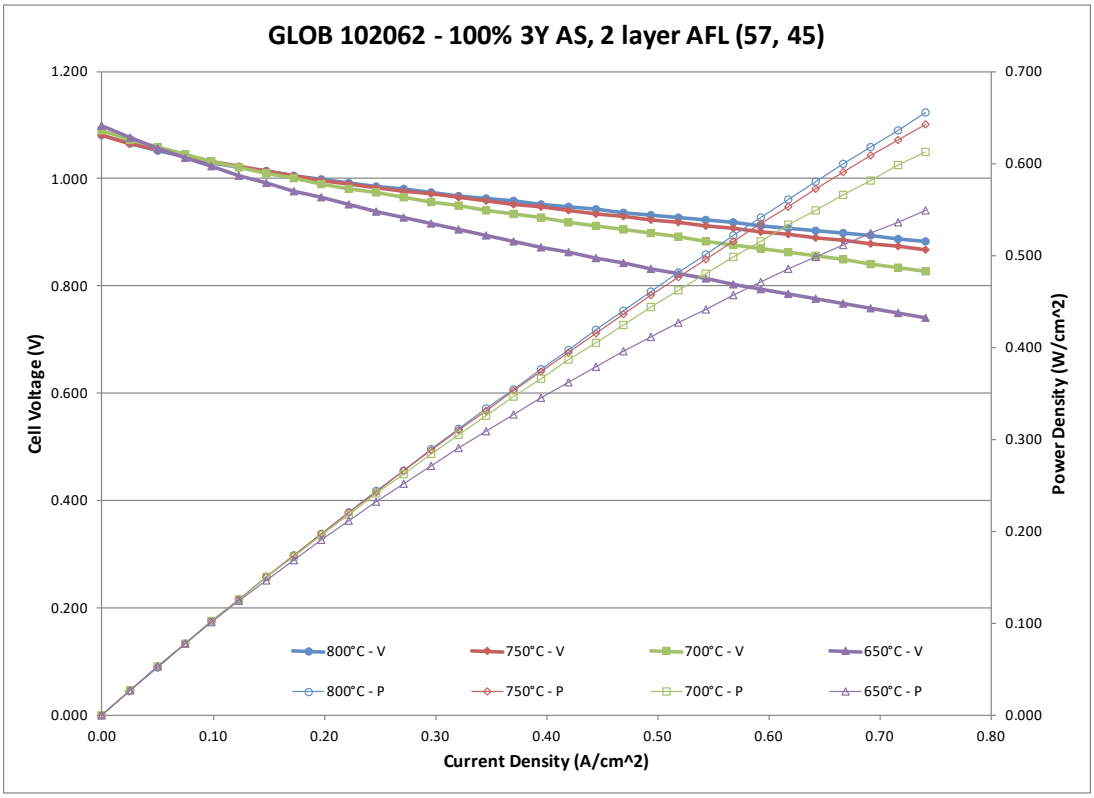

Figure 2.1-71 Test 102062 Initial Performance Curves 650 – 800°C.

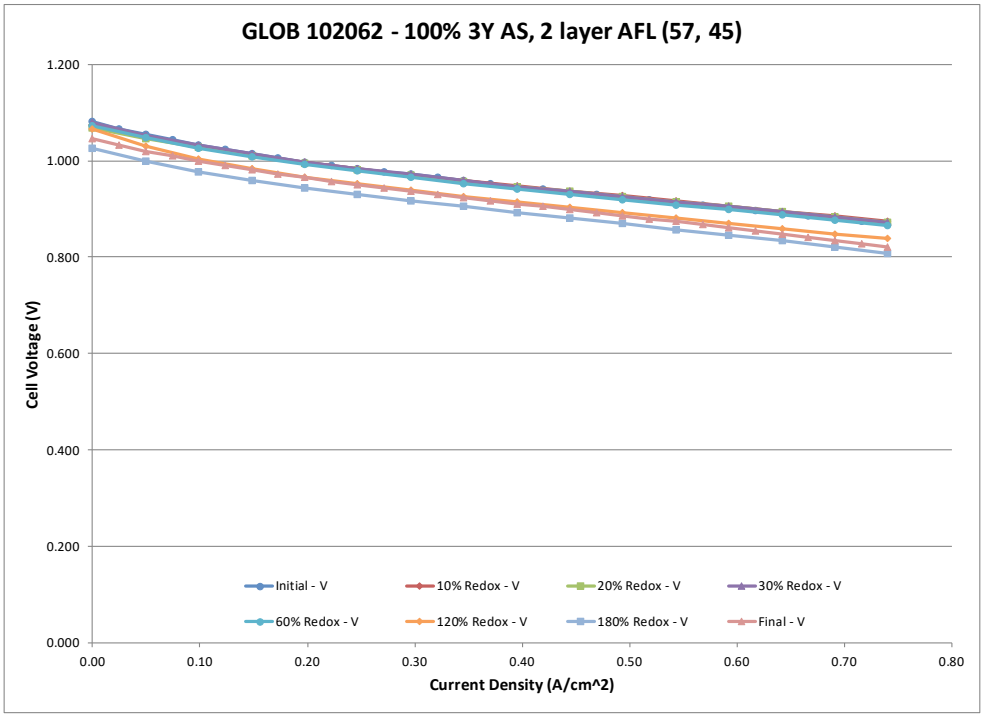

Figure 2.1-72 Test 102062 Performance Curves at Various Redox Depths at 750°C.

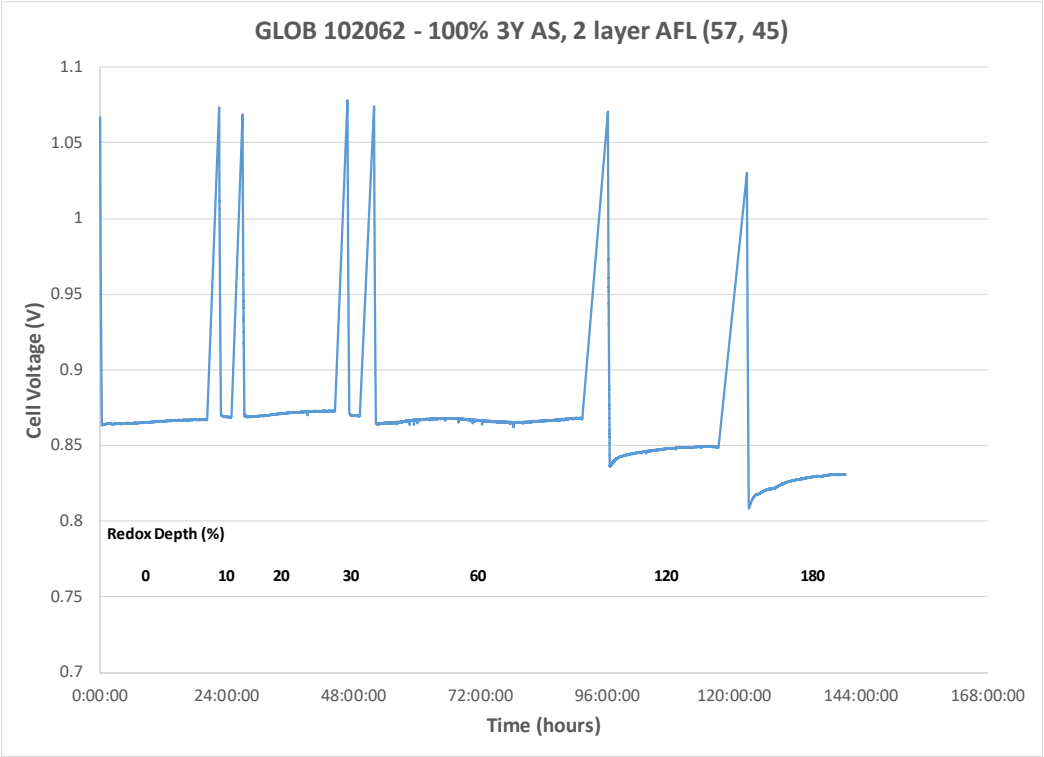

Figure 2.1-73 Test 102062 Steady State Hold Results at Various Redox Depths at 750°C

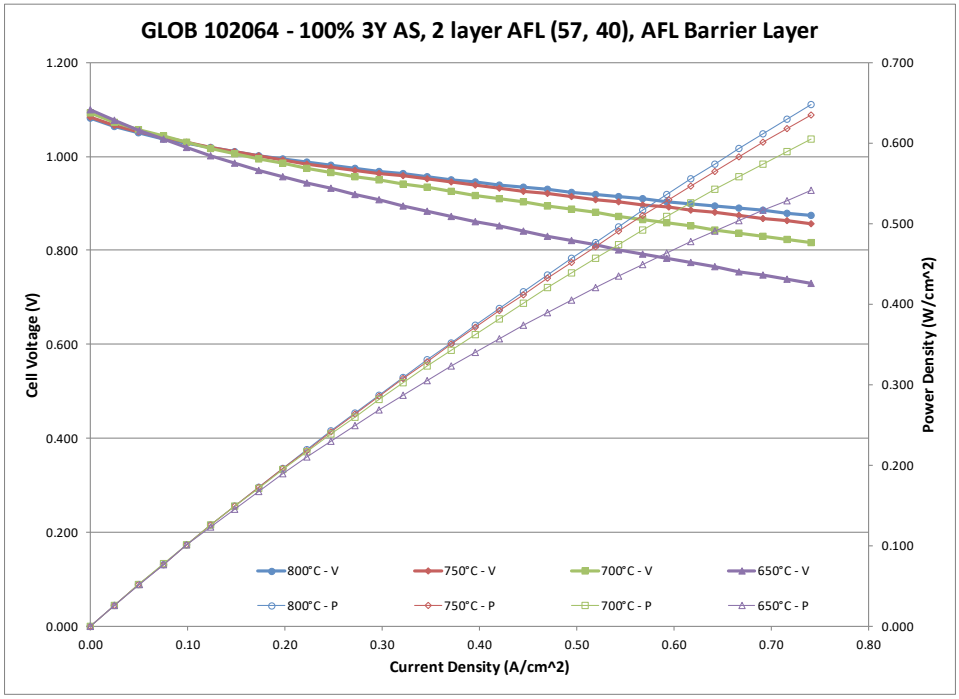

Figure 2.1-74 Test 102064 Initial Performance Curves 650 – 800°C

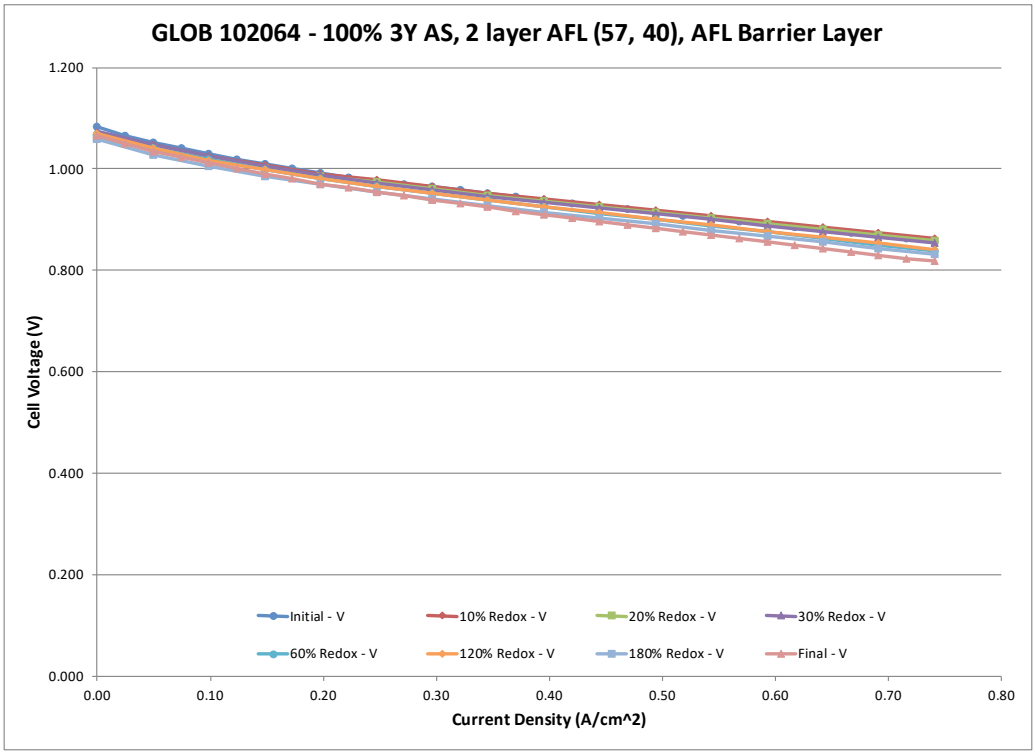

Figure 2.1-75 Test 102064 Performance Curves at Various Redox Depths at 750°C

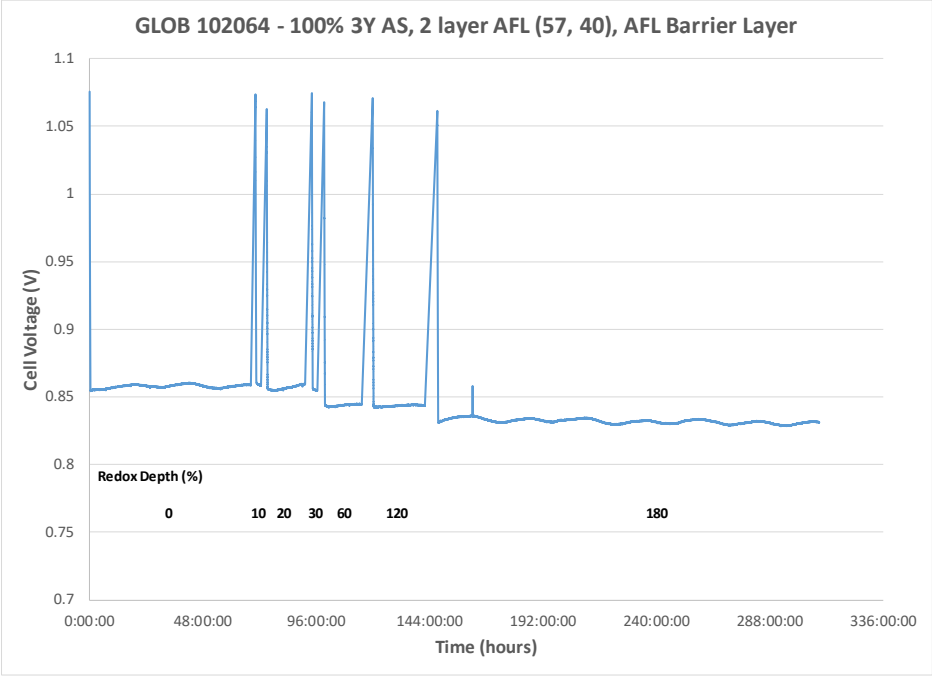

Figure 2.1-76 Test 102064 Steady State Hold Results at Various Redox Depths at 750°C

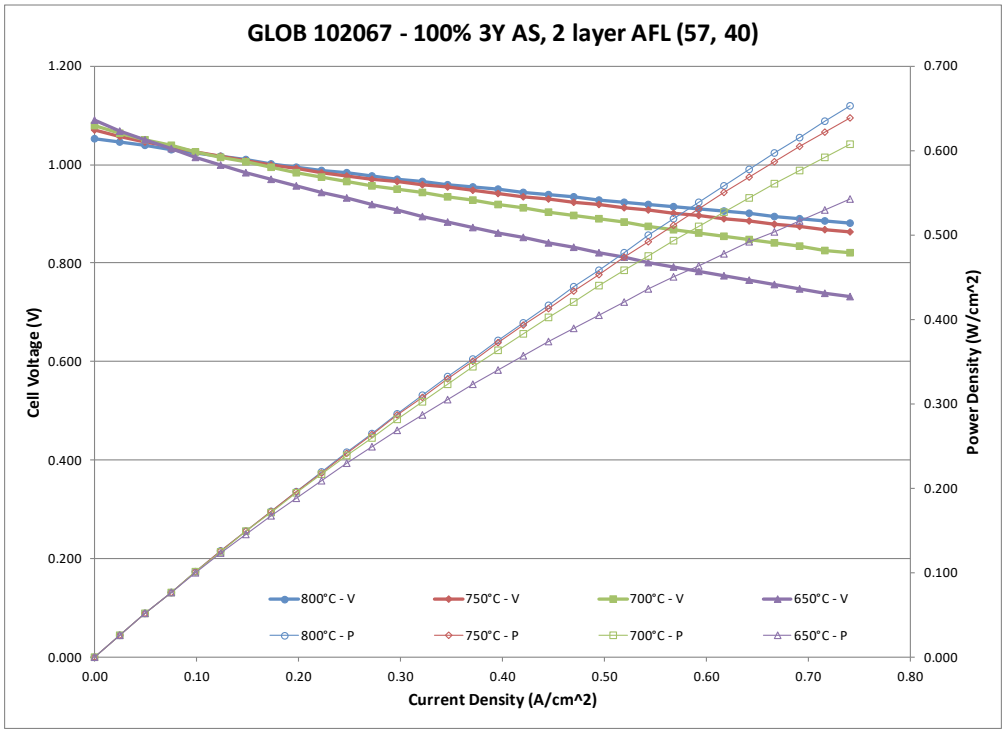

Figure 2.1-77 Test 102067 Initial Performance Curves 650 – 800°C

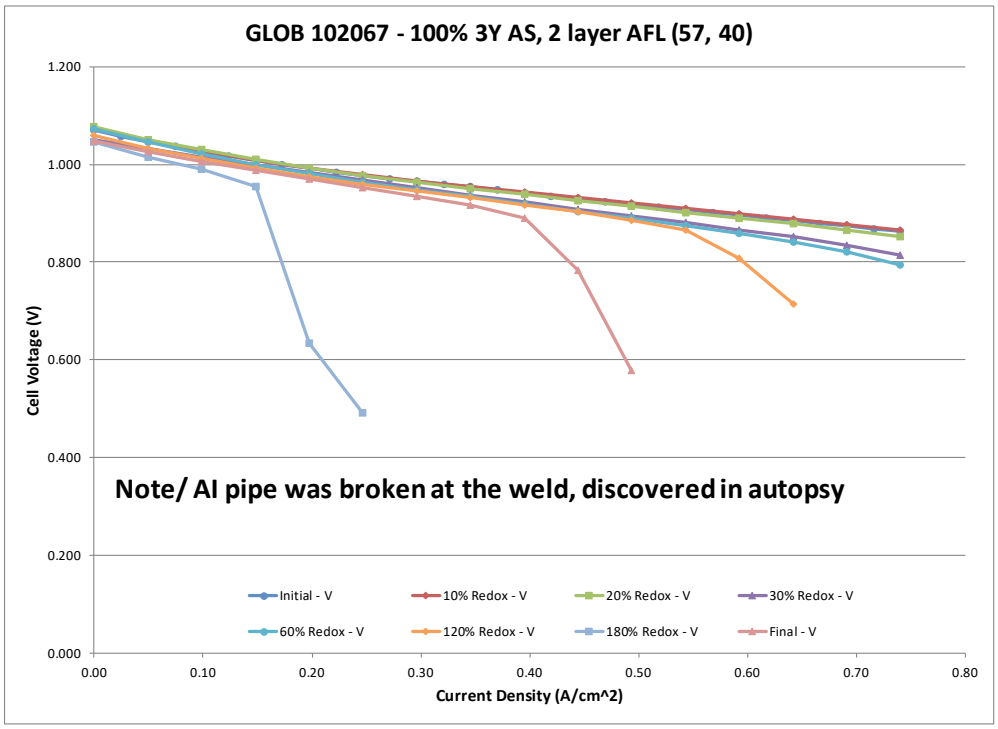

Figure 2.1-78 Test 102067 Performance Curves at Various Redox Depths at 750°C

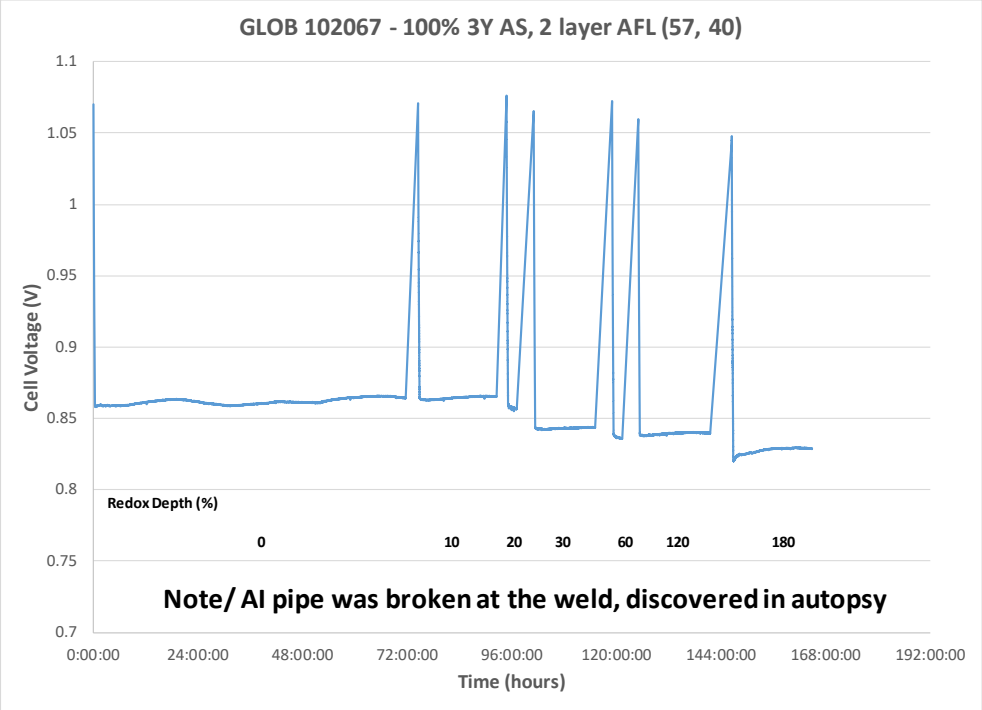

Figure 2.1-79 Test 102067 Steady State Hold to Various Redox Depths at 750°C

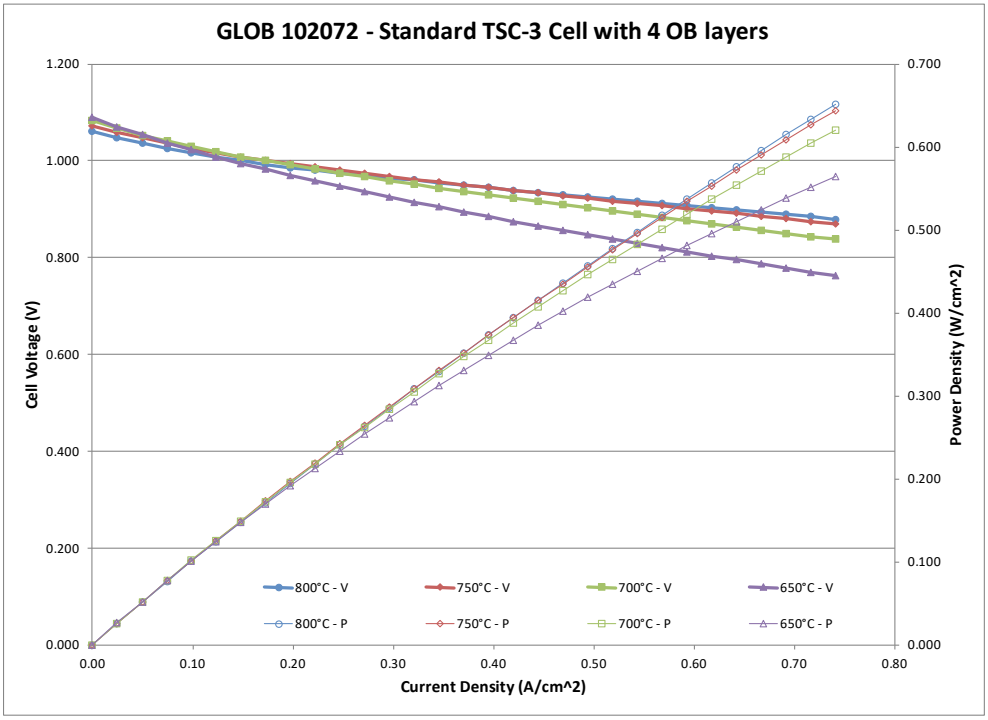

Figure 2.1-80 Test 102072 Initial Performance Curves 650 – 800°C.

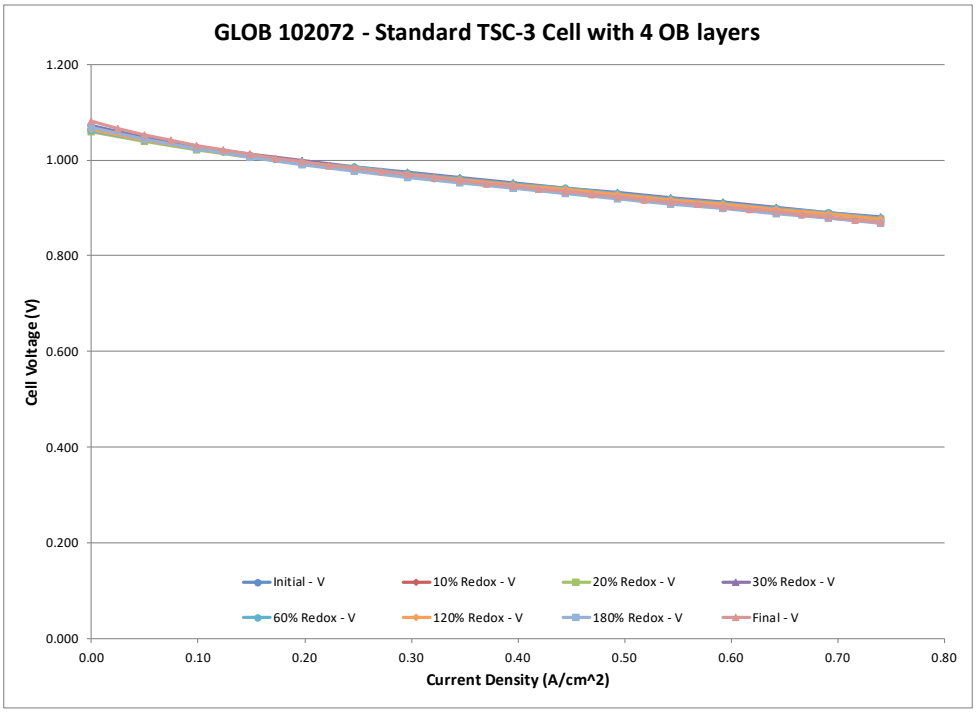

Figure 2.1-81 Test 102072 Performance Curves at Various Redox Depths at 750°C

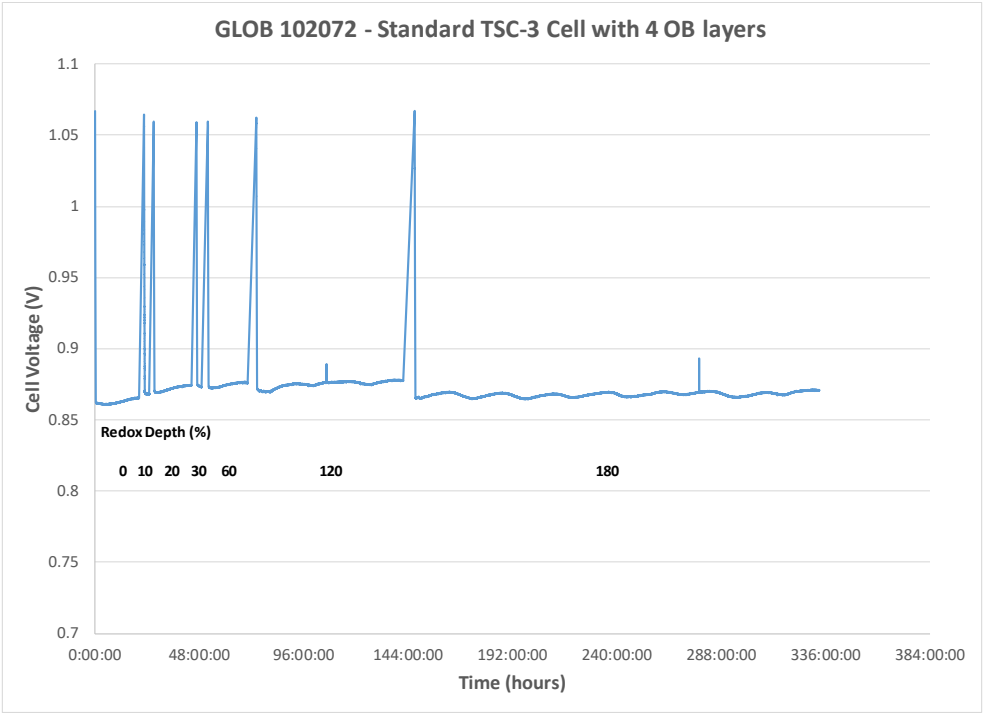

Figure 2.1-82 Test 102072 Steady State Hold Results at Various Redox Depths at 750°C

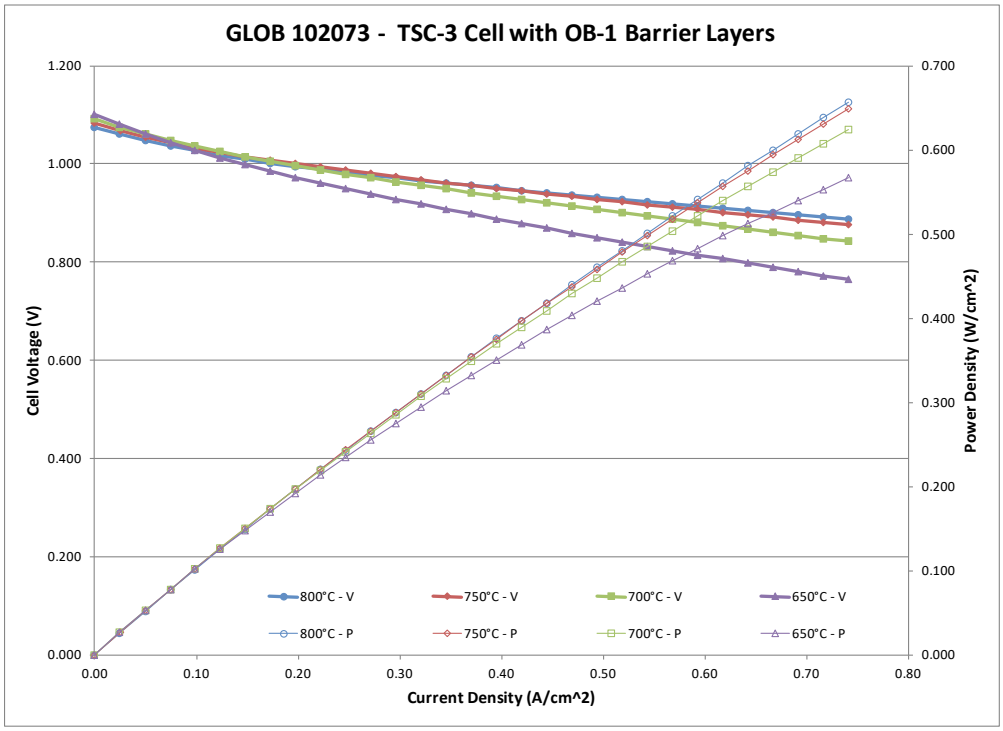

Figure 2.1-83 Test 102073 Initial Performance Curves 650 – 800°C.

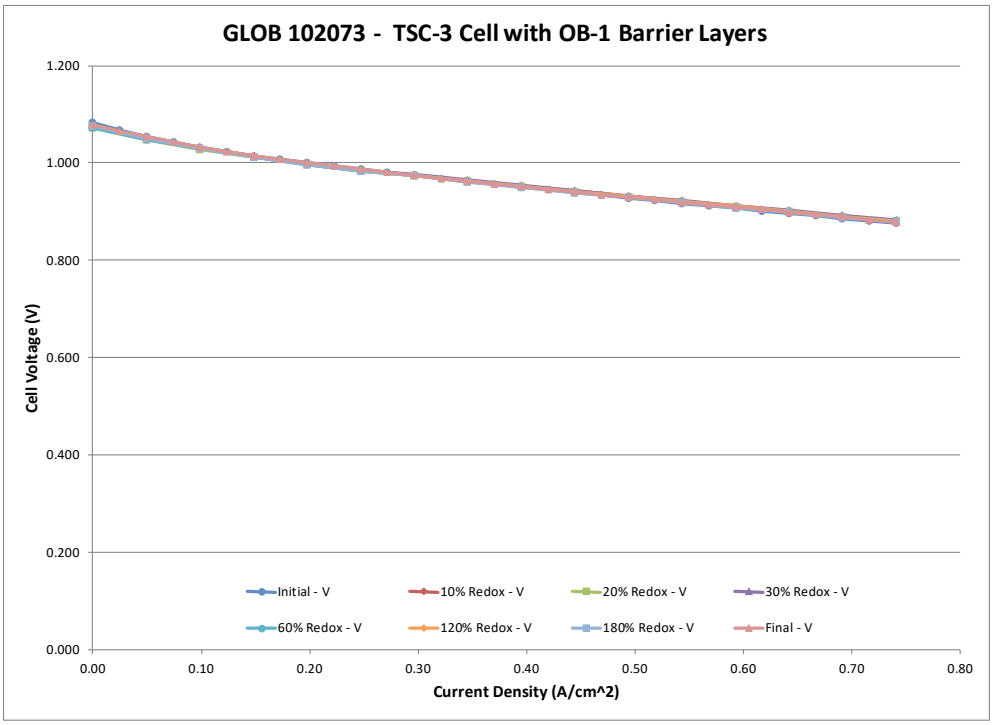

Figure 2.1-84 Test 102073 Performance Curves at Various Redox Depths at 750°C

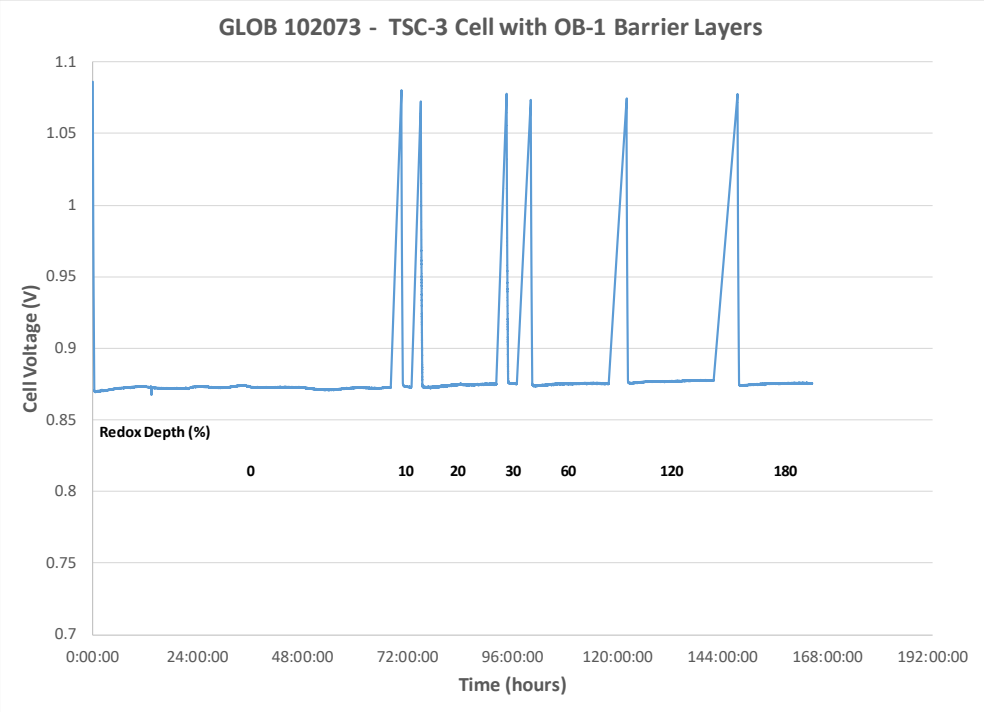

Figure 2.1-85 Test 102073 Steady State Hold Results at Various Redox Depths at 750°C

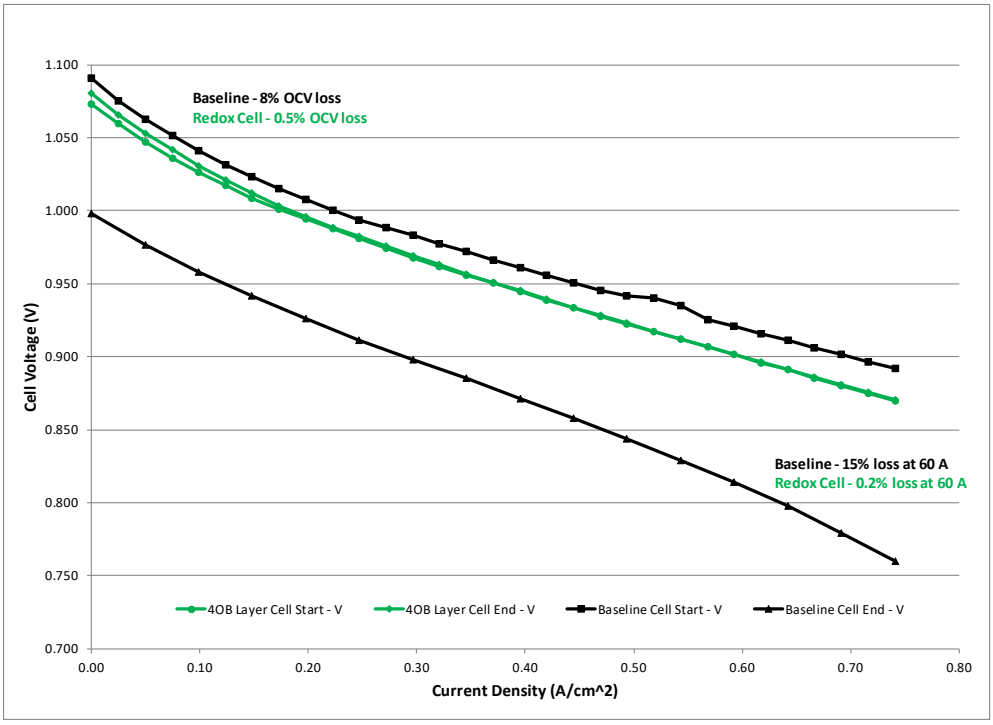

Figure 2.1-86 Initial and Final V-J Curves at 750°C, Baseline (102039) vs Improved (102072) Redox Cell

These results clearly demonstrate the improvements made showing the feasibility of a Redox tolerant cell as required for milestone 2.1.2 with Figure 2.1-86 showing the initial and final power curve comparison after cumulative Redox cycles for a baseline cell and 102072 a cell developed and tested with 4 oxidation barrier layers. Degradation at all conditions has been reduced to <0.5% compared with the baseline cell currently used in large area stacks that displayed up to 15% degradation and was found to be cracked after testing.

Figure 2.1-87 shows initial power curves for 102076, a 600um TSC-3 cell with 2 oxidation barrier layers (configuration OB-2). Figure 2.1-88 shows the effects of redox cycles to different oxidation depths on the V-J curves for this cell and Figure 2.1-89 shows the effects on steady-state holds at 750°C, 50% Uf, 25% Uo (air) and 0.5A/cm^2 for the same test.

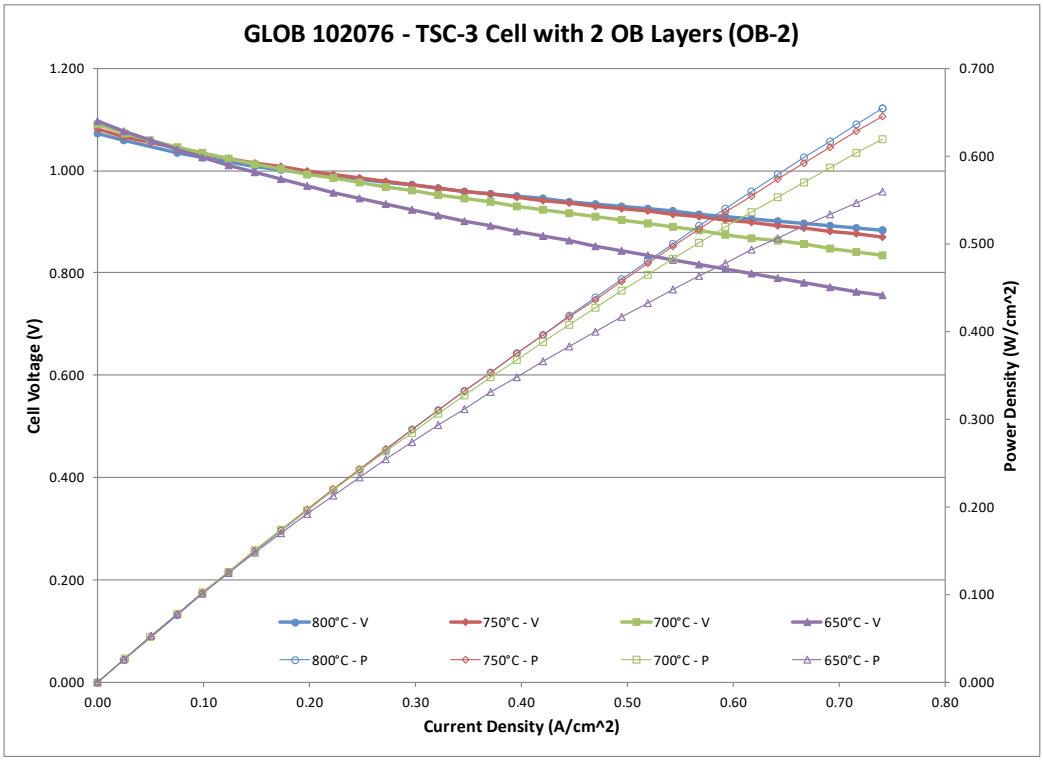

Figure 2.1-87 Test 102076 Initial Performance Curves 650 – 800°C

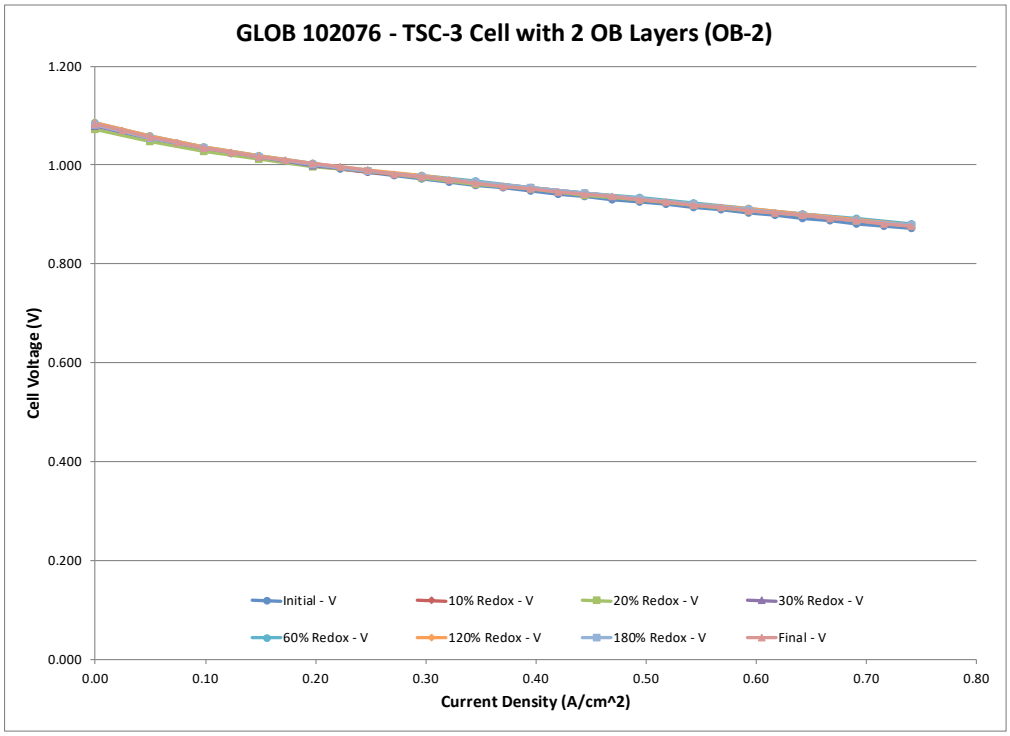

Figure 2.1-88 Test 102076 Performance Curves at Various Redox Depths at 750°C

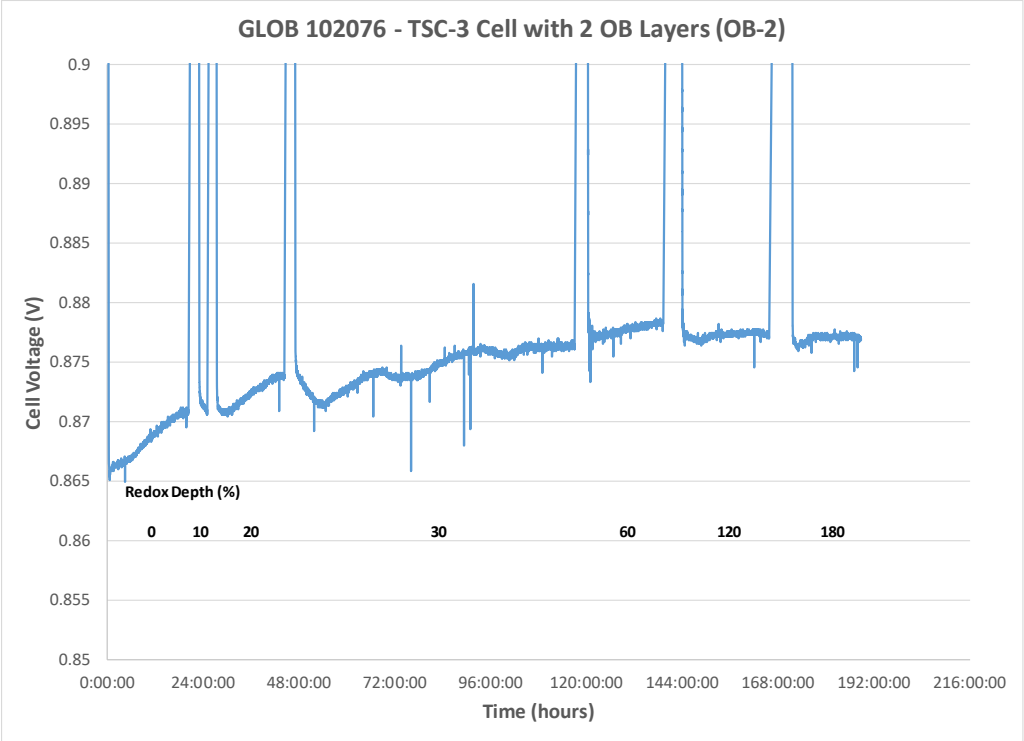

Figure 2.1-89 Test 102076 Steady State Hold Results at Various Redox Depths at 750°C

The cells tested are:

1. Test # 102076, a 600um TSC-3 cell with 2 oxidation barrier (OB) layers (OB-2 configuration);
2. Test # 102078, a 600um TSC-3 cell with 2 oxidation barrier (OB) layers (OB-3 configuration);
3. Test # 102079, a 600um TSC-3 cell with 2 oxidation barrier (OB) layers (OB-4 configuration);
4. Test # 102080 a 600um TSC-3 cell with 2 oxidation barrier (OB) layers (OB-5 configuration);
5. Test # 102082, a 600um TSC-3 cell with 3 oxidation barrier layers;
6. Test # 102083, a 600um TSC-3 cell with 4 oxidation barrier layers for 550°C Preoxidation testing preliminary investigation;
7. Test # 102085, a 600um TSC-3 cell (standard) for 550°C Preoxidation baseline testing;
8. Test # 102086, a 600um TSC-3 cell with 2 oxidation barrier layers (OB-2 configuration), repeat of 1 due to test stand issues.

Figure 2.1-87, Figure 2.1-90, Figure 2.1-93, Figure 2.1-96, Figure 2.1-99 and Figure 2.1-102 show initial power curves measured from 800°C to 650°C for tests 2-7 above respectively. Figure 2.1-88, Figure 2.1-91, Figure 2.1-94, Figure 2.1-97, Figure 2.1-100 and Figure 2.1-103 show the effects of redox cycles to different oxidation depths on the V-J curves for tests 2-7 above respectively. Figure 2.1-89, Figure 2.1-92, Figure 2.1-95, Figure 2.1-98, Figure 2.1-101 and Figure 2.1-104 show the effects on steady-state holds at 750°C, 50% Uf, 25% Uo (air) and 0.5A/cm^2 for the same tests. Figure 2.1-102 and Figure 2.1-103 are worthy of note, since they represent test 102083, the first test to attempt preoxidation treatment at 550°C with a cell with 4 OB layers. Previously 1mm TSC-2 cells would be fully oxidized with the same air flow rate at 550°C with cell voltage reaching 0.000 V long before 24 hours. However, with the addition of the oxidation barrier layers, the cell voltage was over 0.500 V after 24 hours with air flowing and still 0.326 V after more than 50 hours showing how effective the OB layers are at preventing rapid cell oxidation. At this point the Preoxidation process was stopped, and the cell was heated using a standard heatup and reduction profile. Figure 2.1-103 shows the power curves after the preoxidation and Figure 2.1-104 shows a comparison of steady-state hold cell voltage before and after preoxidation. Open circuit voltages are low, so it is likely the cell was damaged, and the test was shutdown at this stage. Cell damage could be due to the preoxidation or the use of the standard heatup and reduction profile. It was therefore decided to baseline a 600um TSC-3 cell with the previous 24 hour preoxidation at 550°C and the shortened heatup and reduction profile used with other Redox cycled cells, test 102085. Figure 2.1-106 and Figure 2.1-107 show the effects of the preoxidation on redox cycling. The cell is nominally the same as 102039 and 102048 and falls at the low end of the Redox degradation for these cells, but Redox degradation is not improved compared with 102039.

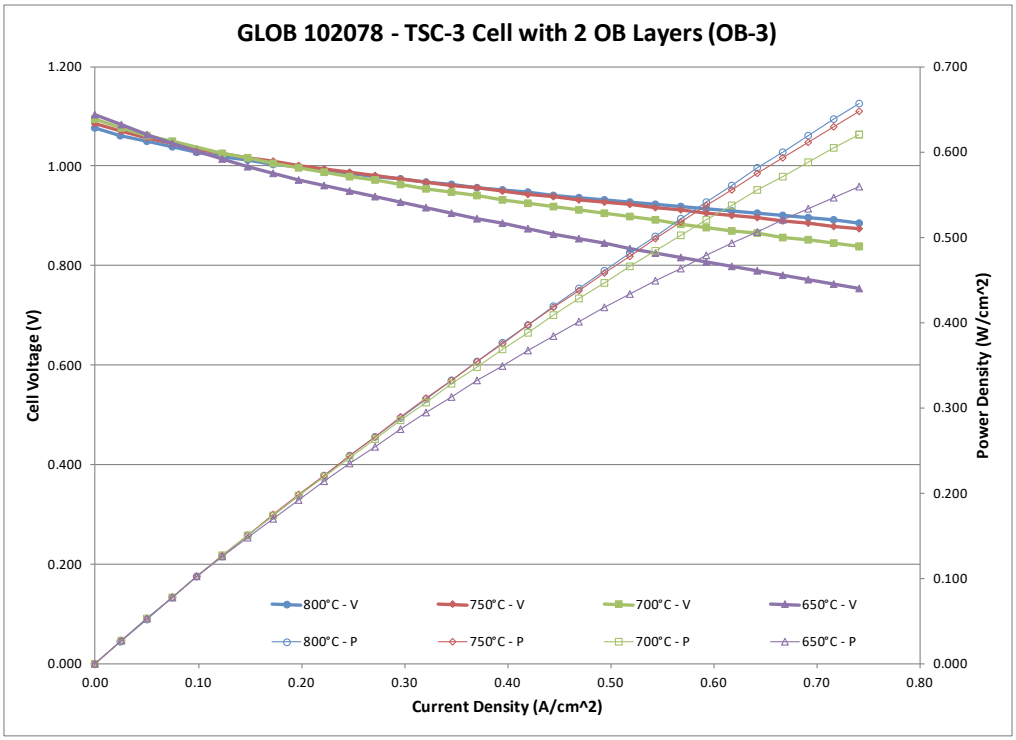

Figure 2.1-90 Test 102078 Initial Performance Curves 650 – 800°C.

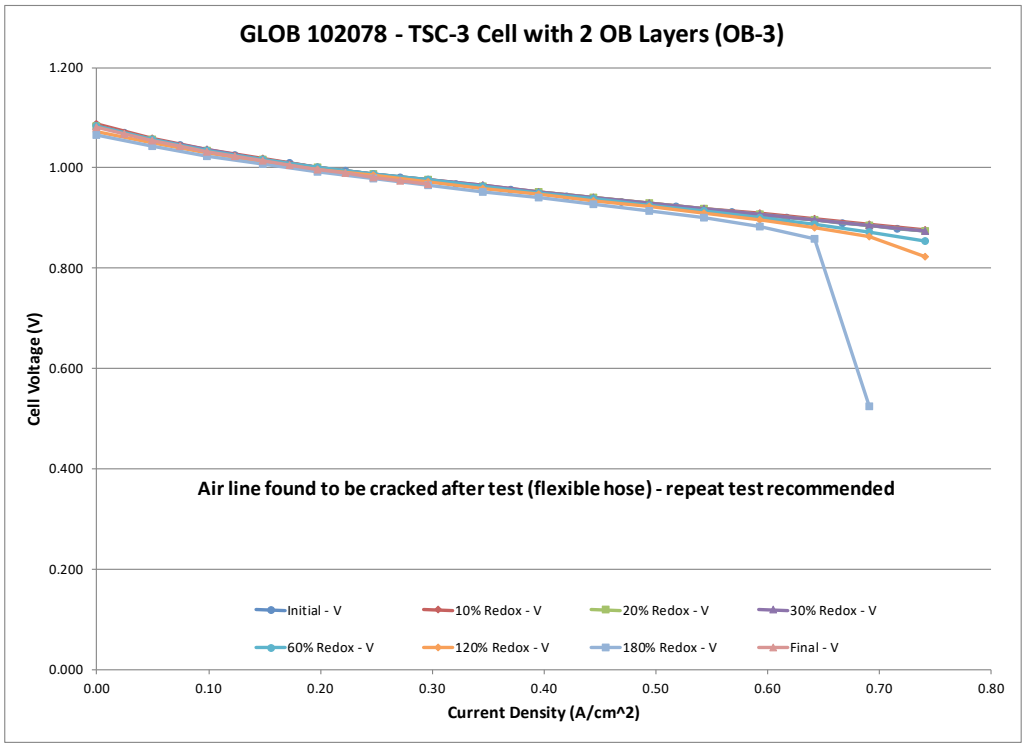

Figure 2.1-91 Test 102078 Performance Curves at Various Redox Depths at 750°C.

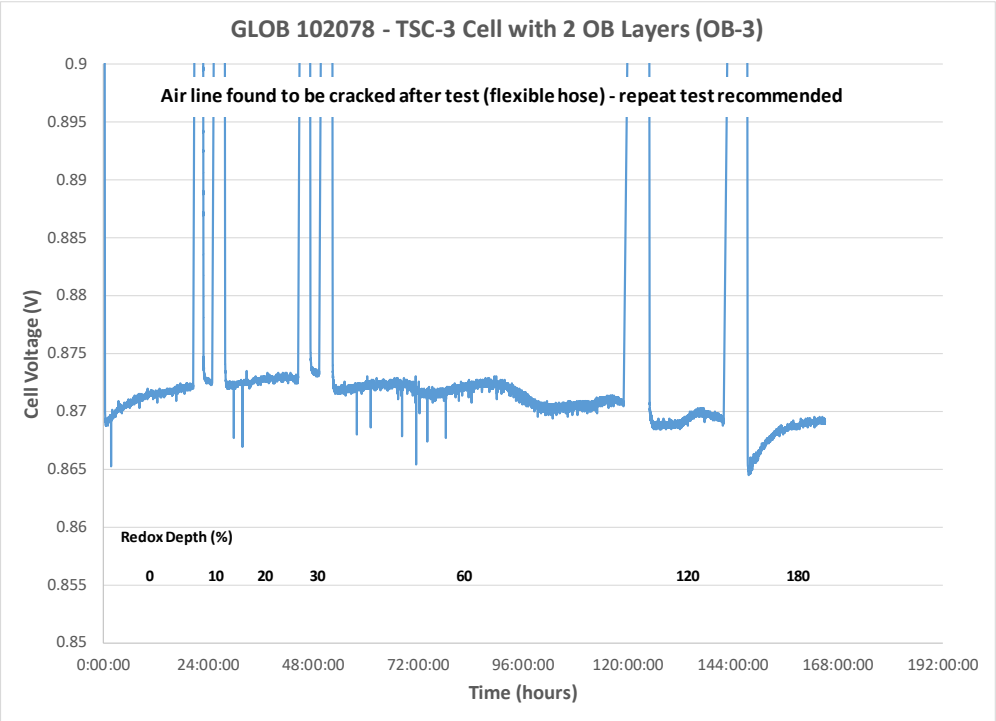

Figure 2.1-92 Test 102078 Steady State Hold Results at Various Redox Depths at 750°

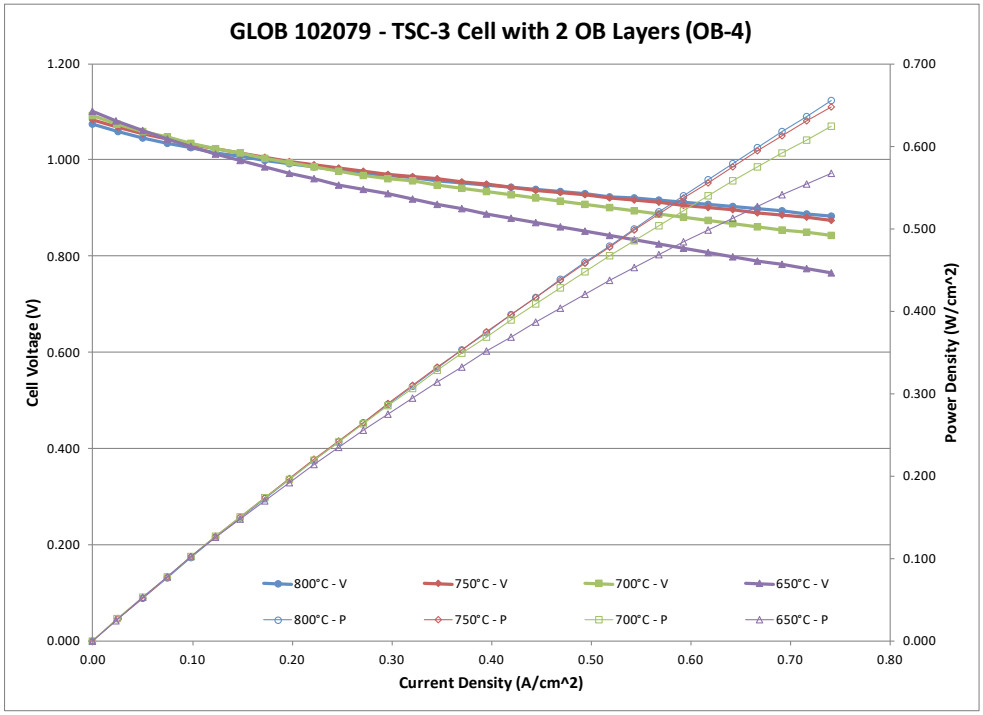

Figure 2.1-93 Test 102079 Initial Performance Curves 650 – 800°C

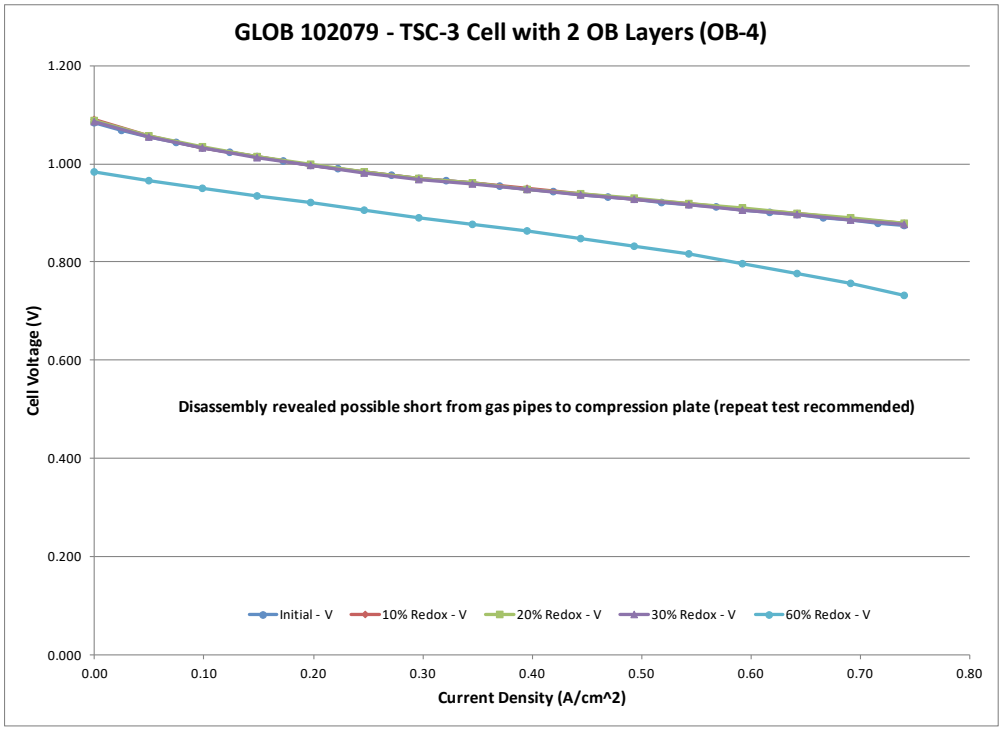

Figure 2.1-94 Test 102079 Performance Curves at Various Redox Depths at 750°C

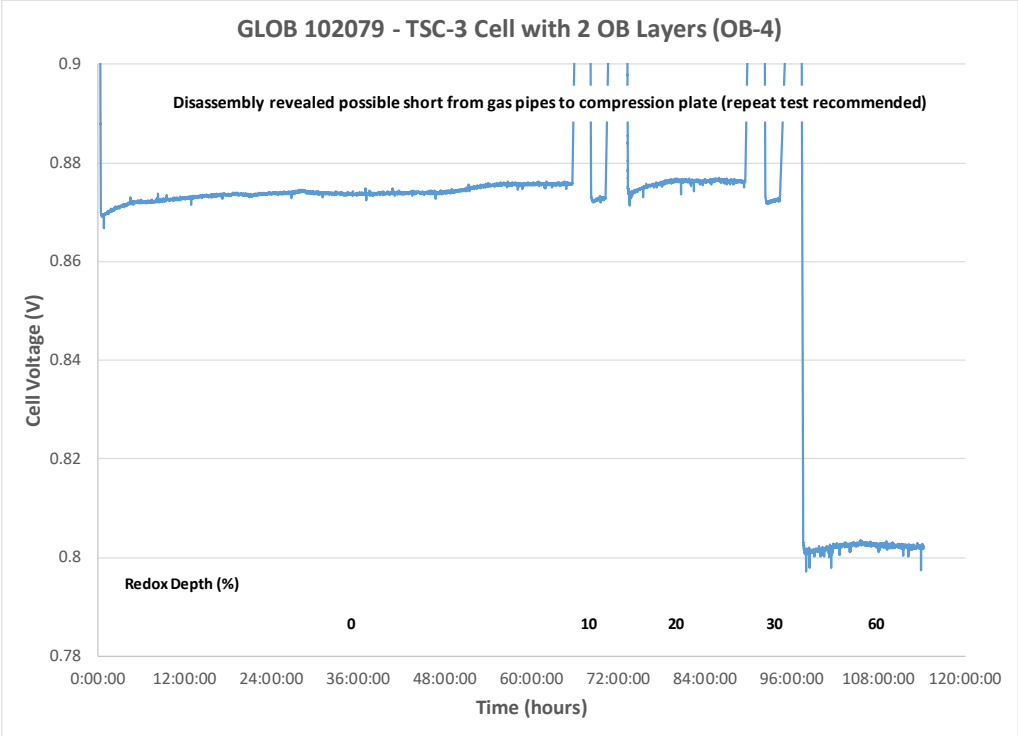

Figure 2.1-95 Test 102079 Steady State Hold Results at Various Redox Depths at 750°C

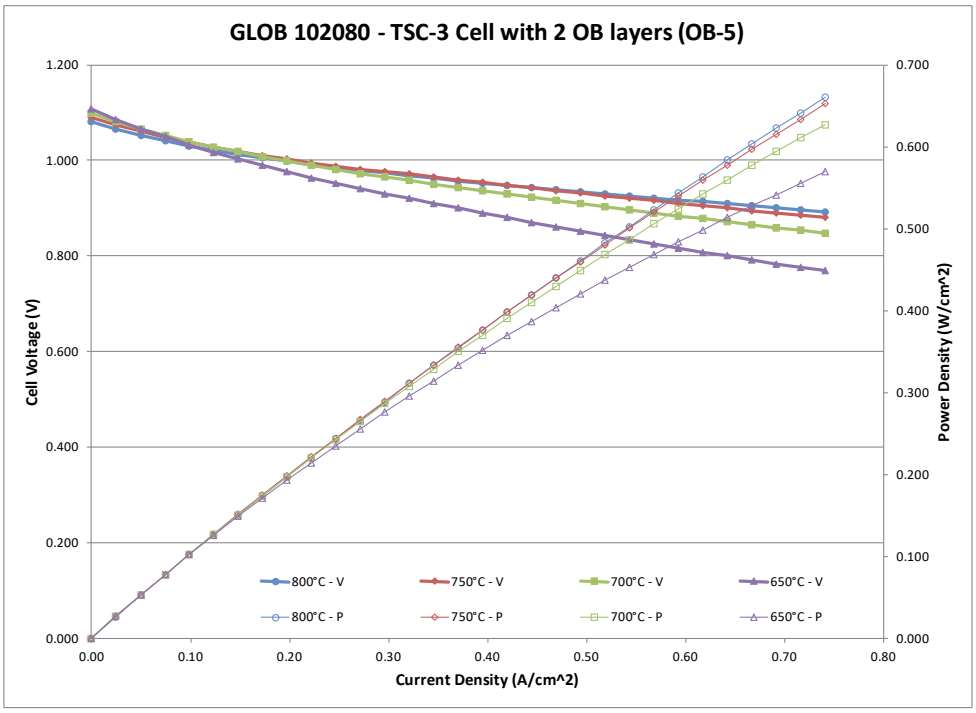

Figure 2.1-96 Test 102080 Initial Performance Curves 650 – 800°C

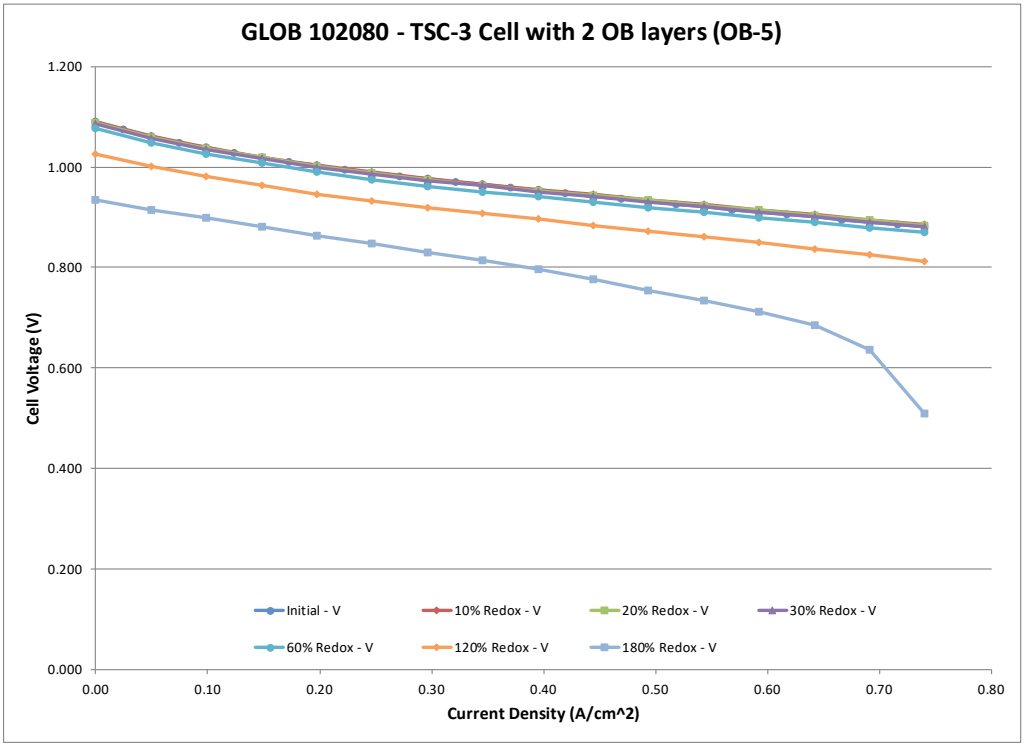

Figure 2.1-97 Test 102080 Performance Curves at Various Redox Depths at 750°C

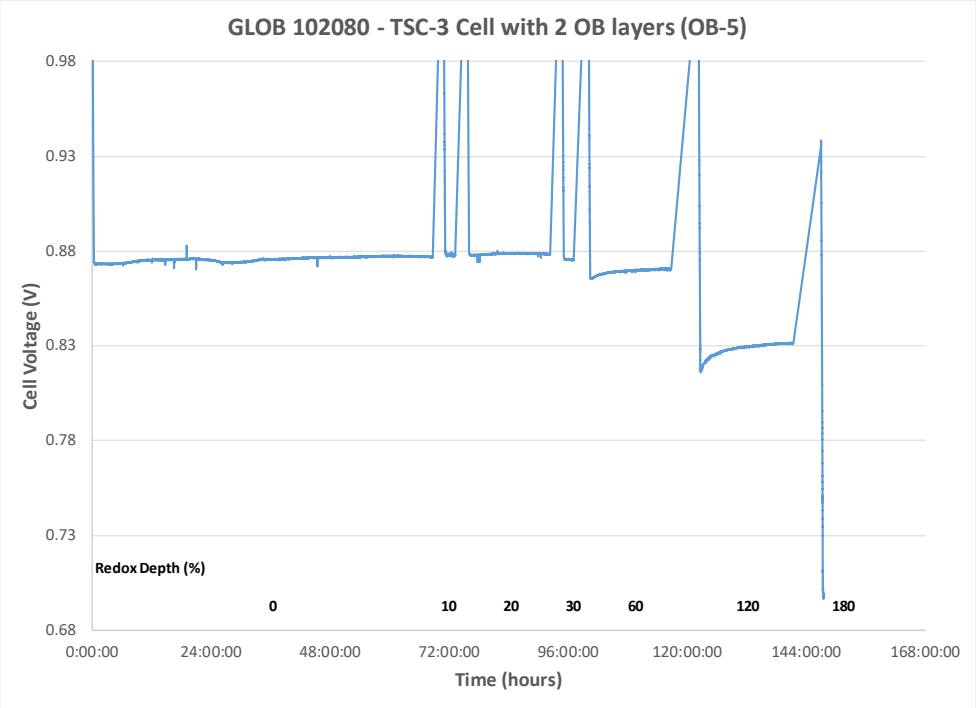

Figure 2.1-98 Test 102080 Steady State Hold to Various Redox Depths at 750°C

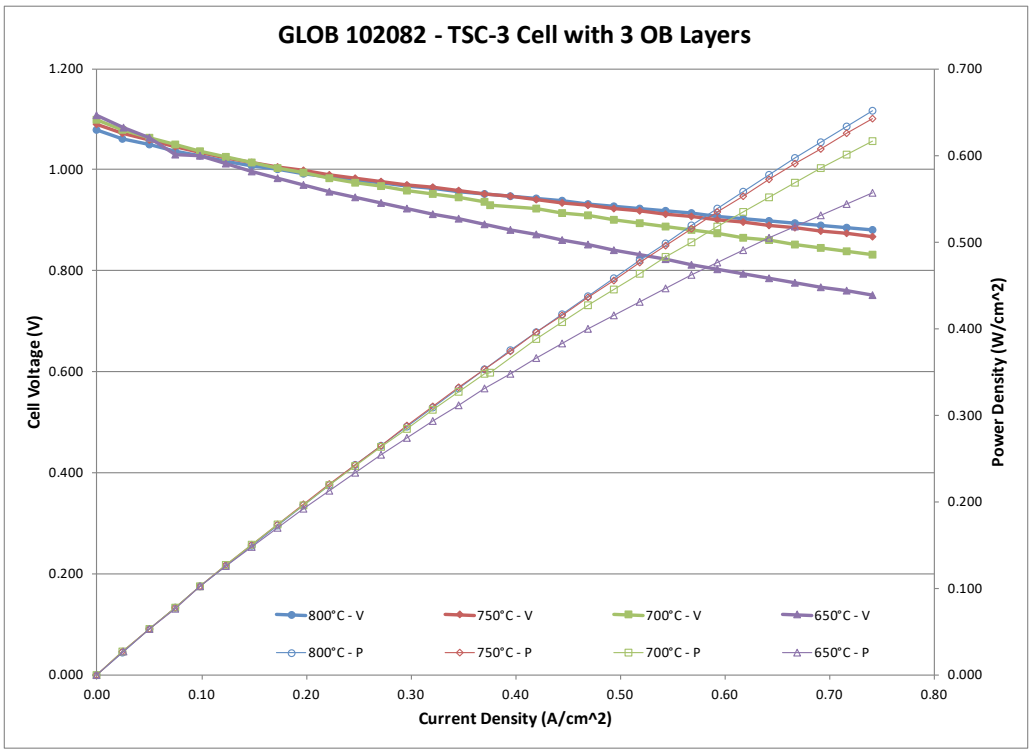

Figure 2.1-99 Test 102082 Initial Performance Curves 650 – 800°C.

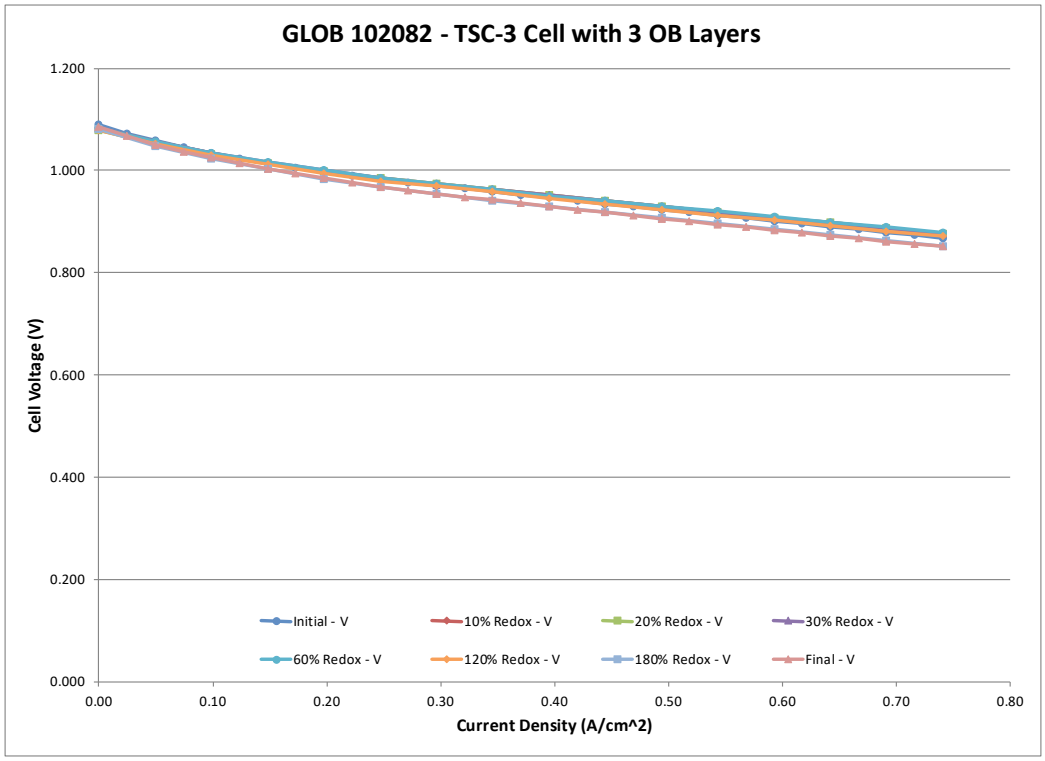

Figure 2.1-100 Test 102082 Performance Curves at Various Redox Depths at 750°C

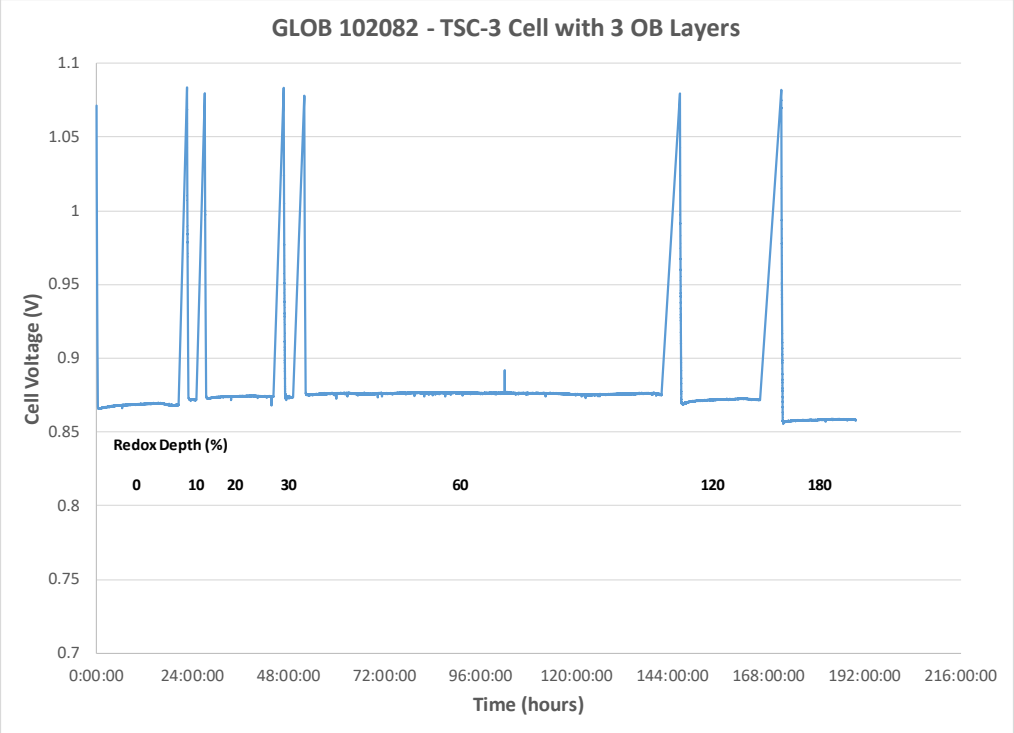

Figure 2.1-101 Test 102082 Steady State Hold Results at Various Redox Depths at 750°C

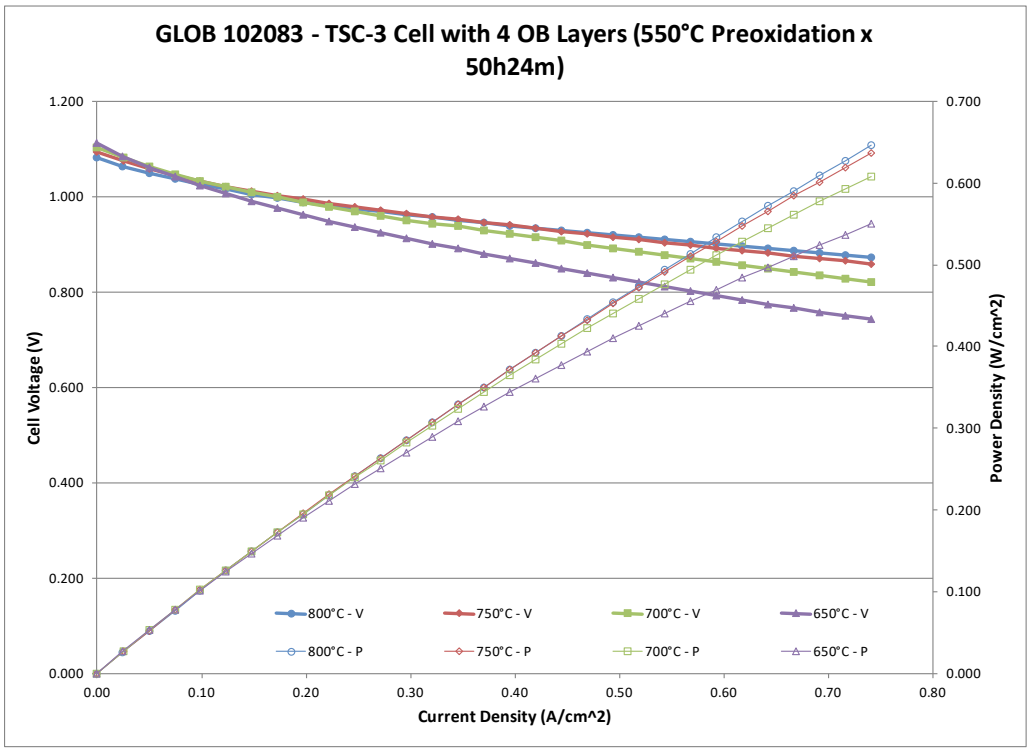

Figure 2.1-102 Test 102083 Initial Performance Curves 650 – 800°C.

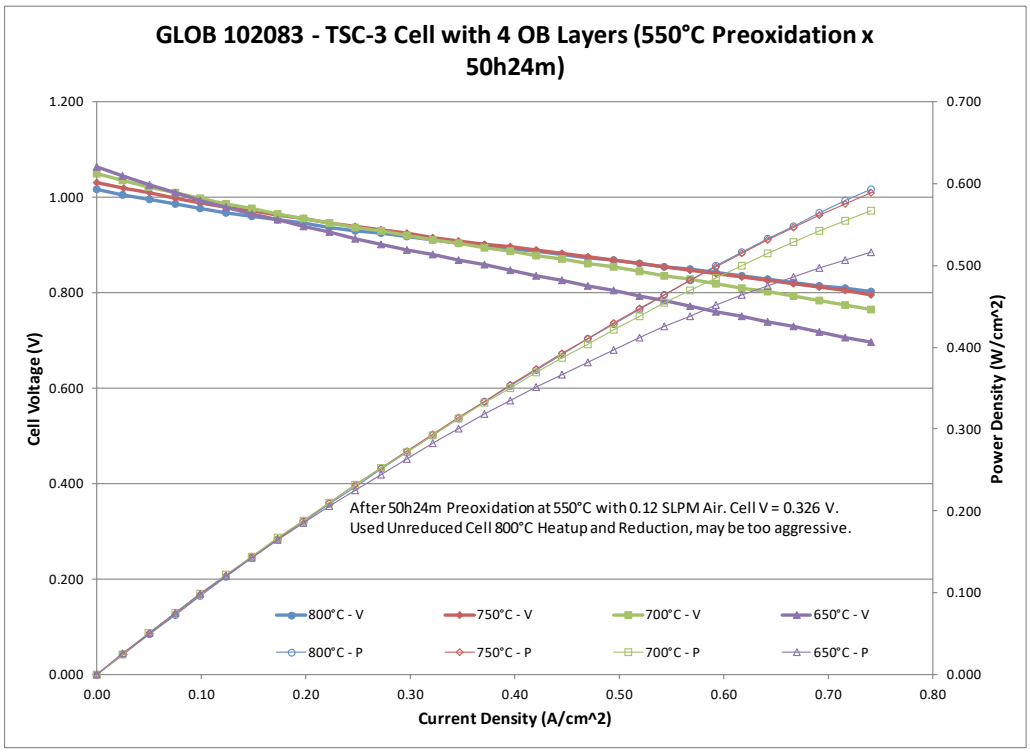

Figure 2.1-103 Test 102083 Performance Curves after Preoxidation at 550°C

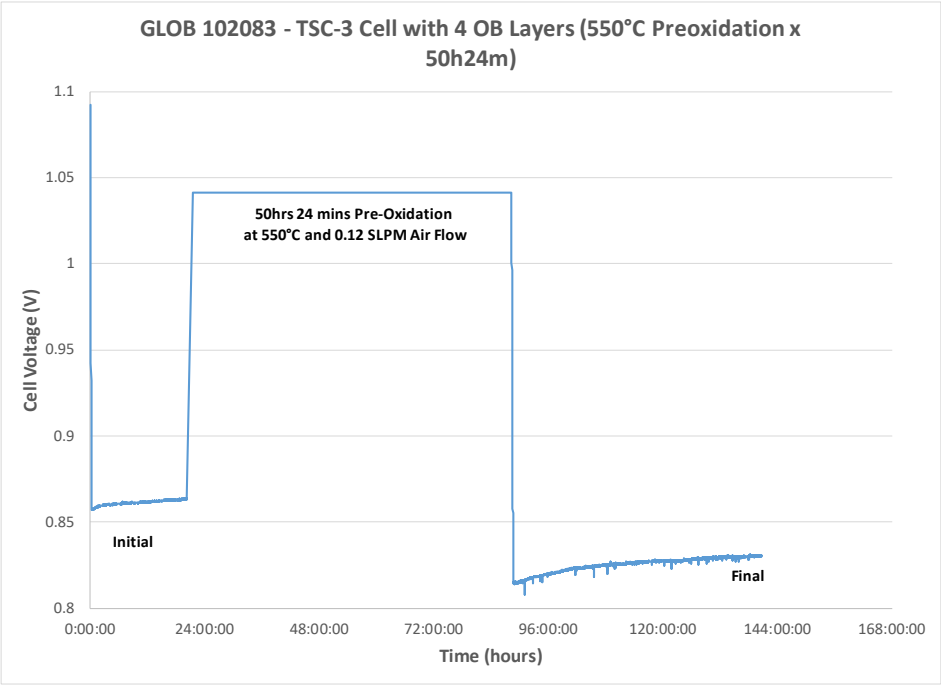

Figure 2.1-104 Test 102083 Steady State Hold Results Before and After Preoxidation at 550°C

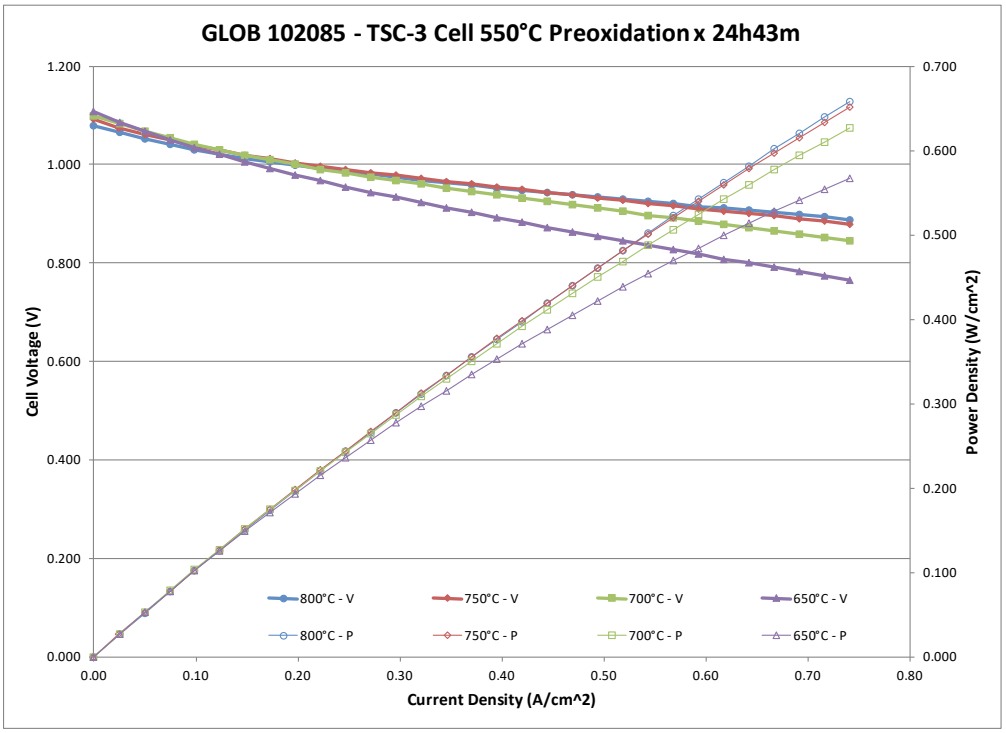

Figure 2.1-105 Test 102085 Initial Performance Curves 650 – 800°C

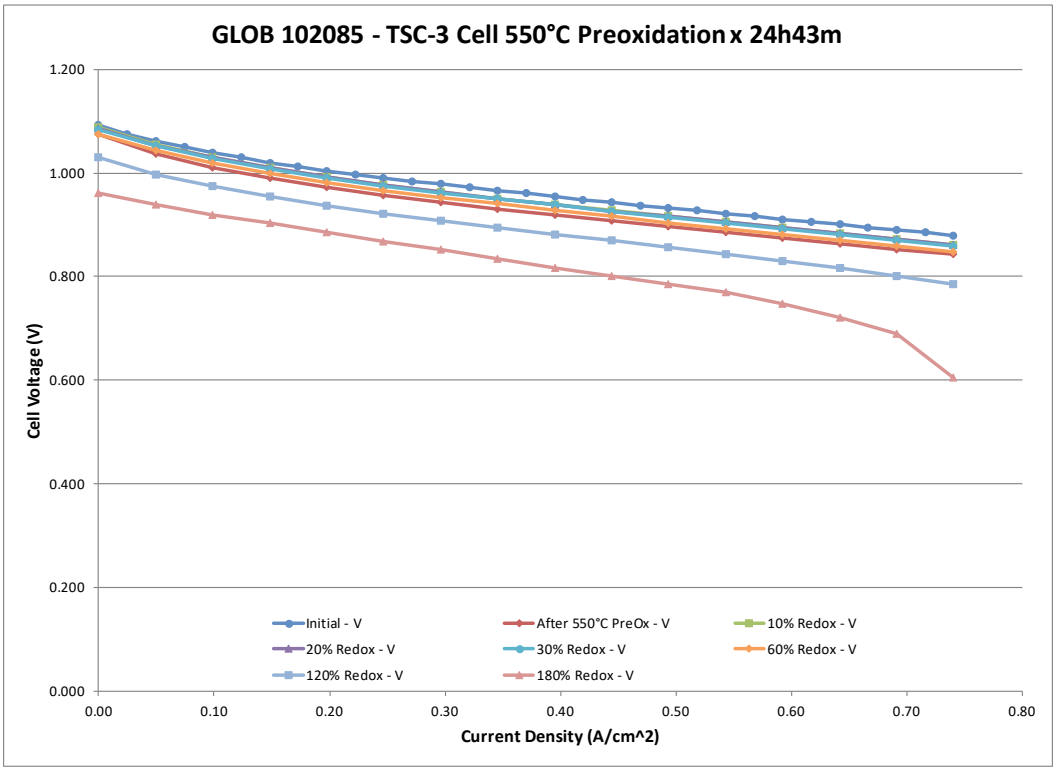

Figure 2.1-106 Test 102085 Performance Curves at Various Redox Depths at 750°C

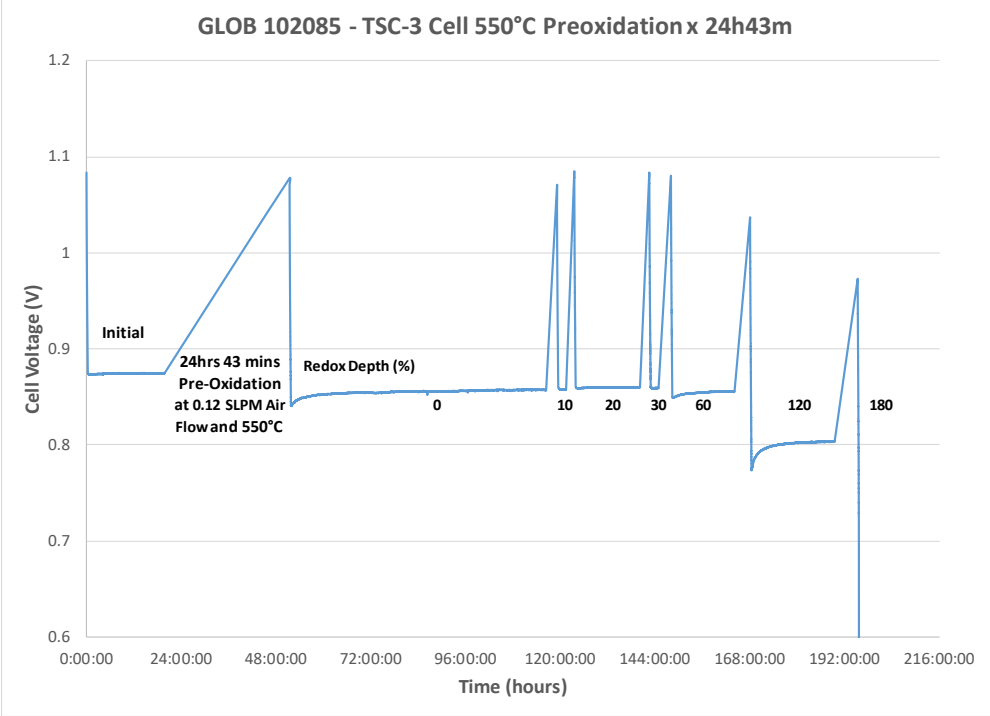

Figure 2.1-107 Test 102085 Steady State Hold Results at Various Redox Depths at 750°C

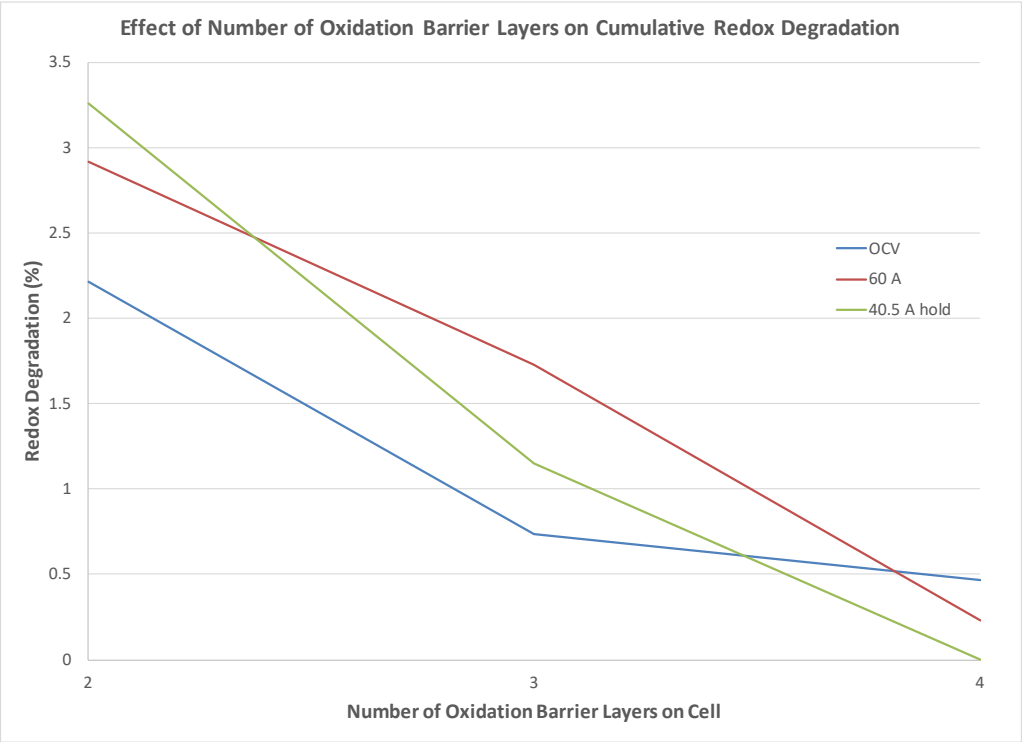

Figure 2.1-108 Effect of Number of OB Layers on Cumulative Redox Degradation at OCV, 60A power curve and 40.5A Steady-State Hold

By adding an oxidation barrier layer very significant improvements are seen and when the thickness and composition of this layer are modified near zero degradation rates are achievable with the same Redox test that shows significant degradation for equivalent cells that have no oxidation barrier layer. Figure 2.1-108 shows the effect of the number of oxidation barrier layers (2, 3 and 4) on the cumulative degradation after Redox testing for the Open Circuit Voltage (OCV), the power curve voltage at 60A and the steady-state hold voltage at 40.5A. Clearly more barrier layers lowers the Redox degradation, however, it is likely that at some point these could restrict gas flow during operation so some compromise is likely required.

These results clearly demonstrate the improvements made showing the feasibility of a Redox tolerant cell with Figure 2.1-109 showing the initial and final power curve comparison after cumulative Redox cycles for a baseline cell and 102072 a cell developed and tested with 4 oxidation barrier layers. Degradation at all conditions has been reduced to <0.5% compared with the baseline cell currently used in large area stacks that displayed up to 15% degradation and was found to be cracked after testing.

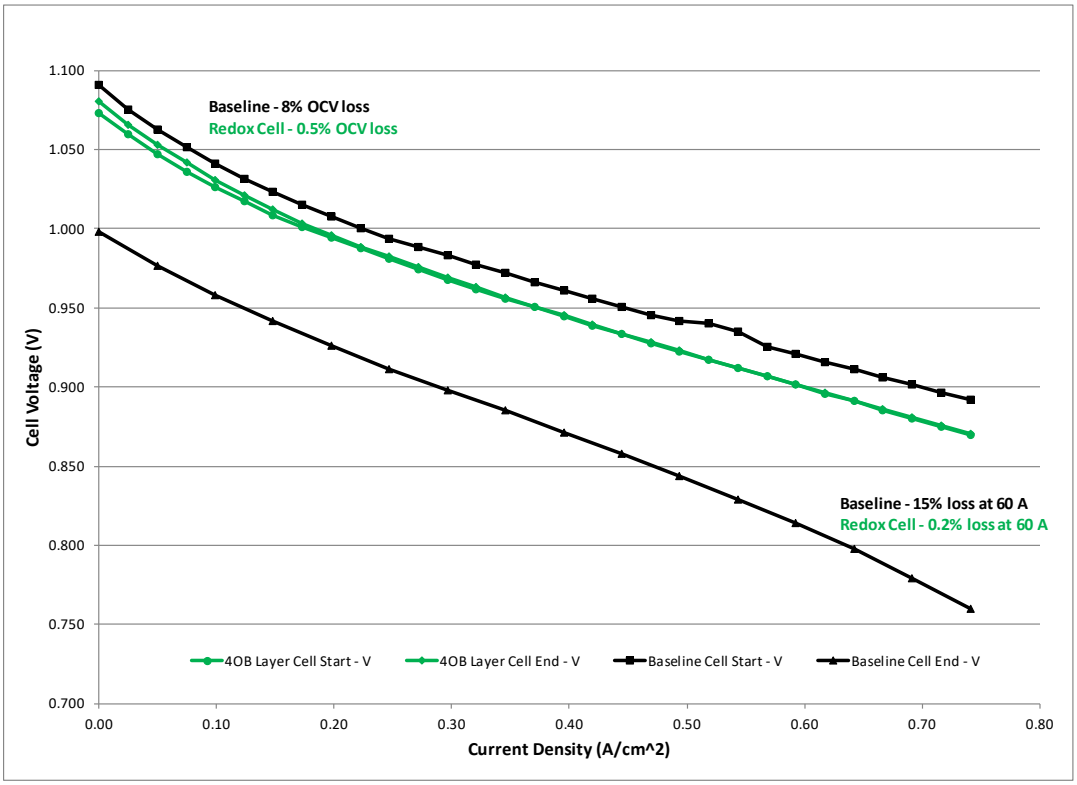

Figure 2.1-109 Initial and Final V-J Curves at 750°C, Baseline (102039) vs Improved (102072) Redox Cells

Testing then focused on demonstration of 10 Redox cycles with the preferred modified cell compared with 10 thermal cycles for the same cell. Ideally, this would be compared with the results for a 'baseline cell'- a nominally 600 um thick TSC-3 cell without any Redox tolerance modifications. It should be noted that this is different than the baseline cell used to demonstrate feasibility of Redox-Tolerant TSC III cell technology; a 1 mm TSC-2 cell that is no longer in production. Those cells were the basis for previous Redox development work and so were used as a benchmark to compare the last decade of cell development in the early stages of this project.

Baseline electrochemical testing was performed comparing initial current-voltage curves and steady-state degradation testing with tests after redox cycles to varying degrees of oxidation or redox depth. Figure 2.1-110 shows initial power curves for 102086, a 600um TSC-3 cell with 2 oxidation barrier layers (configuration OB-2). Figure 2.1-111 shows the effects of redox cycles to different oxidation depths on the V-J curves for this cell and Figure 2.1-112 shows the effects on steady-state holds at 750°C, 50% Uf, 25% Uo (air) and 0.5A/cm^2 for the same test. Autopsy of the cell showed that there was a crack at the FI/AI corner (Figure 2.1-113), the most critical location. It is likely that this caused the significant degradation at the end of the test. The loss of this corner suggests the likely cause is the cell not being ironed flat sufficiently before testing rather than a Redox problem, so a retest is necessary to obtain representative results.

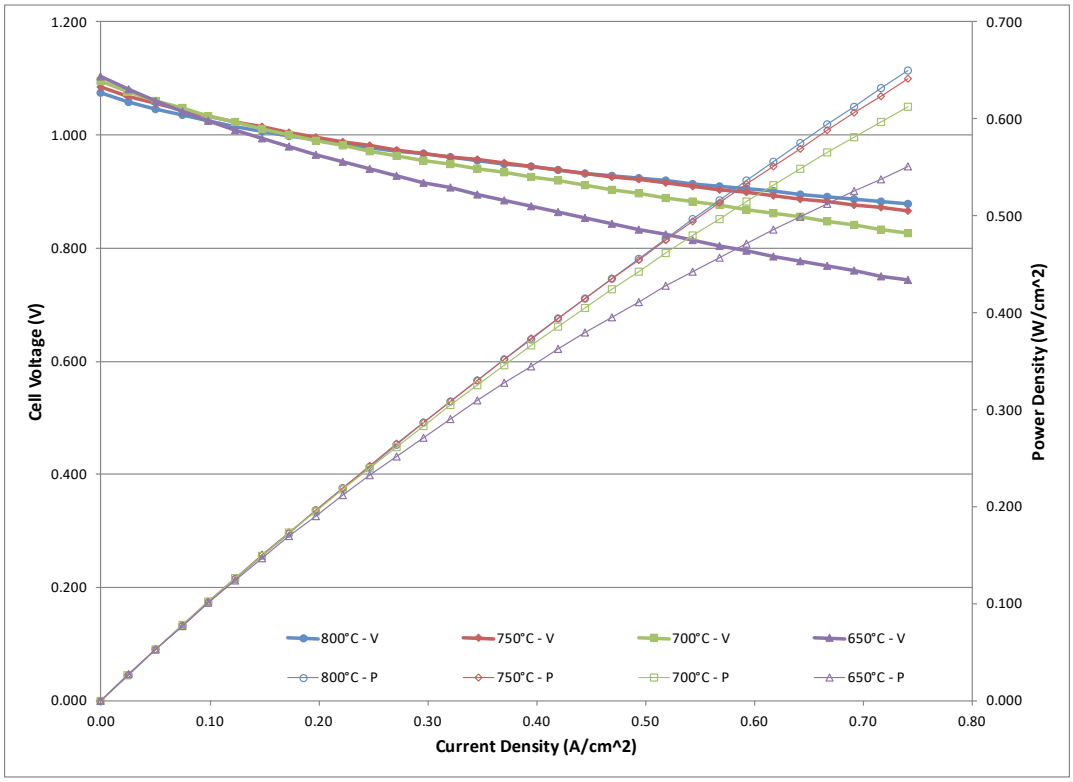

Figure 2.1-110 Test 102086 Initial Performance Curves 650 – 800°C

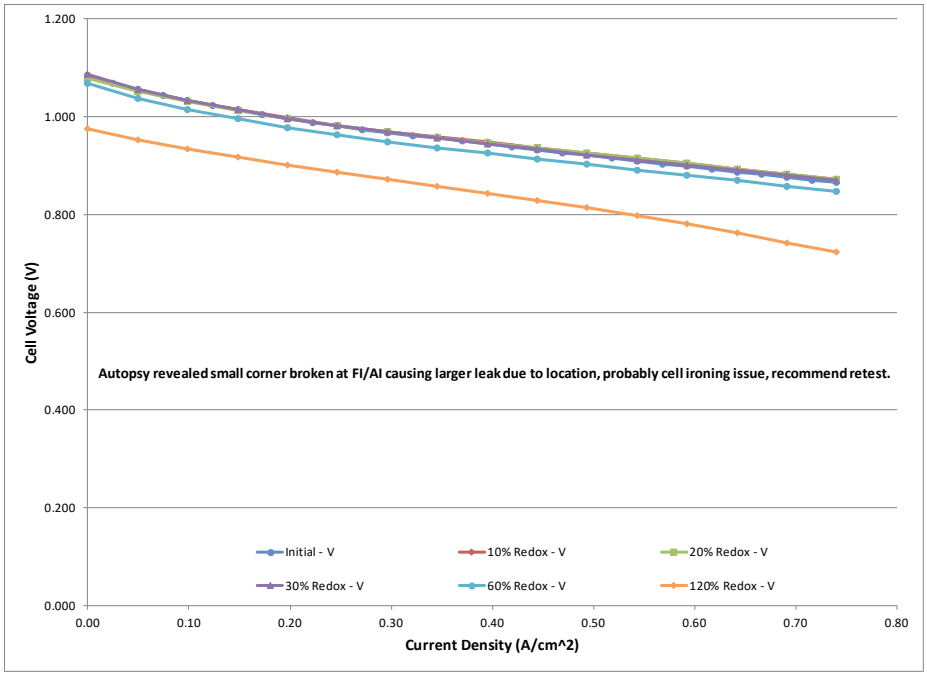

Figure 2.1-111 Test 102086 Performance Curves at Various Redox Depths at 750°C

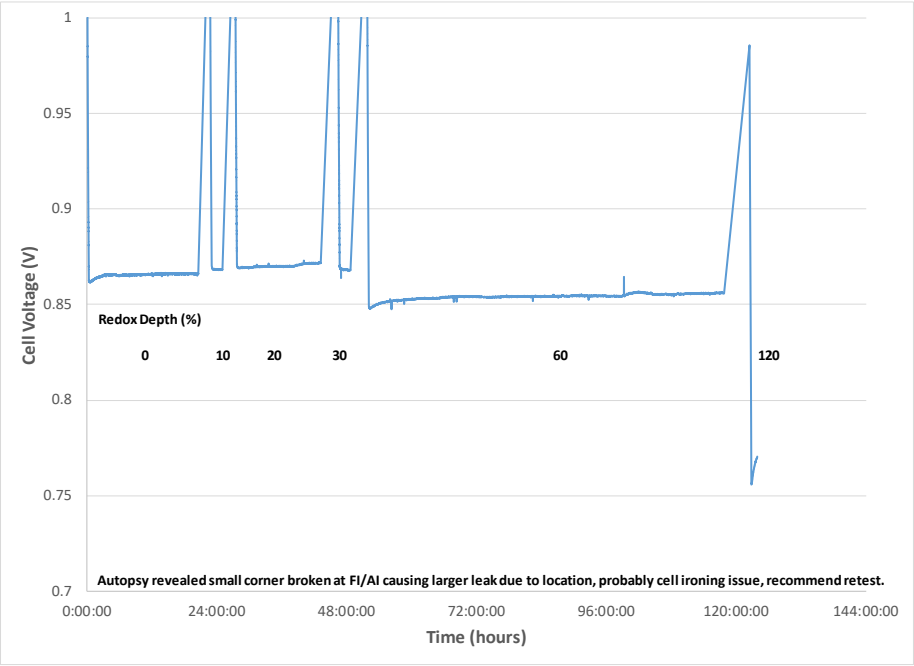

Figure 2.1-112 Test 102086 Steady State Hold Results at Various Redox Depths at 750°C

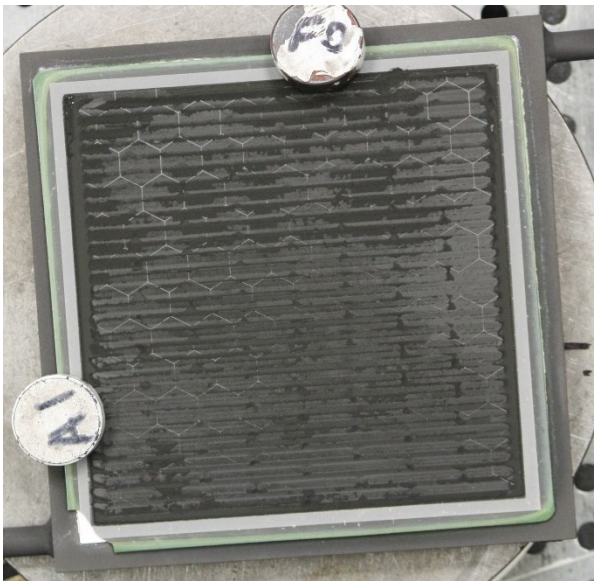

Figure 2.1-113 Test 102086 Cell Autopsy, Crack at Fuel In/Air In (FI/AI) corner

Table 2.1-4 and Table 2.1-5 show a summary of physical properties and electrochemical performance comparison over Redox cycles for all of the tests including 101278, a standard TSC-2 cell tested earlier prior to this project. Clearly the anode modifications and thickness have a large impact on Redox induced degradation. Testing to date shows that iron addition to the anode has the largest negative impact on Redox degradation, followed by cell thickness (the thinner the anode substrate the quicker the onset of degradation). Reducing cell thickness from 1mm to 0.6mm can be more than offset by grading the composition of the AFL. By adding an oxidation

barrier layer, very significant improvements are seen; and when the thickness and composition of this layer are modified, near zero degradation rates are achievable with the same Redox test that shows significant degradation for equivalent cells that have no oxidation barrier layer.

These results clearly demonstrate the improvements made showing the feasibility of a Redox tolerant cell as required for the previously completed 2.1.2 milestone Figure 2.1-114 showing the initial and final power curve comparison after cumulative Redox cycles for a baseline cell and 102072 a cell developed and tested with 4 oxidation barrier layers. Degradation at all conditions has been reduced to <0.5% compared with the baseline cell currently used in large area stacks that displayed up to 15% degradation and was found to be cracked after testing.

Table 2.1-4 Summary of Redox Tests Cell Physical Properties

					SEM Thickness Measurements			Cell Broken	
Test No.	Cell Type	NiO Content of Anode Substrate (%)	NiO Content of AFL (%)	Nominal Cell Thickness (mm)	Half-Cell (mm)	AFL (um)	EL (um)	Y or N	After Redox Depth (%)
101278	**TSC-2**	**57**	**57**	**1**				**N**	
102038	TSC-2	57	57	1	1.101	14	9	N	
102039	TSC-3	57	57	0.6	0.55	9	5	Y	180
102040	65/10	65	57	0.6	0.604	9	7	Y	180
102041	65/10	65	57	0.335	0.314	8	4	Y	120
102042	RSOFC-7	57	57	0.4				Y	180
102043	TSC-2+	57	57	0.6	0.557	12	5	Y	180
102044	57Ni/5Fe 100%3Y 1295°C fired	57	57	0.6	0.606	10	4	Y	20
102046	57Ni/5Fe 100%3Y 1295°C fired	57	57	0.6	0.685	10	4	Y	10
102048	TSC-3	57	57	0.6	0.591	8	6	Y	120
102050	TSC-3	57	57	0.6	0.580	8	4	Y	60
102053	TSC-3 AFL Barrier Layer	57	57, 45, 40	0.6	0.583	12	4	N	
102056	TSC-3 AFL Barrier Layer	57	57, 45	0.6	0.575	10	4	N	
102059	TSC-3	57	57, 45, 40	0.6	0.546	13	4	N	
102062	TSC-3	57	57, 45	0.6	0.565	12	4	N	
102064	TSC-3 AFL Barrier Layer	57	57, 40	0.6	0.576	12	5	N	
102067[a]	TSC-3	57	57, 40	0.6	0.538	12	4	N	
102072	TSC-3 with 4 AFL Barrier Layers	57	57	0.6	0.54	8	3	N	
102073	TSC-3 with 2 AFL barrier layers OB-1	57	57	0.6				N	
102076	TSC-3 with 2 AFL barrier layers OB-2	57	57	0.6	0.524	9	4	N	

					SEM Thickness Measurements			Cell Broken	
Test No.	Cell Type	NiO Content of Anode Substrate (%)	NiO Content of AFL (%)	Nominal Cell Thickness (mm)	Half-Cell (mm)	AFL (um)	EL (um)	Y or N	After Redox Depth (%)
101278	**TSC-2**	**57**	**57**	**1**				**N**	
102078[b]	TSC-3 with 2 AFL barrier layers OB-3	57	57	0.6	0.558	9	3	N	
102079[c]	TSC-3 with 2 AFL barrier layers OB-4	57	57	0.6	0.519	9	4	N	Failed at 60 due to short
102080	TSC-3 with 2 AFL barrier layers OB-5	57	57	0.6	0.58	9	4	Y	180
102082	TSC-3 with 3 AFL Barrier Layers	57	57	0.6				N	
102083	TSC-3 with 4 AFL Barrier Layers	57	57	0.6	0.577	9	4	N	
102085	TSC-3	57	57	0.6	0.575	9	5	Y	180
102086	TSC-3 with 2 AFL barrier layers OB-2 Repeat	57	57	0.6	0.555	8	4	Y	120

[a]102067 had a broken AI pipe weld at end of test causing testing problems.
[b]102078 had a broken test stand airline at end of test causing testing problems. This may have affected 102073 and 102076 testing.
[c]102079 had a short between FI pipe and grounded load plate causing testing problems.

Table 2.1-5 Summary of Redox Tests Cell Electrochemistry

		Cell Voltage (mV) at						Total Degradation (%)		
Test No.	Cell Type	Start (OCV)	End (OCV)	Start (60A)	End (60A)	Start (40.5A)	End (40.5A)	OCV	60A	40.5A
101278	**TSC-2**	**1097**	**1053**	**836**	**746**	**816**	**742**	4	11	9
102038	TSC-2	1078	1046	775	690	795	710	3	11	11
102039	TSC-3	1091	999	892	761	882	816	8	15	7
102040	65/10	1089	1033	874	745	876	831	5	15	5
102041	65/10	1084	873	885	<600	887	<600	19	100	100
102042	RSOFC-7	1084	967	904	693	894	717	11	23	20
102043	TSC-2+	1091	997	826	782	834	<600	9	5	100
102044	57Ni/5Fe 100%3Y 1295°C fired	1091	985	891	683	885	<600	10	23	100
102046	57Ni/5Fe 100%3Y 1295°C fired	1087	1020	886	846	881	<600	6	5	100
102048	TSC-3	1089	1017	879	773	875	<600	7	12	100
102050	TSC-3	1091	981	884	755	881	<600	10	15	100
102053	TSC-3 AFL Barrier Layer	1082	1055	869	840	863	839	2	3	3
102056	TSC-3 AFL Barrier Layer	1090	1061	870	858	863	858	3	1	1
102059	TSC-3	1084	1017	875	800	871	821	6	9	6
102062	TSC-3	1081	1025	868	808	867	817	5	7	6
102064	TSC-3 AFL Barrier Layer	1082	1058	857	832	859	831	2	3	3
102067[a]	TSC-3	1069	1046	863	629	865	829	2	27	4
102072	TSC-3 with 4 AFL Barrier Layers	1073	1068	870	868	865	865	0	0	0
102073	TSC-3 with 2 AFL barrier layers OB-1	1084	1076	876	878	872	874	1	0	0
102076	TSC-3 with 2 AFL barrier layers OB-2	1081	1081	871	878	871	876	0	-1	-1

		Cell Voltage (mV) at						Total Degradation (%)		
Test No.	Cell Type	Start (OCV)	End (OCV)	Start (60A)	End (60A)	Start (40.5A)	End (40.5A)	OCV	60A	40.5A
101278	**TSC-2**	**1097**	**1053**	**836**	**746**	**816**	**742**	4	11	9
102078[b]	TSC-3 with 2 AFL barrier layers OB-3	1085	1066	874	0	872	869	2	100	0
102079[c]	TSC-3 with 2 AFL barrier layers OB-4	1082	0	875	0	876	0	100	100	100
102080	TSC-3 with 2 AFL barrier layers OB-5	1091	934	881	528	877	698	14	40	20
102082	TSC-3 with 3 AFL Barrier Layers	1090	1082	868	853	868	858	1	2	1
102083	TSC-3 with 4 AFL Barrier Layers									
102085	TSC-3	1075	960	843	607	857	506	11	28	41
102086	TSC-3 with 2 AFL barrier layers OB-2 Repeat	1085	975	866	722	866	760	10	17	12

[a]102067 had a broken Al pipe weld at end of test causing testing problems.
[b]102078 had a broken test stand airline at end of test causing testing problems. This may have affected 102073 and 102076 testing.
[c]102079 had a short between Fl pipe and grounded load plate causing testing problems.

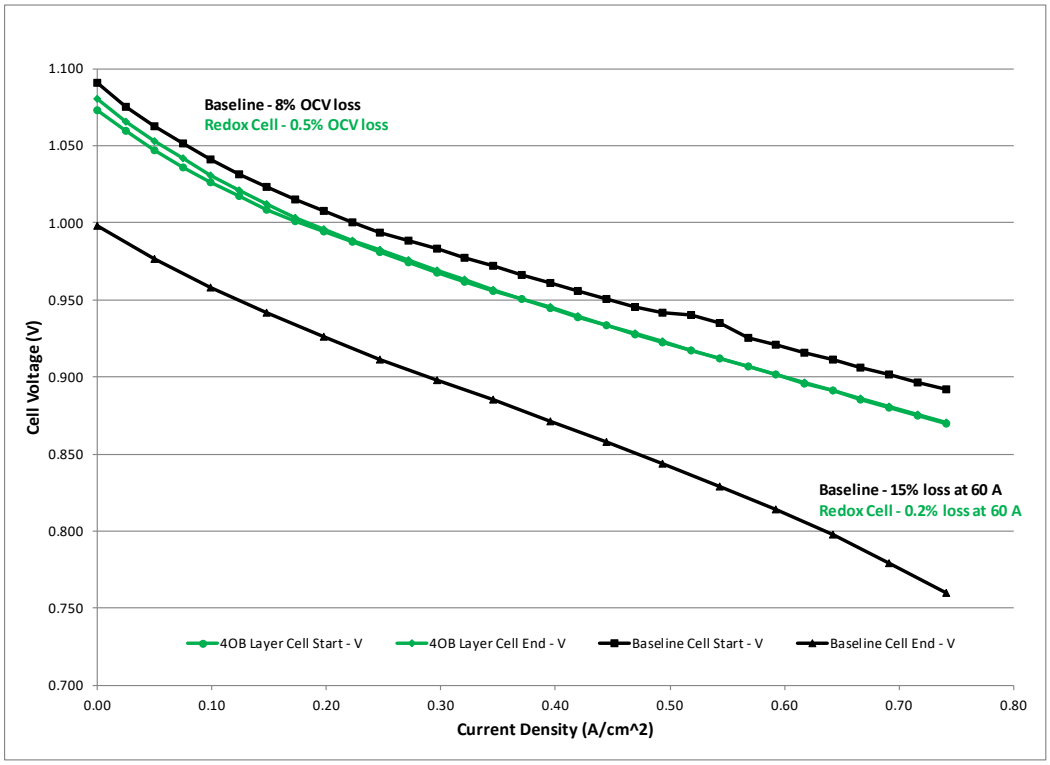

Figure 2.1-114 Initial and Final V-J Curves at 750°C, Baseline (102039) vs Improved (102072) Redox Cells

Preoxidation testing proved to be problematic when trying to implement in conjunction with the highly successful oxidation barrier approach. Previously, regular cells were preoxidised at 550°C overnight after initial cell testing, then were reduced and ready to be used. Such a process could easily be adopted in the stack. However, when using an oxidation barrier that is effective at slowing air flow to the anode even at 750°C, it was found that excessively long oxidation times would be required at 550°C such that the process would no longer be feasible. For example, a typical cell would measure 0 V after only 4-5 hours with 120ml/min air flow at 550°C indicating complete or nearly complete oxidation. The first test with 4 oxidation barrier layers to attempt to combine 550°C preoxidation (102083) was still at 0.326 V after more than 50 hours of air flow. It was decided that these approaches could not be combined and barrier layers are the preferred path forward. Ultimately a combination of barrier layers and graded AFL layers might be the best solution, but more testing of the combination would be required.

The most common causes of Redox degradation are unplanned shutdowns with loss of fuel where the stack would be cooled without any fuel flow and hot holds with loss of fuel where a failure causes the stack to remain hot with no fuel flowing. It was decided to investigate the first one as the primary issue where fuel is lost and the plant cools down as the preferred response. A test was performed with a 'baseline cell', that is a nominally 600um thick TSC-3 cell with no modifications. The cell test, 102088, was characterized with initial power curves and steady-state degradation hold. Figure 2.1-115 shows initial power curves for 102088. Figure 2.1-116 shows the effects of thermal cycles and 5 of these Redox cycles on the V-J curves for this cell and Figure 2.1-117 shows the effects on steady-state holds at 750°C, 50% Uf, 25% Uo (air) and 0.5A/cm^2 for the same test. There is no measurable degradation for these tests indicating that loss of fuel where the plant cools down as an immediate response may not be an issue even with standard

TSC-3 cells. Following these tests, it was decided to add a hot hold with the fuel pipes disconnected prior to cooling down to simulate slower cooling due to higher thermal mass for cells that would be contained in a stack. Redox cycle 6 had a 1 hour dwell, Redox cycles 7 and 8 had 2 hour dwells and Redox cycle 9 had a 4 hour dwell. Figure 2.1-118 shows the effects of thermal cycles and 9 Redox cycles on the V-J curves for this cell and Figure 2.1-119 shows the effects on steady-state holds at 750°C, 50% Uf, 25% Uo (air) and 0.5A/cm^2 for the same test. Again, there is no measurable degradation for these tests indicating that even with reasonably slow cooling due to higher thermal mass of a stack versus a single-cell test loos of fuel with immediate shutdown may not be an issue for regular TSC-3 cells. In the interests of pushing the boundaries for Redox Cycle 10 an 8 hour dwell with no fuel pipes connected at 750°C was used before the cooldown. At this point, some degradation occurred though the cell was still intact and able to operate. Figure 2.1-120 shows the effects of thermal cycles and all 10 Redox cycles on the V-J curves for this cell and Figure 2.1-121 shows the effects on steady-state holds at 750°C, 50% Uf, 25% Uo (air) and 0.5A/cm^2 for the same test. Figure 2.1-122 shows the final power curves for 102088 demonstrating the cell is still operable even after all of these cycles.

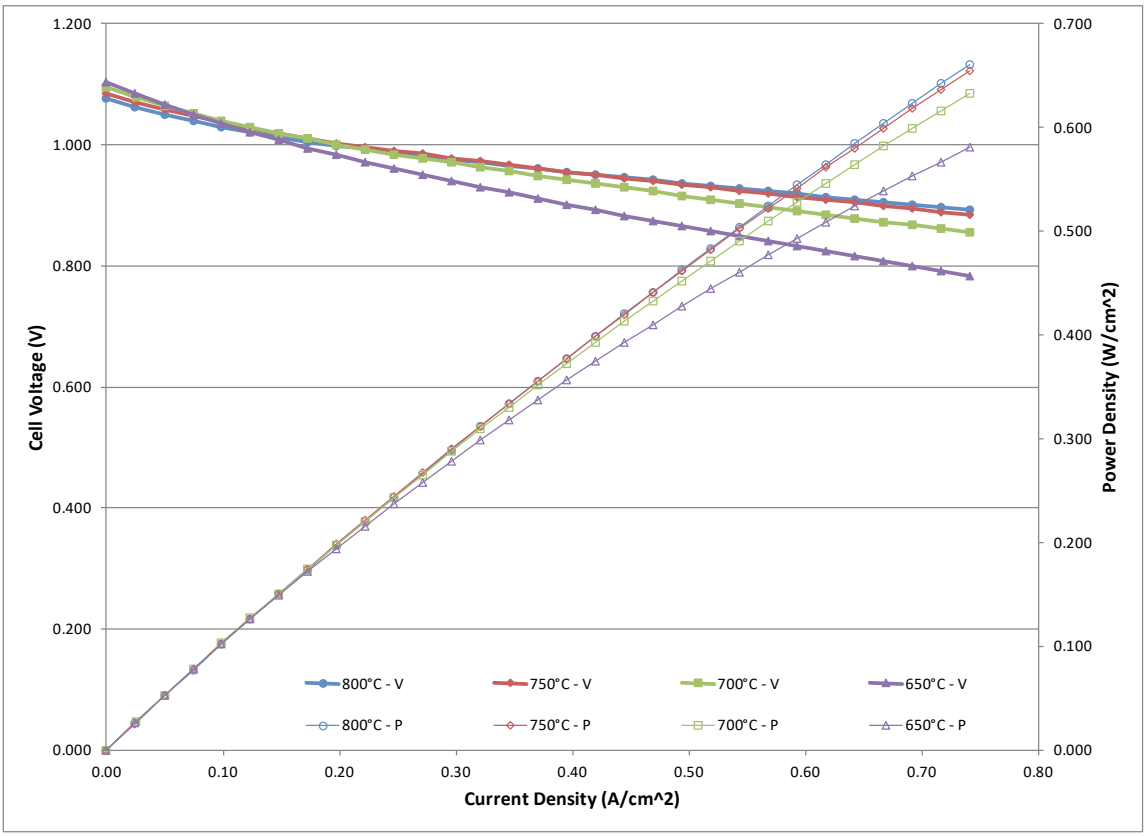

Figure 2.1-115 Test 102088 Initial Performance Curves 650 – 800°C

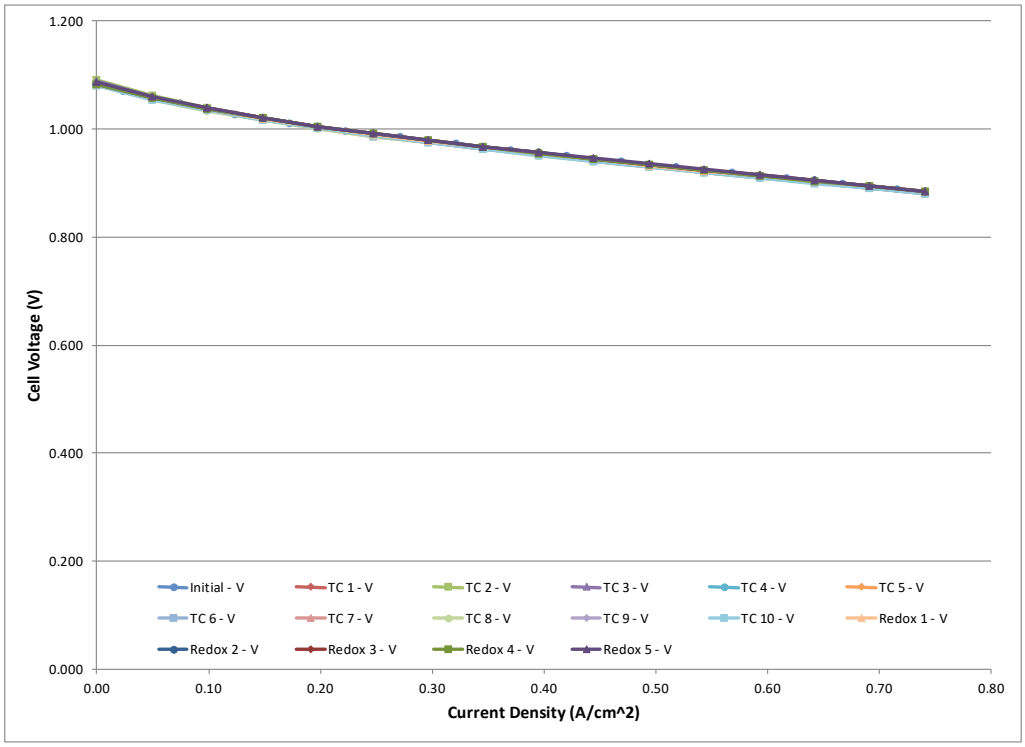

Figure 2.1-116 Test 102088 Performance Curves at 750°C over 10 Thermal and 5 Redox Shutdown Cycles

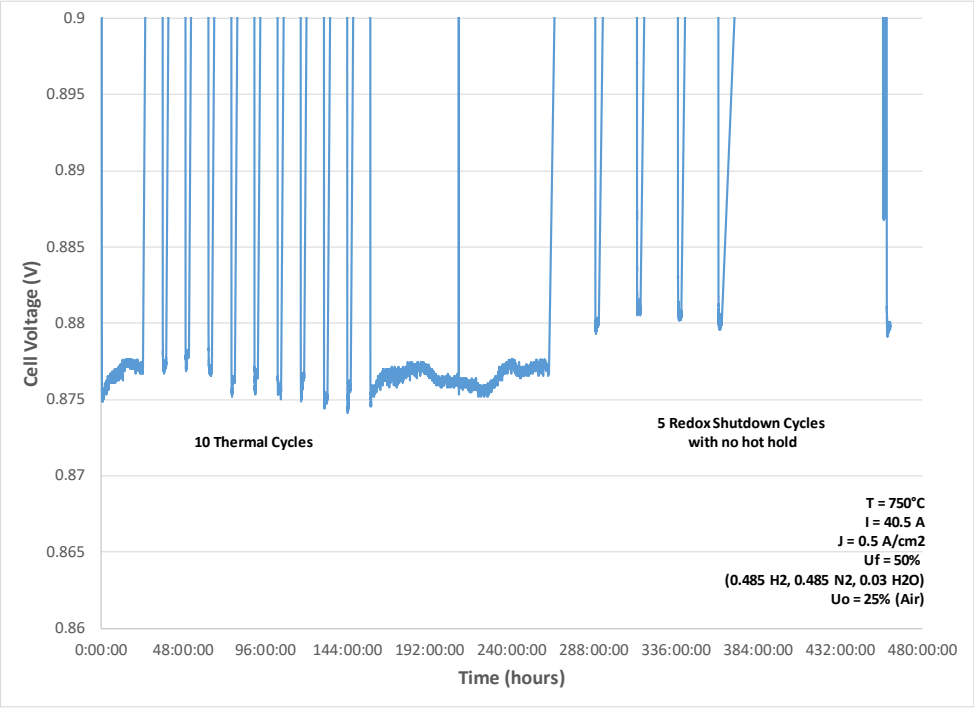

Figure 2.1-117 Test 102088 Steady State Hold Results at 750°C over 10 Thermal and 5 Redox Shutdown Cycles

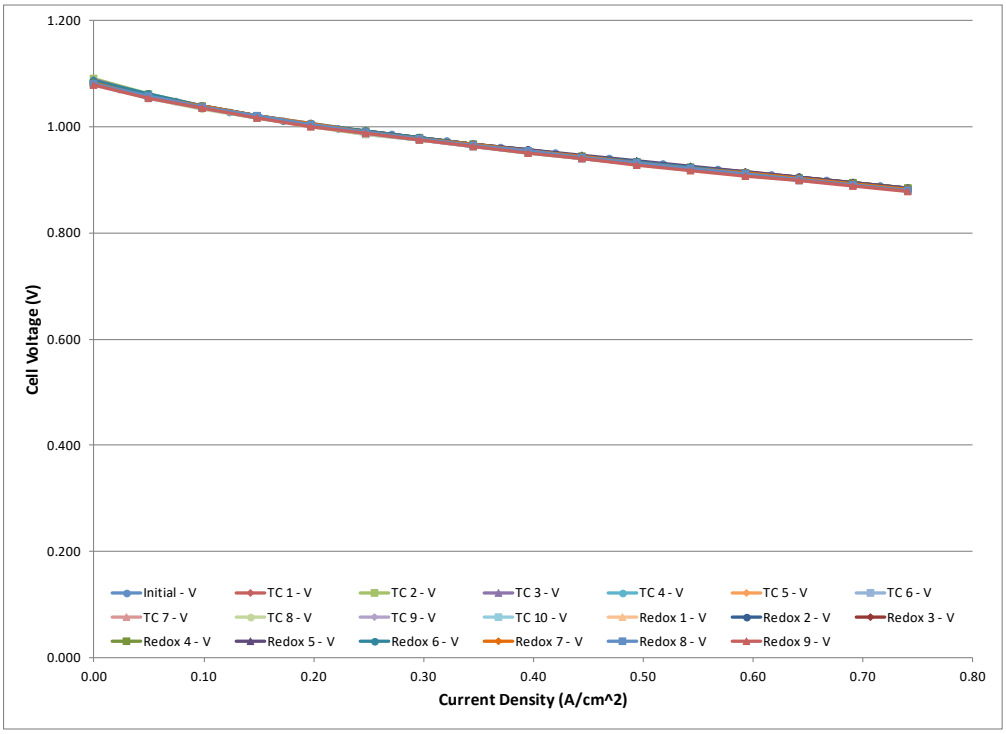

Figure 2.1-118 Test 102088 Performance Curves at 750°C over 10 Thermal and 9 Redox Shutdown Cycles With Various Hot Holds (Fuel Pipes Disconnected)

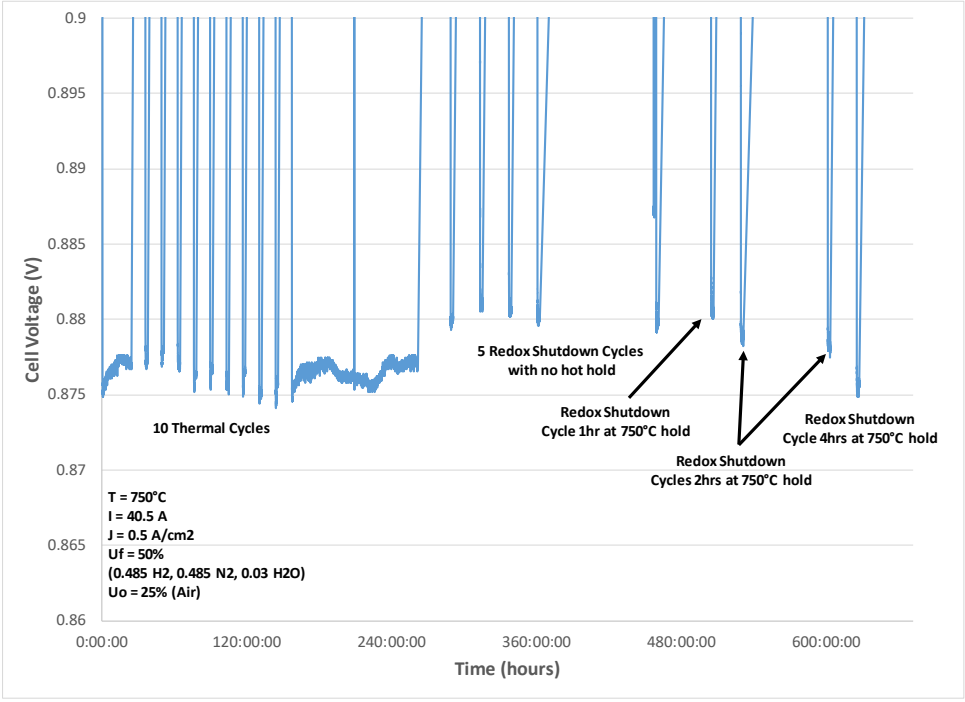

Figure 2.1-119 Test 102088 Steady State Hold Results at 750°C over 10 Thermal and 9 Redox Shutdown Cycles With Various Hot Holds (Fuel Pipes Disconnected)

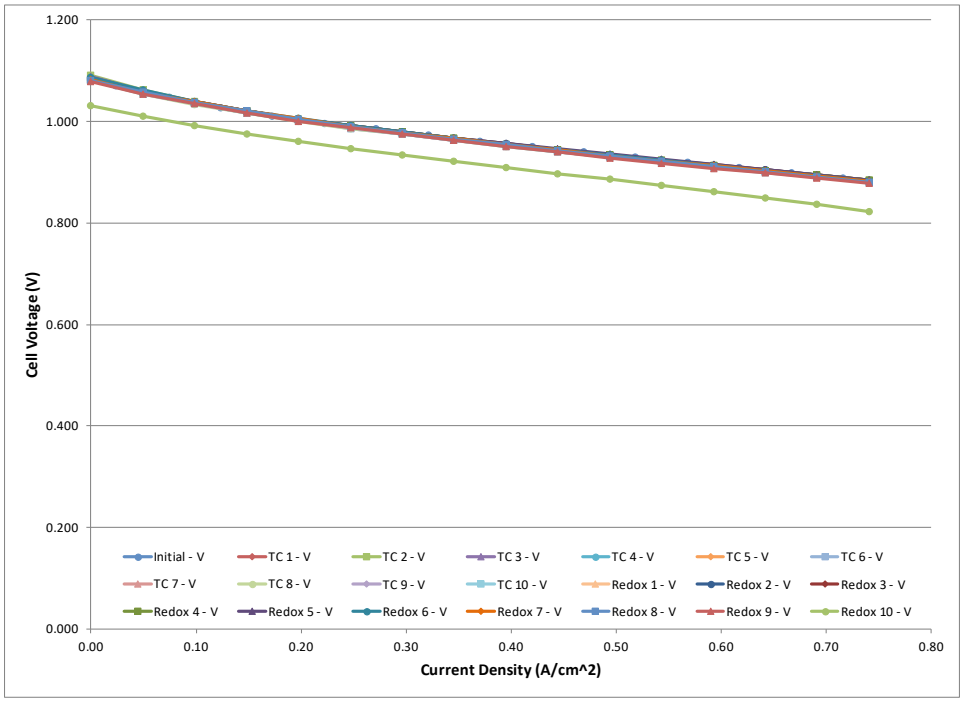

Figure 2.1-120 Test 102088 Performance Curves at 750°C over 10 Thermal and 10 Redox Shutdown Cycles With Various Hot Holds (Fuel Pipes Disconnected)

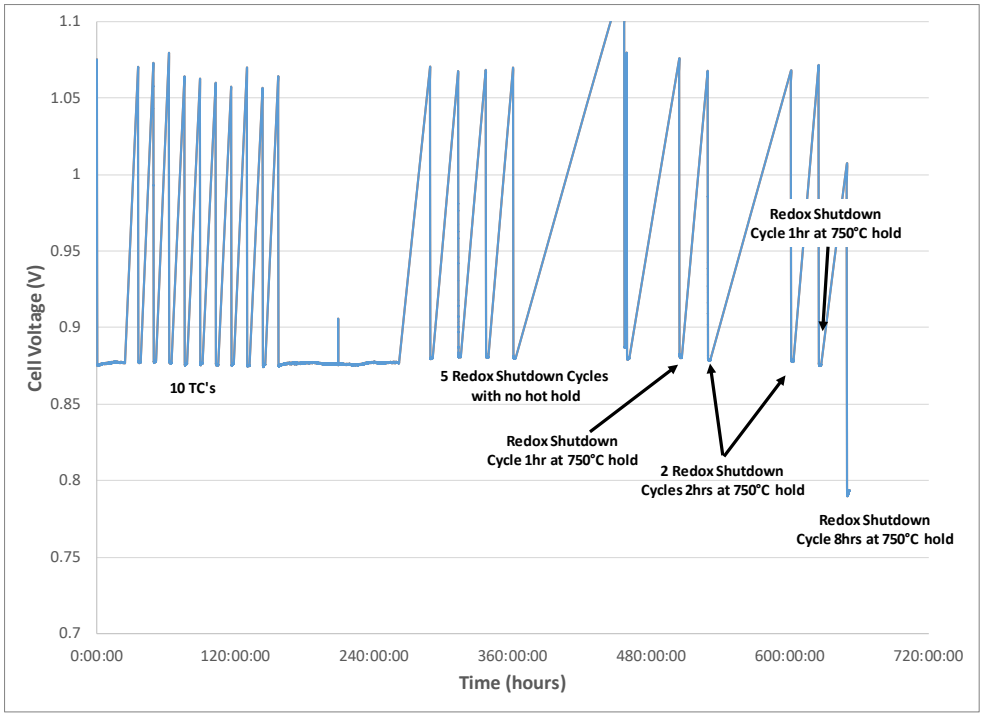

Figure 2.1-121 Test 102088 Steady State Hold Results at 750°C over 10 Thermal and 10 Redox Shutdown Cycles With Various Hot Holds (Fuel Pipes Disconnected)

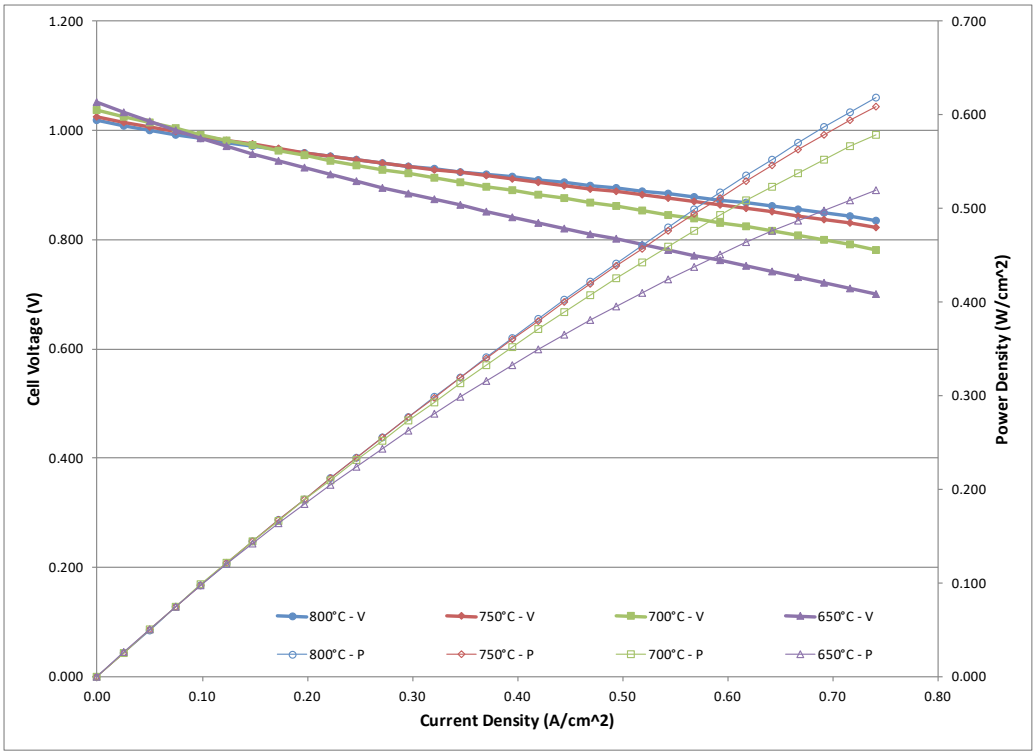

Figure 2.1-122 Test 102088 Final Performance Curves 650 – 800°C

Since it was demonstrated that regular TSC-3 cells could survive a shutdown with loss of fuel, the testing focus was shifted to loss of fuel while the stack remains hot (a system failure condition that could lead to a more damaging redox event). A cell with 4 oxidation barrier layers, test 102090, was run through 10 thermal cycles prior to Redox cycling. However, the cell voltage dropped 63 mV at power curve conditions and 62 mV at steady-state hold conditions over the 10 thermal cycles and the test was shutdown. Autopsy revealed delamination of the cathode on thermal cycling. This indicates a processing problem and so a standard TSC-3 cell was tested with new cathode paste for 10 thermal cycles. The cell, test 102093, showed typical thermal cycling characteristics with low degradation. A cell with 3 oxidation barrier layers was then cleaned and reprinted with fresh cathode paste and 10 thermal cycles run, test 102094. Degradation was acceptably low and this test is currently being used to investigate redox test parameters to simulate loss of fuel. Meanwhile more 4 layer oxidation barrier layer cells were printed and are currently sintering ready to be used in the final milestone test. The test plan was to run 10 thermal cycles followed by 10 redox cycles that simulate loss of fuel and ingress of air.

Development work was concluded to optimize cells for redox tolerance following 26 cell tests that culminated in the development of a new redox cell. Figure 2.1-123 shows the initial and final power curve comparison after cumulative Redox cycles for a baseline cell (102039) and a cell developed and tested with 4 oxidation barrier layers (102072). Degradation at all conditions has been reduced to <0.5% compared with the baseline cell currently used in large area stacks that displayed up to 15% degradation and was found to be cracked after testing.

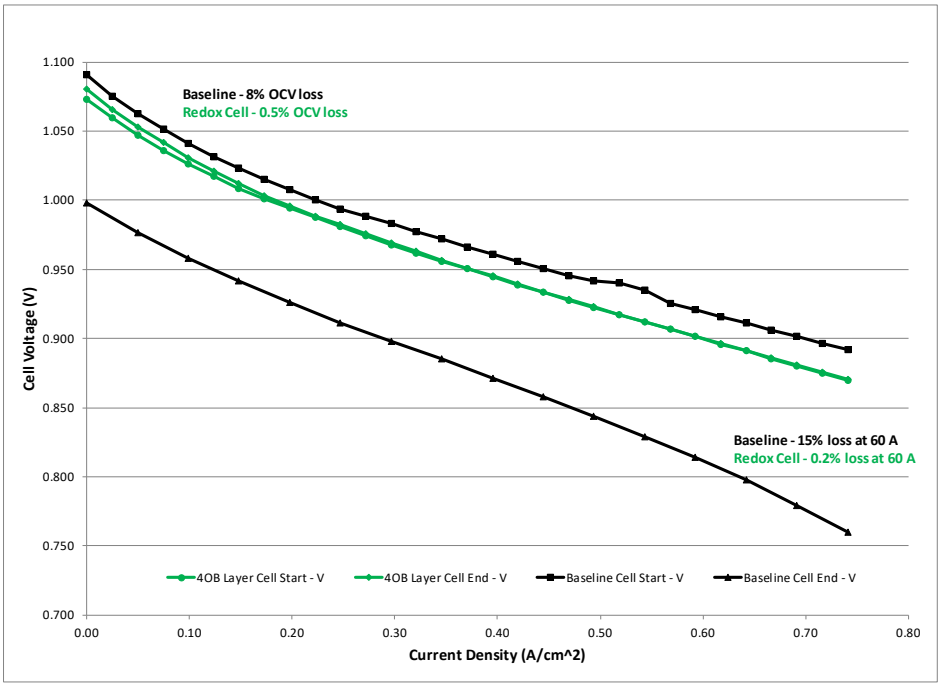

Figure 2.1-123 Initial and Final V-J Curves at 750°C, Baseline (102039) vs Improved (102072) Redox Cells

The most common causes of Redox degradation are unplanned shutdowns with loss of fuel where the stack would be cooled without any fuel flow and hot holds with loss of fuel where a failure causes the stack to remain hot with no fuel flowing. It was decided to investigate the first one as the primary issue where fuel is lost and the plant cools down as the preferred response. The cell test, 102088, was characterized with initial power curves and steady-state degradation hold. Figure 2.1-124 shows initial power curves for 102088. Figure 2.1-125 shows the effects of thermal cycles and 5 of these Redox cycles on the V-J curves for this cell and Figure 2.1-126 shows the effects on steady-state holds at 750°C, 50% Uf, 25% Uo (air) and 0.5A/cm^2 for the same test. There is no measurable degradation for these tests indicating that loss of fuel where the plant cools down as an immediate response may not be an issue even with standard TSC-3 cells. Following these tests, it was decided to add a hot hold with the fuel pipes disconnected prior to cooling down to simulate slower cooling due to higher thermal mass for cells that would be contained in a stack. Redox cycle 6 had a 1 hour dwell, Redox cycles 7 and 8 had 2 hour dwells and Redox cycle 9 had a 4 hour dwell.

Figure 2.1-127 shows the effects of thermal cycles and 9 Redox cycles on the V-J curves for this cell and Figure 2.1-128 shows the effects on steady-state holds at 750°C, 50% Uf, 25% Uo (air) and 0.5A/cm^2 for the same test. Again, there is no measurable degradation for these tests indicating that even with reasonably slow cooling due to higher thermal mass of a stack versus a single-cell test loss of fuel with immediate shutdown may not be an issue for regular TSC-3 cells. In the interests of pushing the boundaries for Redox Cycle 10 an 8 hour dwell with no fuel pipes connected at 750°C was used before the cooldown. At this point, some degradation occurred though the cell was still in-tact and able to operate. Figure 2.1-129 shows the effects of thermal cycles and all 10 Redox cycles on the V-J curves for this cell and Figure 2.1-130 shows the effects on steady-state holds at 750°C, 50% Uf, 25% Uo (air) and 0.5A/cm^2 for the same test. Figure

2.1-131 shows the final power curves for 102088 demonstrating the cell is still operable even after all of these cycles.

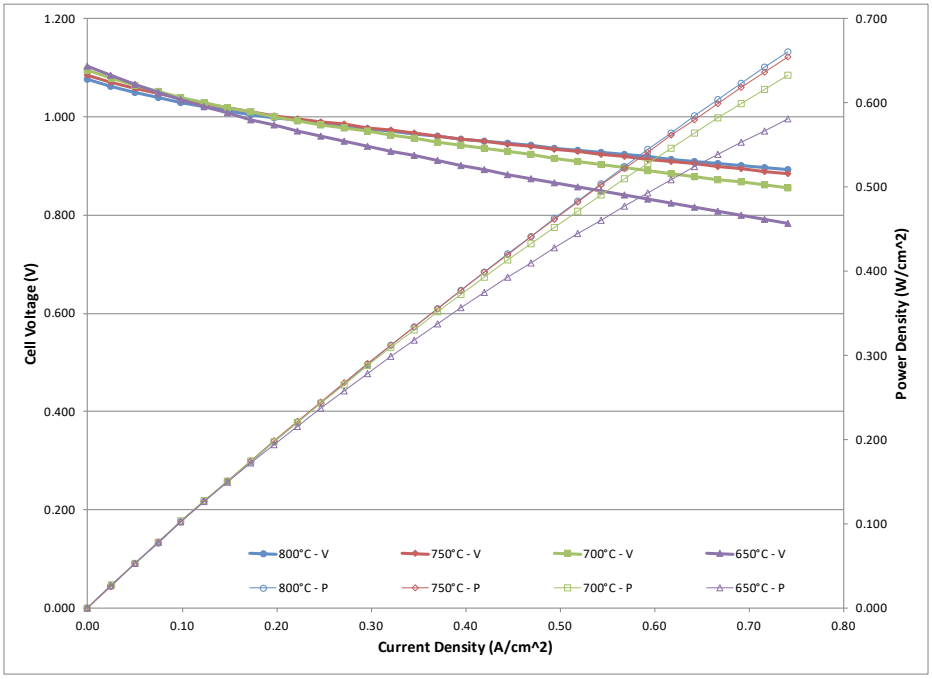

Figure 2.1-124 Test 102088 Initial Performance Curves 650 – 800°C

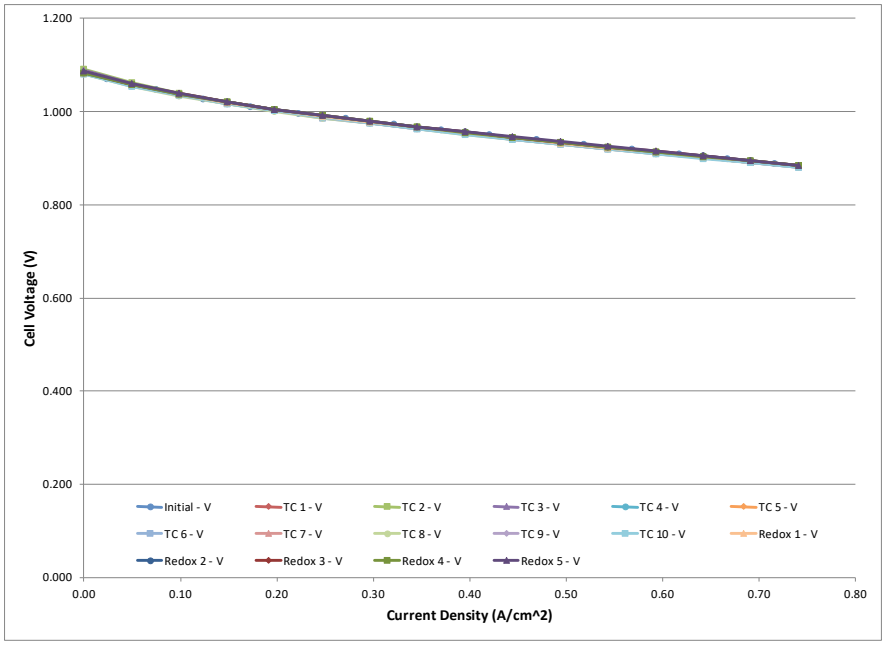

Figure 2.1-125 Test 102088 Performance Curves at 750°C over 10 Thermal and 5 Redox Shutdown Cycles

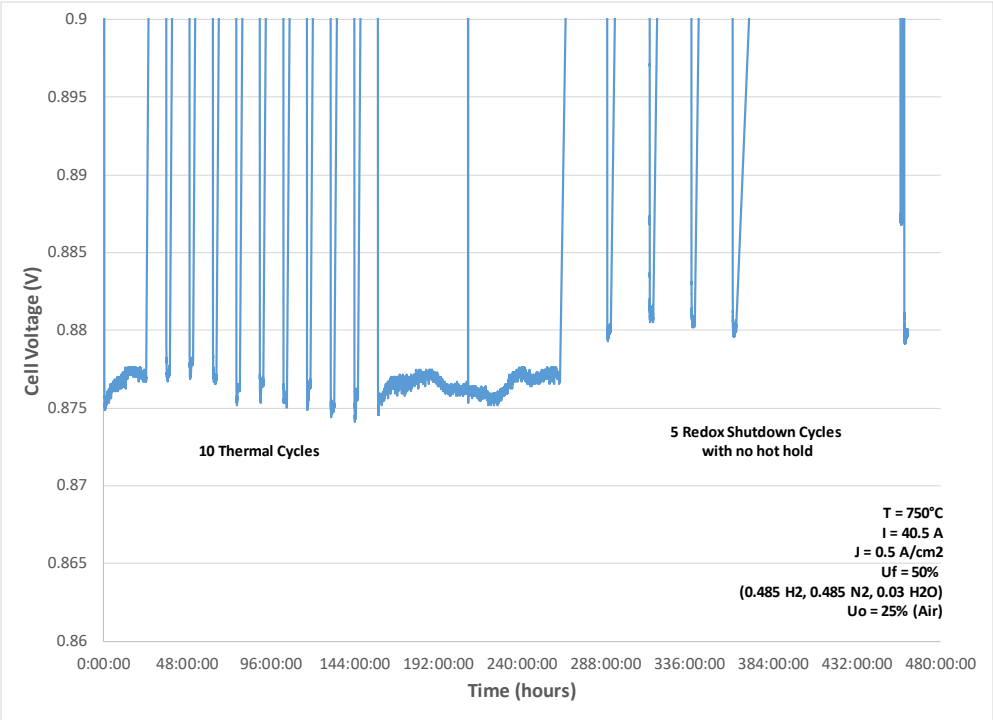

Figure 2.1-126 Test 102088 Steady State Hold Results at 750°C over 10 Thermal and 5 Redox Shutdown Cycles

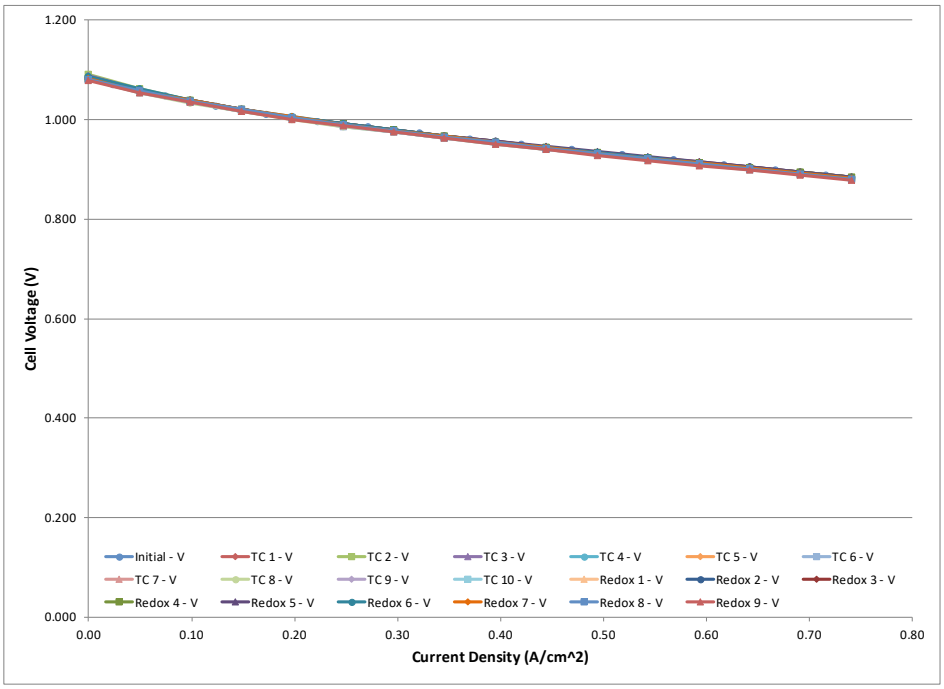

Figure 2.1-127 Test 102088 Performance Curves at 750°C over 10 Thermal and 9 Redox Shutdown Cycles with Various Hot Holds (Fuel Pipes Disconnected)

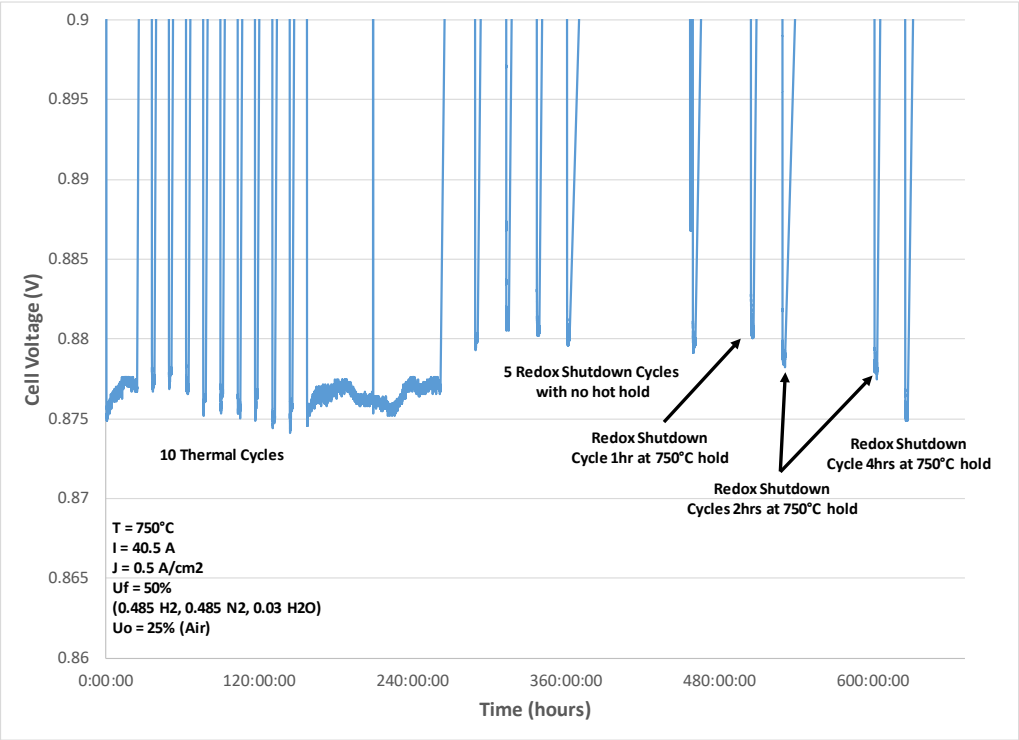

Figure 2.1-128 Test 102088 Steady State Hold Results at 750°C over 10 Thermal and 9 Redox Shutdown Cycles with Various Hot Holds (Fuel Pipes Disconnected)

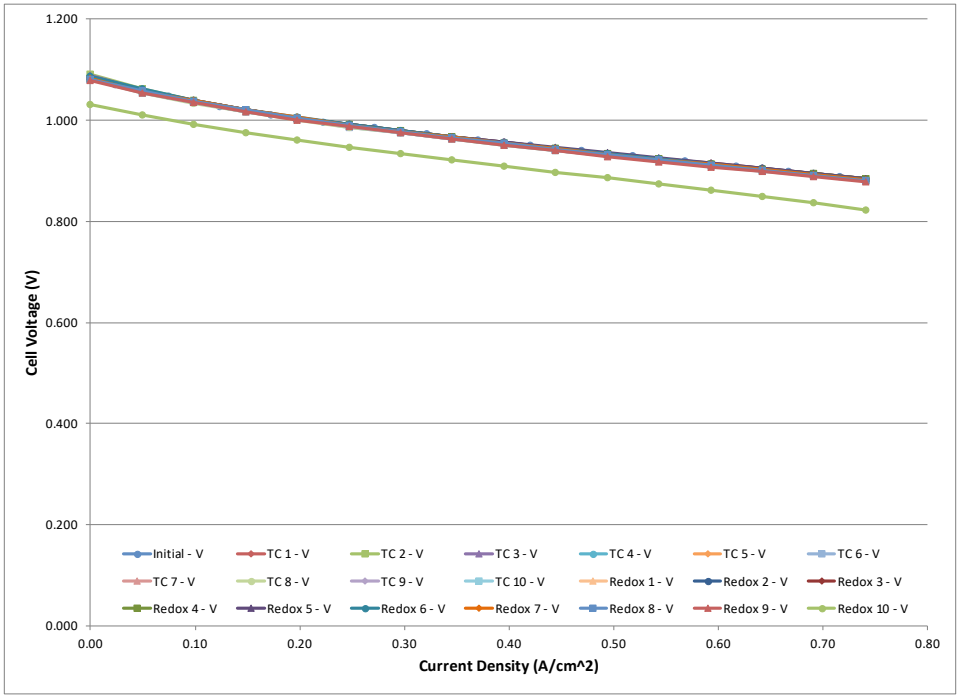

Figure 2.1-129 Test 102088 Performance Curves at 750°C over 10 Thermal and 10 Redox Shutdown Cycles with Various Hot Holds (Fuel Pipes Disconnected)

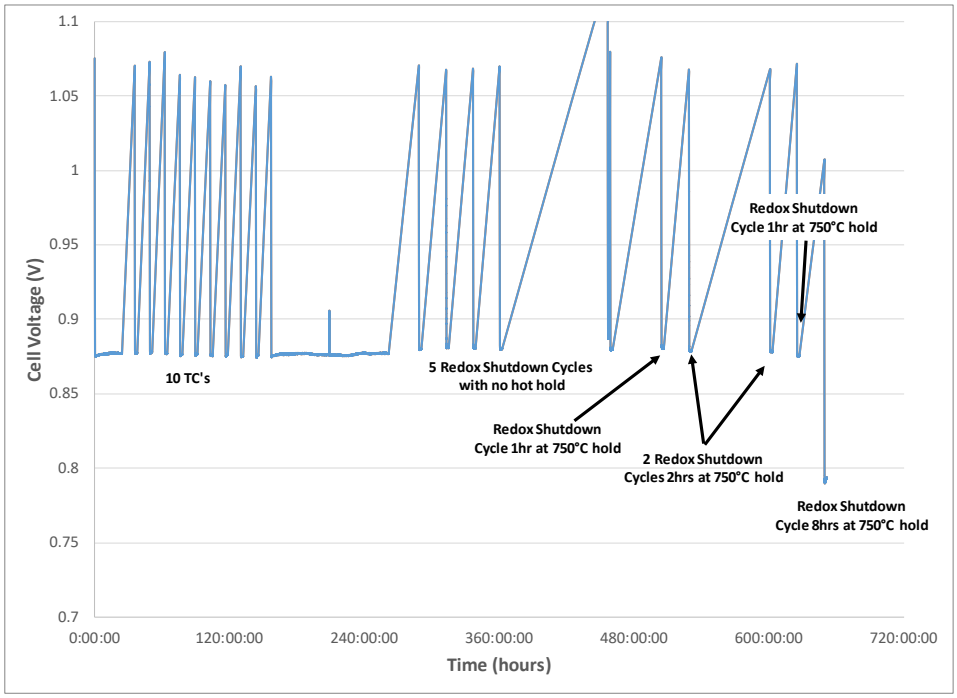

Figure 2.1-130 Test 102088 Steady State Hold Results at 750°C over 10 Thermal and 10 Redox Shutdown Cycles with Various Hot Holds (Fuel Pipes Disconnected)

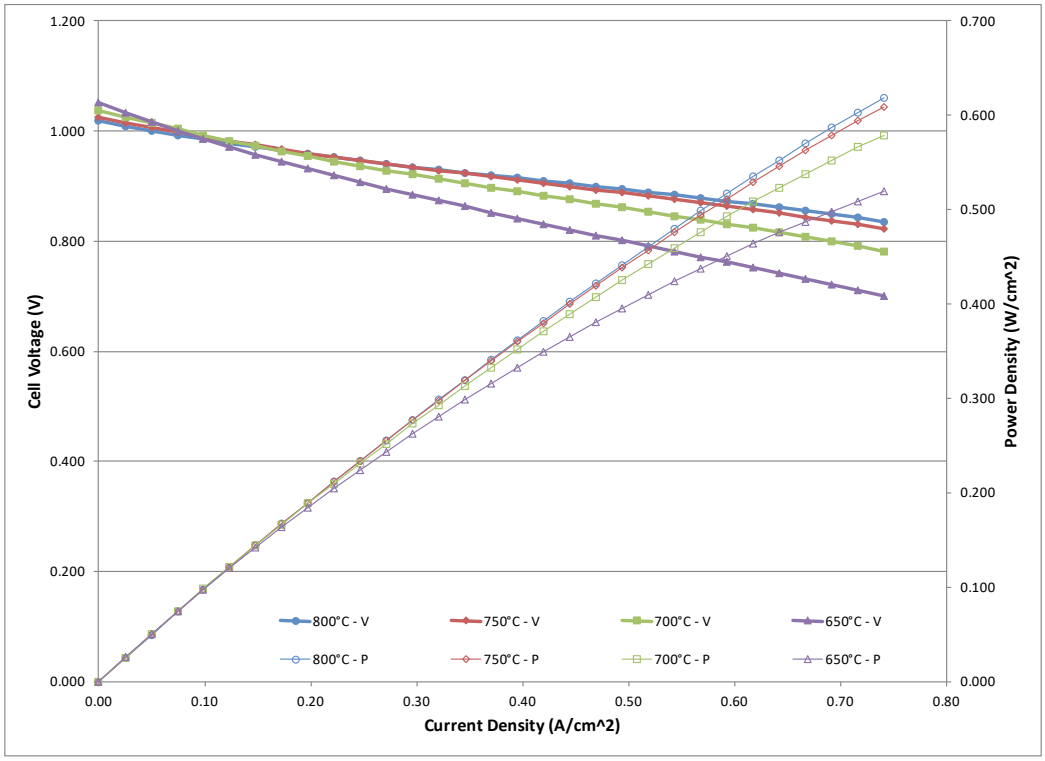

Figure 2.1-131 Test 102088 Final Performance Curves 650 – 800°C

Since it was demonstrated that regular TSC-3 cells could survive a shutdown with loss of fuel, the testing focus was shifted to include a loss of fuel while the stack remains hot for a period of 5 hours (a system failure condition that could lead to a more damaging redox event). A cell with 4 oxidation barrier layers, test 102090, was run through 10 thermal cycles prior to redox cycling. However, the cell voltage dropped 63 mV at power curve conditions and 62 mV at steady-state hold conditions over the 10 thermal cycles and the test was shutdown. Autopsy revealed delamination of the cathode on thermal cycling. This indicates a processing problem and so a standard TSC-3 cell was tested with a new cathode paste batch for 10 thermal cycles. The cell, test 102093, showed typical thermal cycling characteristics with low degradation, and was used as a baseline test to compare with the milestone test. Another cell with 3 oxidation barrier layers was then cleaned and reprinted with fresh cathode paste and 10 thermal cycles run, test 102094, as an initial attempt at the milestone.

The baseline TSC-3 cell 102093 was tested first. The cell ran power curves and steady-state holds as previously described for 102088 before and after each of 10 thermal cycles and 5 redox cycles. The redox cycles consisted of a 5 hour hot hold at 750°C with fuel pipes disconnected followed by cooling to 150°C (with pipes still disconnected). Pipes were then reconnected, purged with nitrogen gas and the cell heated to 750°C for reduction and testing. Each redox cycle was identical and all tests from this point on used this protocol for redox cycles. It was initially intended to run 10 thermal cycles, however, the cell had already degraded too much after 5 of these accelerated degradation redox cycles. Figure 2.1-132 shows the initial, 10 thermal cycle and 5 redox cycle power curves showing the TSC-3 cell had a more than 200mV drop over 5 redox cycles. Figure 2.1-133 shows the steady-state holds for initial, 10 thermal cycle and 5 redox cycles showing more than 600mV drop at this test condition over 5 redox cycles. The cell was found to be broken on autopsy with significant anode oxidation.

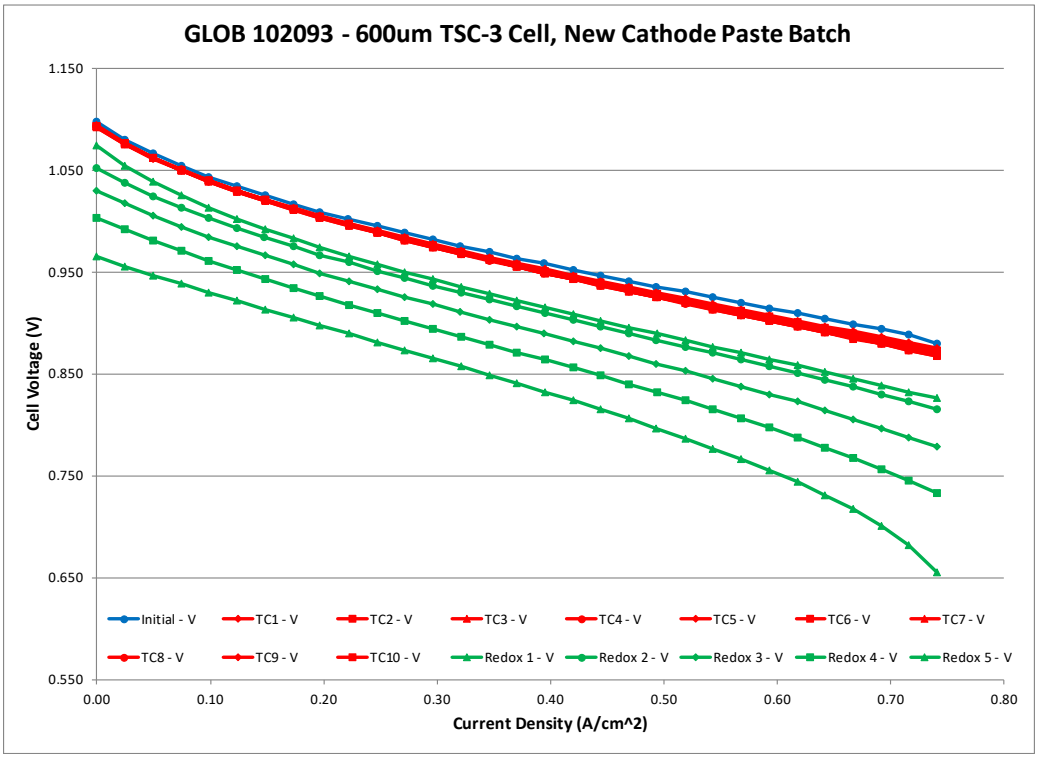

Figure 2.1-132 Test 102093 Performance Curves at 750°C over 10 Thermal and 5 Redox Shutdown Cycles with 5 Hour Hot Holds (Fuel Pipes Disconnected)

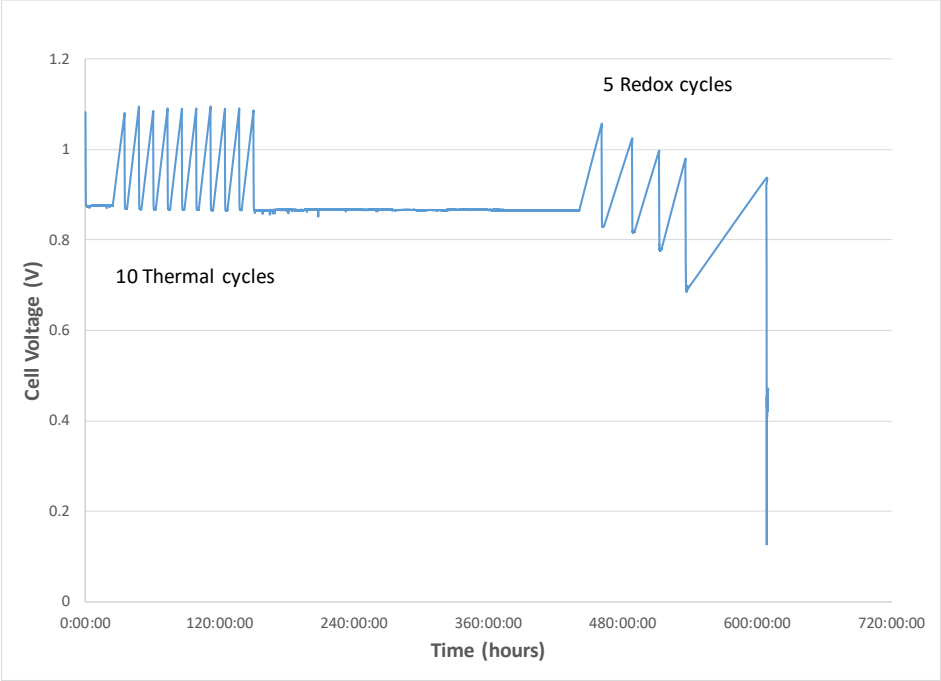

Figure 2.1-133 Test 102093 Steady State Hold Results at 750°C over 10 Thermal and 5 Redox Shutdown Cycles with 5 Hour Hot Holds (Fuel Pipes Disconnected)

Figure 2.1-134 shows power curves for the same test with a modified cell that has 3 Oxidation Barrier layers (except this cell survived 10 redox cycles). This was an attempt to meet the scheduled milestone date with a cell that was not the preferred redox cell, but second choice (as the other first choice cells had been used in prior testing). At the same time, new cells were prepared with 4 Oxidation Barrier layers in case this cell did not meet the milestone requirements for this accelerated degradation test. It can be seen that there is significant improvement over the standard TSC-3 cell that failed catastrophically after 5 redox cycles. This cell ran 10 redox cycles with only slightly higher degradation from redox cycles than thermal cycles. Figure 2.1-135 shows the steady state holds for the same test showing a similar trend and the autopsy revealed the cell was fully in-tact after testing showing significant improvement compared with the standard TSC-3 cell. However, this test did not meet the milestone requirements so another test, 102100, was run using a cell modified for the highest redox tolerance (4 Oxidation Barrier Layers).
Figure 2.1-136 shows power curves for the same thermal and redox cycle test. Since cell voltages overlap, Figure 2.1-137 shows the same data summarized to show initial power curve, after 10 thermal cycles and after 10 redox cycles. It can be seen that the cell drops 8 mV over 10 thermal cycles and a further 9 mV after 10 Redox cycles. Since the redox cycles include a thermal cycle the redox cycle degradation is clearly significantly lower than thermal cycle degradation, and within experimental error is considered the same. Figure 2.1-138 shows steady-state holds for the same test with 7mV drop over 10 thermal cycles and only 5 mV drop over 10 thermal cycles (each including a redox cycle). Similar to the power curves (and slightly better) this is also considered equivalent within experimental error and is a clear improvement over 102093, and a very significant improvement over the standard TSC-3 cell that catastrophically failed after only 5 redox cycles. This improved redox tolerant cell showed equivalent degradation over 10 redox cycles and 10 thermal cycles for both power curve and 2 hour steady-state holds (1 mV higher and 2 mV lower respectively, both within experimental error).

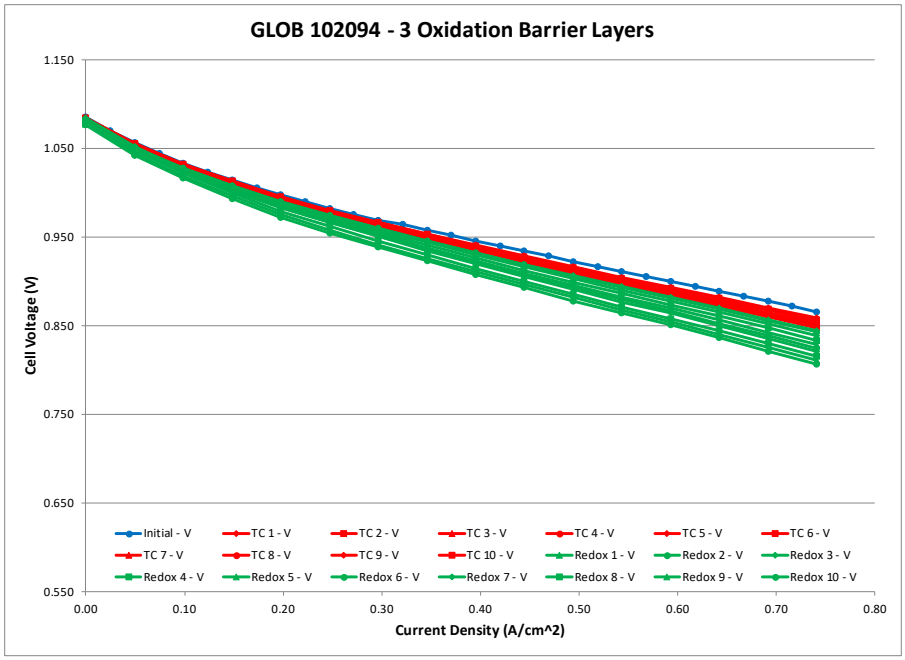

Figure 2.1-134 Test 102094 Performance Curves at 750°C over 10 Thermal and 10 Redox Shutdown Cycles with 5 Hour Hot Holds (Fuel Pipes Disconnected)

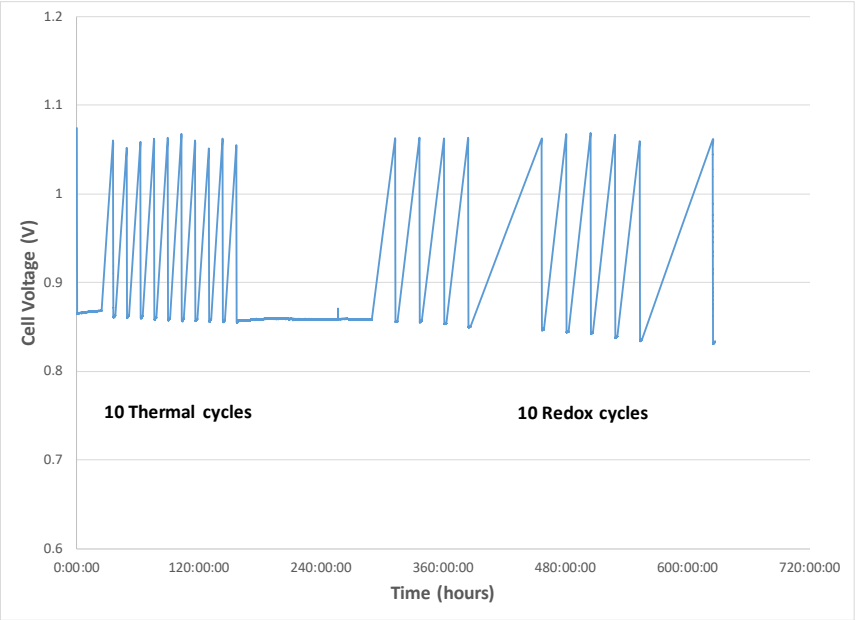

Figure 2.1-135 Test 102094 Steady State Hold Results at 750°C over 10 Thermal and 10 Redox Shutdown Cycles With 5 Hour Hot Holds (Fuel Pipes Disconnected)

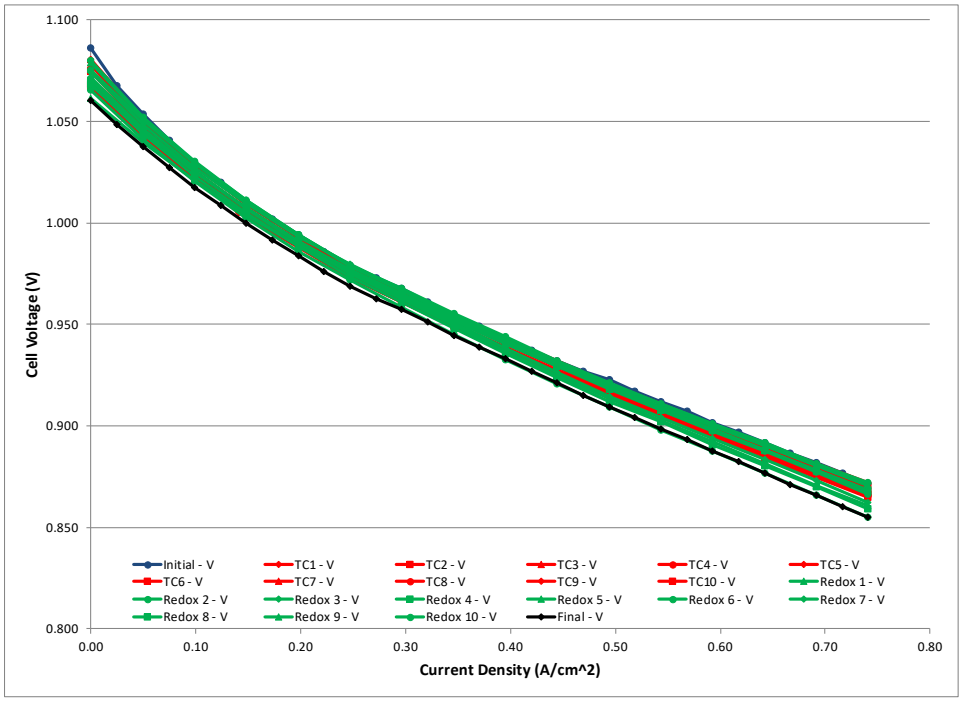

Figure 2.1-136 Test 102100 Performance Curves at 750°C over 10 Thermal and 10 Redox Shutdown Cycles with 5 Hour Hot Holds (Fuel Pipes Disconnected)

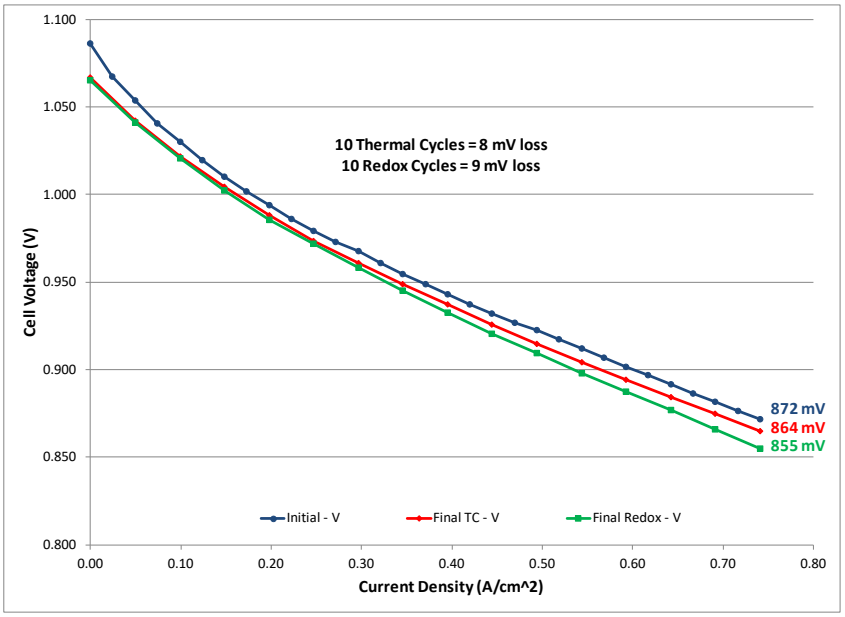

Figure 2.1-137 Test 102100 Performance Curves Comparison at 750°C after 10 Thermal and 10 Redox Shutdown Cycles with 5 Hour Hot Holds (Fuel Pipes Disconnected)

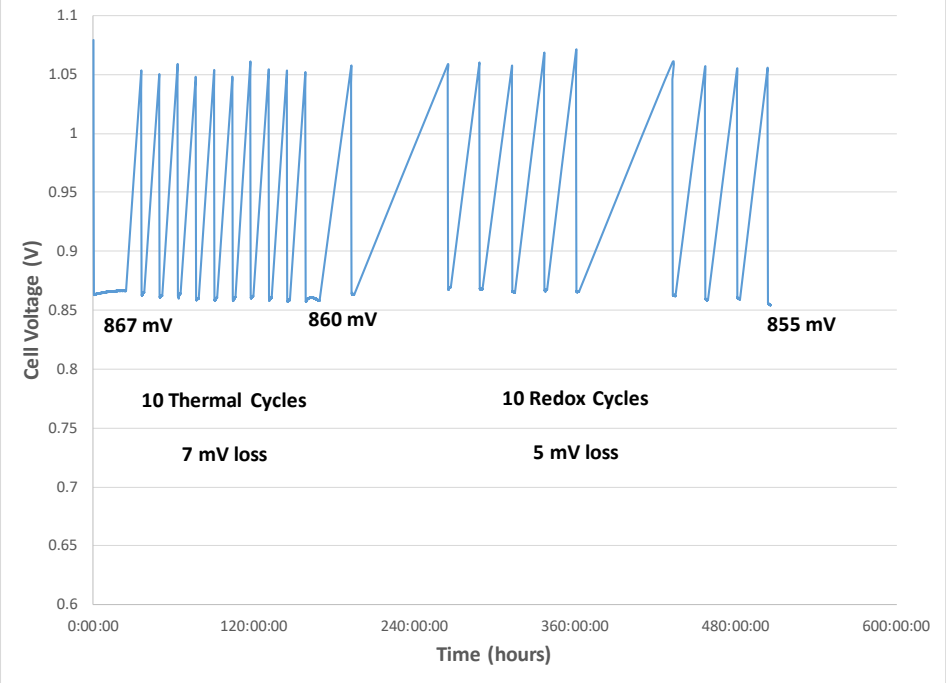

Figure 2.1-138 Test 102100 Steady State Hold Results at 750°C over 10 Thermal and 10 Redox Shutdown Cycles with 5 Hour Hot Holds (Fuel Pipes Disconnected)

2.2 Cell Manufacturing Process Development

Objective:

The objective was to validate and incorporate major cell material improvements, breakthroughs and cost reduction achievements into the improved cells through extensive cell manufacturing process development.

Approach:

The cell fabrication boundary for cell size and thickness were explored for various stack design approaches. Computational thermo-mechanical modeling were developed and expanded for the analysis of various cell designs to improve compliance and reliability during manufacturing and normal operating conditions. Cell geometry, including aspect ratio, were cost-benefit-analyzed and defined. Limited production trials were conducted to explore cell fabrication boundary. Various cell component design parameters were evaluated to identify the optimum cell configuration for system operation. Parameters such as performance (power output, thermal management and efficiency), design simplicity, technical risk, manufacturability, and material and process costs were considered in the final design selection process. Overall, the manufacturing techniques and processes were refined to meet required quality and yield standards.

Results & Discussion:

The cell fabrication boundary for cell size and thickness has been defined based on CSA stack design. Cell process development focus was placed initially in meeting the cell design specifications with both standard TSC3 cell and HiPOD cell formulation.

In order to fabricate sufficient cells to meet CSA stack development needs, cell process engineering was applied to bring CSA cell fabrication from laboratory process to pilot trial as shown in Figure 2.2-1 below. Pilot scale equipment was used to produce large quantity of anode slurry. A 60 foot continuous tape caster was used to cast the 300-600 micron thick anode support. Both anode functional layer (10-20 micron) and electrolyte layer (5-20 micron) were screen printed onto the green (unfired) anode support tape. The green cell was punched out with simple die cutter, and went through co-sintering in a 60 foot push-plate kiln. The cathode layer was screen printed on the sintered half-cell, and went through a cathode sintering process. Along the cell

fabrication process, various cell QC processes were applied to ensure the cell manufacturing process was in control, and cells met all stack design specifications.

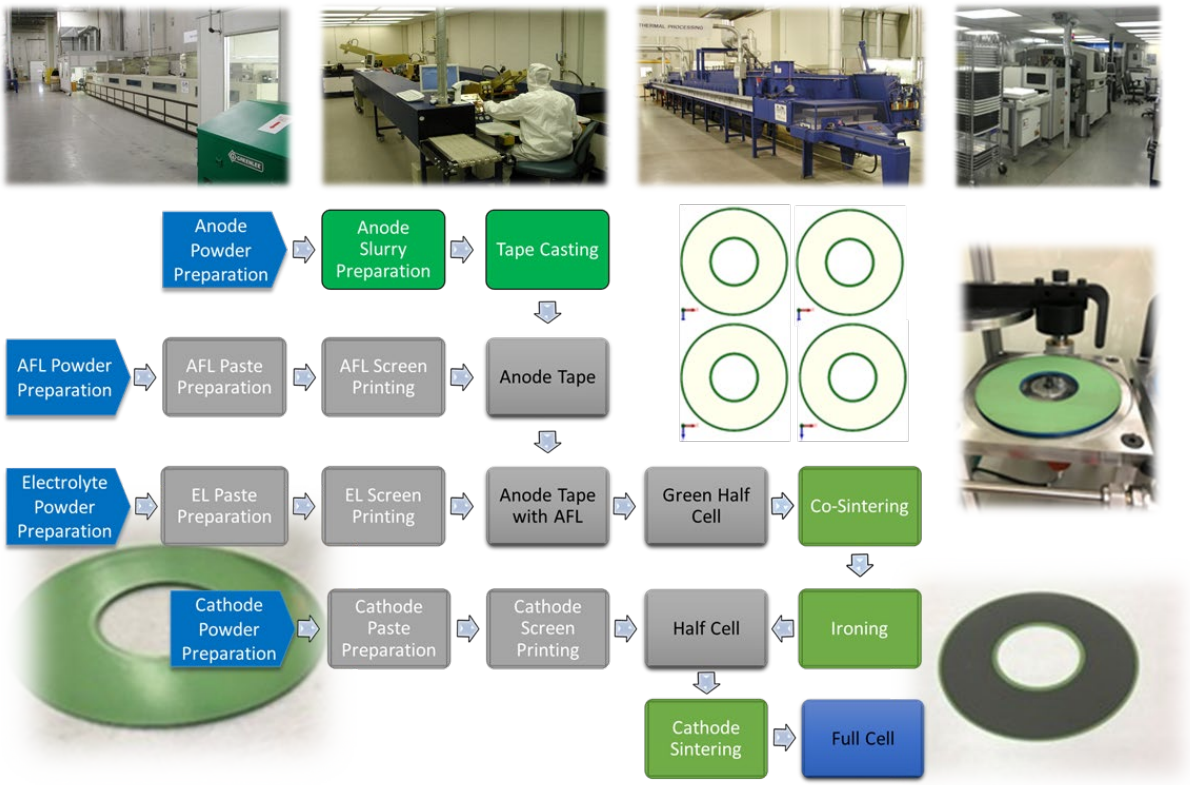

Figure 2.2-1 CSA Cell Fabrication Process Flow Diagram

In this project, hundreds of CSA cells were produced and utilized in a number of 45-cell CSA development stacks. However, the cell process yield was low in meeting the CSA design specifications. This is especially true in meeting the tight cell ID and OD dimensions.

In order for the cell to be accepted, it must pass the QC dimensional requirements (ID, OD, and thickness) and cell leak. The biggest challenge was facing is how to satisfy the cell diameter requirements given the current cell fabrication process. The ID and OD measurements must pass the target lower and upper specifications for both individual and average diameter measurements. A number of engineering efforts are applied at the moment. Those includes both tightening existing CSA cell process controls and improving production tooling. In addition, a trial was performed on die cut sintered cells to demonstrate whether a post-process step can cut these fabricated cells to diameters within specification.

Cell process development focus was placed initially in meeting the cell design specifications with both standard TSC3 and HiPOD cells. However, in order to meet project schedule milestones that required test stack builds, that focus was directed towards the TSC3 cell. Better die cutting controls and visual inspection practices were established and put in place.

Part of that focus has also been mitigating contamination from plant particles which have shown up as part of CSA stack autopsies. These contamination particles can end up in or adjacent to the electrolyte layer; which can cause structural irregularities in the electrolyte layer, resulting in

thermal induced pathways leading to localized oxidation which is detrimental to the life of the cell. Studies have been initiated to isolate sources of contamination and trial process controls have been identified to mitigate this contamination.

In addition to standard CSA cell production, pilot manufacturing process design and development were planned to incorporate advancements. One of those advancements is to incorporate oxidation barrier layers at the outside surface of the anode substrate. The oxidation barrier layer oxidizes and expands during oxidation events; slowing the access of oxidant to anode significantly. The adding benefit of the oxidation barrier layer could counter-balance the sintering stress of anode-electrolyte bilayer. This could be critical in improving cell yield for thinner anode substrate (< 450 microns).

To incorporate the oxidation barrier layer to the backside of anode substrate, additional screen-printing steps on the other side of anode tape (opposite to the functional layers) were needed (Figure 2.2-2). This also brought in more challenges of handling thin anode tape.

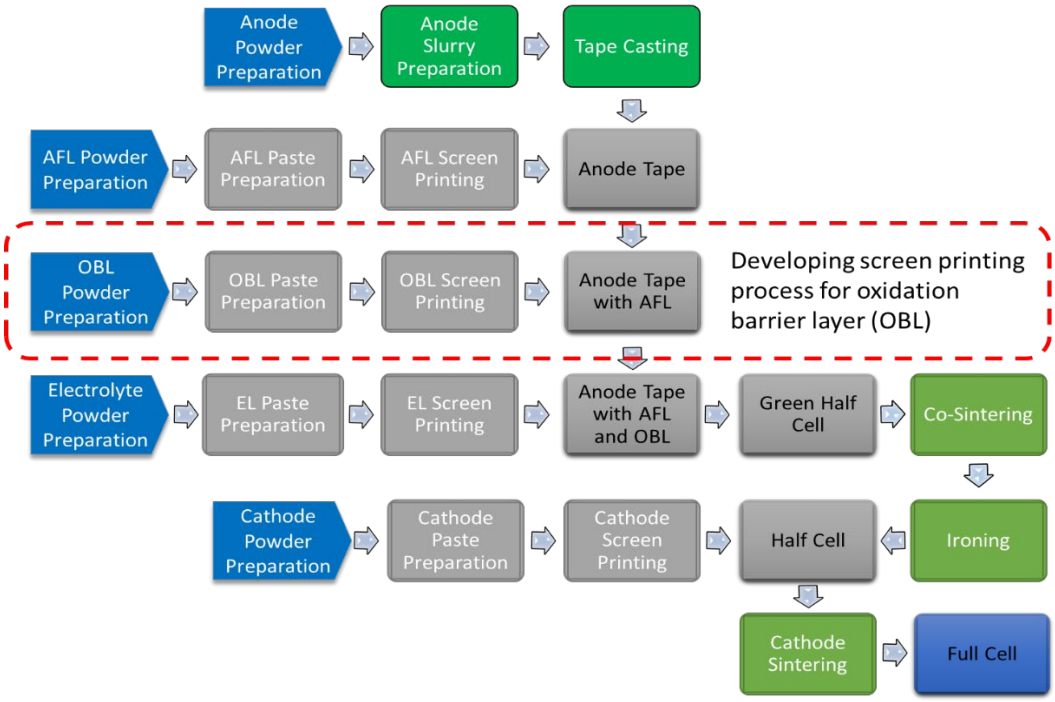

Figure 2.2-2 Cell manufacturing process development with oxidation barrier layer (OBL)

Focus was placed on meeting the cell diameter requirements with TSC cell fabrication process. The inside diameter (ID) and outside diameter (OD) measurements must pass the target lower and upper specifications for both individual and average diameter measurements. A number of key cell manufacturing process improvements were made. One of the most significant activities is to study the half-cell ID and OD sintering shrinkage to better meeting cell dimensional specs in. Due to the small sintering shrinkage difference of an anode tape along the casting direction and perpendicular to the casting direction, a CSA green half cell cut in round shape are oval after the sintering. To combat this effect, a detailed study was launched to reduce the elliptical in sintered cell with engineered oval off-set cutting.

A number of CSA cells with oxidation barrier layer (OBL) were made with modified TSC III manufacturing process as shown in Figure 2.2-3. An additional step of OBL printing was inserted

between anode functional layer printing and electrolyte layer printing. Several OBL variations, such as, thickness and configurations were proposed and tested. One of those has yielded better results with flatter cell indicating much less residual sintering stress after co-sintering. Further investigation is still needed to improve the process consistency and meeting all CSA cell specifications.

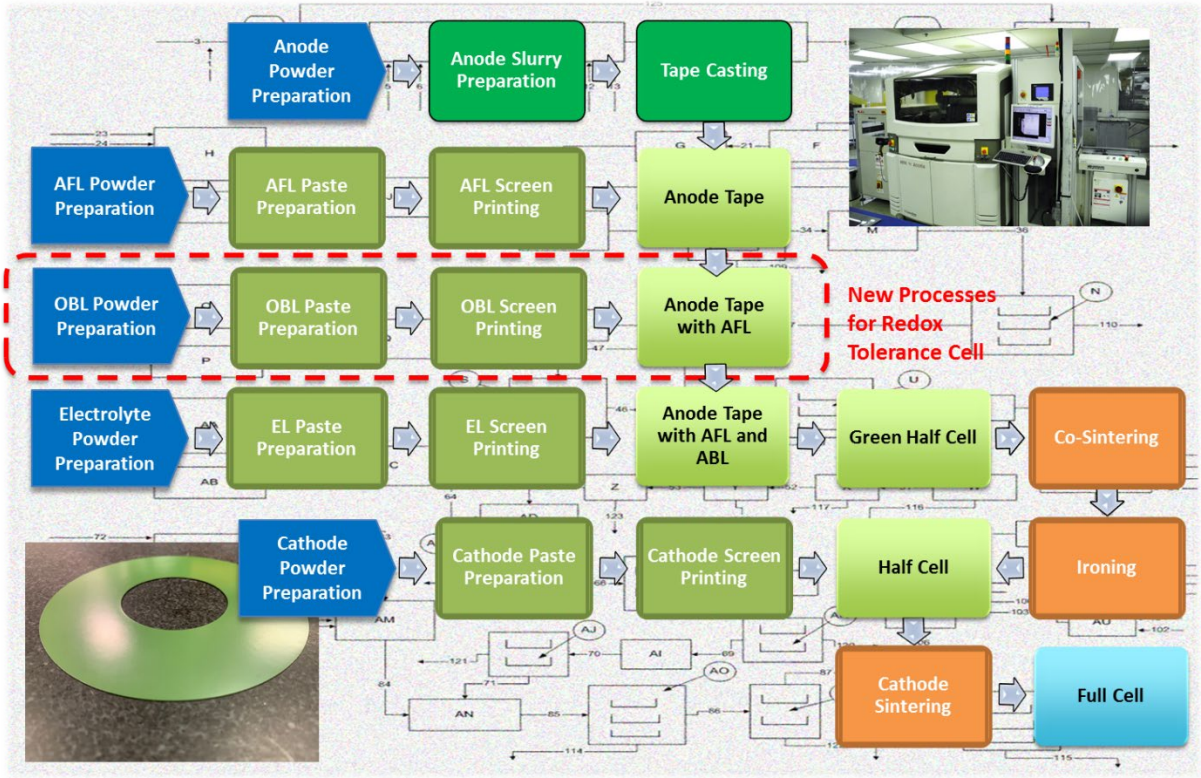

Figure 2.2-3 CSA cells were made with TSC III cell manufacturing process development with oxidation barrier layer (OBL).

3 Innovative Stack Architecture Design

This effort was focused on integrating key system-level design functionality within the stack itself, and incorporating the cells fabricated using technologies developed in Section 2. The objective of this effort is to surpass current SOFC technology in terms of cost, robustness, reliability, and endurance.

3.1 Stack Components and Design

Objective:

The objective was to evaluate and design innovative stack concepts which integrate transformational cell materials and perform functionality previously-assigned to balance of plant systems

Approach:

Development was focused in the following concept areas:

- **Thin Interconnect/Flow Field:** A single-piece thin interconnect design was developed.
- **Fuel Reformer and Exhaust Oxidizer Design:** Integration of fuel reforming and inlet process stream heat exchanging functions into the stack was developed. The integrated stack design featured catalyst-coated flow channel within the interior and exterior of the stack where direct radiative thermal heat transfer may occur.
- **Fuel and Oxidant Manifold Geometries:** The stack fuel and air manifolds were designed to interface directly with the integrated oxidizer(s) and reformer(s), while facilitating uniform flow distribution.
- **Integrated Fuel Recycle:** To reduce the balance of plant cost and complexity associated with the anode recycle system, a passive anode recycle system was designed into the integrated stack. A variety of methods were evaluated, including ejection nozzles, waste heat displacement pumps and forms of pulsed injection.
- **Insulation-free Touch-safe Stack Containment and Cathode Preheater:** Design concepts were developed to: i) provide a minimal footprint housing, ii) provide adequate heat shielding to allow for touch-safe replacement of stack while other nested stacks remain on-load, iii) allow the inlet cathode gas to have a first round of heat up, prior to heat exchange with the internal oxidizer, by utilizing the thermal radiation from the stack core, iv) facilitate assembly of repeating cell package components and fuel-oxidizing tubes, and v) utilize common sheet metal forming and welding operations.
- **Horizontal Stack:** Merits of horizontal stack design concepts with lower center of gravity amenable for large number of cells were explored.
- **Hot Stack Swap-ability:** Design concepts were analyzed which would allow for replacement of the stack (or a group of stacks) during power production,
- **Additional stack repeating and non-repeating parts:** The components including contact media, power take-off plates, compression system, instrumentation and seals were reviewed and modified as needed to accommodate the integrated innovative stack design architecture. Repeating component development was focused on high priority items to improve stack robustness and factory cost reductions.

Results & Discussion:

A main design goal was to integrate system functionality into the physical and thermal boundary of the stack. The benefits are of great significance including, but not limited to: serviceability, reduction in plant footprint and higher overall plant efficiency. Conceptually, a design layout was established (Figure 3.1-1) for initial evaluation activities. The concept integrated air-preheating, fuel recycle, water vaporizer, fuel reformer and catalytic oxidizer functionality. These integrated elements were evaluated throughout the design activities of this project; with input from energy balance analysis, heat transfer and mechanical stress calculations, manufacturability, and process modeling. This system was referred to as the Repeatable Power Unit (RPU) throughout. The RPU is approximately the size of a 20-liter soda bottle with DC power capacity of 7 kWe. The RPU includes a field replaceable core, called the Integrated Stack Core (ISC). The ISC features flexible dielectric joints and contains the repeating SOFC units, radiative fuel reformer (shown as #4 in Figure 3.1-1), and catalytic oxidizer (#5) for air pre-heating. Figure 3.1-2 illustrates this concept as a packaged unit while emphasizing the benefits targeted as an output of the RPU design.

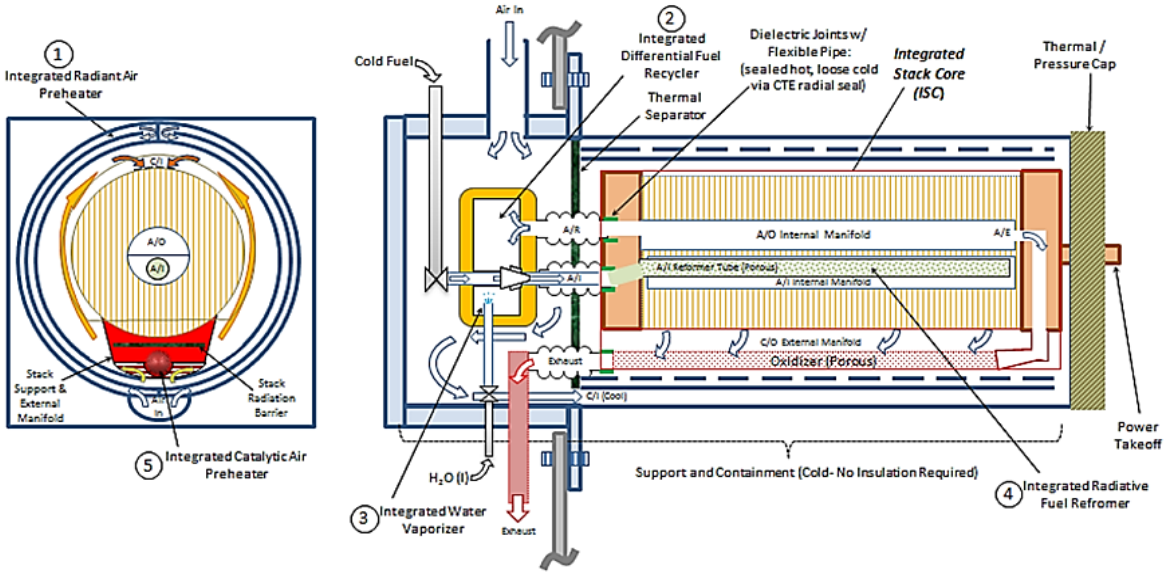

Figure 3.1-1 Early Concept of RPU Architecture

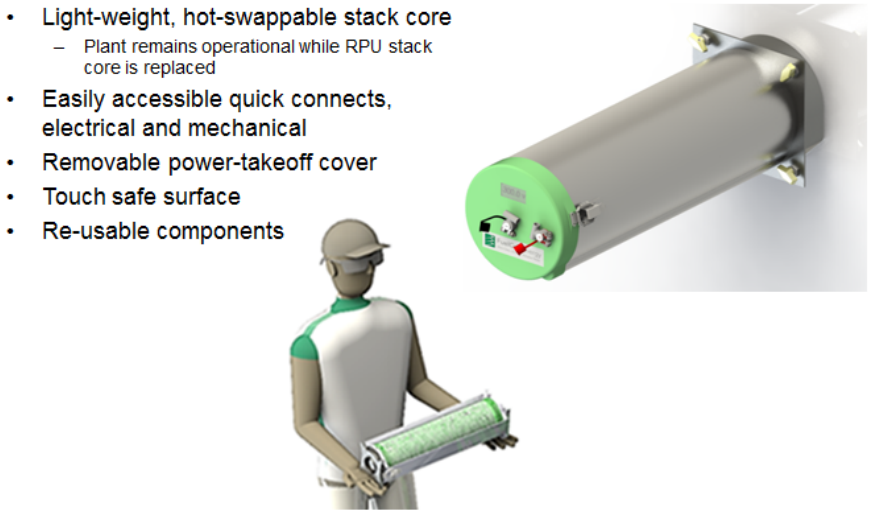

Figure 3.1-2 Anticipated Benefits of RPU

The work scope included a combination of the following: plant process simulations; computational fluid dynamic (CFD) simulations; and 3D CAD modeling. These elements are closely-coupled (from a high level) as the output of each element feeds into the other elements (Figure 3.1-3). The ISC (shown in Figure 3.1-1) was the first area of investigation in the RPU design efforts. At the ISC, the radiative fuel reformer resided within the inner space of the repeatable cell units, and the catalytic oxidizer was located in the outer space of the repeatable cell units. These were the two most closely coupled integrated systems with the SOFC stacks. They were critical to flow distribution of the reactant gases, anode fuel and cathode oxidant, and thermal management of the SOFC; while utilizing the working fluids and thermals for their own respective integrated functionality. The radiant air pre-heater shell structure (Figure 3.1-1, #1) was designed to mitigate radiative heat losses of the ISC but is significantly less integrated mechanically to the ISC than reformer and oxidizer. Hence, assembly (and fabrication) considerations were less of a concern in the design of pre-heater.

The CAD modeling articulated realistic and feasible design concepts, serving as input into process simulation and CFD modeling. It also functioned as part of the check and balance needed during the coupled development process for manufacturability. Summary of CAD modeling and process simulation activities are described later.

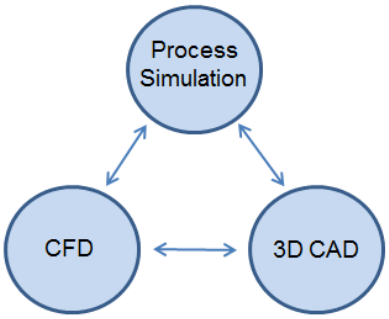

Figure 3.1-3 Close-Coupled Design Strategy

CAD Modeling

The ISC design, initially, built upon the work, results, and lessons learned from compact stack architecture (CSA) developed during a concurrent DOE funding opportunity, Innovative SOFC (DE-FE0026199). The CSA architecture primarily focused on SOFC technology that met the DOE program cost targets while demonstrating successful testing of a 5kWe stack for at least 1000 hours at Normal Operating Condition (NOC). The main approach to accomplish this was de-integrating supply and exhaust manifolds from the interconnect (IC) and, instead, adding externally mounted manifold(s) (Figure 3.1-4). This eliminated 70% of the seals required and resulted in ensuring better contact between cells under compression. An important approach to this was focusing on a repeating unit cell geometry (in this case a compact disc) that would be a more appropriate fit for high volume manufacturing and handling by both service and production workers.

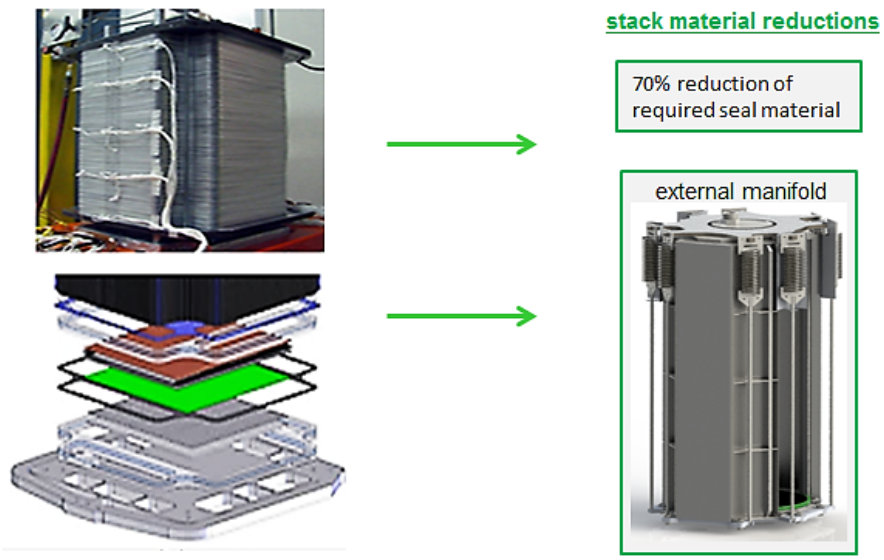

Figure 3.1-4 Building upon the CSA Architecture

FCE has previously demonstrated efficacy of use of a radiative fuel reforming unit inside a power module for a 50kW SOFC system. The reformer helped regulate the on-cell temperatures along the stack by radiative cooling the hotter sections of the stack and using that heat to achieve steam methane reforming and preheating in the anode inlet gas. The heat transfer potential is large due to the high temperatures inherent of an SOFC and is bolstered by use of an endothermic reaction as a sink for transferred heat.

The ISC features an integrated radiative fuel reformer (Figure 3.1-1, #4), residing within the inner space of the SOFC stack assembly, resulting in a significant reduction in footprint. This integration allows the radiative reformer to cool the stack uniformly as it is thermally connected to the entire circumference of the cells, i.e., maximizes the radiation shape factor for the geometry. These attributes served to lower on-cell temperature gradients. A baseline design concept for the ISC featured a catalyst coated porous (reforming) tube residing within a chamber divided to transfer both anode in and anode out gas flows (Figure 3.1-5). These chambers were sized to optimize pressure drop relative to adequate flow distribution entering and exiting the anode flow channels of the cells along the height of the ISC. The reforming tube was sized to a space velocity to allow

for indirect internal reforming and fuel utilization requirements while also meeting stack thermal requirements.

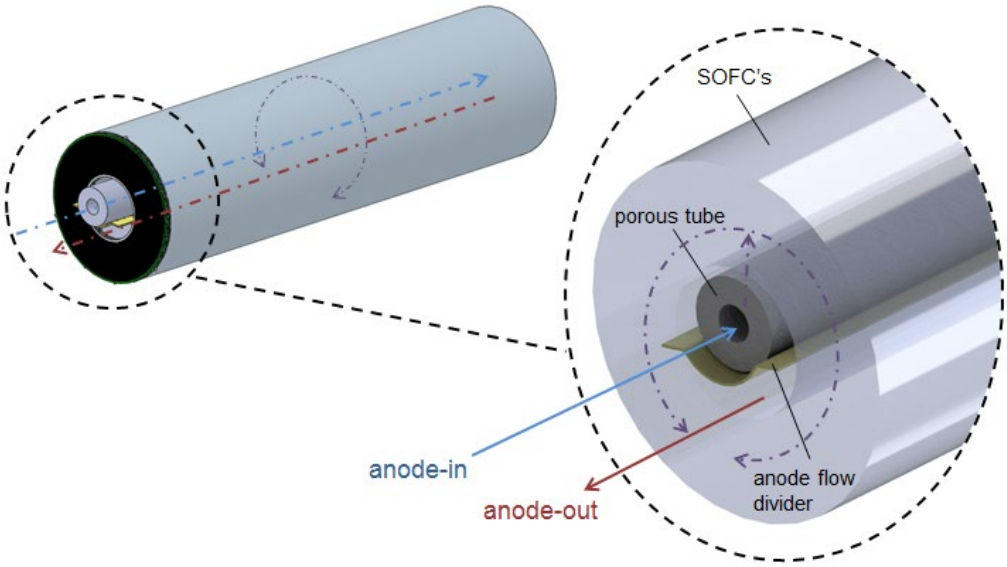

Figure 3.1-5 Integrated Radiative Fuel Reformer

The ISC also featured an integrated catalytic oxidizing air preheater (Figure 3.1-1 #5) residing on the outside surface of the SOFC stack. The space was made available by placing the radiative fuel reformer within the inner space of the ISC. The integration of an external manifold allowed for a more closely packaged oxidant preheating solution and provided the structural support needed of the ISC while resting inside the RPU while lying horizontal, a key design requirement that allows for ease of service and replacement. The use of this integrated design would be a driver for significant cost savings and reduction in system footprint.

The baseline design concept for the ISC featured catalyst coated monolith, housed within the external manifold (Figure 3.1-6), where anode exhaust gas is oxidized with cathode exhaust recovering energy converted chemically. The resultant hot oxidized exhaust gas exchanged heat with the colder cathode-in gas at finned, narrow passages along the outside surface of the manifold. The final geometry, size, and location of this oxidizing monolith and manifold fin geometry was determined through sizing calculations, process simulations and CFD. A key feature within this manifold was radiative shielding to protect the cells from exceeding maximum safe operating temperatures. Once initial process simulation and CFD modeling were completed and shown adequate, a prototype and test fixture were planned to be procured and bench tested for performance. Critical performance parameters included percentage of anode exhaust oxidized, exit temperatures of the exhaust and cathode-in gases, and temperature of the outside surface of the SOFC stack.

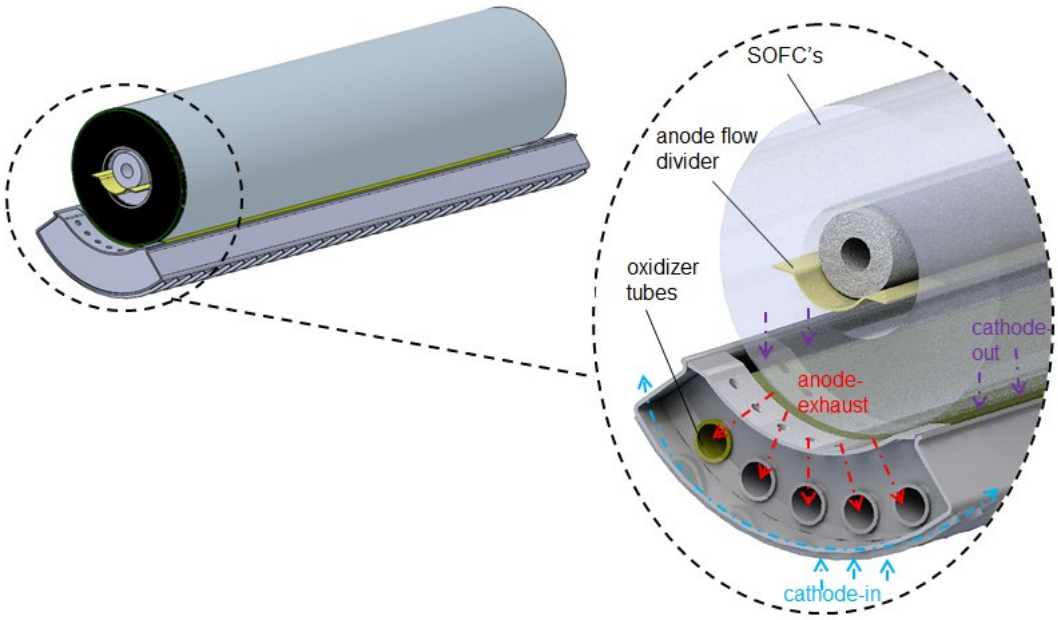

Figure 3.1-6 Integrated Catalytic Air Pre-heater

The routing and the geometry of the IC flow channels were not needed to be revised to accommodate optimal placement of the radiative fuel reformer and oxidizer manifold. While this does not impact the requirements for maintaining operable on-cell maximum temperatures and thermal gradients, it does, however, allow for lower pressure drops across the stack in order to achieve significant SOFC plant improvements including overall efficiencies, equipment life, e.g., blowers, and costs.

Plant Process Simulation

Model development work for the process simulation, including heat and material balance, was completed using the CHEMCAD 7.1.1 software package. An important enhancement that was incorporated to this software package was a VBA custom unit operation (UOP) imbedded in the simulation that integrates with standard unit operations in CHEMCAD. This custom UOP provides the ability to control SOFC stack-level parameters and flexibility in thermal management of the design through the use of mathematical heat transfer formulas written into the VBA code. For example, the heat transfer interaction between the surfaces that make up the inside diameter of the stacked SOFC and the radiative fuel reformer was simulated within this code by a simplified heat transfer formula requiring only the use of surface temperatures; the remainder of the formula constructed of a coefficient that incorporates anticipated surface areas, shape factors, and Stefan-Boltzman coefficient.

A process elements such as: Gibbs reactor for direct internal reforming (DIR); as well as mass transfer simulation PFD schematic (Figure 3.1-7) was developed to illustrate and model the core part of the RPU system. Embedded in this model is a process simulation model that represents the stack – including, heat generation, and electrical power generation phenomena characteristic of the stack. Heat and material balances interact with the VBA heat transfer formulas, approach temperatures can be set, and the model performs iterations until convergence of process stream temperatures occurs.

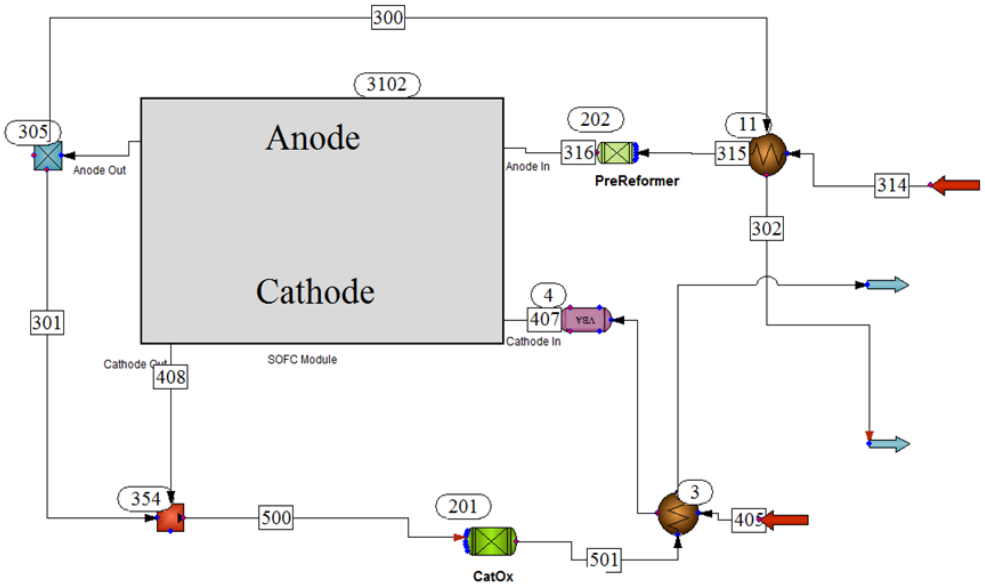

Figure 3.1-7 Example Process Model Layout of ISC

Thin Interconnect/Flow Field:

An interconnect designed for use with a single manifold has a number of advantages in both stack design simplification and integration capabilities. For this interconnect design, the cathode out gas exits from one side of the stack instead of two. This tempers the magnitude of gas streams leaking by reducing of the manifold seal surface area, reduces part count, and allows for a direct route of the cathode exhaust gas to be utilized for other integrated unit operations, i.e., catalytic oxidation to pre-heat inlet gas streams.

This interconnect design facilitates one of the more transformational features of this design; that a single functionalized SOFC Module, or Repeatable Power Unit (RPU), can be serviced while the majority of the other RPUs continue to produce and provide power. During operation, the active SOFC stack, or Integrated Stack Core (ISC), lay along the inside surface of the radiant shell structure and was ideally the only part of the RPU that would require replacing after removing the power-take-off cover for access. This required the ISC to become disengaged from the RPU base once it has cooled sufficiently, which, in turn is aided if the number of process connections is minimized- making it practical enough for the service person to slide in a replacement ISC and line up the process connections to the RPU base. With two manifolds, either additional process connections would be required, or flow channels would need to be incorporated into the ISC end plates. The single cathode exhaust manifold enables further simplification of the stack by designing the manifold as a permanent part of the RPU base, with cathode sealing being established when the ISC is installed.

The primary impact with a single manifold interconnect design is an increase in pressure drop across the stack, resulting in more power required by the cathode air blower. Increases in blower horsepower have a direct impact on overall plant efficiency. However, the CFD results of the dual manifold interconnect showed pressure drops of 4 to 5 IWC across the stack. While these values were not a major portion of the pressure drop budget of the entire system, other SOFC plant comppnents require equivalent horsepower to provide 40 IWC pressure head, increasing them

would have impact on efficiency. While stack pressure drop can be addressed by flow field height, the depth of the channels is currently limited by both the method of forming and high strains of the material. Forming strains with the current method are limited to prevent tears from occurring through the wall thickness of the parts. An alternative forming process is required to overcome these limitations, regardless of move to a single manifold.

The design goal was to integrate catalytic oxidizing and air-preheating capabilities within the physical envelope of the oxidant exhaust (cathode out) manifold. The original concept was such that this integration would occur within a single manifold design. Albeit based on further analysis, a dual manifold – enabling oxidizing exhaust and heat transfer capabilities in two manifolds instead of one was selected. This doubled the surface area available to transfer the heat, generated by combustion, outward radially towards the radiant shells of the Repeatable Power Unit (RPU) and limited the exposure of the ISC to the elevated temperatures of the oxidizer. This still enabled preheating of the supply air (cathode in) flowing within the space between the shells (Figure 3.1-8). This is balanced against the advantages of the single manifold including both increasing leak risk by doubling length of the exhaust manifold gasket and increase in ISC cost due to additional non-repeat components.

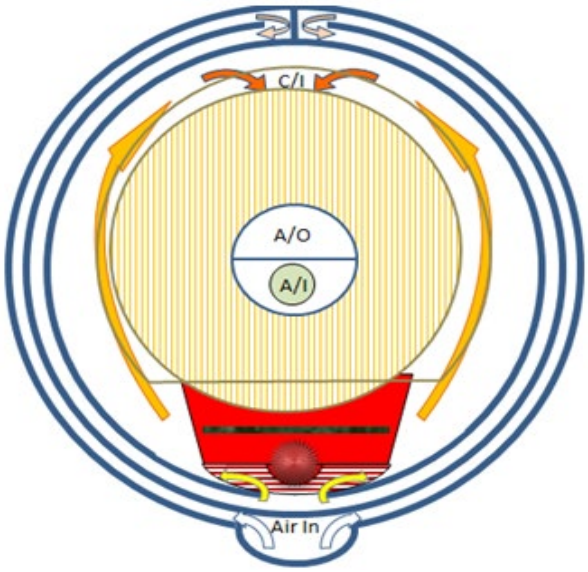

Figure 3.1-8 Single Oxidizing Manifold Design Concept

The existing IC's are fabricated using a process less favorable to high volume low cost manufacturing. Extrapolating low volume quotes (Figure 3.1-9a) from the current vendor to higher volumes (Figure 3.1-9b) show the potential to reach part cost less than one dollar per part. However, costing of larger quantities (>>10,000 parts) is required to determine accurate high-volume projections. Alternative forming processes were investigated as a replacement for the current baseline IC manufacturing process.

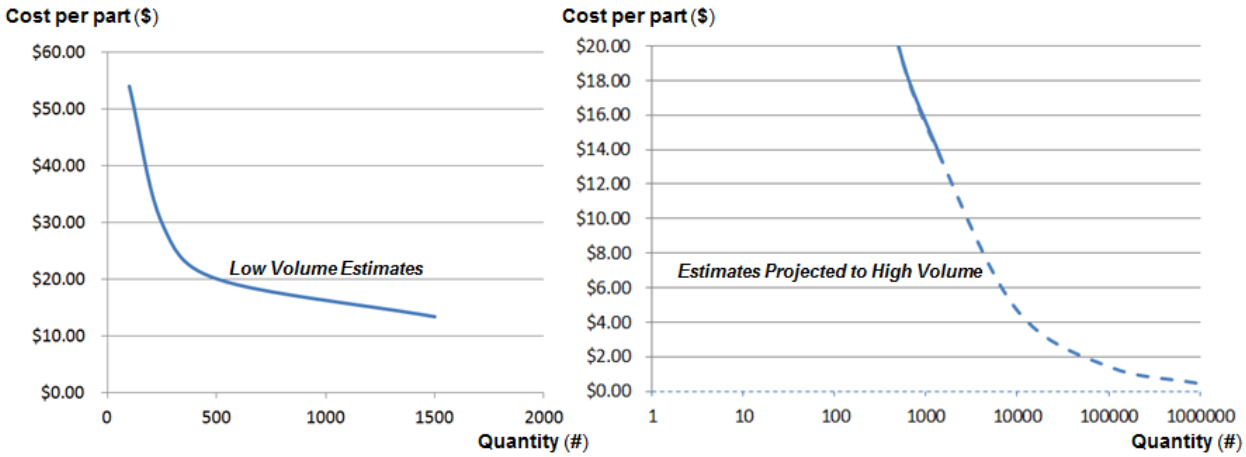

Figure 3.1-9 a) Early IC Design Concept; b) Initial Single Oxidizing Manifold Design

The current interconnect sheet metal forming process, which utilizes hydraulic motive force against the work piece and die, offers reasonable throughput and low tooling costs. However, this process has limitations to the size of the corner radii's as well as the ability to form deeper with baseline radii without localized tears. As used as a bipolar plate, deeper channels and smaller corner radii would have direct benefits to the stack and SOFC system. These forming enhancements would help distribute the heat more evenly across the cell, lowering on-cell temperature differentials; increase the proportion of contact area with the neighboring cells, increasing the heat transfer rate and reducing ohmic interconnect loss; and allow for a design control knob used to decrease pressure drop with deeper channels, lowering the power required by air supply and anode recycle blowers in the plant.

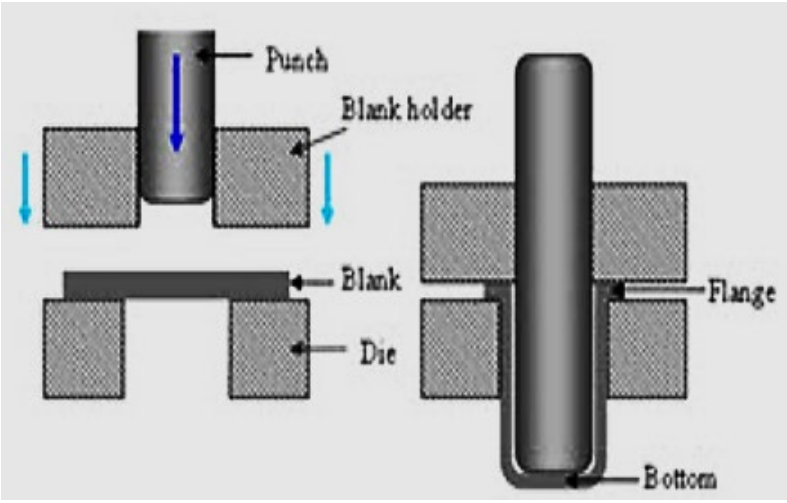

Figure 3.1-10 Traditional Forming (Deep Drawing)

A potential replacement forming process was identified that has the possibility to be both a good fit for high volume fabrication and also expand the design space needed for these aforementioned enhancements. The process is non-traditional for sheet metal forming in the sense that the work

piece, or sheet metal blank, is accelerated onto the die versus the die accelerating onto the work piece. Deep drawing is a traditional method (Figure 3.1-10) but typically requires several stages to achieve the extreme amount of deformation targeted. With the replacement process, extreme deformation speed over short distance is achieved via energy discharge which renders the metal visco-elastic resulting in enhanced formability without affecting material strength.

Fuel Reformer Design:

Background

The intent of integration of the fuel reforming and pre-heating the anode inlet stream was to locate these operations within the open space of the ID of the stack. The anode inlet stream may be designed to undergo steam methane reforming with a catalyst monolith. The endothermic SMR reaction allows the monolith to maintain a cooler temperature, enabling direct radiative heat transfer from the inside surface of the active cells, as show in Figure 3.1-11. The cells benefit from the cooling effect of this heat transfer; allowing for higher operational current densities. The location is limited in size and space allowance for the manifold is required to be economized to also allow for low pressure drop anode outlet manifolds and sufficient dielectric isolation. This led to a requirement for the monolith's metal substrate material to have extremely high surface area-to-volume ratios. Solutions were investigated such as open-cell metal foams, which would help maximize the catalyst loading per unit volume and amount of indirect internal reforming (IIR) completed.

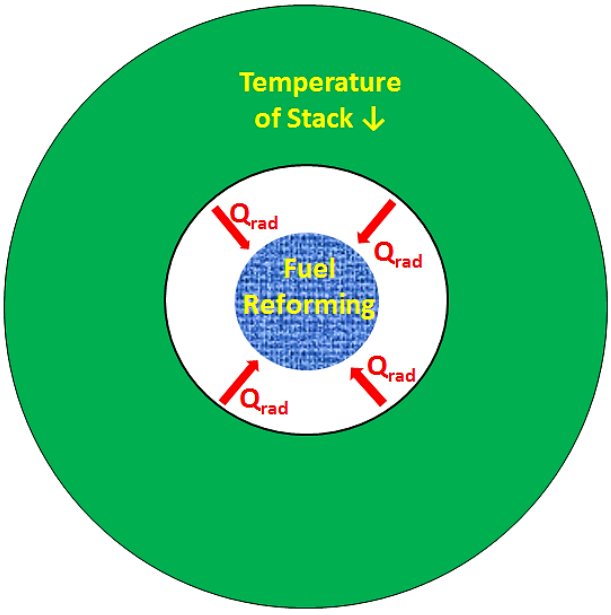

Figure 3.1-11 Utilization of Open Space for Fuel Reforming

Catalyst Coating Material and Performance Investigation

Due to the interdependence of the SMR and current density distribution, vis-à-vis heat transfer and reactant concentration, the amount of reforming achievable in this configuration is difficult to predict accurately. To provide a baseline for estimating the effects and benefits of locating the reforming monolith within ID of the stack, ex situ catalyst evaluations were required. The scope

of these activities included conducting catalyst coating trials with vendors, assessing pressure drop across the thickness of the coated metal substrate, and measuring the catalyst performance by method of gas chromatography (GC).

Three different porosities for the support were selected as high(H), middle(M), and low(L). The M-porosity fits the theoretical surface area required for the target steam reforming SR. The H- and L- porosities were utilized to determine the expanded design space suitable to work within. The coating of porous media reduced the effective hydraulic diameter of the substrate; therefore, pressure drop measurements were included to evaluate potential system impacts. The support with the H-porosity could accept a greater amount of coating compared to M-/L-porosities for constant surface area specific (mg/m^2) loading targets. Alternatively, the loading target was adjusted to the specific porosity such that the total weight of the coating was the same.

The metal foam substrate materials were carefully selected based on availability for high volume production in the market. One of the materials is relatively less expensive compared to the others. However, this material requires an additional step before applying the SMR catalyst coating. Thus, this needed further testing to assess its compatibility to determine value.

A detailed summary of the investigation goals is as follows:

- Measure pressure drop of supports with different porosity with and without catalyst to confirm its flow performance meets target.
- Screen catalyst supports with different porosity (H, M, and L) with a constant surface area specific loading (mg/m^2) target to determine optimal catalyst loading for the best SMR activity.
- Screen catalyst supports with different porosity (H, M, and L) with constant catalyst weight to study the optimal catalyst thickness, effect on pressure drop and SMR activity.
- Determine the best support material for catalyst compatibility/SMR reforming activity of these materials with catalyst vendor.

Sample Preparation and Experimental Procedure

Disc-shaped specimens were cut from sheet materials received to roughly one-inch diameter. The full-sized catalyst coated substrate, for the physical space allowed and estimated flowrates, resulted in a target gas hourly space velocity (GHSV) of 28,310 h^{-1}. This GHSV was used to calculate the catalyst coating amount for the different specimens. The support size is targeted to be 9 to 10 mm in thickness. Sample sizes were chosen to account for unforeseen challenges with coating and test setup issues. These were then wash-coated. Pressure drop measurements were conducted on coated and uncoated specimens. Catalyst activity performance tests were tested with an existing catalytic reactor (Figure 3.1-12). The incoming gas mixture were heated to a desired temperature of ~700°C before entering the reactor. The exhaust gas mixture contained water vapor and were kept above 100°C to avoid condensation prior to being sequestered for GC sample tests.

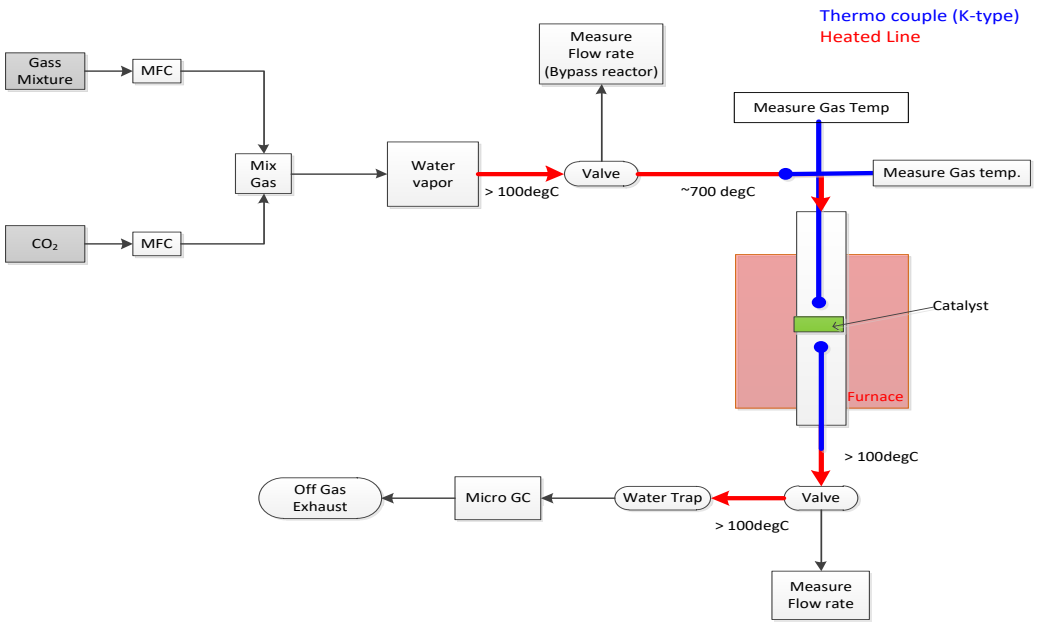

Figure 3.1-12 SMR Catalyst Reactor Fixture Design

Pressure drop recording were tabulated and compared amongst different porosities and wash-coat loadings. The adhesion of the catalyst was evaluated using SEM. The reaction conditions of the steam reforming were as follows: H_2: 12.1%, CH_4: 12.8%, CO: 4.9%, CO_2: 24.6%, H_2O: 44.2%, N_2: 1.4%. The total flow rate is 28.7 Std. L/h and the GHSV is 28, 310 h-1. Effluent gases of H_2, CH_4, CO, CO_2, and N_2 were continuously analyzed by micro GC (Agilent Technologies 490 Micro GC, equipped with 10 m Molsieve 5A column, 10 m PoraPLOT U column, and thermal conductivity detectors). The temperature of the catalyst bed was monitored by a K-type thermocouple (Omega), placed at the inlet of the catalyst bed, and controlled using Eurotherm 2408 series temperature controller. These results were also used directly to update CFD and process simulation models to determine impact on percentage DIR and temperature differentials within the stack.

The fuel reforming performance was dependent on the volume of coated material that can exist within the volume space of the inside diameter region of the ISC. Critical aspects such as pressure drop, temperature of the reformed anode gas under varying thermal conditions, and percentage of the anode gas reformed were part of the data collected from testing. The potential impact of these catalyst characteristics included stack thermal distribution, the need for any additional upstream fuel processing, and SOFC system efficiencies, vis-à-vis power consumed by the anode recycle blower.

Uncoated metal substrates of various porosities, Figure 3.1-13, were coated with a catalyst which has shown the most promise from prior bench testing. The prior bench testing was conducted for a prior SOFC system as a material incorporated into a radiative fuel reformer that was external to the stack, but within the containment module. For that application, physical space was not a limitation and for this reason adequate coating surface was easily achieved with non-porous substrate. The application met SOFC system requirements but at significantly less power density

than targeted. Catalyst loading target is measured in milligrams of coating per surface area of substrate. For fuel reformer testing of coated substrates, the specimens was evaluated using two different loading target methods: 1) hold the loading target constant over the range of substrate porosities; 2) hold the total amount of catalyst coated constant over the range of substrate porosities. The first method results in the amount (mass) of the catalyst varying over the range of porosities.

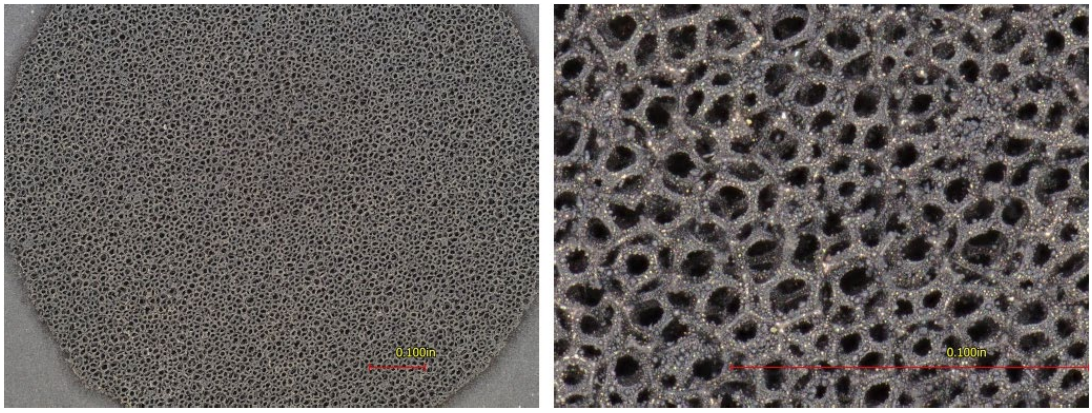

Figure 3.1-13 12x and 80x Images of Uncoated Substrates

Initial loading targets (mg/m^2) proved to be too heavy. The cells of the porous substrate appeared to be mostly filled at lower magnification (Figure 3.1-14) and very few cells appeared to be open even at much higher magnification. To determine whether this visual attribute was consistent through the volume of the substrate, specimens were sectioned and examined with use of the same optical microscope. Results showed that this phenomenon was prevalent throughout the volume space of the substrate specimens (Figure 3.1-15). A new loading target, 35% that of the initial target was chosen to ensure sufficient coating of most of the substrate exposed surfaces. A fresh set of specimens was coated at this new target and was determined by visual examination (Figure 3.1-16) to be sufficient to move forward with reforming performance testing for which these specimens have been prepared ready for test.

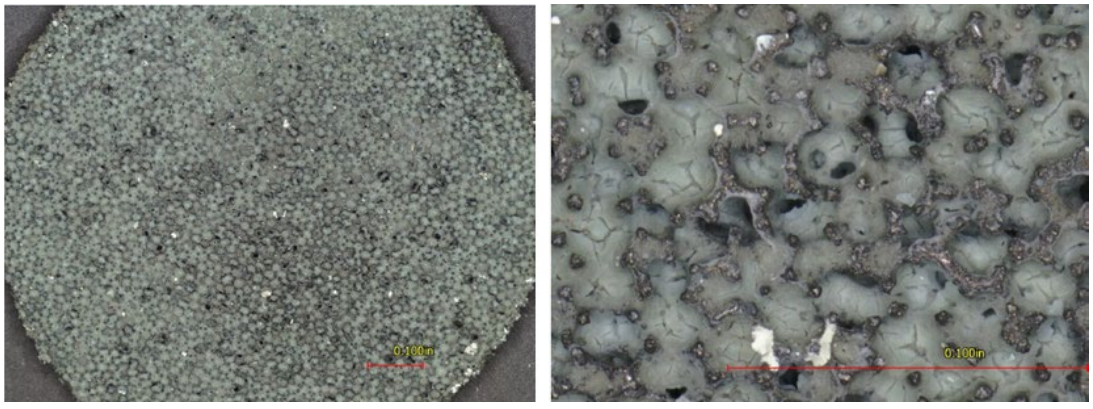

Figure 3.1-14 12x and 80x Images of Substrates Coated at Initial Loading Target

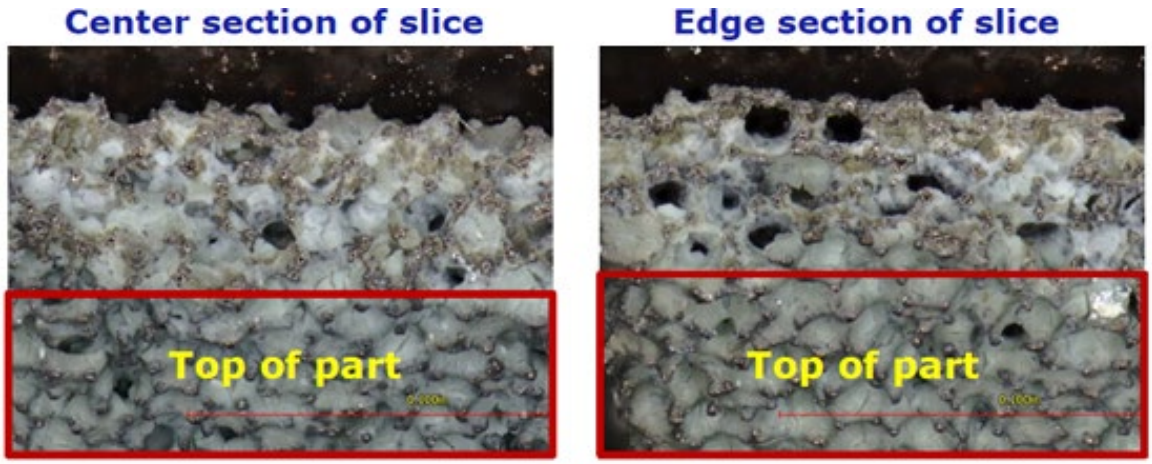

Figure 3.1-15 80x Images of Substrate Cross-Sections at Initial Loading

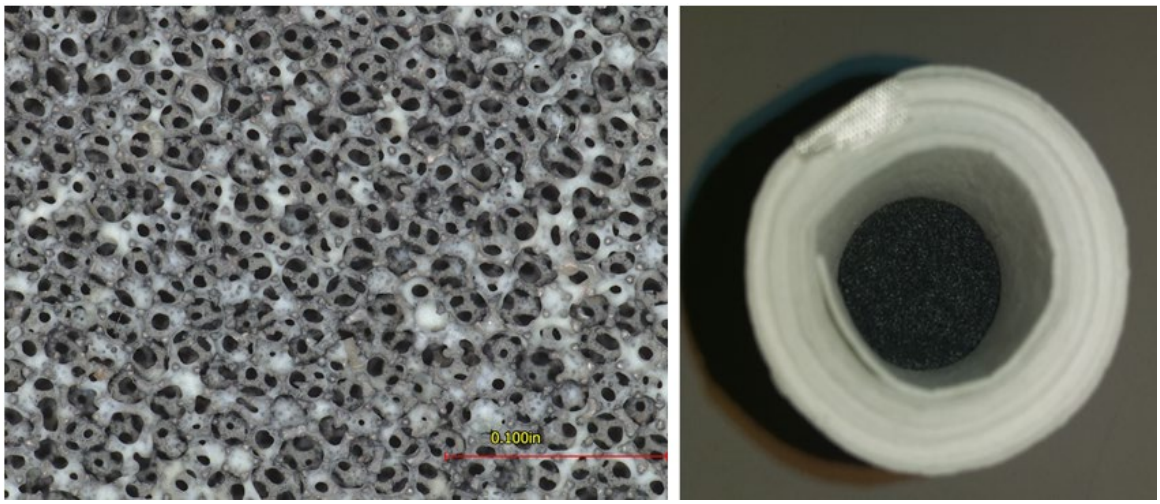

Figure 3.1-16 40x Image with Revised Loading - Sample Wrapped in Test Fixture Insulation

The test station utilized for testing the reforming catalyst is shown below in Figure 3.1-17.

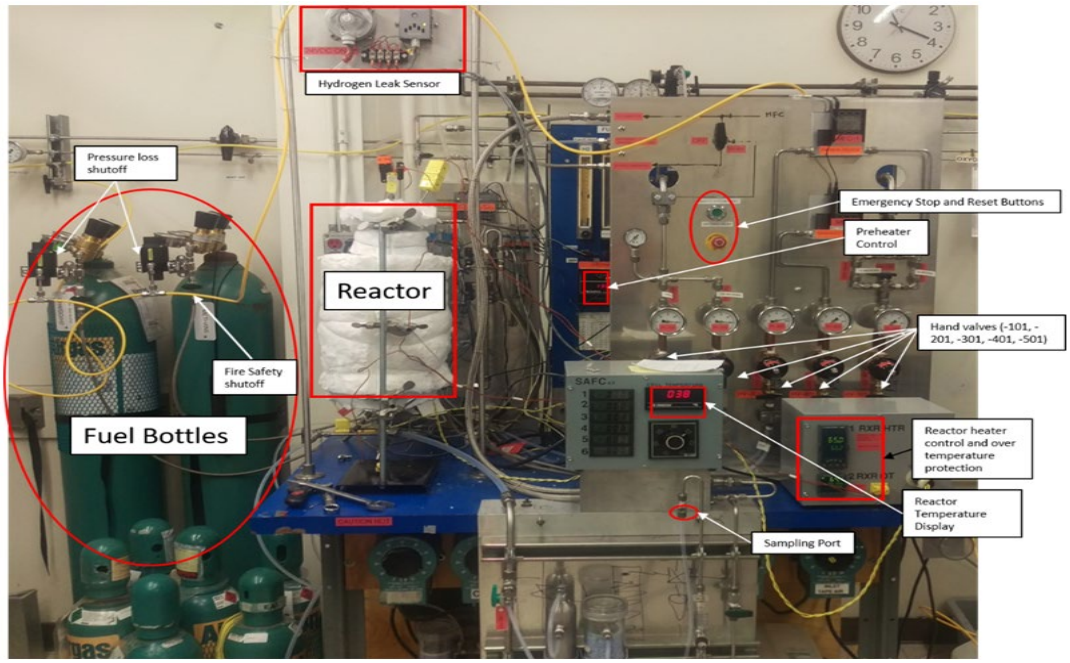

Figure 3.1-17 Coated Substrate Catalyst Reforming Performance Test Fixture

The coated substrates required several hours of conditioning in order to sufficiently reduce the coated catalyst. In order to make efficient use of test operator hours, this reduction step was initiated in the afternoon and allowed to continue overnight (Figure 3.1-18). A second reactor (Figure 3.1-19) was included in the test station to allow quicker change out after GC sampling. With the next sample previously loaded, the second reactor could then be installed to begin another catalyst reduction cycle. This enabled testing of one sample per day.

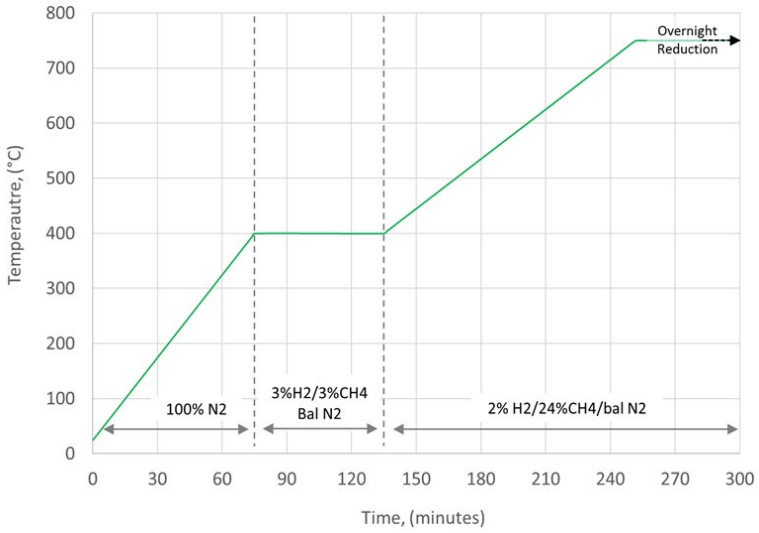

Figure 3.1-18 Catalyst Reduction Conditioning Cycle

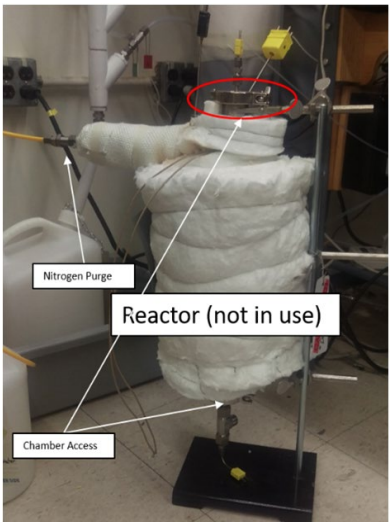

Figure 3.1-19 Additional Reactor

Development and refinement of the catalyst reformer test fixture required more time to configure properly and incorporate details of the design to accommodate the coated substrates. There were inherent characteristics of the individual pieces and test specimens that made it more challenging to mount and install the sample without resulting in gas slip and poor distribution of heat throughout specimen. First, each individual substrate was in the form of a cut one-inch disc, one to two millimeters thick. The resulting piece left behind a jagged porous structure around the outside diameter. This made it challenging to seal gases, and prevent from slipping around the perimeter without contacting catalyst, especially with lower porosity (higher resistance) substrates. To model reactor design wall thickness, test samples were made up of a stack of four to six substrates which compounded the risk due to alignment tolerances. The substrates were prepared this way due to material availability, material procurement time, and limiting the cost of samples during initial material selection trials. Second, the stacked substrates are aligned axially with the clamshell heater during testing. This arrangement was necessary due to limited space inside the clamshell heater for the test sample. As a result, the heat radiating from the clamshell needed to penetrate the middle of the substrates from the outside diameter. The parts were highly thermally conductive so this would not be an issue with a cleaner cut continuous material at the outside diameter. However, good contact between the outside diameter and sample holder vessel was needed for proper heat transfer via conduction. A final round of reactor, plumbing, and instrumentation modifications were completed due to challenges described above in order to enhance control of thermal distribution and prevent slip (Figure 3.1-20).

Figure 3.1-20 Configuration of Test Fixture after Modifications

Two catalyst loading target methods were assessed to help determine the level of loading and porosity of full-scale components to be tested. In one group the loading target, in catalyst mass per substrate surface area was held constant while the total mass of catalyst was held constant in the other group.

The full-scale prototypes would have enabled assessment of stack level capabilities prior to validation testing within a functional fuel cell stack. The space-time-velocity (STV) was varied as well in order to understand how significant catalyst loading variations effect performance relative to the isothermal equilibrium curve, and how modifications to the volume of the integrated reactor design have an effect on the percentage direct-internal-reforming (% DIR) required by the stack. Initial results, % DIR plotted vs. inlet (and outlet) temperature of gas, confirm the importance of inlet temperature and STV on stack operating conditions (Figure 3.1-21).

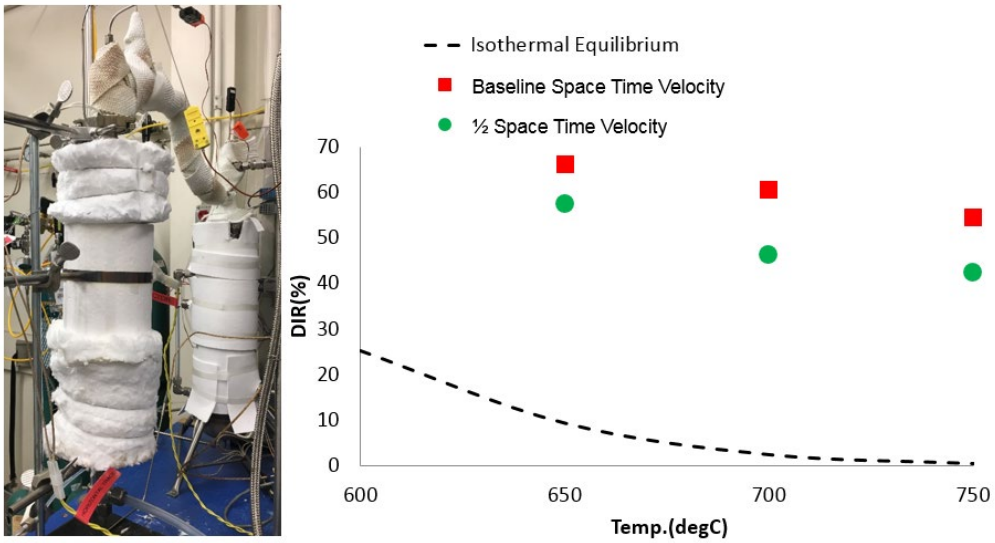

Figure 3.1-21 Initial Reforming Results, Final Fixture Upgrades

The catalytic activities of various configurations of coated metal substrates were investigated under two catalyst loading groups. In one group, the porosity of the metal substrate was varied while the coating target density, mass per surface area, was held constant. By holding a constant coating target density, the thickness of the coating on the surface area should be constant within the pores of this group. Here, the coating weight varied. In the second group, the porosity of the metal substrate was varied while total coating weight was held constant. Here, the coating target density varied (i.e – coating thickness). There were five coating configurations amongst the two groups where results of a baseline configuration, B, were included in both groups. Including configuration B in both groups helps illustrate whether the coating total weight or thickness played a stronger role in catalytic activity with varied substrate porosity.

Table 3.1-1 summarizes the coating configurations of the first group – constant coating density. Each configuration is shown with level of porosity, coating density, and coating weight. In this group, the coating density remained constant resulting in varying levels of coating weight. Three specimens were prepared for each configuration resulting in specimen labeling as follows: A1, A2, A3; B1, B2, B3; etc. All were prepared with the same wash coat mixture, i.e., their catalytic activities should be similar to each other. Every specimen was tested with the same gas composition flowing through it at the same three inlet temperatures. Three STV's were tested at each of these temperatures while the gas outlet temperature was measured. Each outlet temperature was held stable for 30 minutes prior to taking a gas chromatography (GC) sample. The steam reforming performance was calculated from (GC) samples.

Table 3.1-1 Constant Coating Density (i.e. – thickness)

Coating Configuration	Porosity	Coating Density (mg/m2)	Coating Weight (mg)
A	Lowest	Medium	Heavy
B	Low	Medium	Medium
C	High	Medium	Light

Figure 3.1-22 shows steam reforming performance as a function of temperature for the constant coating density group – i.e. varying coating weight. Testing of two of the specimens from each coating configuration was completed except for configuration C. Configurations A and B showed consistent results and C2 appeared to be within these groupings. Coating configuration A, with the heaviest (highest amount) coating, showed slightly better reforming performance compared to the other configurations, especially at higher temperatures, where the mass transfer/gas diffusion were the rate-limiting steps for the catalytic reaction, and lower STV's. Even at these high space velocities, 15% to 30% reforming can be achieved at medium inlet temperatures which may be enough prior to entering the anode side of the active fuel cells. However, a heavier coating on a lower porosity substrate may have a non-preferable pressure drop.

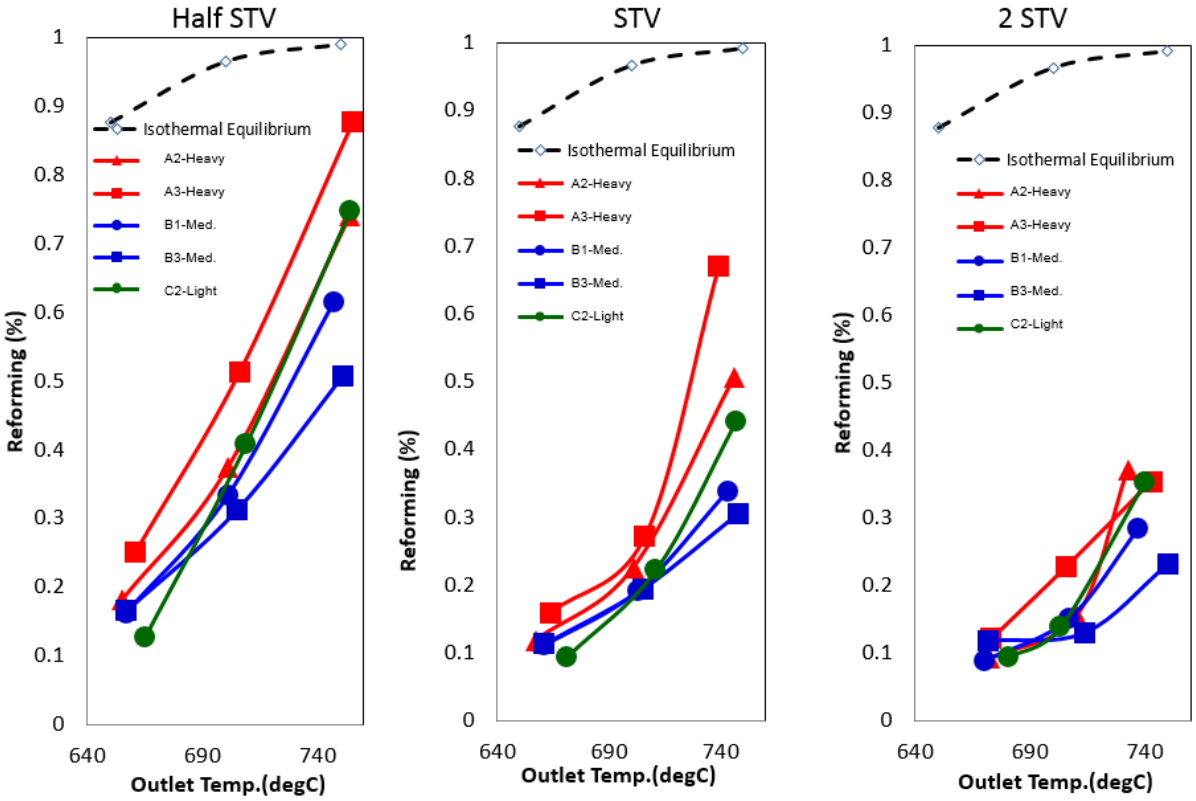

Figure 3.1-22 Steam Reforming Results – Constant Coating Density

Table 3.1-2 summarizes the coating configurations of the second group – constant coating weight. Each configuration is shown with level of porosity, coating density, and coating weight. In this group, the coating weight remains constant resulting in varying levels of coating density (i.e.-

thickness). Three specimens were prepared for each configuration resulting in specimen labeling as follows: E1, E2, E3; B1, B2, B3; etc. All were prepared with the same wash coat mixture, i.e., their catalytic activities were similar to each other. Specimens was tested with the same gas composition flowing through it at the same three inlet temperatures. Three STV's were tested at each of these temperatures while the gas outlet temperature was measured. Each outlet temperature was held stable for 30 minutes prior to taking a gas chromatography (GC) sample. The steam reforming performance was calculated from (GC) samples.

Table 3.1-2 Constant Coating Weight

Coating Configuration	Porosity	Coating Density (mg)	Coating weight (mg)
E	Lowest	Thin	Medium
B	Low	Medium	Medium
D	Highest	Thick	Medium

Figure 3.1-23 shows steam reforming performance as a function of temperature for the constant coating weight group – i.e. varying coating thickness. Testing of two of the specimens from each coating configuration was completed. Each configuration showed consistent results except for coating configuration E. E2 may have been an outlier or have been a sign of the challenges of coating such a low porosity substrate consistently as E1 had much lower results. Even though E2 showed very good results, the fact that E1 had much lower than both E2 and D, raised a concern for process capability in production.

Coating configuration D, with the thickest coating, showed consistent better reforming performance compared to the other configurations, especially at higher temperatures, where the mass transfer/gas diffusion were the rate-limiting steps for the catalytic reaction. This phenomenon was more prominent at ½STV (i.e. lower velocity) compared to that at 2STV (i.e. higher velocity). At ½STV, the gas diffusion should not be problem, since gas has slower residence time to pass through the catalyst compared to the faster flow rates (STV & 2STV). Even at these high space velocities, 15% to 30% reforming were achieved at medium inlet temperatures which may be enough prior to entering the anode side of the active fuel cells. These results were very encouraging for the higher porosity substrate, D. Inherently, this was the lowest pressure drop associated with it. Results from the constant coating density tests indicated there was the potential for even better reforming performance – barring an acceptable increase in pressure drop.

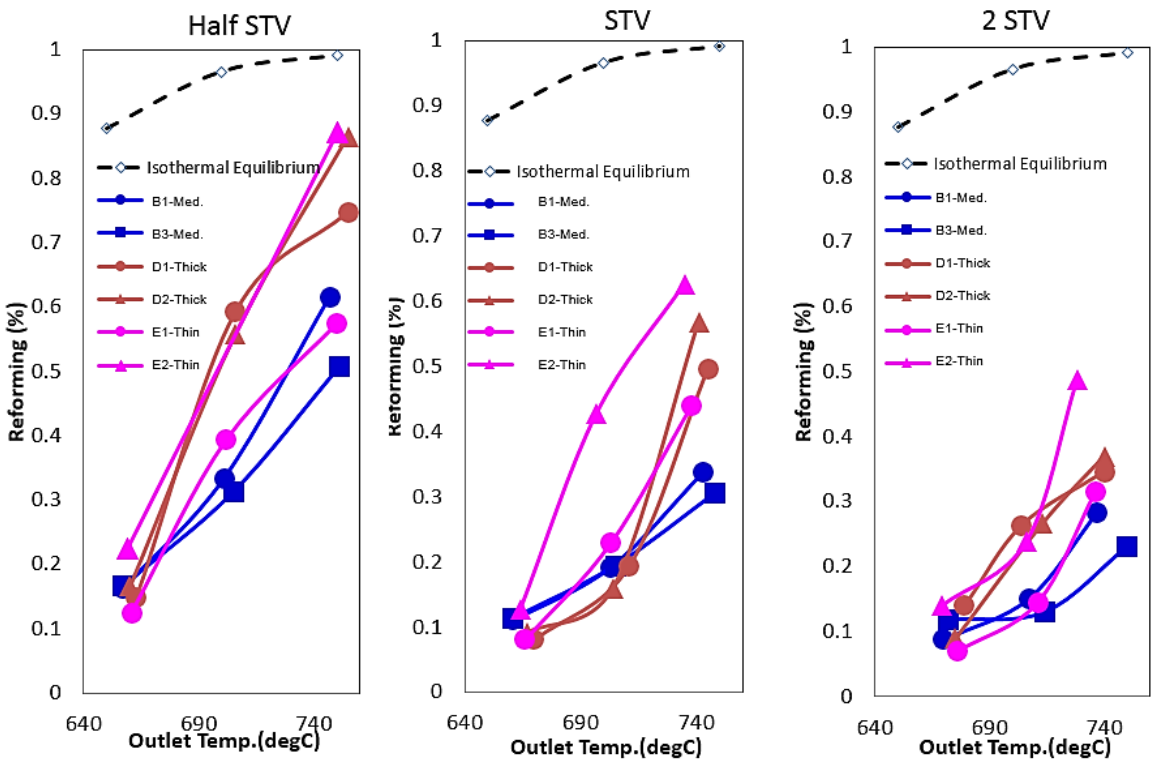

Figure 3.1-23 Steam Reforming Results – Constant Coating Weight.

The pressure drop performances constant coating density group were evaluated. Figure 3.1-24 shows pressure drop of A1, A2, B3, C1 and C2 as a function of flow rate. A1 and A2 showed very similar results, indicating excellent reproducibility of the test set-up and substrate parts. Also C1 and C2 showed similar data. All samples showed less than 0.1 IWC pressure drop up to 5 L/min. Coating configuration C was able to achieve up to 15 L/min. This was very encouraging for consideration of a range of porosities for use in the integrated fuel reformer unit for design, fabrication, and testing. This was an important implication to system performance and recycle blower sizing. A1 and A2 showed the highest pressured drop compared to B3 and C1 and C2, where B2 is higher than C samples. These results were reasonable, supporting the fact that low porosity results in higher pressure drop than higher porosity ones. There was no issue such as plugging with these samples. In short, specimens within each coating configuration showed consistent results within the configuration and the order of highest to lowest pressure drop for each coating configuration correlated with the porosity of the porous metal substrate. This was also encouraging in that application of the coating did not impact the porosity of metal substrate resulting in reliable pressure drop data for design purposes.

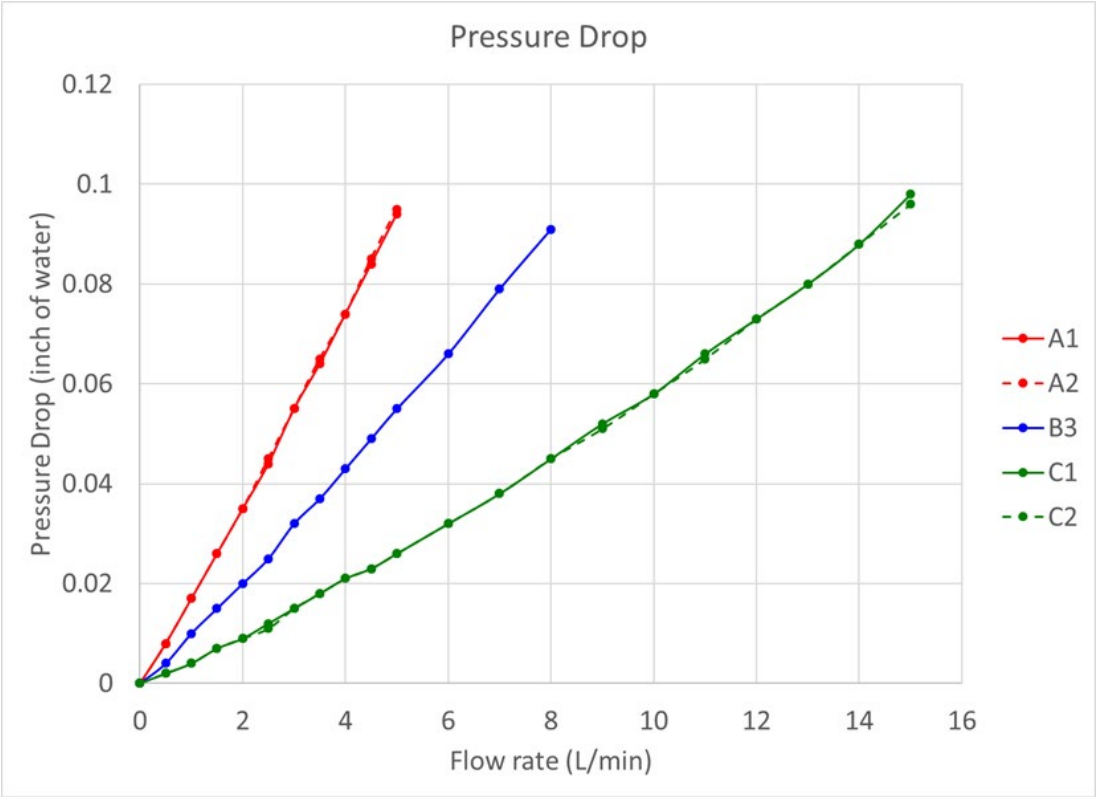

Figure 3.1-24 Pressure Drop Results – Constant Coating Density Group

The pressure drop performances constant coating weight group were evaluated next. Figure 3.1-25 shows pressure drop of B3, D2, D3, E2 and E3 as a function of flow rate. Much like the constant coating density group, each coating configuration demonstrated excellent reproducibility of the test set-up and substrate parts. All samples showed less than 0.1 IWC pressure drop up to 5 L/min. Coating configuration D was able to achieve up to at least 20 L/min. Much like the constant coating density group, this was very encouraging for consideration of a range of porosities for use in the integrated fuel reformer unit for design, fabrication, and testing and was an important implication to system performance and recycle blower sizing. E2 and E3 showed the highest pressured drop compared to B3 and D2 and D3, where B3 is higher than D specimens. These results were reasonable, supporting the fact that low porosity would result in higher pressure drop than higher porosity ones. There was no issue such as plugging with these samples. In short, specimens within each coating configuration showed consistent results within the configuration and the order of highest to lowest pressure drop for each coating configuration correlated with the porosity of the porous metal substrate. This was also encouraging in that application of the coating does not impact the porosity of metal substrate resulting in reliable pressure drop data for design purposes.

In conclusion, when the coating thickness was constant with different porosity, the reforming performance was not affected. But, when the coating thickness was varied with different porosity, the highest porosity with the thickest coating showed the best catalytic performance, probably due to the tortuosity of the porous metal substrate. As a result, coating configuration D was the lead candidate as it had further upturn with coating thickness if reforming performance needed to

be improved with the least increase in pressure drop. Next, these results were incorporated into a full scale fuel reformer for prototype testing.

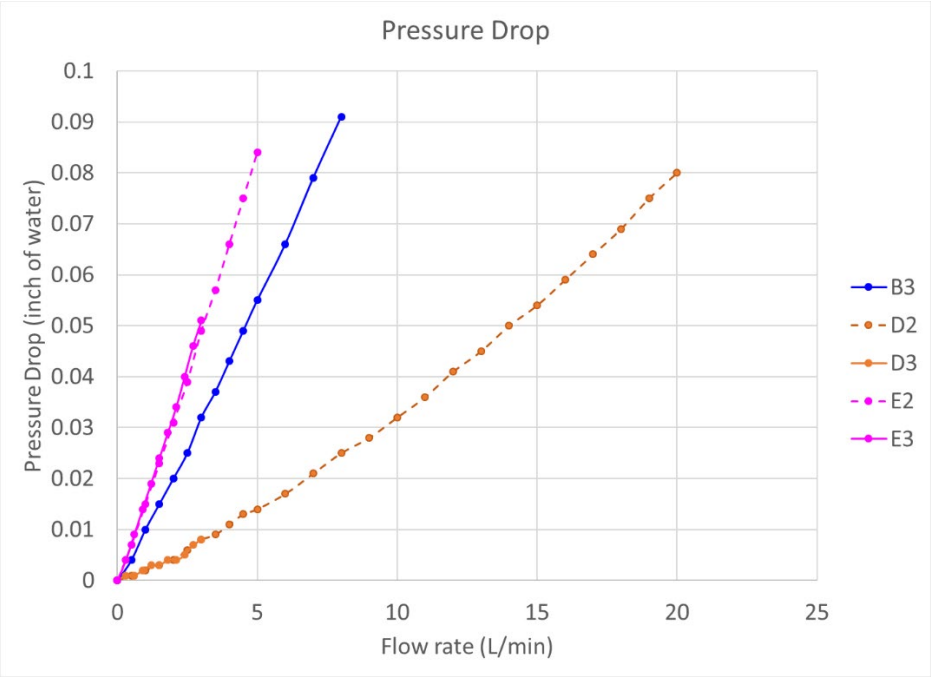

Figure 3.1-25 Pressure Drop Results – Constant Coating Weight

An additional study was performed to evaluate different base substrate metals. Here, a second metal with the same porosity as coating configuration C was procured with the same level of coating (coating density and weight). This additional configuration, F, was tested for catalytic reforming activity in the same manner as all of the other coating configuration specimens. Results (Figure 3.1-26) show the catalytic activities of the two different base metals closely matching each other.

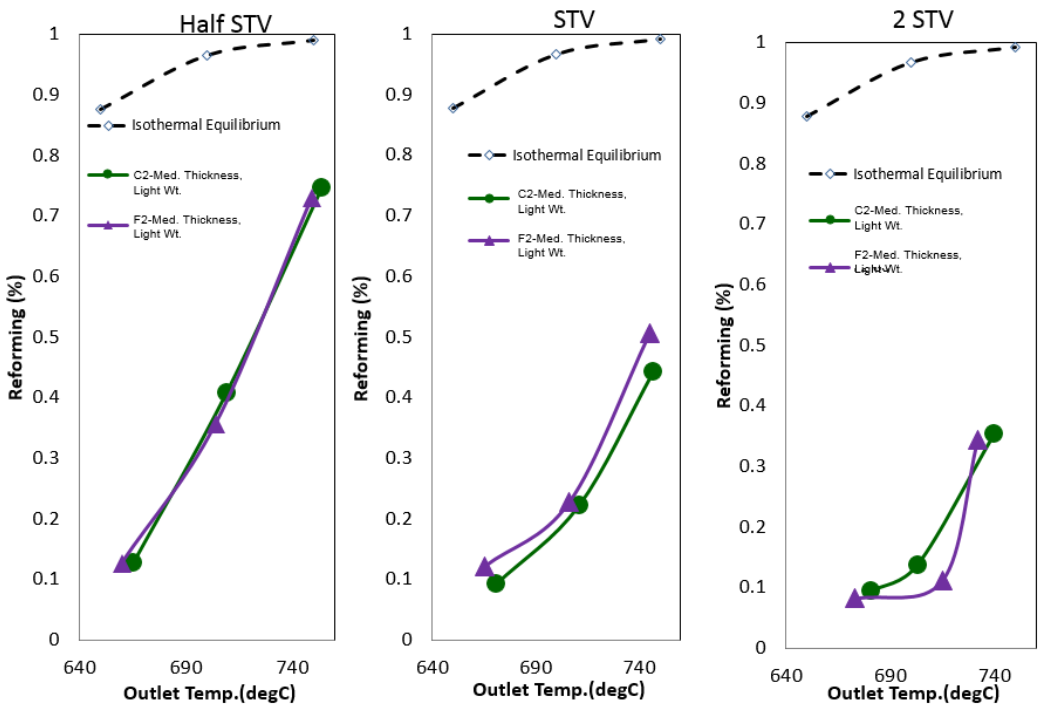

Figure 3.1-26 Steam Reforming Results – Different Substrate Metals

Manifold Seal:

Prototypes were built to test key combustion performance metrics including proportion of combustibles in the exhaust stream, how much heat duty can be harnessed by the cathode inlet stream, and temperatures proximal to the stack. To supply fuel to the combustion reaction, anode exhaust gas from the stack was plumbed to the manifold by passing first through the top end plate at the free end of the stack (Figure 3.1-27). A sealing gasket resides between the manifold and both the end plate(s) and stack, which is lightly compliant at room temperature but becomes sintered hard at operating temperatures. It is critical that sealing is adequate at room temperature as the amount of contact at the seal interface was permanent once fired and cross leaking of gas streams needs to be prevented. The cathode-in air was at a higher pressure than anode and cathode exhausts (Figure 3.1-27). A small amount of leakage of this air into the cathode exhaust is not of great risk; however, leaking into the anode exhaust stream at this seal interface would result in premature combustion that could damage the cells, the seals, or other components requiring replacement of the stack. Premature mixing of the anode and cathode exhausts could also have this same effect but the impact was lessened due to absolute pressures of the exhaust streams being similar.

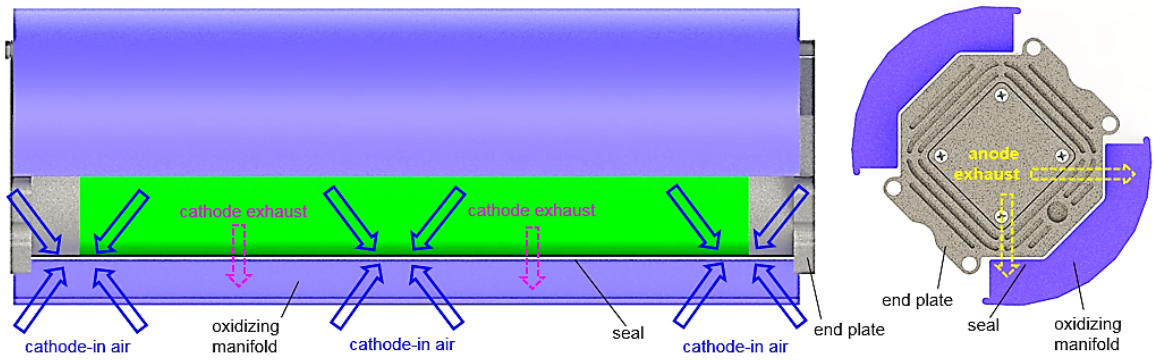

Figure 3.1-27 Gas Streams in Relation to Manifold Seal

The current method for the compact stack architecture (CSA) is to utilize spring clips around the perimeter of the end plates (Figure 3.1-28). There is room for improvement in order to ensure sufficient and evenly distributed pressure along the length of the stack and end plates. With the spring clips, a possible approach would be to add spring clips in the region along the middle of the stack to distribute the force along the seal. However, this would require adding intermediary plates with no fuel cell functionality. Another approach is to wrap a couple of sheet metal straps around the circumference of the manifolds. The force required to clamp the straps against the manifolds, thereby compressing the seals, would be provided by an insert that engages the ends of the straps (Figure 3.1-28). This approach results in even distribution of load along the length of the stack keeping pressure along the gasket at the manifold to end plate and manifold to stack interface seals more consistent. The control of that compression force can then be achieved by easily fabricated components, varying the wall thickness and effective spring length to designed target design. In order to assess the fabrication method manufacturability, a mock setup including rapid prototype components, compression system hardware, and a variety of thickness of sheet metal, was procured. A mock stack was represented by a stainless tube (Figure 3.1-29). A CAD model rendering is shown for comparison (Figure 3.1-30). Once the fabrication is assessed and a more accurate design is identified, parts were procured for a hot leak test to demonstrate sufficient seal at operational temperatures.

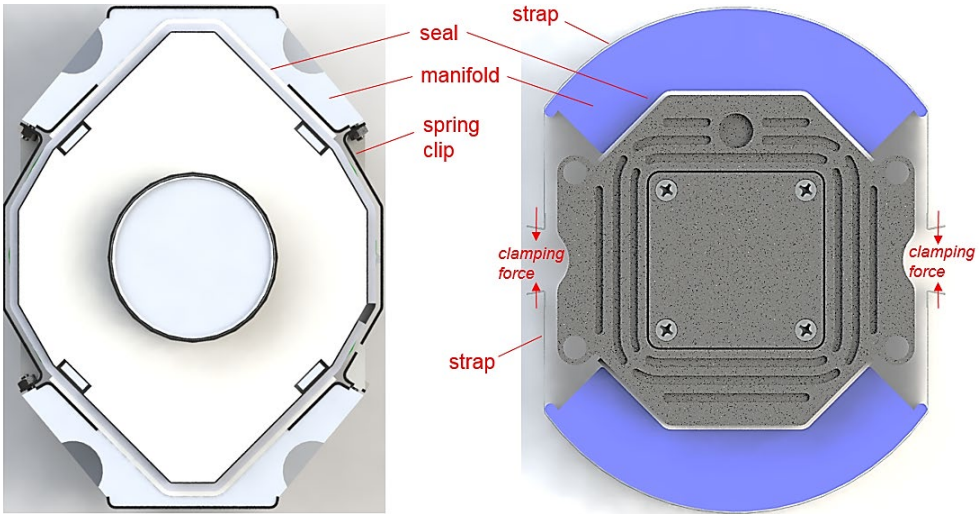

Figure 3.1-28 Manifold Seal Compression Designs

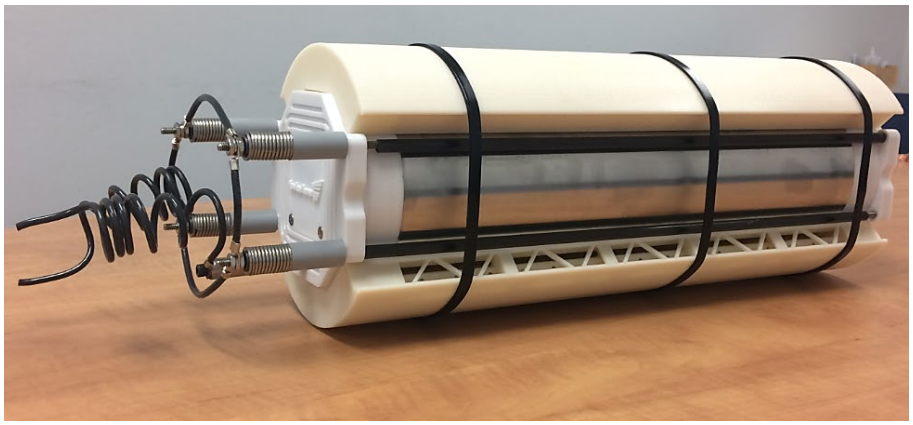

Figure 3.1-29 Fabrication Mock Stack for Seal Compression Development

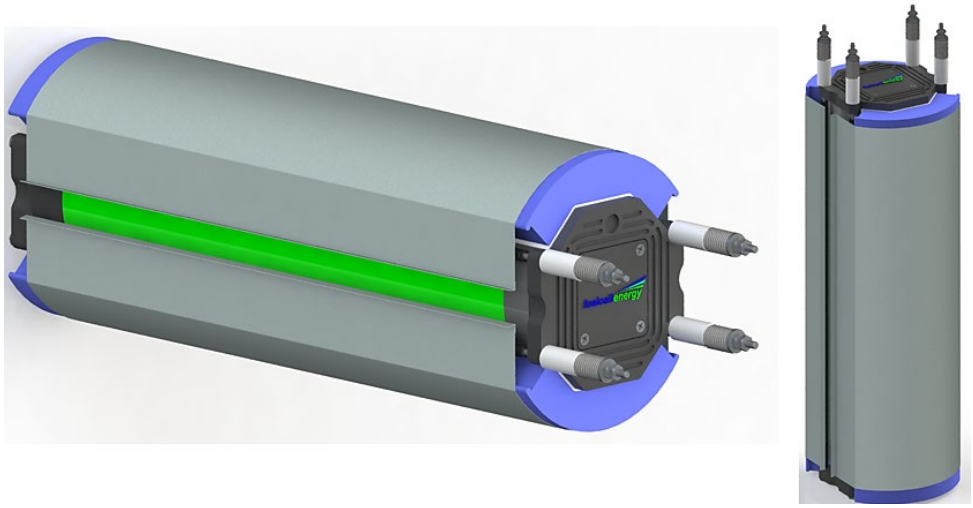

Figure 3.1-30 CAD Model Rendering of Mock Stack

Exhaust Oxidizer Design:

Background

The intent of integration of the exhaust oxidizer was to reduce the overall SOFC power-specific system footprint and costs. The approach was to locate the catalytic oxidizer within the cathode exhaust manifold. The anode exhaust can be routed to mix directly with the cathode exhaust, to provide heat from the oxidized mixture directly to the cathode in / anode in streams through either convection or radiation. The temperature of the stack can be protected by use of a radiation baffle and/or routing the anode in stream between the oxidized gas stream and stack. An example configuration of this is shown below in Figure 3.1-31.

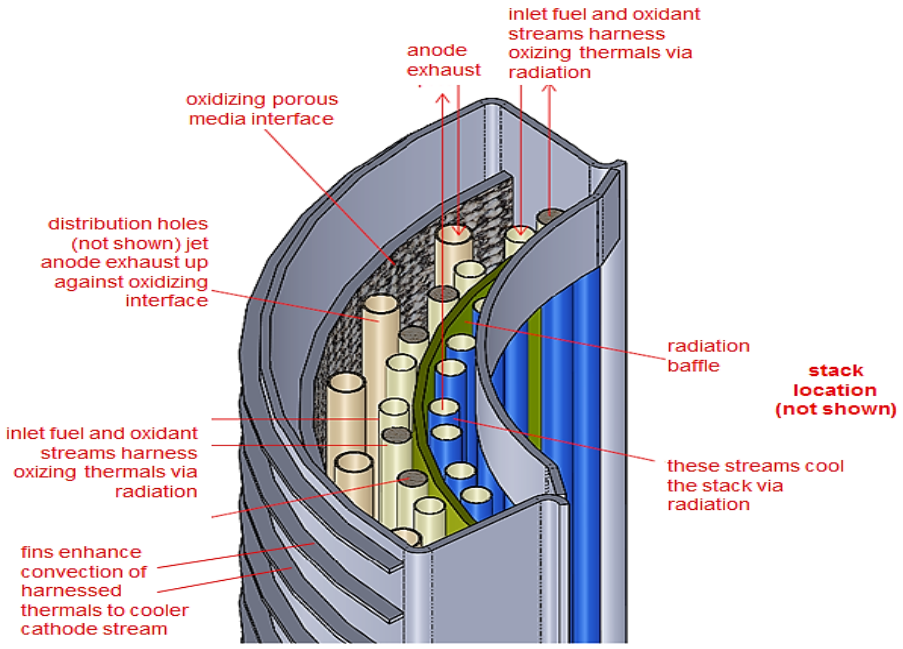

Figure 3.1-31 Example of Exhaust Oxidizer Integration

The integration of the catalytic oxidizing manifold revealed significant engineering design challenges. It required careful design to jet and mix the anode exhaust gas sufficiently with the cathode exhaust to acceptable air-to-fuel ratios at contact with the oxidizing catalyst. It also required careful selection of catalyst support media to achieve sufficient distribution of heat and mitigation of any flame generated. Precautions needed to be made to protect the stack from over-heating. Prior to commencing this intensive work, a baseline assessment was made using process simulations.

Plant Process Simulation

Model development for the process simulation was completed using CHEMCAD 7.1.1 software package. Custom unit operations (UOP) were embedded in the model to more accurately simulate the most relevant heat transfer mechanisms (radiation, convection) at the appropriate fluid interfaces as well providing added control of some stack-level parameters. The formulae to approximate UOP heat transfer mechanisms, were constructed of a coefficient that incorporated identified surface areas, shape factors, heat transfer coefficients, and Stefan-Boltzman coefficient. The ISC was the primary focus of this work as upstream and downstream heat exchange equipment were sized accordingly to account for the entire black box energy balance of the RPU. However, after running some initial cases, it was found that some refinements were required to sufficiently model the process accurately. The updated PFD of the system model is shown in Figure 3.1-32. These updates were as follows:

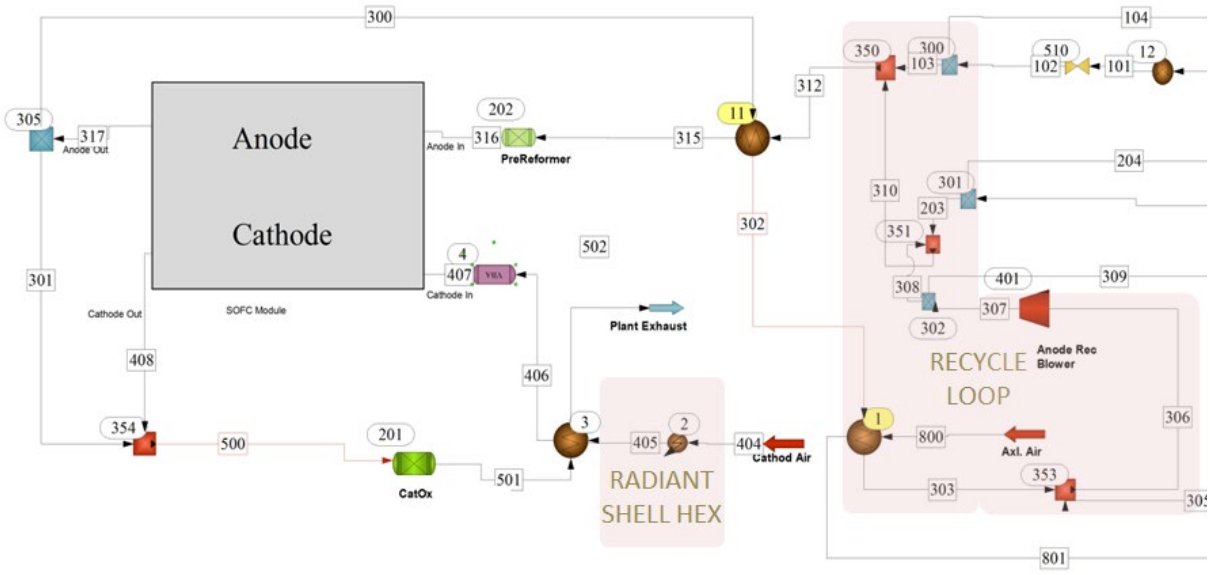

Figure 3.1-32 Revised PFD for Process Simulation

1. The simulation model was augmented to include anode recycle loop, the relevant unit operations including anode recycle blower and other recuperating heat exchanges – namely the convective heat exchange occurring through the passages of the cathode in radiant shell heat exchanger. This was an important upgrade as the stack level anode flow rate and its effects, vis-à-vis, stack temperature, per pass fuel utilization and steam to carbon ratio, could be calculated more precisely.
2. Stack temperature is a critical variable in the ISC process model configuration and, thus, important to be calculated correctly. Calculation of the stack temperature was revised to be a weighted average of the four anode and cathode inlet and outlet streams:

$$T_{stack} = T_{AI}{}^{*}\,\alpha_{AI} + T_{AO}{}^{*}\alpha_{AO} + T_{AI}{}^{*}\,\alpha_{CI} + T_{CO}{}^{*}\,\alpha_{CO}$$

where:

$$\alpha_{AI} = C_{AI} / C_{tot}$$

$$C_{AI} = (\dot{m}^{*}c_p)_{AI},\ C_{AO} = (\dot{m}^{*}c_p)_{AO},\ C_{CI} = (\dot{m}^{*}c_p)_{CI},\ C_{CO} = (\dot{m}^{*}c_p)_{CO}$$

$$C_{tot} = \sum \{(\dot{m}^{*}c_p)_{AI},\ (\dot{m}^{*}c_p)_{AO},\ (\dot{m}^{*}c_p)_{CI},\ (\dot{m}^{*}c_p)_{CO}\}$$

3. The latest version of SOFC Performance Model was used to calculate the cell voltage so that inlet to outlet temperature differences can be estimated more precisely, for both anode and cathode.

4. The VBA (Visual Basic for Application) code included implementation of the Newton's method for numerical solution of the system of nonlinear equations. It calculated the analytical derivatives of the system of nonlinear equations to solve for the three unknown shell layer temperatures. Figure 3.1-33 illustrates the heat transfer mechanisms at these

shell layers. This included the radiant heat transfer propagating radially outward from the ISC to the environment and the convective transfer of heat to the cathode-in stream flowing through the passages between the shells.

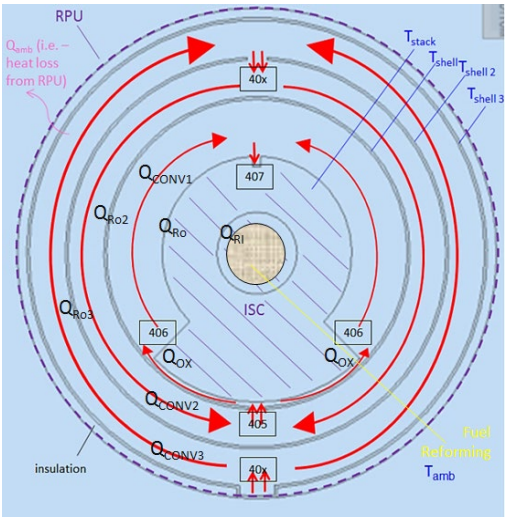

Figure 3.1-33 Radiant Shell HEX Heat Transfer

The governing equations were updated to solve for the shell temperatures and improve upon initial boundary condition assumptions. The governing equations were as follows:

$$Q_{RO} = Q_{conv1} + Q_{RO2}$$

$$Q_{RO2} = Q_{conv2} + Q_{RO3}$$

$$Q_{RO3} = Q_{conv3} + Q_{amb}$$

where:

$$Q_{CONV} = (UA)_{CONV} * [((T_{stack}, T_{shell})_{avg}) - T_{49}]$$

$$Q_{CONV2} = (UA)_{CONV2} * [((T_{shell}, T_{shell\ 2})_{avg}) - T_{40x}]$$

$$Q_{CONV3} = (UA)_{CONV3} * [((T_{shell\ 2}, T_{shell\ 3})_{avg}) - T_{40x}]$$

$$Q_{RO} = (UA)_{RO} * (T_{stack}^4 - T_{shell}^4)$$

$$Q_{RO2} = (UA)_{RO2} * (T_{shell}^4 - T_{shell2}^4)$$

$$Q_{RO3} = (UA)_{RO3} * (T_{shell2}^4 - T_{shell3}^4)$$

The process simulation base case was set at the following condition parameters: overall fuel utilization of 90%; air utilization of 60%; minimum steam to carbon ratio of 2 at anode inlet; ambient heat loss of 300 W; and stack temperature of 700°C. These utilization values were targeted to

help significantly reduce the plant parasitic power consumption of the blowers required to recycle anode gas and supply process air. The utilization targets result in large reduction in process stream pressure drop which directly relates to significant reductions in total blower power required. As much as 50% reduction in blower power was achievable resulting in increased overall plant efficiency by 0.5%. Fresh fuel and air flow rate are set based on the desired utilization and stack power. Anode recycle ratio was calculated in such way to achieve the desired steam to carbon ratio at anode inlet. During simulation, the inlet air stream temperature and pre-reformer inlet temperature were manipulated so that the desired stack temperature can be obtained from the VBA UOP output data while adhering to the remaining baseline conditions and UOP governing equations.

The initial base case was run and provided a starting reference point to assess stack integration locations and geometries of both the anode fuel reformer and the catalytic oxidizing manifold. A number of other operating condition scenarios were then considered and chosen to study the effect of some important system parameters including: percentage of IIR; heat duties and changes in temperature along the different heat exchange interfaces; anode in, cathode in, maximum delta, and maximum stack temperatures; and thermal energy removed and recuperated from the stack. These cases studied the effect of change in: overall target stack temperature; heat loss to the environment; internal fuel reforming approach temperature; overall fuel utilization (U_f); and fuel reformer inlet temperature. The results are summarized in Table 3.1-3 below.

Simulation results collectively showed that achieving a sufficiently high anode inlet temperature is a difficult task when locating fuel reforming within the open space of the ID of the ISC. This is due to the coupling of the heat of reforming in the pre-reformer unit with the radiative power from the stack. It appeared that it would be more effective to couple pre-reformer heat requirement with other units, e.g., the oxidizer, if permitted by the configuration and space limitation.

Table 3.1-3 Summary ISC Process Simulation Results

Description	Baseline (Ufpp78 StoC2)	Avg stack temp = 725	Qamb = 150W	Tapp = 200F, prereform	Uf over = 80	ReformIn Temp = 750
QRO W	1126	1175	1124	1177	1410	1336
QRI W	348	495	349	254	277	208
QCONV W	-82	-84	-81	-76	-174	-78
S:C@AI	2.05	2.00	2.05	2.13	2.01	2.04
UFPP	**0.782**	**0.782**	**0.782**	**0.782**	**0.554**	**0.782**
Stack_HeatLoss W	-1126	-1175	-1124	-1177	-1410	-1336
TStack C	700	726	700	700	700	701
TotPower W	-7229	-7076	-7229	-7229	-7076	-7076
DIR%	**79.0**	**77.2**	**79.0**	**81.8**	**81.7**	**78.6**
Anode_dT C	**151**	**170**	**151**	**107**	**100**	**155**
Cathode_dT C	**17**	**18**	**18**	**14**	**-53**	**33**
Qamb W	300	300	150	300	300	300
Ufoveral	0.90	0.90	0.90	0.90	0.80	0.90
Ua	0.60	0.60	0.60	0.60	0.60	0.60
CD(mA/cm2)	300	300	300	300	300	300
CIT C	**715**	**744**	**715**	**710**	**760**	**706**
COT C	732	762	732	724	707	739
AIT C	**581**	**592**	**581**	**616**	**607**	**583**
AOT C	732	**762**	**732**	**724**	**707**	**739**
ReformInTemp C (#315)	700	700	700	700	700	750
CathInShellTemp C (#404)	**435**	**457**	**408**	**422**	**330**	**375**
OxExTemp C (#502)	**835**	**836**	**806**	**798**	**926**	**802**
RecyBlowInTemp (#303)	160	160	160	160	160	160
OxInTemp C (#501)	**918**	**947**	**918**	**909**	**1112**	**924**
FUEL SUPPLY (kg/hr)	0.75	0.75	0.75	0.75	0.84	0.75
RecycleRatio	**0.60**	**0.60**	**0.60**	**0.60**	**0.69**	**0.60**

Oxidizer Manifold Development

A metallic substrate with high surface area, was selected for an oxidizing catalyst (CO and H_2). This was an initial effort to develop in-house coating process development, which included an optimization of a wash-coat formulation, and of coating on metallic substrates.

The process gas condition was about 750°C for pre-combustion of H_2/CO and approximately 1000°C for the post-combustion. At these relatively high temperatures, catalytic performance was not kinetically controlled, but rather mass transfer controlled. In other words, having a high precious metal loading did not improve the catalytic activity, but a turbulent flow would improve it. Hence, we decided to have relatively low precious metal loading (~1wt.%), and to have porous metal sheet, which would result in high tortuosity.

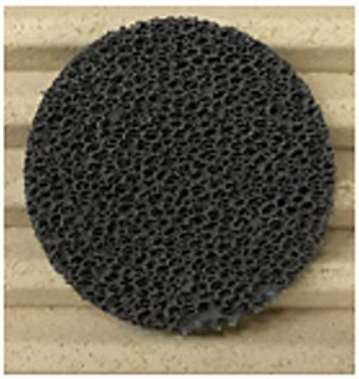

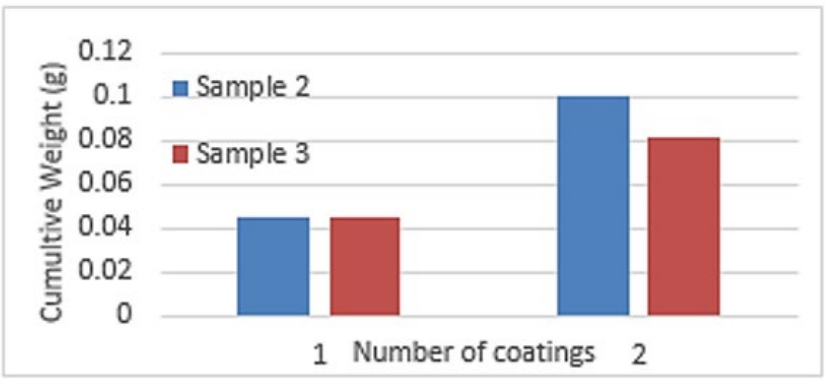

Figure 3.1-34 High porosity substrate, 1" diameter (left). Relationship between cumulative weight and number of coatings. After 1st coating, the coated sample was dried at 120°C for 30 minutes. After the second coating, the sample was calcined at 550°C for three hours. Sample 1, 2, and 3 were from the same batch of the porous substrate. Sample 1 was uncoated porous substrate (not shown).

An unoptimized wash-coat formulation was prepared using alumina (Al_2O_3) powder, distilled (D.I.) water, and additives without precious metals. A high porosity metal substrate, seen in Figure 3.1-34 (left) was coated with this unoptimized wash-coat. This meant that additive amounts were not controlled. Figure 3.1-34 (right) shows relatively good coating weight gains with sample 2 and 3 after the first coating as well as after the second coating. These results indicate that the unoptimized coating needed two coatings to achieve the coating target, approximately 90 mg. Figure 3.1-35 shows the scanning electron microscope (SEM) image of the sample 1. This sample had no coating. Figure 3.1-36 shows the SEM image of sample 2 with the non-optimised coating, which showed irregular coatings on the pores, which were seen as white color crumbles. Sample 3 showed similar images as sample 2. This result suggested that the unoptimized wach-coat required optimization in order to achieve smooth coating on porous metal substrate.

The optimal additive amount to control rheology was studied with the intent to improve coatability. The wash-coat was optimized and given well-controlled coatings on the same porous metallic substrate - specifically sample 4 and 5. The weight gains for sample 4 and 5 were +12% and +10% from the coating target, respectively. Due to the optimization of the rheology, the optimized wash-coat had much higher solid content compared to the unoptimized wash-coat. The high solid content enabled us to use single dip coating to achieve the coating target. Figure 3.1-37 and Figure 3.1-38 show SEM images of sample 4 for 35 times and 150 times magnifications, respectively. The SEM images of sample 5, which were similar to those of sample 4 are not shown. These images show uniform coatings on the surface of the porous metal substrate, indicating the success of optimizing wash-coat with the particular additive we selected.

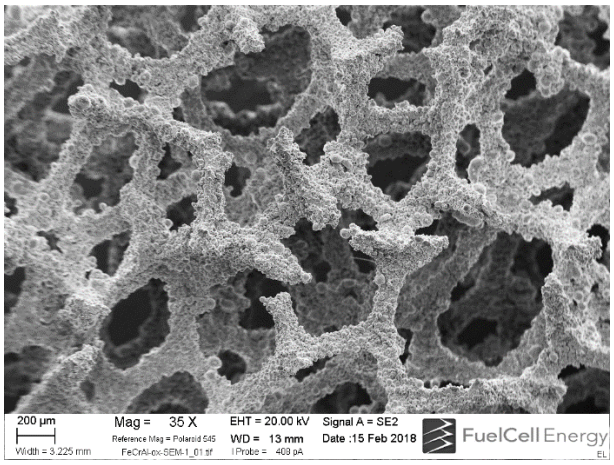

Figure 3.1-35 Sample 1 High Porosity Substrate w/o coating

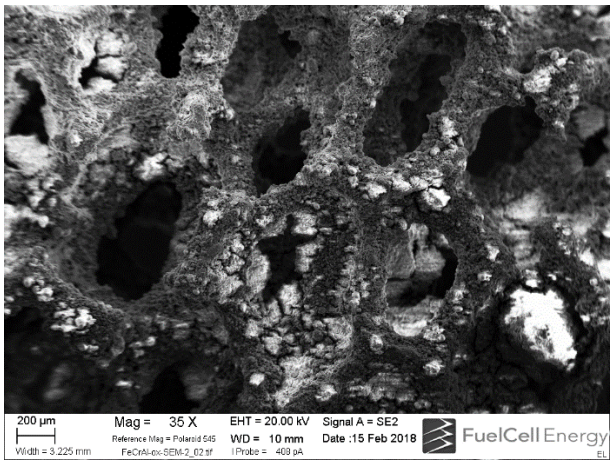

Figure 3.1-36 Sample 2 High Porosity Substrate w/ coating

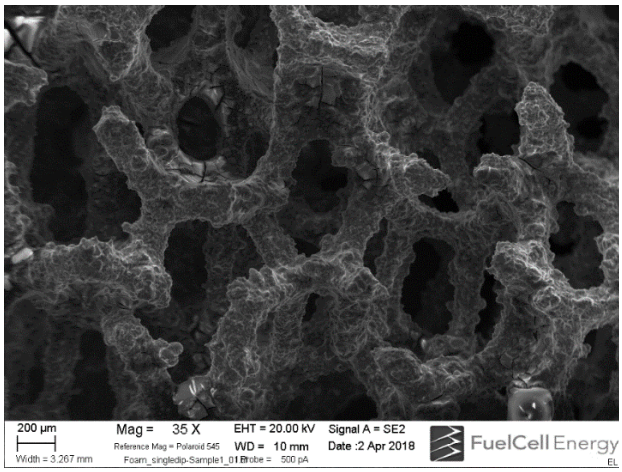

Figure 3.1-37 Sample 4 with 35 times magnification

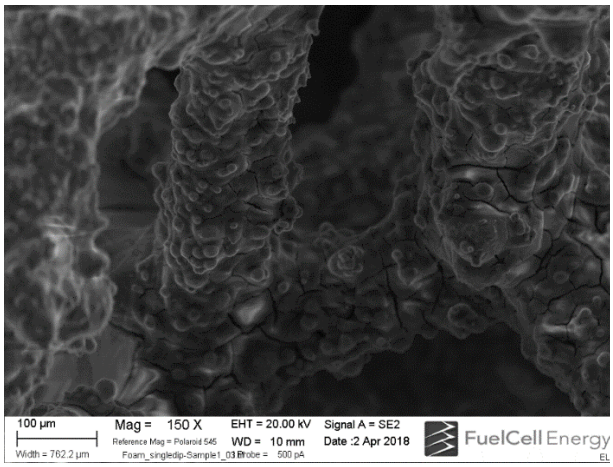

Figure 3.1-38 Sample 4 150 times magnification

Figure 3.1-39 shows pressure drop results for uncoated and coated porous metal substrates. Sample 1 was uncoated while Sample 2 and 3 were coated and showed much higher pressure drop compared to the sample 1. Figure 3.1-39 supports this result that the irregular coating increased the pressure drop compared to the uncoated sample in Figure 3.1-35. Sample 4 and 5 had similar values and they showed small increase from the uncoated sample. SEM images of the sample 4 shows very smooth coating, which supports low pressure drop results. In summary, the optimal wash-coat coating process was successfully developed for the porous metal substrates.

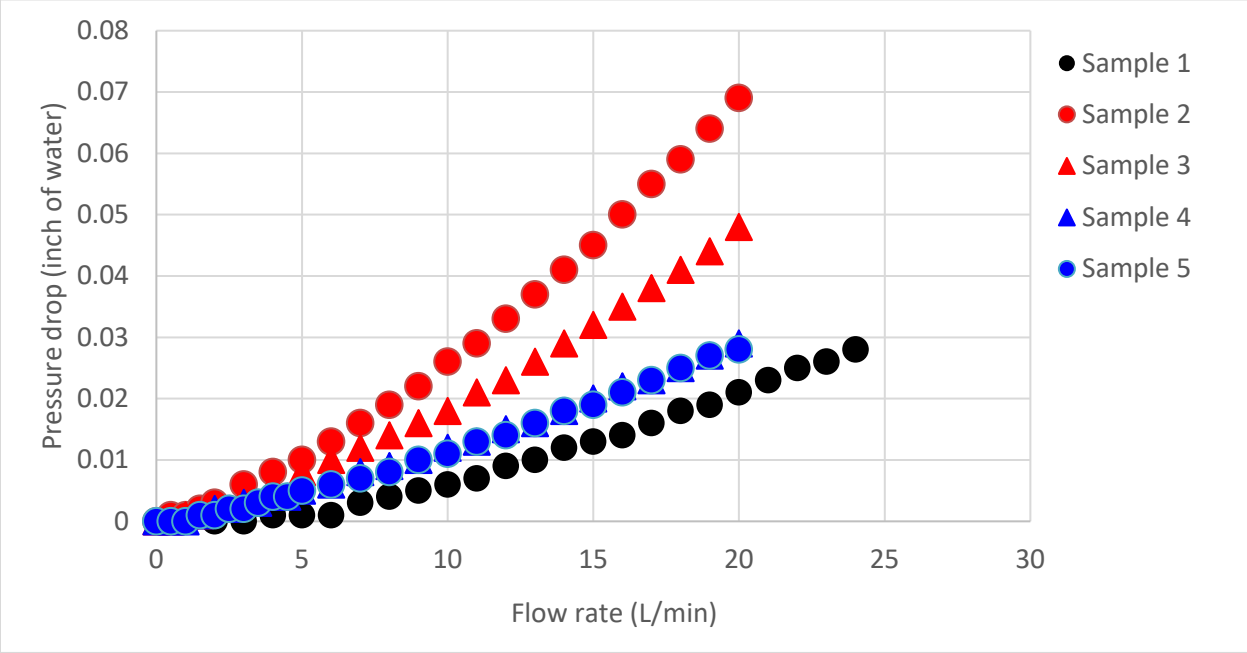

Figure 3.1-39 Relationship between flow rates and pressure drop. Sample 1: Porous metal substrate w/o coating, sample 2 & 3: Porous metal substrates with unoptimized coating, and sample 4 & 5: Porous metal substrates with optimized coating

The porous metal substrate material initially coated were expensive and very rigid. Due to significant cost advantages, flexible porous substrate samples were tested for coating trials as well. Three different porosities were used: Low, Medium, and High (Figure 3.1-40). One-inch discs were prepared from raw sheets of flexible porous substrate materials.

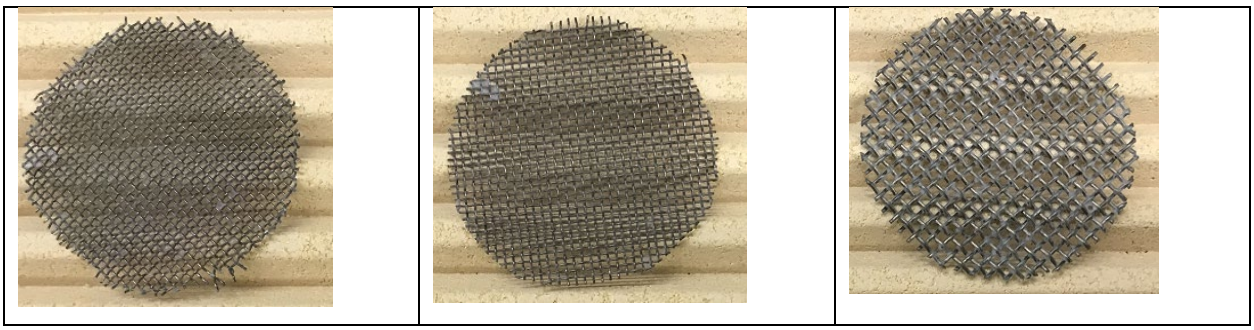

Figure 3.1-40 Flexible Substrate Porosities: Low (left), Medium (middle), and High (right)

The same optimized coating, developed for the rigid porous metal substrates, was applied to these different porosities of flexible metal substrates. Figure 3.1-41 shows cumulative weight gains after each coating for all porosities. There was calcination between each coating. The High porosity substrate picked up coating better than Medium and Low porosity substrates. However it became the flakiest due to the thicker coating. The Medium and Low porosity substrates picked up less weight, per coating and cumulative, compared to the High porosity substrate, but the coating was not flaky. From a catalyst point of view, a thick coating is not desirable, since only the surface metals are active species for catalytic reactions. If a flexible metal substrate were to be selected, the Low porosity version would be chosen and with only a single coating. Here, the

coating would be more evenly distributed, the resultant coating would not flake off, and the loaded weight of washcoat per coating could be controlled more accurately.

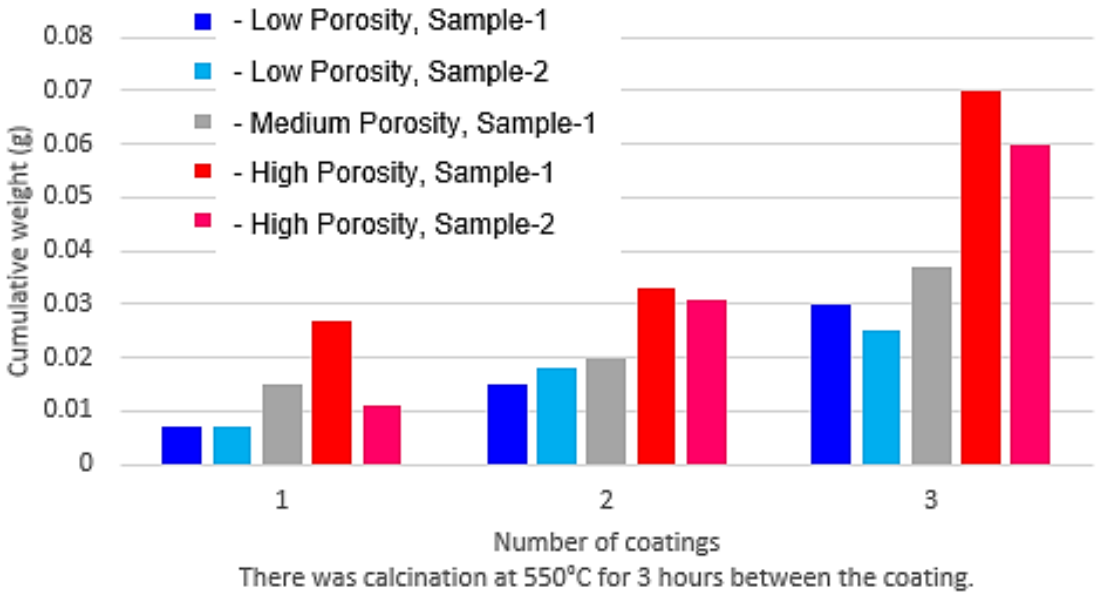

Figure 3.1-41 Relationship between cumulative weight and number of coatings. After each coating, the sample was calcined at 550°C for three hours. Flexible substrate porosity sizes of Low, Medium, and High were used.

In summary, the rigid porous substrates were easier to coat than the flexible porous substrates. with no consideration for the cost, rigid porous substrates would be chosen due to the higher surface area, resulting in the coating target by single dip-coat. The flexible porous substrates required multiple coats to achieve the same coating target. If the flexible porous substrates were selected over the rigid ones, a single coat and an architecture having multiple layers should be considered. However, there is also the possibility that forming the flexible substrates into a corrugation may be sufficient enough to fully oxidize anode exhaust gas streams and superheat cooler cathode supply gas prior to entering the stack cells. The fabricated part would fit into the same volume space as the rigid porous substrate material but take up much less volume, resulting in a significant reduction in pressure drop; a benefit to plant efficiency. Also, if sufficient, this would result in further cost reduction due a significant decrease in precious metal use.

Stack Containment Vessel

Initial design efforts, from conceptual CAD layout through detailed fabrication drawings, were focused on the close integration of system functionality to the core SOFC stack. The core SOFC stack, built upon the compact stack architecture (CSA), is located within the greater structure of the repeatable power unit (RPU). It includes the repeatable SOFC cells and interconnects, the end plates, power take-off post, tie-rod compression components, internal anode manifold, oxidizer manifolds, and cathode-in containment shells. Analysis of the CAD model designs) and detailed fabrication drawings were released for manufacturing procurement. The stack containment vessel (the rest of the RPU) included items such as insulation, structural housing with instrumentation access ports, process connection interface adapter, purgatory zone, and lid. The instrumentation included items such as thermocouples, pressure taps, voltage leads, power take-off (PTO) cables with connectors, and power supply cables. There were a number of system

integration elements that needed to be closely monitored so the first few smaller scale (45-cell and 150-cell) technology stacks built were highly instrumented to determine how feasible it is to operate the stack with these integrated elements as well as to determine optimal operating parameters to use for these elements through the various operating modes.

The majority of the stack containment vessel components utilize common sheet metal forming, tube rolling and brazing operations in order to improve ease of manufacturing. The design of the outer housing of this vessel was developed to be removable from the in-house test stand. It was designed in layer-cake fashion to enable upper and lower portions (Figure 3.1-42) to be removed individually to facilitate the swap out of technology stacks without the need to disconnect process supply and exhaust lines running through an adaptive mounting plate from the lower cabinet of the test stand. This also provided flexibility in incorporating compact heat exchange equipment immediately below lower end plate of the SOFC stack.

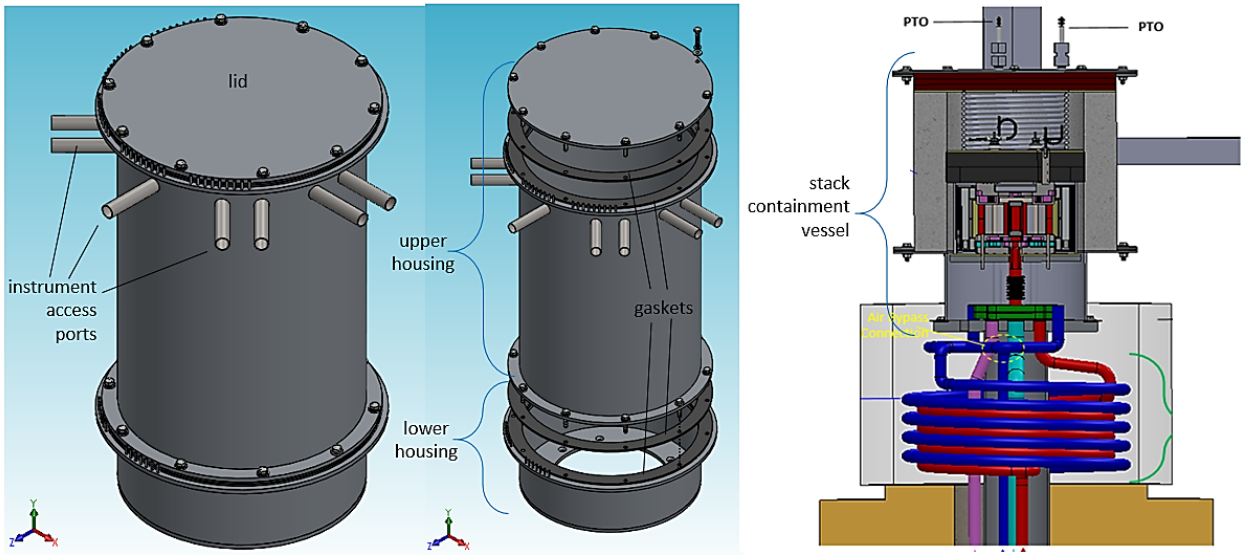

Figure 3.1-42 Stack Containment Vessel Housing Assembly

An adaptive interface with flexible connections was incorporated within the lower housing of the stack containment vessel called the adapter plate assembly (Figure 3.1-43). The assembly fabrication utilized brazing and welding along with standard machining methods. As the design of the section of the RPU developed further, efforts were focused more on design for higher volume manufacturing. At the top, the adapter plate assembly interfaced with the stack, while, at the bottom, it interfaced with the test stand mounting plate.

The ends of the gas supply and exhaust connections was designed to have a thermally activated dielectric sleeve installed prior to installation of the SOFC stack. They fitted within openings in the bottom end plate of the stack, expanded radially as they heat up, and created a seal during the stack heat-up. These connections included expansion joints to compensate for thermal expansion and to provide some compliance with sufficient force during line up with opening in end plate during stack installation. Since the lower housing of the stack containment vessel is removable, the size of the lower housing (Figure 3.1-42), that the adapter plate assembly resides in, could be changed to accommodate compact heat exchange equipment. This heat exchange equipment offered recuperative heating and pre-reforming capabilities using the high value sensible heat of the anode recycle and oxidizer exhaust flow streams.

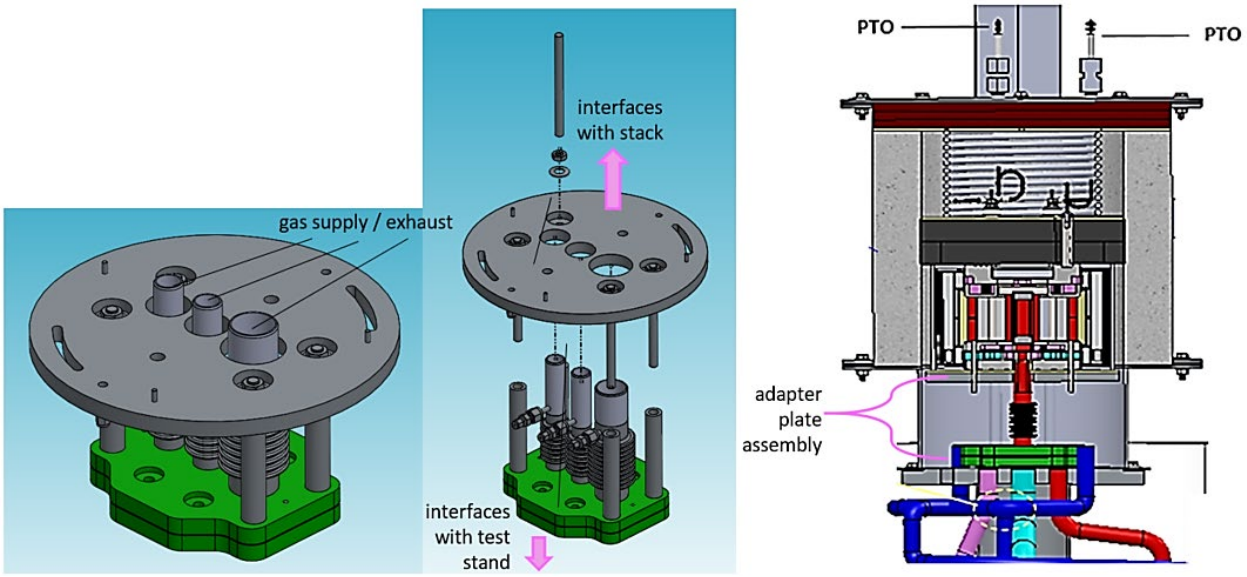

Figure 3.1-43 Adapter Plate Assembly for Process Connections

Hot Stack Swap-ability:

One of the key features of the design was to enable stack replacement at End-of-Life (EOL) without shutting down the SOFC power plant. One could envision such a system (Figure 3.1-44) where small quantities – or "strings" - of ISC's (stacks) are tied into compact transformer-less inverters, with the capability of electrically disconnecting and isolating an individual string. Once stacks are cooled to safe enough levels, an operator can open a single RPU within that string to replace the ISC that has reached EOL. Only the stacks within that string, ideally two to four, would need to be electrically disconnected, all the remaining strings of the SOFC system can continue to produce power. String size can be optimized to allow for temporary power increase to offset the string in outage, as a tradeoff between minimizing this increase in power versus amount of tie-in equipment. For example, a 200kW SOFC system comprised of 12 strings, disconnecting one string would require the remaining strings to make up 1/12 – or 8.3% - of the targeted. The current density would need to increase by 10% on each of the remaining strings temporarily while a technician replaces and restarts the string being serviced. This allows a significant advantage to both plant availability and capacity factor, while also minimizing the number of the stacks being stressed through a thermal cycle.

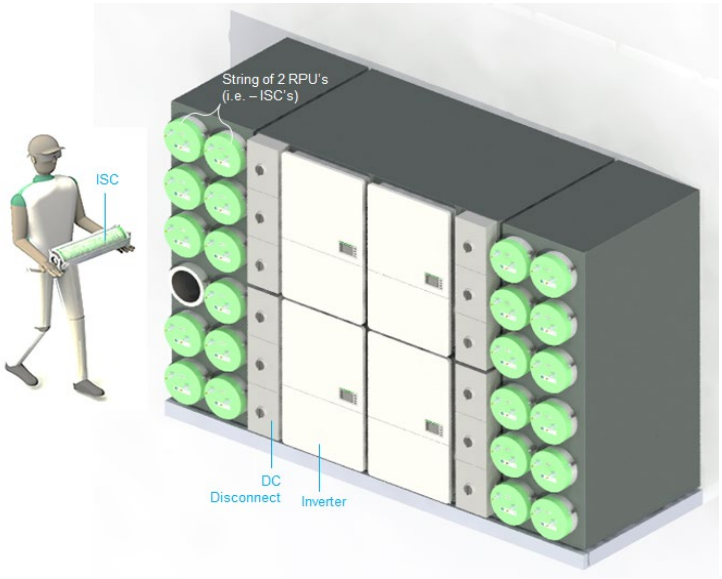

Figure 3.1-44 Example of 200kW SOFC System with String DC Disconnect

There are critical electrical aspects of the ISC, RPU and SOFC system plant design required in order to allow this operation to proceed in a safe manner. Starting at a high level, the correct inverter can eliminate the need for a step-up transformer. A transformer-less inverter accomplishes this and a multi-string version would result in smaller packaging envelope of the plant. DC disconnect hardware can be added between the string of ISC's and the inverter to allow for electrical disconnect of an individual string. However, the ISC is required to be a floating ground from the plant (RPU) process connections and strung together in series to achieve a high enough voltage. Transformer-less inverters are meant to work with floating ground DC sources and, in addition, minimum DC sources greater than 830 volts eliminate the need for any DC boost to get 480 VAC. The interconnection of ISC's can surpass the minimum DC voltage requirement. In order to ensure the ISCs are electrically floating, there is a need to have the process connections from the RPU base that tie into the fixed end of ISC to be dielectrically isolated. This requires a design that achieves this for manifold (anode and cathode) seal interfaces to the end plates. In addition to dielectric isolation, these as being able to perform as radial seals while at the same time allowing the ISC to be installed into the RPU at room temperature. As the assembly heats up, these radial seals expand, contact and fill out any remaining gaps between the supply tube of the RPU and a pocket hole in the end plate of the ISC where it is housed. A material with high dielectric strength and high coefficient of expansion was identified to accomplish all of these functions.

Two types of bench tests were conducted to demonstrate the efficacy of this radial seal design. One of was a leak test performed under pressure differentials anticipated during system operation. A sleeve of the dielectric material was placed between the ID of a dead-ended hole in a metal block and the OD of a metal tube (Figure 3.1-45). The metal block had a relatively low coefficient-of-thermal-expansion (CTE) as compared to the dielectric sleeve and the metal tube had a CTE value in between the values of these. The metal tube had a machined lip that allowed the end of it to remain sufficiently high enough off to prevent plugging of flow and standoffs were added at the bottom of the holes in the metal block to allow air to attempt to flow between the wound layers of material within the dielectric sleeve. An adapter was welded to the metal tube to allow for connection to supply air. A flow meter with 0.001 SLPM precision was selected and

supply air fixture connections were examined before and throughout the duration of the tests to detect any leaks. The test was performed in an oven (Figure 3.1-45): pre-conditioned first with two thermal cycles; and leak rates were measured during a third thermal cycle, from room temperature all the way to 700°C. Of particular interest, was the level of leak at the fuel enable temperature operational step.

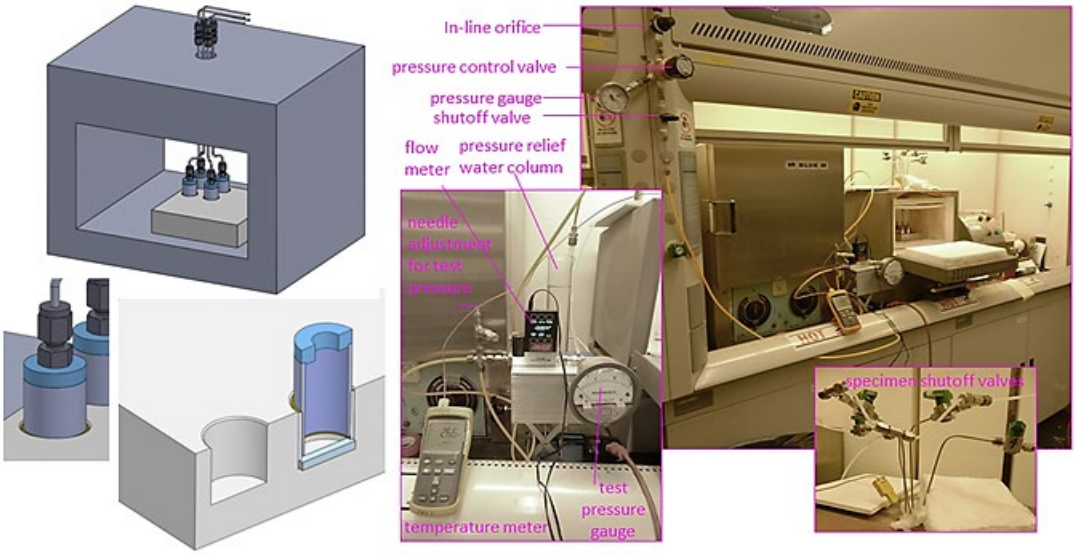

Figure 3.1-45 Test Specimens and High Temperature Leak Test Fixture

The results showed leak rates significantly less than 0.3% of that of the process gas design flow rate (Figure 3.1-46). This maximum leak rate was achieved before fuel enable temperature is reached and maintained all the way up through gas operating temperatures. This level of leakage has been determined sufficient enough to be of no risk to damage of the cells from cross-mixing process gas streams.

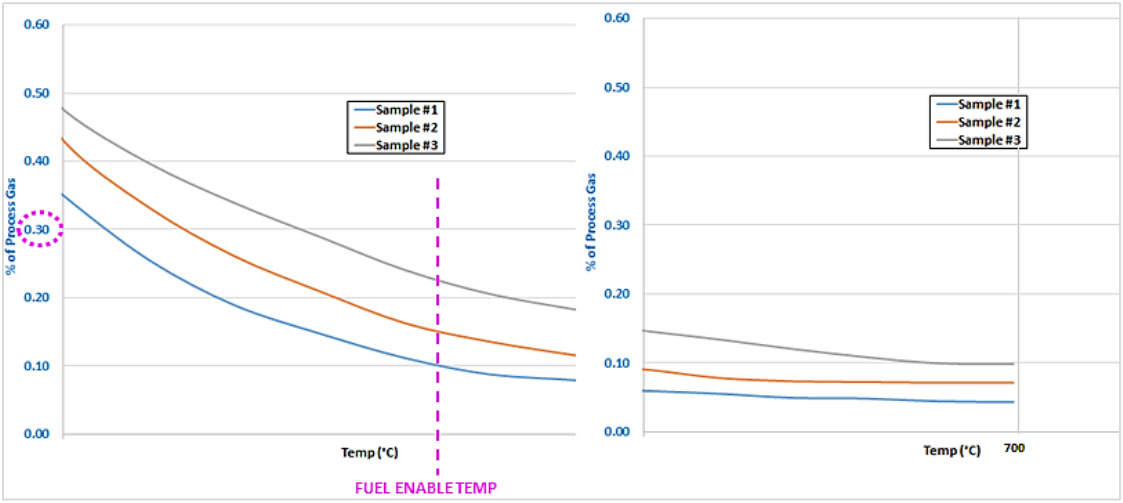

Figure 3.1-46 Leak Rate as Percentage of Process Gas Flow vs. Temp

The second of the aforementioned tests conducted was an electrical test. HIPOT testing was completed to determine whether voltage levels resulting in current flow (from metal tube through mica sleeve to metal block) met the minimum levels required by the FC1 Fuel Cell Standards. This standard is set at 1500 VAC / 2120 VDC. The 1500 VAC was chosen as the test requirement since the available HIPOT tester was configured for this voltage. The tubing used for leak testing was removed and replaced with high temperature voltage leads. The voltage leads allowed electric potential to be placed across the test circuit in order to perform the test at process gas stream operational temperatures. The hot electrode from the HIPOT tester was clamped to the other end of this lead when testing the specific sample (Figure 3.1-47). The ground connection was connected to the metal block base in similar fashion. Initial seal configurations were tested using a one second pulse mode at set voltage levels (500 VAC increments) of the tester. “Continuous Mode” was utilized on later configurations.

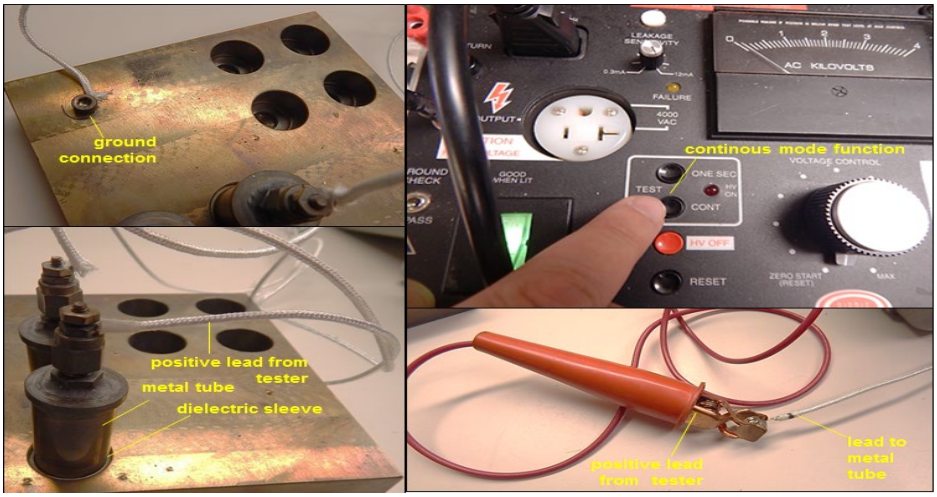

Figure 3.1-47 HIPOT Test

The results of the electrical HIPOT testing, using the one second pulse mode, showed that the best performing of seal configurations was able to prevent current flowing through the dielectric sleeve at 2000 VAC. Once the test specimens reached 700°C, the results showed two of four specimens failing at 1500 VAC. The other two eventually failed at 2000 VAC but still met the FC1 Standard. The “continuous mode function” was utilized on other seal configurations only after the best performing configuration was tested using the “one second pulse” mode. The “continuous mode function” allowed the test operator to determine a more accurate voltage at which current flowed in the event a failure occurred before reaching the FC1 standard VAC. A thicker dielectric sleeve material would have increased electrical resistance of this configuration. The intent was that the thicker wall would allow the seal to meet the FC1 Standard spec.

Hi Pot Test @ Room Temp (22.8 °C)							
Unit #1		Unit #2		Unit #3		Unit #4	
500 VAC	P	500 VAC	P	500 VAC	P	500 VAC	P
1,000 VAC	P	1,000 VAC	P	1,000 VAC	P	1,000 VAC	P
1,500 VAC	P	1,500 VAC	P	1,500 VAC	P	1,500 VAC	P
2,000 VAC	P	2,000 VAC	P	2,000 VAC	P	2,000 VAC	P
Hi Pot Test @ Max Temp (701 °C)							
Unit #1		Unit #2		Unit #3		Unit #4	
500 VAC	P	500 VAC	P	500 VAC	P	500 VAC	P
1,000 VAC	P	1,000 VAC	P	1,000 VAC	P	1,000 VAC	P
1,500 VAC	P	1,500 VAC	F	1,500 VAC	F	1,500 VAC	P
2,000 VAC	F	2,000 VAC	F	2,000 VAC	F	2,000 VAC	F

Figure 3.1-48 HIPOT Test Results – One Second Pulse Mode

A material was identified with high dielectric strength and high coefficient of expansion for use at the supply and exhaust gas process connections. This material was needed to accomplish a number of functions to allow the stack to be “hot swappable” at end of life (EOL). These functions included: thermally activated radial seal; and dielectric isolation from anticipated maximum operating voltage. Testing was conducted which showed leak rates significantly below that of the process gas design flow rate as well as the large area stack architecture stacks. Most importantly, minimal leak rate was achieved prior to reaching the fuel enable operating mode temperature. However, the HIPOT testing results did not quite meet system requirements. Some specimens tested failed at 1500 VAC, the minimum requirement of the FC1 Standard. Thicker wall dielectric sleeve material were procured and fabricated parts were tested for both fluid leak and electrical HIPOT.

Leak test results show that all 1.5x thick dielectric sleeves demonstrated more consistent fluid leak measurements than the 2x thick sleeves and still met the minimum fluid leakage requirements after thermal cycling (Figure 3.1-45). Electrical HIPOT testing was conducted using the “continuous” mode of the test instrument instead of “one-second pulse” mode. This allowed for a more precise and accurate measurement of the voltage at which the dielectric seal failed. Testing was conducted up to 2000 VAC for information purposes, but the requirement matched the FC1 Standard of 1500 VAC. Results showed that both the 1.5x thick sleeves and the 2x sleeves met and exceeded the FC1 Standard requirement at both room and 800 degrees Celsius after thermal cycling (Figure 3.1-50). Based on the fluid leak and electrical HIPOT testing, the 1.5x thick sleeves have been chosen to be procured for functional prototype and validation testing. A functional prototype was designed to test these seals as well as oxidizing manifold performance. Any revisions to the design, after conclusion of test results, was to be rolled into final design of fabrication of the fuel cell functional validation stacks.

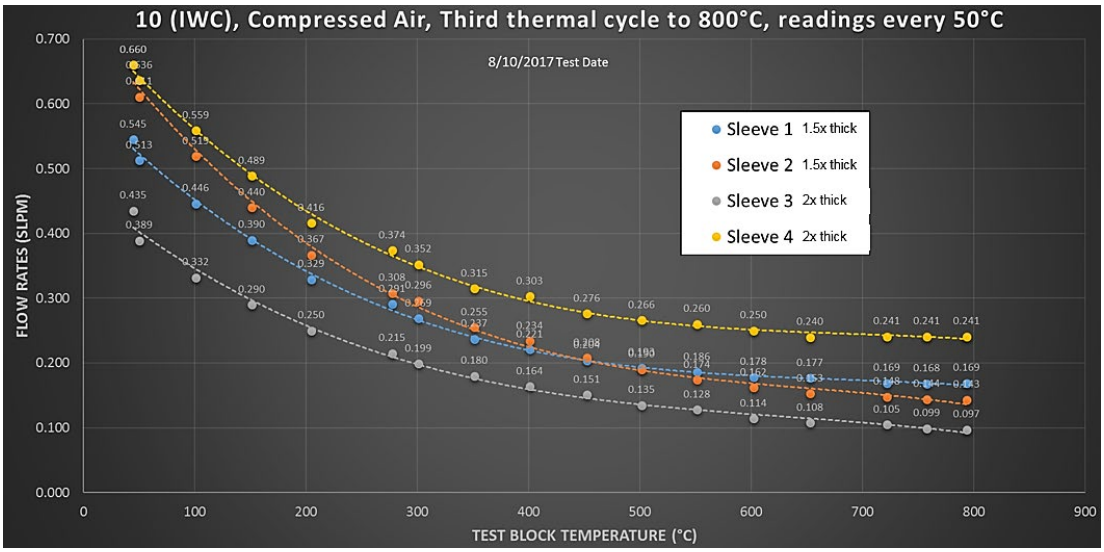

Figure 3.1-49 Leak Rate vs Temperature during Thermal Cycling

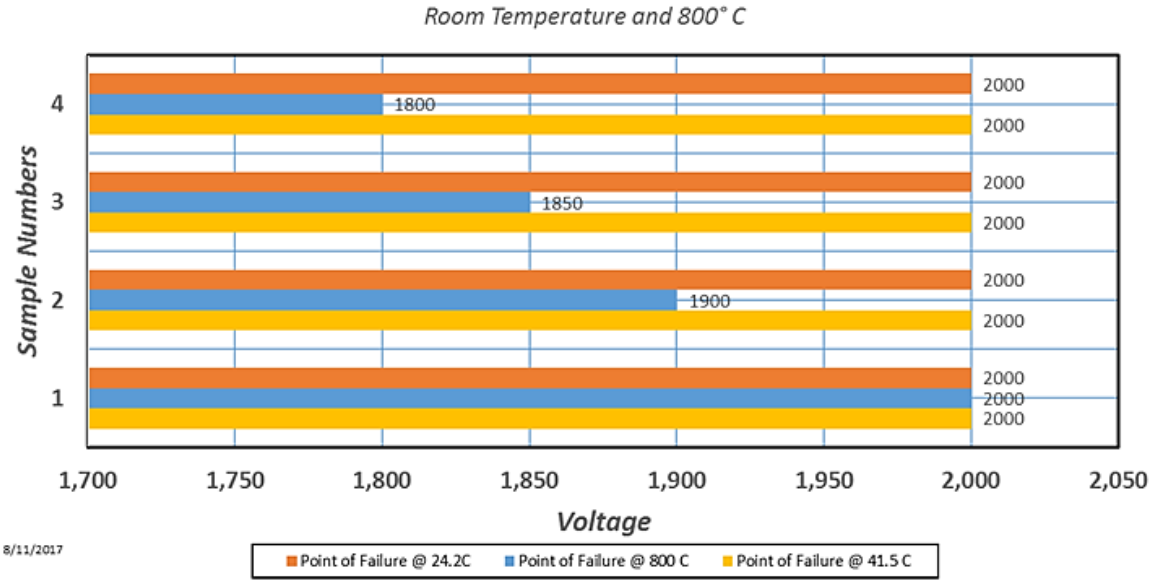

Figure 3.1-50 HIPOT Test Results, Room Temp & 800°C

Additional Stack Component and Feature Development:

The stack cathode manifold and end plates are prime examples of components to be utilized for many functions including providing the ISC to RPU interface, managing the flow of inlet and exhaust gas streams, and playing critical roles in thermal management of the SOFC stack. Figure 3.1-51 illustrates some of the high-level CAD models of design features developed in this project.

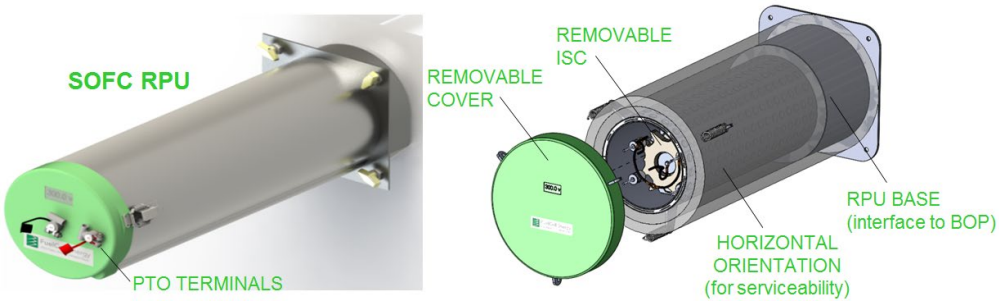

Figure 3.1-51 Layout of the RPU during CAD Design Activities

3.2 Modeling (CFD Analysis and FEA)

Objective:

The objective of this activity was to model components related to the integrated stack architecture design as well as the integrated system components such as the reformer and oxidizer tubes, and conduct analyses to guide design activities.

Approach:

Computational fluid dynamics (CFD) analysis and finite element analysis (FEA) were used to model the components utilized in the integrated stack architecture design as well as the integrated system components such as the reforming and oxidizer tubes. These tools were also be employed to maximize engineering understanding and achieve the end goal of maximizing robustness, reliability and stack life while reducing overall system cost. Detailed analyses were conducted to quantify the thermal profile, current density map, contours of anode and cathode gas compositions, extent of internal reforming, and pressure profile within the stack.

Results & Discussion:

The radiant air pre-heater (Figure 3.2-1, #1) shell structure is part of the reusable hard mounted portion of the RPU and helps manage heat losses of the ISC. It encompasses the ISC (which houses integrated fuel reforming and catalytic air preheater). The basic concept (Figure 3.2-1) is to allow heat to radiate through the walls of the multi-layered shell structure where the walls allow cooler cathode air to recuperate this lost heat through convection. In combination with heat transferred from the catalytic air preheater manifold, this reduces the supplemental heat exchanger capacity required to heat the air to required inlet temperature of the ISC. With this and the use of this low-cost simple sheet metal form, the cost and footprint of the SOFC plant reduces significantly.

For this design configuration, there is opportunity for this heat to be recuperated before and after the cathode in gas is heated by the catalytic air preheater manifold (Figure 3.2-1). Cooler air is introduced into the outer most shell passage and flows from there circumferentially, back-and-forth, continuing inwards through the labyrinth of shells closer to the ISC. This "1st stage" of heating allows the cooler air to interact with a large amount of surface area of the radiant air pre-heater structure. Here, the shell walls are cooler farther away from the stack but sufficiently hot enough for measurable heating of the cathode gas. The air is then literally 'pinched' where it hits the elevated temperature surfaces of the external manifold (and fins). This "2nd stage" of heating provides a significant boost in temperature that may be sufficient enough to meet inlet temperature requirements. The air continues a last pass through a gap between the ISC and the

inner shell wall of the radiant air preheater. Here, during this "3rd stage" of heating, the air is exposed to the hot outside surface of the stack as well as the hottest wall of the shell structure and should provide any additional heating if not hot enough after the "2nd stage".

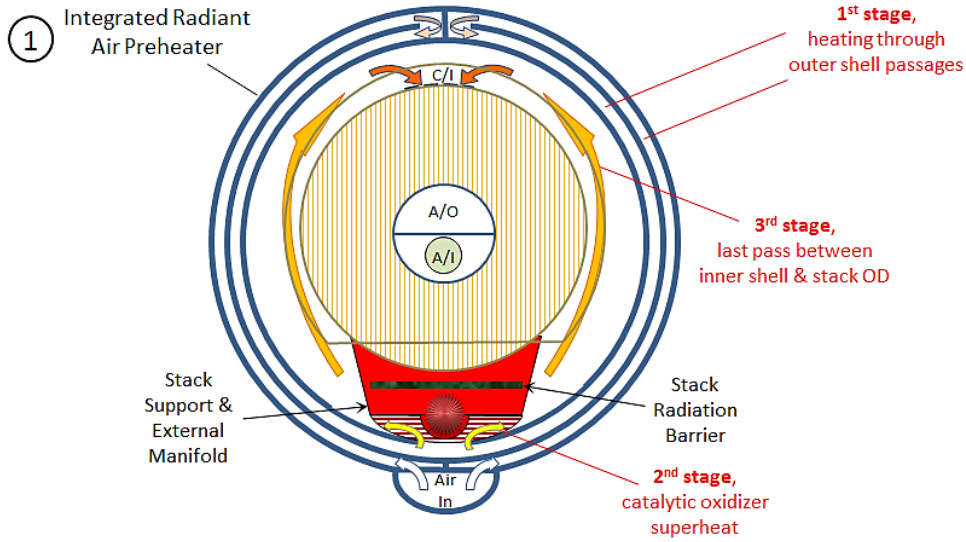

Figure 3.2-1 Radiant Air Preheater Concept

The current SOFC stack technology operates under air utilization (Ua) of typically 20-40% to supply required oxygen available at the electrochemical active surfaces of the SOFC but also enough thermal mass to dissipate the heat of the fuel cell reaction at appropriate temperatures to avoid risk of degradation to the cells. However, this means higher flow rates required of the process air blower. A key attribute of the CSA-derived SOFC's is that the lateral conductive thermal resistance path is significantly reduced due to the use of a hollow-disk cell design. Heat can be removed at both the inner and outer surfaces and higher air utilization (lower flow rate) is possible. Lower flow rates have a direct impact on blower power required, a significant contributor to parasitic losses of the power plant. A sizeable increase in Ua of 40% to 60% is possible with this approach. From past SOFC process simulation modeling, it is anticipated this would decrease the amount of air required by 35%. Using laminar flow and blower power calculations, this would result in a 50% blower power reduction to supply the cathode-in air.

CFD assessments were carried out on an initial configuration without an external catalytic air-preheater manifold to better understand Ua change effects and establish limits of increasing U_a. Cathode in air supply temperature and Ua (flow rate) were varied. The following data were obtained: outside surface, stack, and inlet temperatures; and remaining energy required by an integrated air-preheater manifold. Temperatures were plotted versus Ua with minimum required inlet temperature and touch safe temp requirements as shown in Figure 3.2-2. Results show the slope of the temperature curves flatten out at higher temperatures (as expected) indicative of flexibility on the Ua for the process design with more predictable cathode inlet temperatures. This meant that the air was required to enter the radiant air preheater shell structure after an initial pre-heat through a heat exchanger in the base of the RPU. This is an acceptable outcome as exhaust gas stream exiting from the catalytic air-preheater manifold needed to be cooled prior to exiting the RPU to allow for lower-cost process instrumentation, valves, etc. to handle this gas exiting the plant. Results also showed that insulation were required to meet touch safe temperature requirements and allow a larger portion of the stack heat loss to be recovered by the cathode

stream. Results also show that ~3kW of heat duty was required by the oxidizer manifold for '2nd stage' heating.

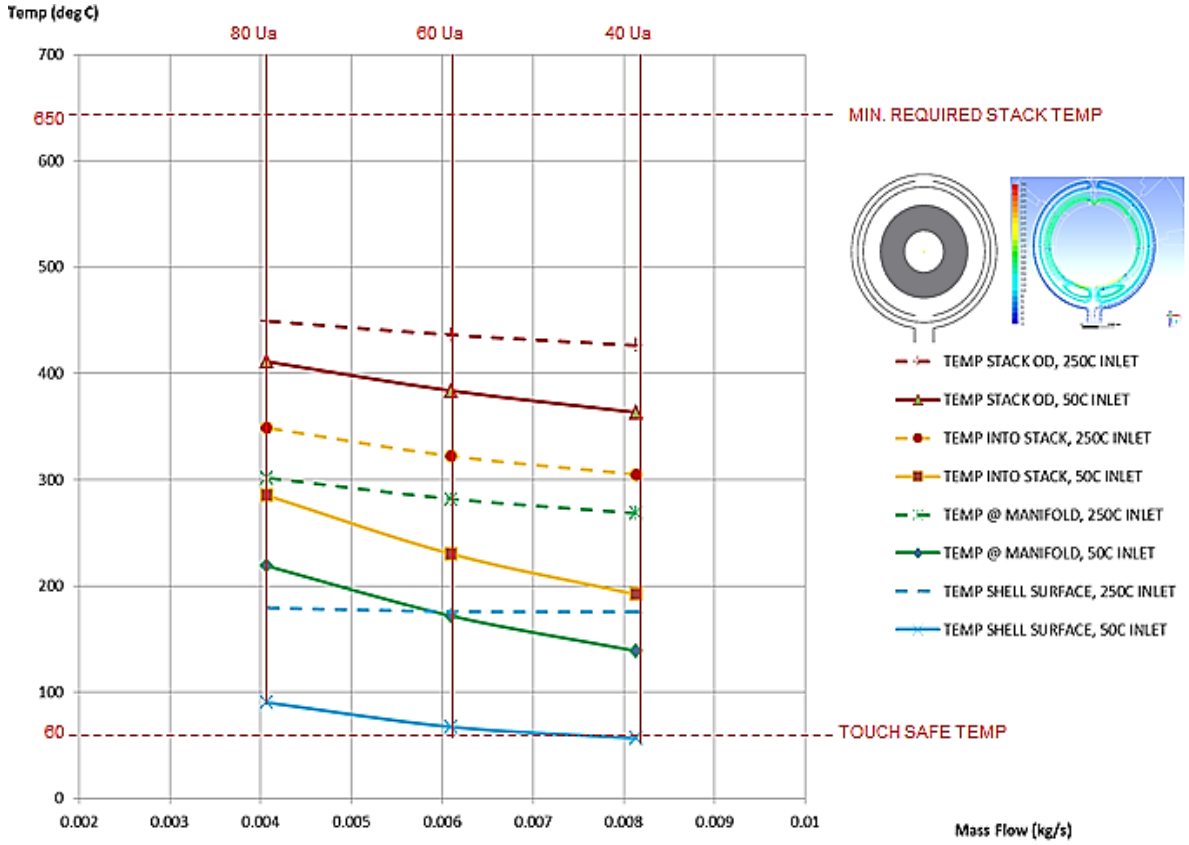

Figure 3.2-2 Radiant Air Preheater Concept

Additional CFD was conducted to illustrate the effects of varying the number of shell walls to radiate through. The more walls, the more passages exist, increasing surface area to collect thermal energy through convection. The results appear to follow the same phenomena regardless of number of shells and that there can be a point of diminishing returns due to thermal resets established every time the air has to flow around a corner, 180 degrees, to the next inward shell. This can be seen in the heat transfer coefficients that are mapped along the surfaces (Figure 3.2-3) of two of the inner shell walls. Here, the image on the left shows the 'heat-transfer coefficient' approaching 15 W/m^2K just before it turns and hits the 3rd pass. The image on the right shows the 'heat-transfer coefficient' approaching $25W/m^2K$ just before it turns and hits where external oxidizer manifold would reside. With each reset, the heat transfer coefficient restarts at close to 0 W/m^2K beginning its journey towards thermally fully developed flow. Though it is noted that the heat transfer coefficient develops to a higher value with each passage it gets closer to the stack suggesting that perhaps only a few shell walls are worthy of construction for this design configuration.

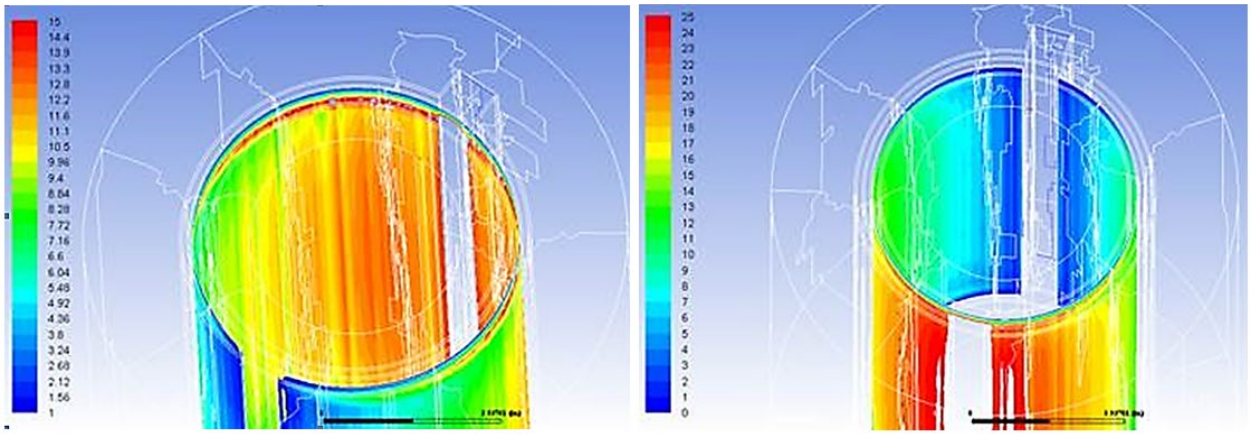

Figure 3.2-3 Heat Transfer Coefficient Reset Phenomena

CFD modeling was completed primarily on the design of the radiant air-preheater shells of the Repeatable Power Unit (RPU). Most critical was determining how much energy could be recuperated from the ISC and integrated cathode out / oxidizer manifolds into the cathode air inlet stream prior to entering the ISC. The intention is that the RPU shells act as radiation barriers between the ISC and the environment outside of the RPU insulation. Considering the relatively high temperatures of the ISC, a small temperature differential between the ISC outside diameter and the RPUs most inner shell resulted in significant amount of cooling the ISC. For prior SOFC system designs, a measurable amount of this heat was lost through the insulation and structural steel of the stack module vessel/enclosure walls to the environment without recuperating for use in system process streams. For the RPU design, air enters the insulated most outer shell (Figure 3.2-4) and captures heat through convection as it continues radially inward through the inner shells towards the ISC. One final superheat occurs when the air exits the inner shells and impinges along the cathode out/oxidizer manifold prior to entering the cells of the ISC. There is an even greater potential for superheating along this manifold if anode exhaust oxidizing capability is integrated within the manifold. The more energy transferred to this cathode air prior to entering the ISC, the lower the temperature allowance can be of the cooler air entering the most outer shell of the RPU, lowering the heat duty required of any upstream heat exchanger. This lower duty allows for a smaller heat exchanger and that more heat is available to be utilized for reforming and superheating of the anode in gas stream.

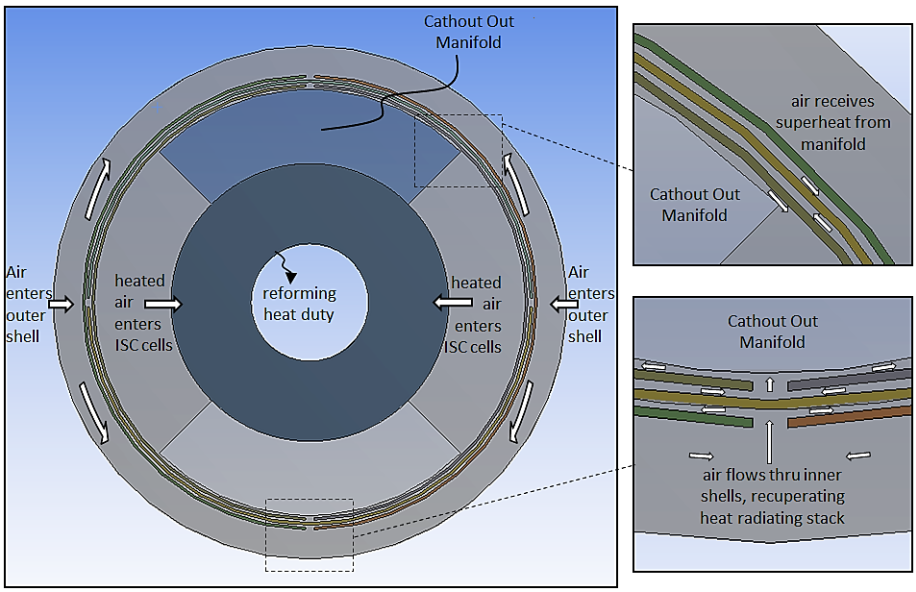

Figure 3.2-4 Air Recuperating Heat – General Arrangement

A CFD study was conducted to determine: 1) the minimum temperature required of the cooler cathode in air into the outer shell; and 2) how much heat duty could be provided from the cathode out manifold without assuming the anode exhaust oxidizing capability has been incorporated. It was anticipated that the development stack builds would utilize all integrated elements, except for oxidation of anode exhaust within the cathode out manifold. It should be noted that once this feature is integrated, that temperature requirements of the air entering the RPU outer shell should decrease significantly; again allowing more energy from ISC exhaust gases to be utilized for other process functions.

For the initial design with no integrated oxidizer, CFD results (Figure 3.2-5) showed air temperatures greater than 400°C are required at the outer shell of the RPU. For the initial round of development stack testing, this heat was to be provided by an air preheater or heat exchanger tied into the ISC exhaust gas stream. The recuperating capabilities from the results showed that almost 70% of the heat loss from the stack, not including the ISC exhaust gas streams, can be recuperated from the radiant air preheater shells and cathode manifold. The remaining heat lost is split amongst fuel reforming and heating of anode in gas as well as a portion lost to the environment through the insulation of the outer shell. The manifold is only providing 20% of this recuperative air pre-heating. Thus, there is much greater potential for that superheat duty of the cathode-out manifold once anode exhaust oxidizing capability is integrated into this. Results of the analyses showed maximum on-cell temperatures differentials that exceeded expectations.

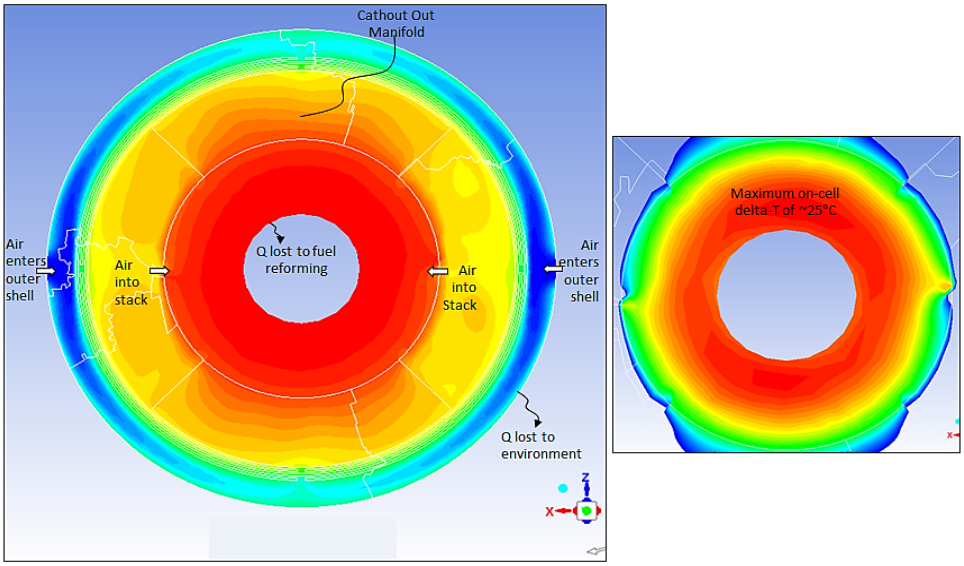

Figure 3.2-5 Air Recuperating Heat – General Arrangement.

The CFD results above focused on determining a baseline temperature at which the cathode air supply must enter the radiant recuperating shells to then interact with the cathode manifold, followed by entering the stack at a higher than a minimum allowable temperature. This baseline represented a non-oxidizing cathode manifold whereby anode and cathode exhaust streams would not mix and combust until further downstream away from the physical space of the stack, albeit still within the repeatable power unit (RPU). The greater potential for reducing the air temperature entering the recuperating shells can be achieved by adding oxidizing capability to the cathode exhaust manifolds. The more energy transferred to this cathode air prior to entering the stack, the lower the temperature allowance for the cooler air entering the most outer shell of the RPU, lowering the heat duty required of any upstream heat exchanger. This lower duty allows for a smaller heat exchanger and that more heat is available to be utilized for reforming and superheating of the anode in gas stream.

The heat duty at the oxidant manifold is the most critical factor to lowering the allowable cathode inlet temperature. The more thermal energy that can be harnessed from the exhaust gas the lower the inlet temperature of air can be upon entering the recuperating shells. This has a significant impact on the cost of upstream plumbing, instruments, and valves – all significant cost contributors.

A simplified model was used for initial analysis with full scale height channels representing the combustion exhaust gas stream and the cathode in air stream in a counterflow arrangement (Figure 3.2-6). Both heat exchange without oxidizing and with oxidizing were modeled while varying the air utilization (Ua) – thus, varying the mass flow rates. The fuel utilization (Uf) was held constant since the anticipated operating range was much smaller than the range of the Ua. The air temperature into the recuperative shells was varied until an adequate stack cathode-in temperature was reached. Gas stream compositions and estimated combustion stream bulk temperatures were estimated using ChemCad process simulation modeling results. Hence, the bulk temperature of the combustion stream for 80% Ua is going to be much hotter than the combustion stream for the 40% Ua case. Here, the mass flow of the supply air is much lower which reduces the stack cooling capacity of the cathode-in stream.

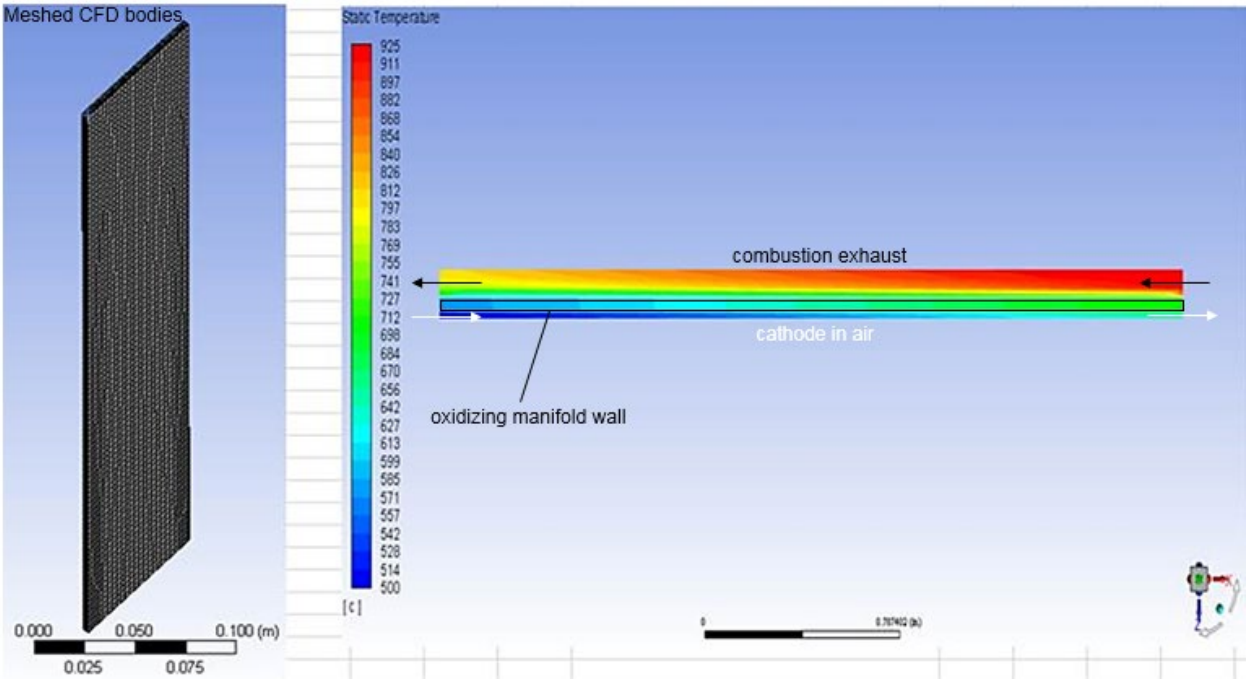

Figure 3.2-6 Results of dP CFD Study: Reduced Number of Process Connections

Output performance measures included dP of air at manifold, temperature of air at manifold, temperature of combustion exhaust outlet, manifold heat duty, temperature of air into the shells, and final exhaust temperature. The temperature of the air at the manifold establishes a requirement for the design of any upstream plumbing and heating features within the physical space of the CSA stack. This includes, but not limited to, final geometry configuration of the recuperative shells, and CSA / RPU insulation. The temperature of the air into the shells, along the same logic, establishes a requirement for the design of any upstream plumbing and heating features outside of the physical space of the CSA stack, but within the physical space of the RPU. This includes, but not limited to, heat exchangers for both air and anode gas supplied from the system blowers as well as temperature ratings of instrument and valves.

The manifold heat duty illustrates how significant an impact that the addition of oxidation capability can have on system and upstream pre-heating design. The final exhaust temperature establishes, along with mass flow, how much heat duty would be left if first using the combustion gas exiting the manifolds to pre-heat air supplied by the blower. This remaining capacity can be used for heating the anode-in gas, reforming, or other critical functional needs. Results are summarized below (Table 3.2-1) and show how significant of an impact the oxidizer can have on the system. For example, at 80% Ua, adding oxidizing capability satisfies almost all of the heat duty required to pre-heat the air from the system blower – leaving significant heat capacity for anode-in gas and/or reforming. This is not the case without oxidizing capability. Here, the need for additional means of pre-heating air outside of the stack physical space was required; adding a heat exchanger. Neither show capability to keep the end plate temperature high enough to limit heat loss at ends of the stack. However, this can be addressed by increasing the temperature of the air entering the recuperative shells. The 40% and 60% oxidizing cases show that the combustion exhaust temperatures would be high enough for the end plates and still have a significant capacity remaining to pre-heat the blower air and provide some additional heat

exchange capabilities, i.e., heating the fuel from the anode blower. Pressure drop results appear to be reasonable for the geometries chosen for this study.

Table 3.2-1 Summary of the Effects on Integrating Oxidizing Capability in Manifold

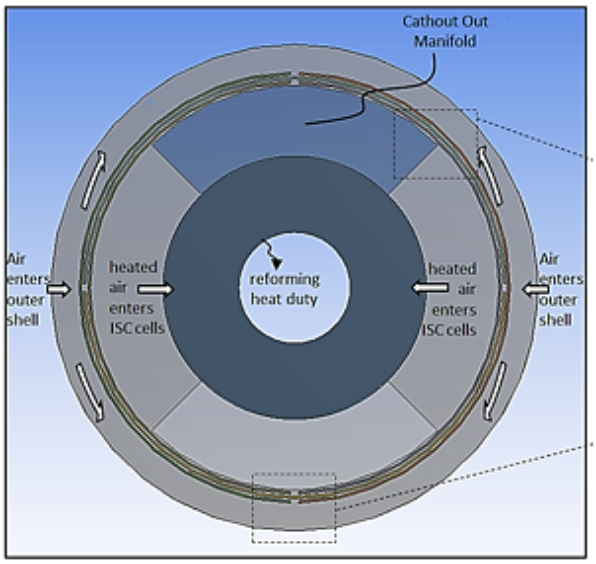

		WITHOUT OXIDIZING		
Uf		85	85	85
Ua		40	60	80
dP, air across manifold	IWC	2.93	1.95	1.44
T, air at manifold	C	600	575	550
T, combust. exhaust out	C	654	652	649
Manifold Heat Duty	W	1838	1747	1685
T, air into shells	C	506	437	365
T, combust exhaust final	C	173	225	281

		WITH OXIDIZING		
Uf		85	85	85
Ua		40	60	80
dP, air across manifold	IWC	2.86	1.76	1.16
T, air at manifold	C	500	325	60
T, combust. exhaust out	C	774	734	640
Manifold Heat Duty	W	5314	7315	9570
T, air into shells	C	450	300	50
T, combust exhaust final	C	379	517	640

The temperature of the combustion exhaust exiting the manifold controls the heat loss at the end plates of the stack. It is critical to keep the free and fixed ends of the stacks sufficiently hot to limit the impact of heat loss on flow distribution and electrochemical performance. From prior testing and CFD modeling experience, the last few cells at the ends of the longer (higher cell count) stacks receive less than average amount of supply gases – with significant performance impact, particularly when this distribution effects anode gas. This is not so much a geometry / fluid mechanic driven phenomena as it is from that of heat loss. Analysis has shown that the temperature of the end plates significantly effects the properties of the gas; which is especially vulnerable while in the laminar flow regime. There is no heat being generated in the end plates, as there is within the cells, and the end plates act as highly thermally conductive heat capacitors. Properly insulating the ends of the stack is part of the solution. An additional approach is to incorporate flow channels within the end plates and flush the hot exhaust gases through end plates prior to exiting the black box of the stack. This greatly reduces the temperature difference and, hence, the heat transfer rate. The results from this CFD study (Table 3.2-1) show whether the outlet exhaust temperature was sufficient enough to maintain good thermal distribution at the ends of the stack; hence, whether the designated air utilization is operable.

The baseline design of the stack has four connections at the bottom – one for anode supply, one for anode exhaust, and two for cathode exhaust. Cathode air does not need a connection directly to the stack. It is injected from the region flush with the outside of the stack. Reducing the direct connections to the stack from four to three reduces the probability of failure by 25%. In order to accomplish this, the two exhaust streams of the cathode gas (and oxidized anode gas) would flow into and mix within the fixed end plate prior to exiting through one outlet instead of two. The challenge with this that a much larger process connection is required with limited space to locate it; while keeping flow balanced for the gas entering from the manifolds. This is weighed against

limiting the pressure drop through this outlet for twice the flow rate. A CFD study was completed to evaluate the effects of the diameter and entrance / exit features on the pressure drop (dP) through the end plate outlet. These results were compared to the baseline CSA end plate design with the goal being to keep the total dP no more than that of the baseline design. Initial results from CFD showed too much choking of the flow at the outlet of the new design with 3 IWC dP just through that hole. The baseline design showed only 2 IWC total through the end plate. After some modifications to the entrance / exit features and an increase in hole diameter, the analysis was run again and showed only 1.83 IWC; 1.33 IWC through the outlet hole itself (Figure 3.2-7). The results meet the intended goal of reducing the number of process connections without exceeding the dP of the baseline design.

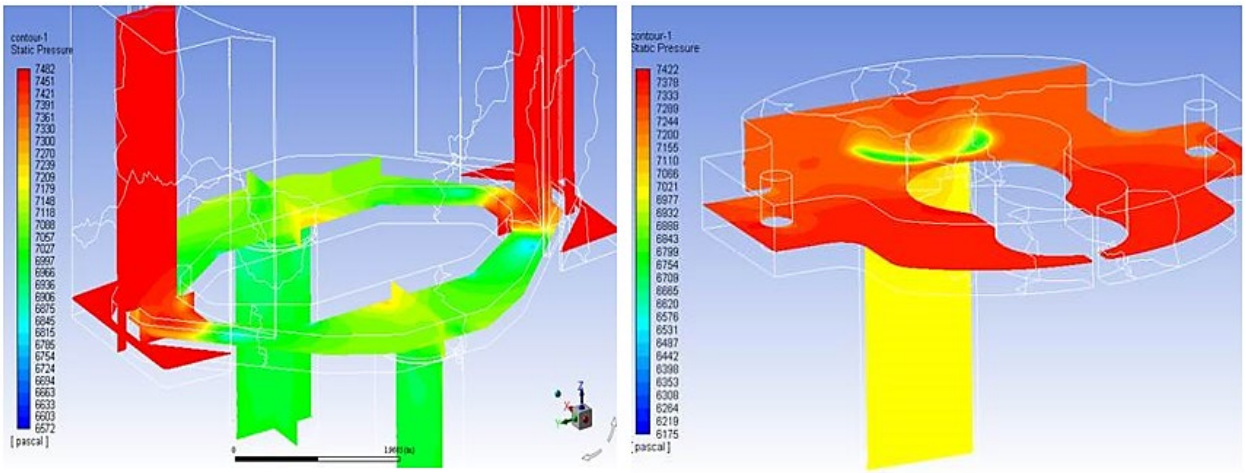

Figure 3.2-7 CFD Study: Effect of Reduced Number of Connections on dP

The CFD and FEA results above focused primarily on oxidizing heat exchange surface, oxidizing manifold, and the bottom end plate. Most of this was CFD work to demonstrate the effects of integrating oxidizing capability into the cathode out manifold. A simplified CFD model focused on a local region at the heat exchange surface where the cathode-in and oxidized anode-exhaust gas meet. Both oxidizing and non-oxidizing scenarios were analyzed to validate the efficacy of adding oxidizing capability before moving to a detailed model. The detailed model included recuperative radiant shells, bulk stack thermals, and process stream manifold within the stack. Results showed how significant on an impact the oxidizer can have at the system level where 80% air utilization satisfies almost all of the heat duty required to pre-heat the supply air; leaving significant thermal capacity to heat and reform anode-in gas. Analysis of the bottom end plate focused on pressure drop performance using CFD - for exhaust, anode recycle, and anode in streams – to validate reduction of process connections to improve reliability.

Subsequently the efforts were focused primarily on the fluid mechanics within the oxidizing manifold, distribution of flow within the end plates, and structural analysis of the top and bottom end plates. The end plates were the critical clamping members to which compression was applied to the fuel cells within the stack. Here, both stiffness and creep strength are critical. If there is too much deflection under load, the amount of surface the end cells are under contact would have been reduced resulting in significant power losses and increased on-cell temperatures. Stresses inducing a high enough creep rate would reduce the bulk load compressing the stack which could open up cross leaks of process gases and also reduce amount of surface area in contact between

the components making up the SOFC stack (i.e. – interconnects, cells, contact paste, mesh contacts layers). The effect would be lower air and fuel utilizations, localized hot spots due to combustion, increased on-cell temperatures, and reduced power output. The stack design utilizes tie rods (Figure 3.2-8) as part of a compression system when installing fastening hardware. One end of the tie rod is attached to the bottom end plate while other end is connected to a bushing via the fastening hardware. During the installation of the hardware, the bottom and top end plate are pulled closer to one another – both deflecting towards the cells between them.

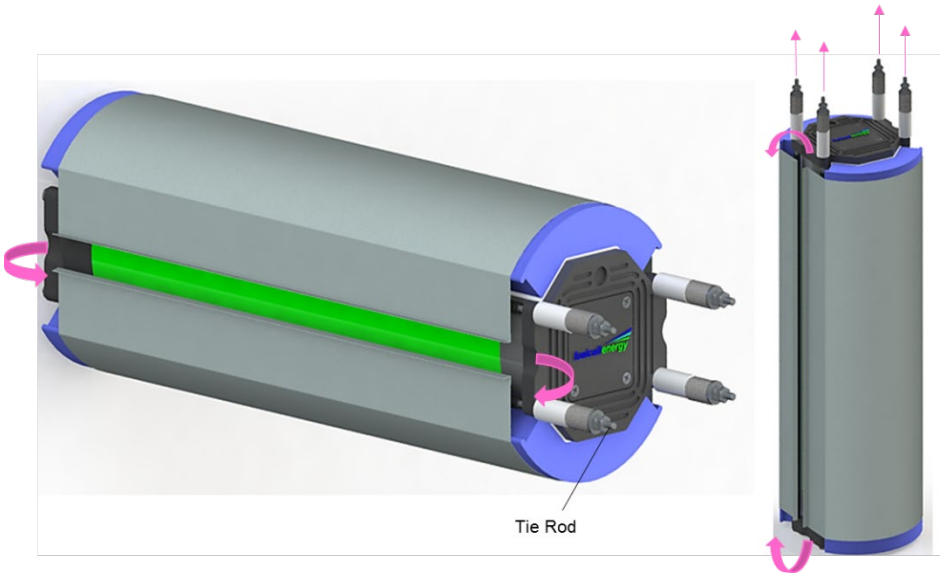

Figure 3.2-8 Deflection from Tie Rod Compression System

An FEA was performed on both end plates to evaluate any risks resulting from deflection or stresses under creep. CAD models were manipulated within a FEA software package. Here, material grade was chosen with properties assigned at elevated temperature condition. Based on the maximum compression load to be applied during installation and use, a safety factor was applied, and the resulting pressure and force boundary conditions were applied to the CAD model along with appropriate constraints. These boundary conditions for the bottom end plate are illustrated below in Figure 3.2-9. The results (Figure 3.2-10) show very low acceptable deflections ($<4x10^{-5}$ in) and stresses well below the material yield strength. Resulting stresses were checked against those for rupture at 1000 hours and 1% creep in 10,000 hours and showed to be an acceptable level below these values.

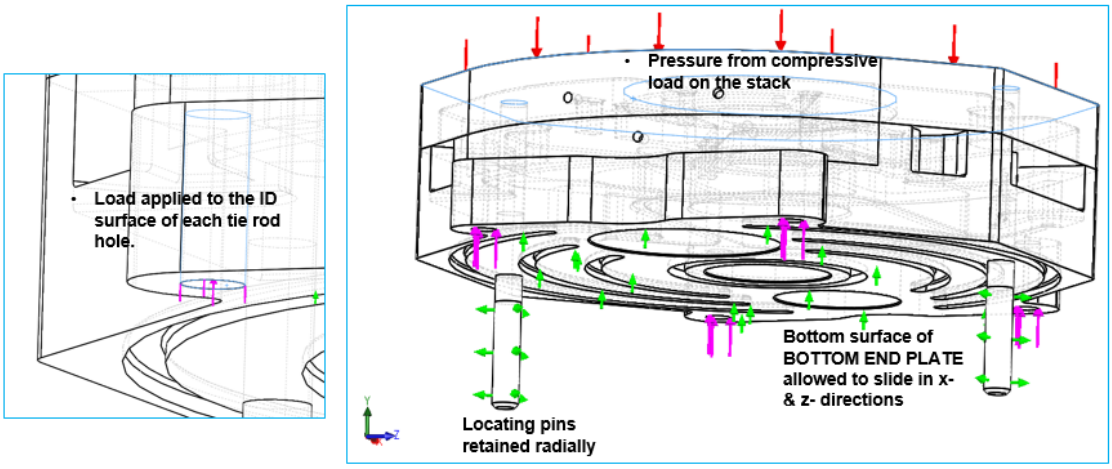

Figure 3.2-9 Boundary Conditions: Bottom End Plate

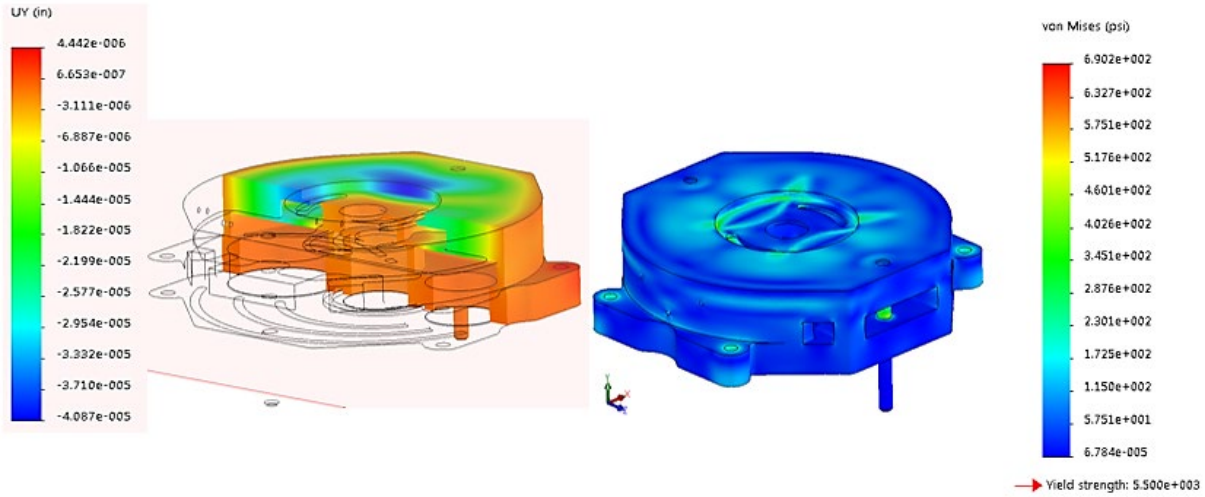

Figure 3.2-10 Deflection and von Mises Stress: Bottom End Plate

The same procedure was applied to the top end plate. The results (Figure 3.2-11) show very low acceptable deflections (<$2x10^{-5}$ in) and stresses well below the material yield strength. Resulting stresses were checked against those for rupture at 1000 hours and 1% creep in 10,000 hours and showed to be an acceptable level below these values.

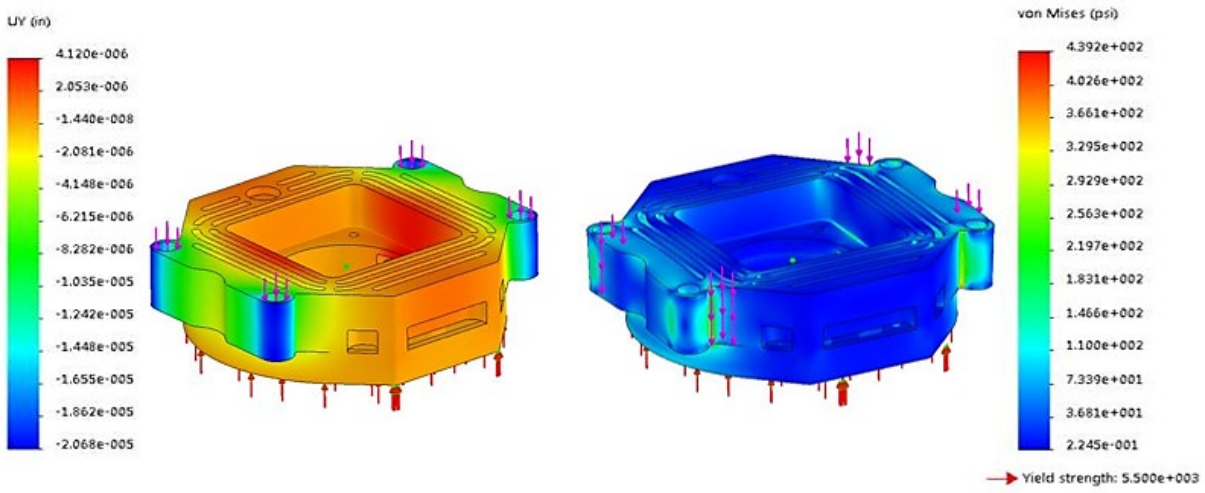

Figure 3.2-11 Deflection and von Mises Stress: Top End Plate

Cathode out and anode out gases immediately exit the thermodynamic envelope of the CSA stack hold valuable available energy (exergy) that would encounter losses through heat transfer to the environment through plumbing running from the stack to the BBOP. It's more efficient to utilize this available energy as close as possible to the outlet manifolding of the stack prior to flowing through exit plumbing. By exchanging this thermal energy with cooler gas streams approaching and entering the inlet manifolding of the stack, the temperatures of the inlet gas stream can be brought much closer to the stack temperature and the size of BOP heat exchangers can be reduced, or even eliminated. The outlet stream flow into the exit plumbing and out to the BOP at a much lower temperature which may not seem preferable. However, this gas stream has already provided an efficient heat exchange task prior to exiting, it has a much lower potential to lose available energy to the environment with the lower temperature, and it increases the likelihood of using lower temperature rated (lower cost) valves, instruments, and equipment for other plant purposes.

It's important that any of the fluid streams flowing through the end plates does not add significant increase to the pressure drop across the stack. There are system level improvements in the compact stack architecture which are driven from low pressure drops. The upper chamber of the bottom end plate through which anode recycle gas flows has been shown to have no measurable increase in pressure drop. More critical is the oxidized exhaust gas flowing from the manifold, through and out the bottom end plate. The mass flow of this gas stream is a higher than just the cathode out flow stream since anode out gas has been added to use in combustion. A CFD study was performed on a model of the bottom end plate to evaluate, quantitatively, the pressure drop and, qualitatively, the flow distribution of this oxidizer exhaust flow stream. The results of the study showed (Figure 3.2-12) the pressure drop through the bottom end plate was kept at the 2 IWC allocated as dictated by the currently tested compact stack architecture. Two openings were added to the oxidizer-end plate interface. Prior CFD studies showed sub-par flow distribution – or washing – of the end plate with one central opening. Follow-on studies showed (Figure 3.2-13) that keeping three windows at the interface maximizes the amount of cell contact area that would be washed with fresh hot oxidizer exhaust – in the same region as the anode recycle gas.

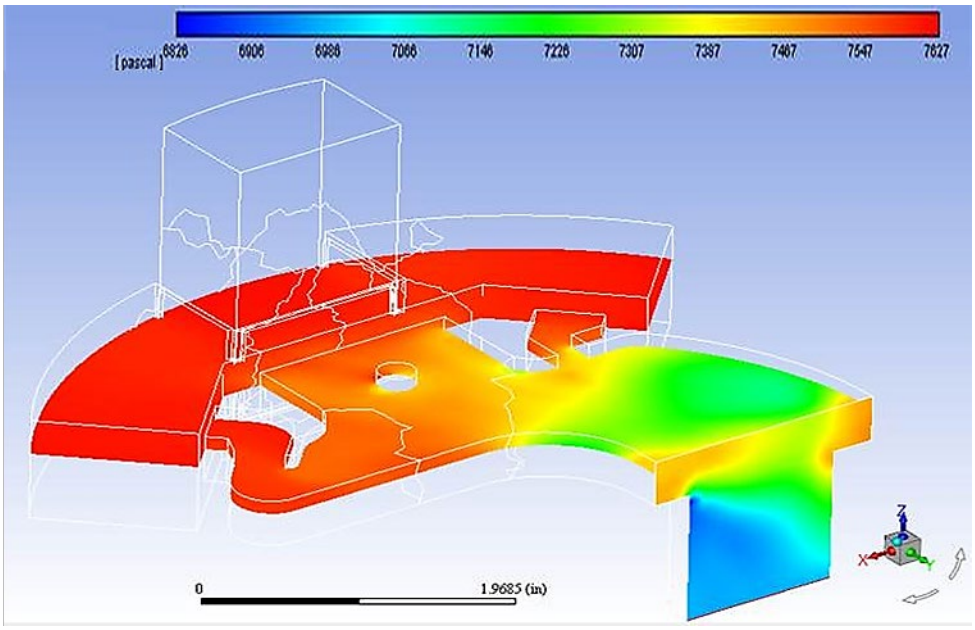

Figure 3.2-12 Pressure Distribution Results: Bottom End Plate

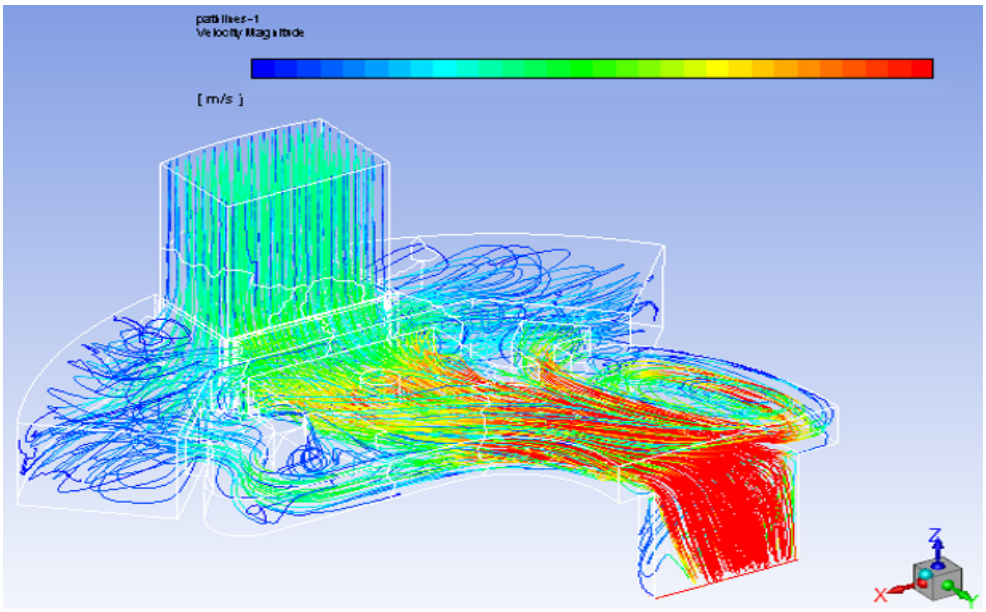

Figure 3.2-13 Flow Distribution Results: Bottom End Plate

Similar CFD studies were performed on the top end plate for the anode exhaust slip stream. The results showed (Figure 3.2-14) the pressure drop to be very low – less than 0.3 IWC – which results in no significant impact to the pressure drop across the entire stack. The pressure drop from anode-in to anode-out locations of the compact stack architecture showed this to be 3 IWC. This was anticipated as the flow rate of this stream roughly half that of the anode recycle stream – and much less than the oxidizer exhaust stream. The path lines of the flow stream generated by the CFD software (Figure 3.2-15) showed the anode exhaust to be evenly through the three manifold openings.

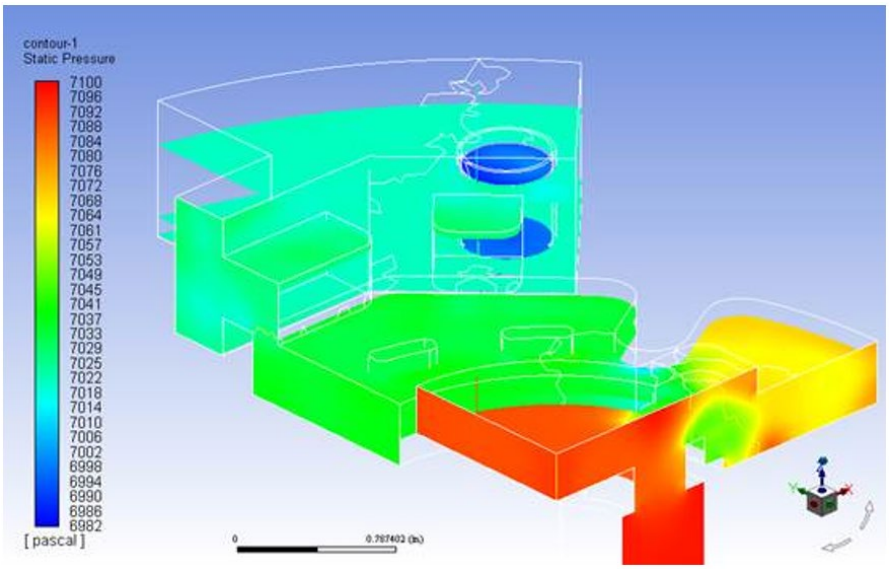

Figure 3.2-14 Pressure Distribution Results: Top End Plate

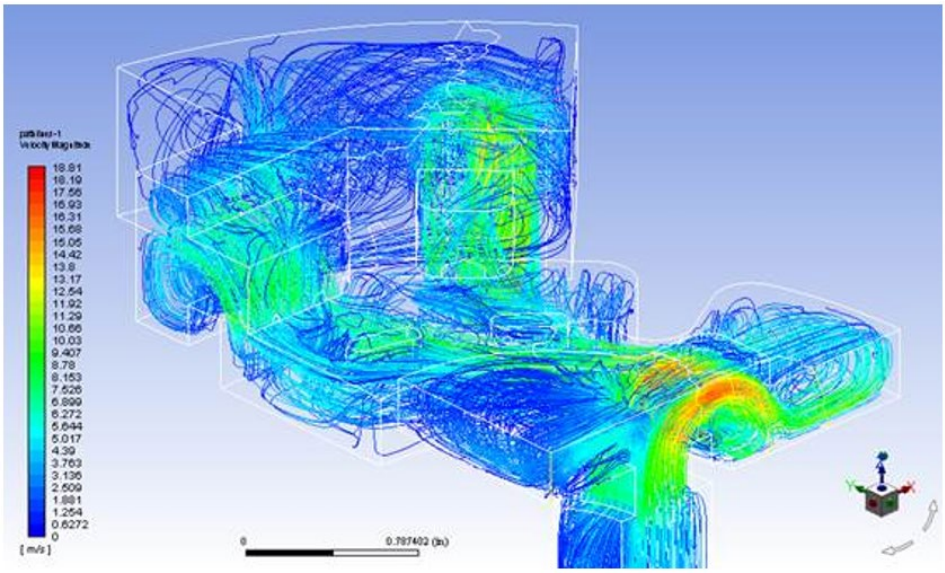

Figure 3.2-15 Flow Distribution Results: Top End Plate

There are a number of critical transformational design integrations that require a high level of instrumentation. These high level of instrumentation results in a significant number of penetrations in the insulation placed in close contact with the top end plate of the stack and, as a result, heat losses need to be mitigated as much as reasonably possible. Therefore, the thickness of the insulation improvements becomes significant. CFD simulations were used to assess just how thick this insulation should be. The top portion of the stack, perimeter containment vessel structure, simplified instrumentation hardware, and an insulation layout was modeled using CAD software. This was then meshed and imported into CFD software. Boundary conditions, including radiation properties and natural convection, were designated on the imported mesh, convergence criteria were established, and computational iterations were competed until convergence. Both heat loss from different regions of the vessel outer surface and temperature within the upper purgatory zone were assessed (Figure 3.2-16). The temperature within the upper purgatory zone was more critical for the materials of construction within the instrumentation. The upper insulation thickness was varied until the purgatory zone temperature was sufficiently lower than the maximum operating temperatures of the instrumentation and incremental changes in thickness no longer showed significant heat loss improvements.

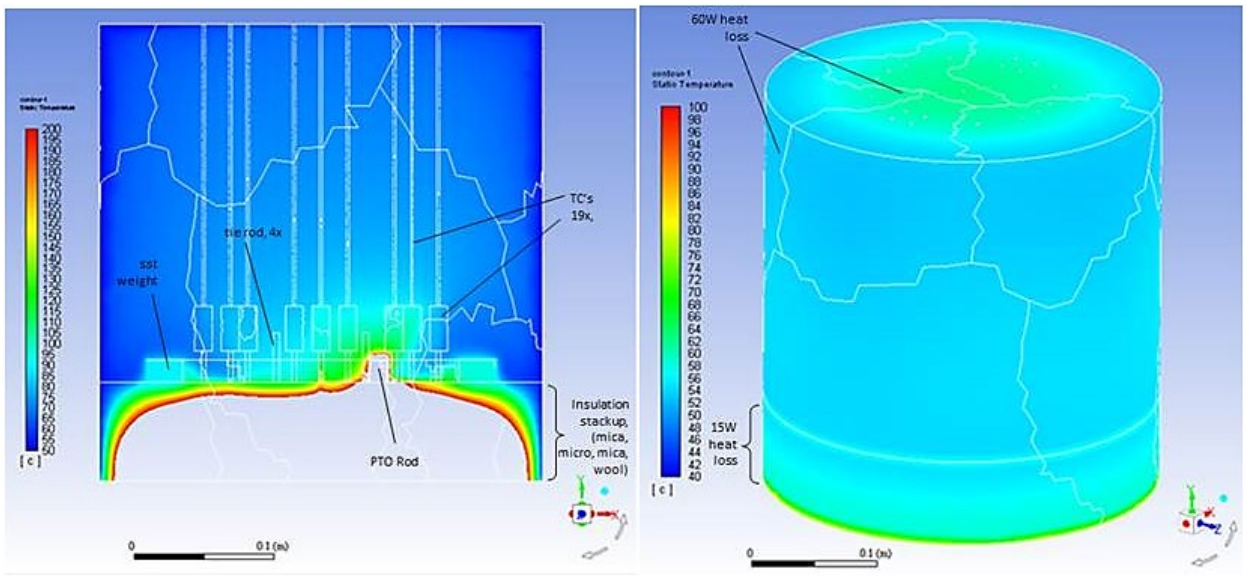

Figure 3.2-16 Temperature Plots with Calculated Heat Loss

3.3 Stack Manufacturing Process Development

Objective:

The goal was to develop robust, low-cost stack manufacturing processes that were easily scalable to high volumes.

Approach:

The Design for Manufacturing and Assembly (DFMA) approach was utilized throughout the stack design process to minimize the number of unit cell components. Manufacturing process equipment, tooling and fixtures were procured or fabricated to enable the manufacture, handling and assembly of new advanced cells, interconnect assemblies, seals and integrated stack assembly. Manufacturing process control methods were employed to ensure component and stack quality and high manufacturing yields. Additionally, process development and programming for the execution of the stack builds, firing and conditioning were completed.

Results & Discussion:

The multi-functional interconnect (IC) components for compact stack architecture (CSA) utilize a hydro-forming process to obtain repeatable components (Figure 3.3-1). This is a low-to-medium volume operation that is useful as a step towards higher volume operations while being a low cost tooling investment. Aside from limited manufacturing throughput, this process has some challenges obtaining forming depths needed to allow for greater reductions in pressure drops of the gas supplies (anode and cathode). A combination of high strains, strain rates, forming speeds and other factors can lead to cracks at or close to component feature radii. The efforts from the Innovative SOFC project pushed the formability limits as far as considered possible with this hydroforming process. A different metal forming operation was required to meet market-entry production volume targets and formed to achieve deeper forming depths that would provide the ability to lower the costs.

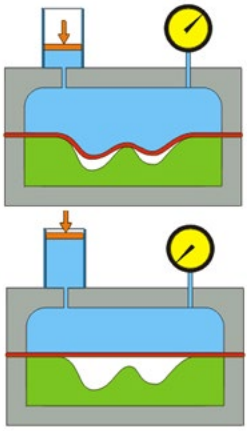

Figure 3.3-1 Forming Process of the Interconnect (IC)

High throughput forming manufacturing methods were explored. It was targeted to achieve 25% greater depth than with current forming process. Using Darchy-Weisbach equation ($\Delta P = f^*(L/D_H)^*\rho^*(V^2/2)$) to estimate the pressure drop (for Laminar flow, friction factor, f, is equal to $64/Re_D$), a 25% increase in the depth of the cathode flow channel would result in a 20%

decrease in pressure drop across the stack. Assuming the stack makes up only 50% of the plant resistance for the air blower, that results in a 10% decrease in blower power required.

A majority of the manufacturing processes anticipated for use are sufficiently matured methods utilized across a number of high-volume industries. Still, there were other manufacturing requirements of the concept that necessitate investigation throughout the duration of this project. These included: dealing of dissimilar materials for applications such as: dielectric joints that allow for disconnect during stack changeout; joint design of the anode bypass gas plumbed to the oxidizer manifold to prevent any leaking into the cathode in stream; and sealing the free end of the radiative touch-safe shell. Catalyst coating porous substrates was investigated as well.

The bulk of the stack manufacturing process development activities were conducted after design activities were completed. One development activity completed was in regard to fabrication of the oxidizer manifold structure (Figure 3.3-2). The oxidizer manifold is constructed of a ferritic stainless steel to match the coefficient of thermal expansion characteristics of the SOFC stack core – repeatable cell and metal components. The ferritic stainless metal group is good for use in high temperature applications where strength is not extremely critical, but corrosion resistance is important. Specific to SOFC applications chromium evaporation is critical and stainless by itself – even austenitic does not protect sufficiently against this. Liberated into the flow stream on the cathode side of the cell, this can deactivate the fuel cell cathode. The hot cathode-in stream flows up against and around the oxidizer manifold prior to entering the stack. Thus, it's important to protect those exposed surfaces with a coating. Aluminizing stainless is a proven method to do this and ferritics lend themselves better to the aluminum adhering and diffusing into the stainless.

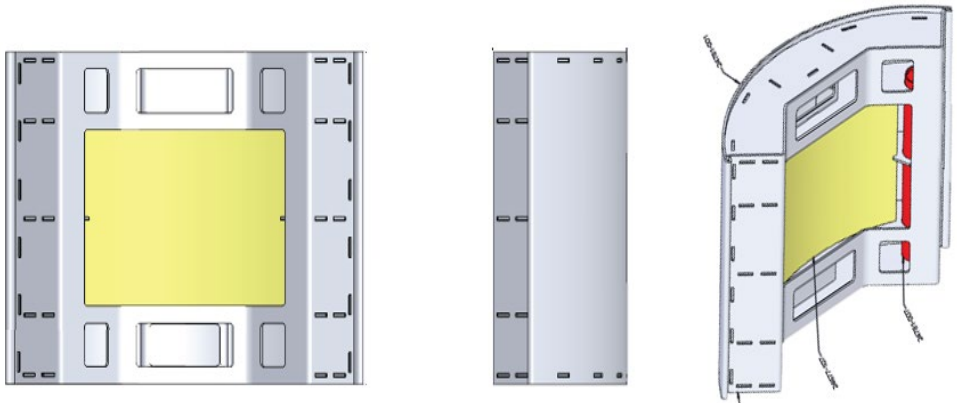

Figure 3.3-2 Oxidizer Manifold Structure

The fabrication strategy for the first oxidizer manifold units relied on welding of the ferritic stainless. This is a more rapid route to follow than the creating precision fixtures for brazing in a vacuum furnace. Brazing was also considered. The parts themselves are being designed in such a way that mostly accommodate brazing with a few minor adjustments potentially needed later on in the development path closer to production. Welding trials were required to isolate a suitable welding technique and weld joint design prior to ordering parts for the full-sized oxidizer manifold prototypes. Ferritic stainless is more challenging to work with than austenitic when welding. Some applications require: 1) installing a heat sink in close contact with the work piece so as to keep the weld zone from getting too hot; 2) and others where an external heat source to maintain minimal temperatures for a portion of time after the weld. Within the ferritic group, the trials focused on those stainless grades with better strength properties at elevated temperature and better weldability.

Coupons representing the most challenging weld joints anticipated for fabrication were designed and fabricated out of different grades and thicknesses of ferritic stainless. The various thicknesses were required to understand how much this plays a role in weldability. Also, the thinner the sheet can be the less the manifold would weight. An example of 0.024 inch thick grade 441 is shown in Figure 3.3-3a. One of the mating coupons allowed for multiple trials to compare welding methods where minor alterations or even sequence of weld operations is found to be important. The results of the trials helped specify the weld callouts in the prototype fabrication drawing (example in Figure 3.3-3b). Welding operations were performed, starting with the thicker coupons, using a number of operations (plug weld, fillet, fusion, etc.), order of operations and heat management techniques. Some of examples of the weldments throughout the trials are shown in Figure 3.3-4. Specimens were examined using optical microscopy for defects, heat distortion, and alignment of mating components. The results of the trial found a suitable welding method, order of welding operation, joint design, and welding thickness.

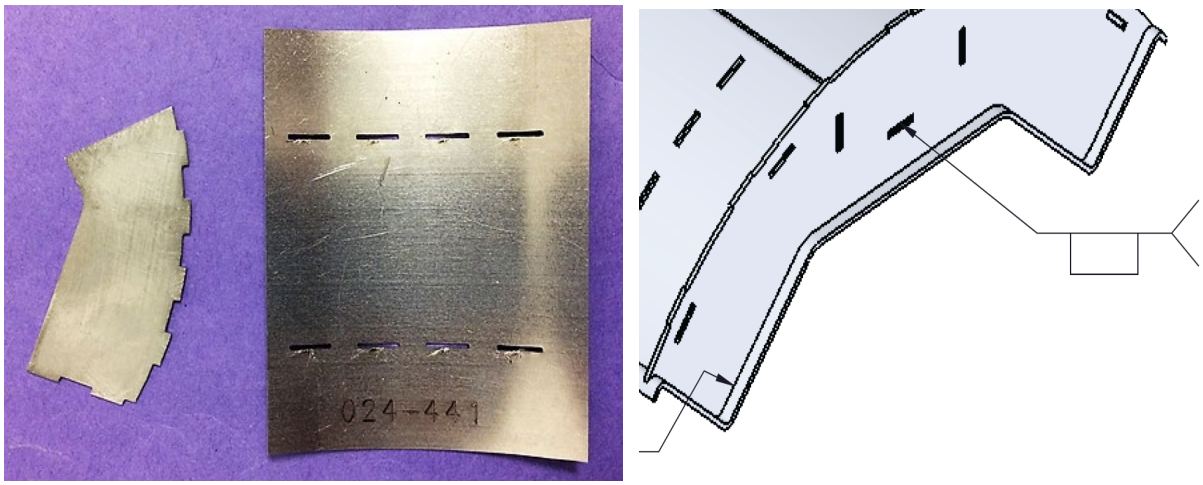

Figure 3.3-3 a) Fabricated Coupons b) Welding Callout Example

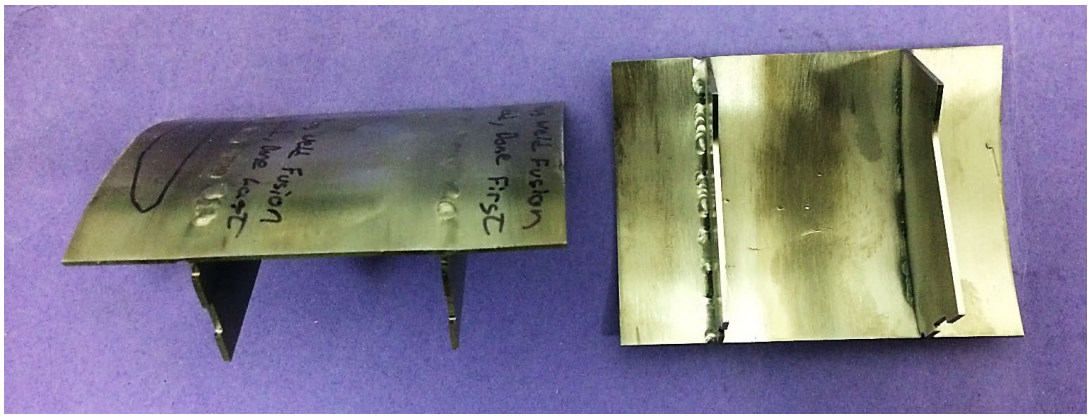

Figure 3.3-4 Weldment Examples from Ferritic Welding Trials

As an outcome, a suitable welding method, order of welding operation, joint design, and welding thickness were determined as input to the procurement of prototypes scaled for initial 45-cell sized stack tests. These prototypes were used to first evaluate superheat duty performance for cathode gas supply and then be assembled into a fully functional SOFC stack for performance testing.

A first article of the oxidizer was fabricated as shown in Figure 3.3-5. Design-for-manufacturing improvements were rolled into a revised design. To facilitate the attachment of the cover that housed oxidizing catalyst, a useful hem bending tool that was designed and built.

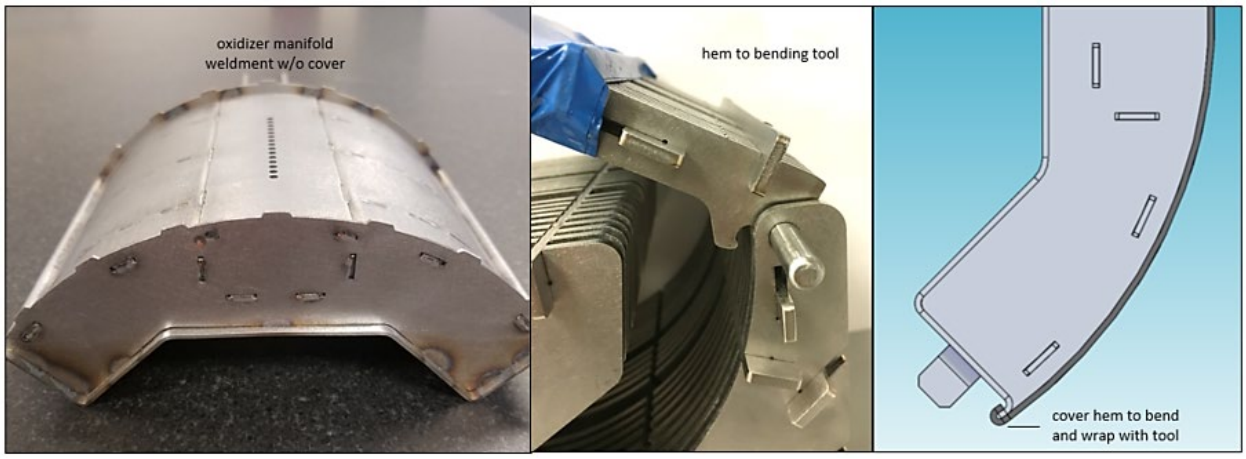

Figure 3.3-5 Fabrication of Oxidizer Manifold

The stack end plates were developed further to allow for the flow through of hot exhaust gases (both anode and oxidizer) as well as anode recycle. The strategy was to limit heat loss from the ends of the stack by keeping them flush with hot exhaust gases. Prior developmental CFD work for fuel cell stacks has showed that the temperature of the cells at the ends of the stack can be much cooler than the bulk of the stack, resulting in significant flow deviations from the bulk of the stack – even with reasonable insulation strategies. End plates are made of thermally conductive alloys that act as a heat sink. By thermally moderating these end plates with hot (>700°C) exhaust gases, it increases the distance from the end cells to where the thermal gradient of the insulation occurs – i.e. adding thermal resistance between the cells and the insulation as well as the heat sinking end plates. This should tighten up the flow distribution at the ends of the stack. FCE has worked to machine, braze and post-op these end plates. These end plates (Figure 3.3-6) were leak checked.

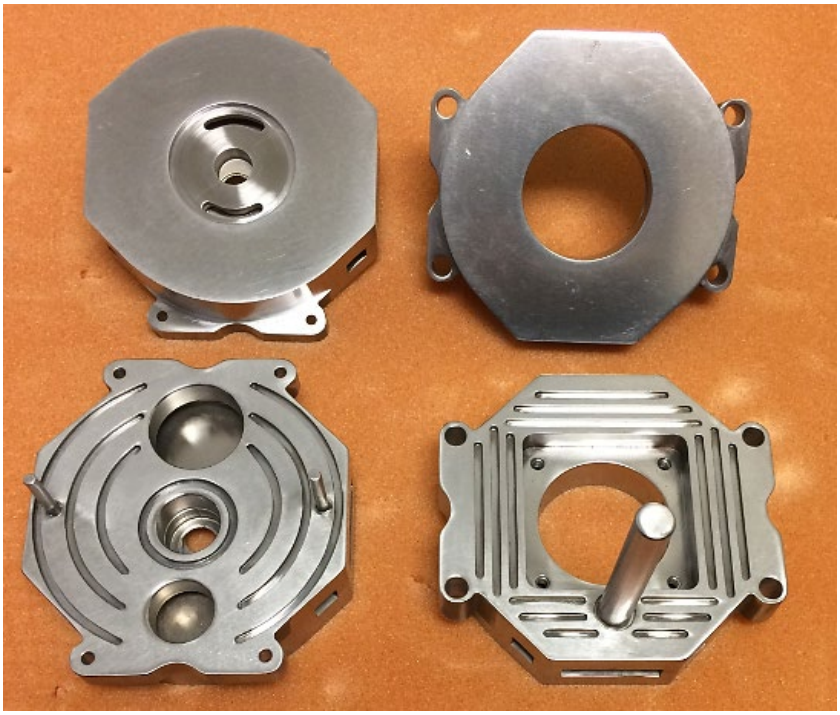

Figure 3.3-6 Flow-through End Plates

A few iterations of design development were completed on the oxidizer manifold retainment design. A transformational improvement for this was pursured to provide higher confidence in dielectric isolation of the manifolds from the stack. It takes advantage of a high strength compliant c-spring design (Figure 3.3-7) that would maintain spring force at higher operating temperatures for the duration of life of the stack. The bulk of the components are made from materials that match the coefficient of thermal expansion of the oxidizer manifolds, end plates, and SOFC stack core so that, in combination with the c-spring, tension is maintained on the straps as the thermal mass of the entire stack increases from room temperature to higher operating temperatures. Significantly sized air gaps are a beneficial end result of this design that significantly reduces the likelihood of a short and provides more confidence in compression being applied to the manifold seals to the stack. Final fit checks with end plates, manifolds, and mock stack (Figure 3.3-8) occurred prior to installation into the test stand. Engineering drawings specifications were completed. The mock stack allowed a number of important system integration elements and seals to be evaluated prior to use with a high-valued fully functional stack.

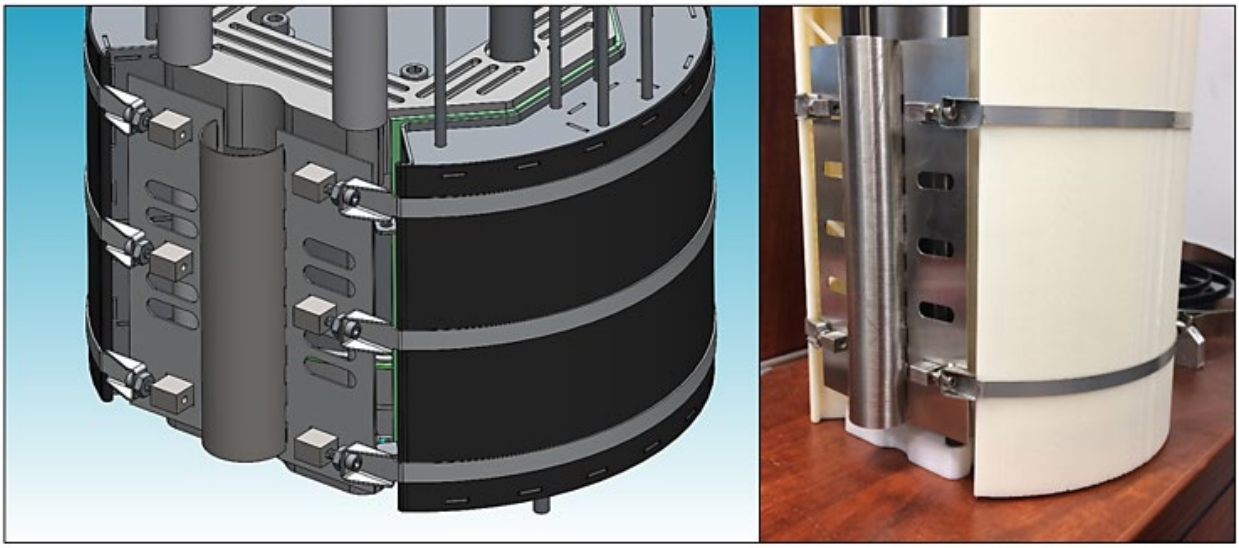

Figure 3.3-7 Manifold Retainment Straps

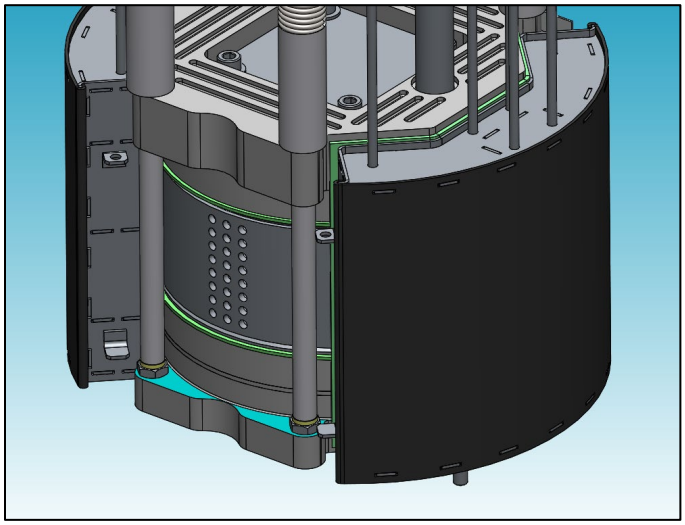

Figure 3.3-8 Transformational Stack Assembled w/ Mock Stack

The design of the integrated CSA stack features thin shells that wrap around the circumference of the assembled stack, end plates, oxidizer manifolds, and assembly straps. These are composed of an inner metal shell and an outer low conductive shell. The low conductance non-metal outer shell provides an insulating barrier for the metal shell; where the metal shell needs to be closely matched in thermal expansion with the stack. The outer shell is taller and provides a sealing slip plane to gaskets on either end to prevent cooler cathode air from short circuiting past the manifolds without getting preheated. For the initial process development efforts, different diameters were fabricated in order to evaluate best fit with the stack and between the inner and outer shells (Figure 3.3-9).

Figure 3.3-9 Various sizes of the inner and outer shells

A critical aspect to how the integrated CSA interfaces with the test stand, and eventually the modular SOFC plant sub-system, is the design of the process connections. These process connections dielectrically isolate the stack from the process connections, allowing for multiple stacks to be electrically connected into series-parallel arrays. The combined electrical potential of the series connections arrays provides a significant benefit, allowing for the removal for a DC-DC booster, a large piece of EBOP power conversion hardware. The connection sleeves are non-metallic, and seal with holes in the bottom end plate (and bellows tube stubs below them) upon initial heat up of the system.

This design was demonstrated at the component level earlier in the project with hi-pot testing across multiple thermal cycles. These process connections obtained sufficient sealing, through thermal expansion, well before the temperature is reached for fuel enable mode of operation. Figure 3.3-10 shows these fabricated components fitted onto tube stubs of bellows. The sleeves would be fabricated at high volumes as a low-cost, consumable component for when a stack is in need of replacement. Figure 3.3-11 shows the interface plate that these connections would fit through and into the holes of the stack end plate. Electrical insulation was placed between the stack and this plate to prevent shorting.

Figure 3.3-10 Dielectric process connections

Figure 3.3-11 interface plate

There are a number of instances where gaskets are required including: stack assembly sealing, stack interface sealing with the containment vessel, and sealing of the components of the containment vessel. The materials range in application from cold to hot connections. Materials include ceramic paper, alumina gaskets, and silicone. Regardless of application and specific material, all require the use of steel rule die for fabrication. These dies have been fabricated to be incorporated in an automated in-house press. A collection of these dies is shown in Figure 3.3-12.

Figure 3.3-12 Dies for Gasket Fabrication

A number of mica components were required to be fabricated for use within the stack and the guts of the containment vessel. Several of these components are shown below in Figure 3.3-13.

Figure 3.3-13 Fabricated Mica Components

4 Technology Stacks Validation Tests

The objective of this task was to validate the advanced cell architectures and stack design features by fabricating and testing technology stacks. Validation testing of a 2-5 kW deliverable stack was planned for ≥1000 hours to demonstrate the performance and stability improvements of the integrated stack design.

4.1 Technology Stacks Fabrication and Testing

Objective:

The objective was to conduct fuel cell stack fabrication, assembly and testing to validate the stack architecture and to refine and optimize design parameters based on electrochemical and thermal performance.

Approach:

The activities included fabrication and testing of reduced cell-count technology stacks (250 W to 500 W) to study and prove-out the cell/stack design features and manufacturing processes developed in design activities. Post-test analysis were conducted along with analysis of results from electrochemical diagnostic tests. Design characteristics which display promising test results were further tested and incorporated into the new stack architecture after both steady-state and transient validation tests.

Results & Discussion:

The test stand to be used to carry out various prototype mock stack and fuel cell functional tests were upgraded. A mock stack is one that has no real fuel cells assembled but allow the testing of critical features such as the oxidizing manifold and thermally activated dielectric radial seals. The first mock stack test was planned to evaluate the super heat performance of the oxidizer manifold. Here, the air supply temperature was varied and the cathode-in temperature was measured over a range of air utilization targets. Cartridge heaters were embedded in the mock stack structure to heat the cathode out and anode out gas streams to realistic operating temperatures. Various catalyst coated flow media were tested within the oxidizer manifold. A test vessel enclosure was designed as part of the upgrades that allowed the test stand to mimic operation of the stack. The large furnace can be turned off during this use while a smaller drop-in clamshell furnace is placed under the base of the stack to maintain the capability of heating the supply gas streams. A concept of this test stand layout with the vessel enclosure is illustrated in Figure 4.1-1.

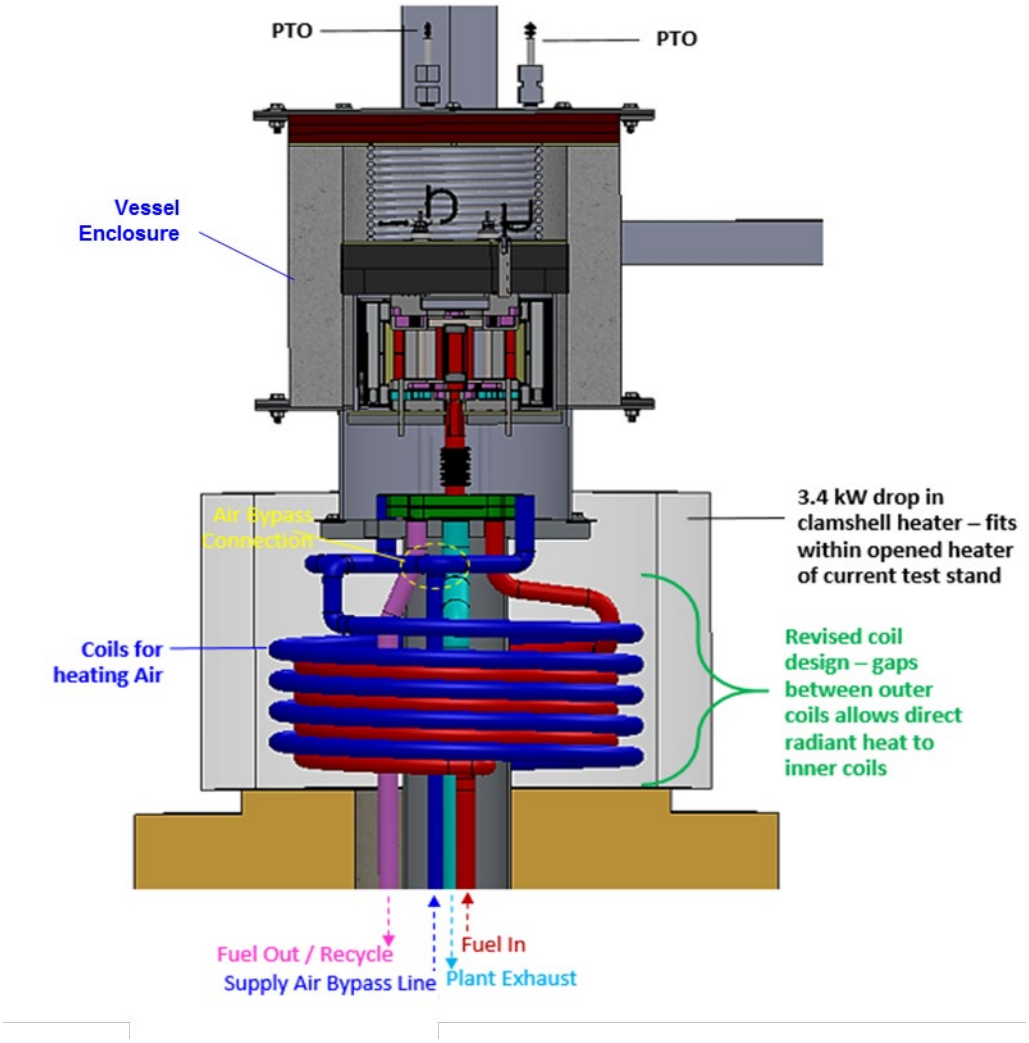

Figure 4.1-1 Upgraded Test Stand with Vessel Enclosure and Drop-in Furnace

The first mock stack test was to evaluate the superheat performance of the oxidizer manifold. Here, the air supply temperature was varied and the cathode-in temperature was measured over a range of air utilization targets. In order to vary the air supply temperature, a stream line branch was added to the air supply line to bypass (Figure 4.1-2) the lower clamshell furnace that is used to heat the anode-in gas. The bypass line has its own pre-heater located in the lower cabinet of the test stand.

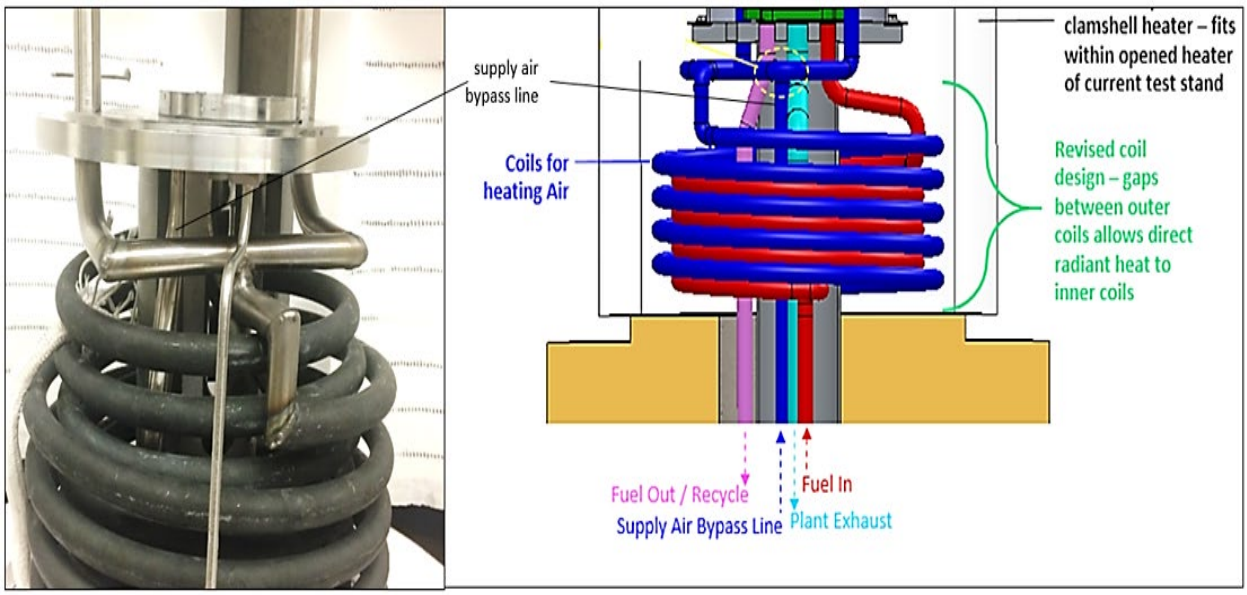

Figure 4.1-2 Test Stand with Supply Air Bypass Line Added

The first mock stack test planned was to evaluate the heat exchange performance of the oxidizer manifold. Prior to this testing, it was necessary to perform a series of system checkouts – operational, leak, etc. The first step was to safely run the test stand with a cross-over plate in place of a stack. The purpose of the cross-over plate was to contain and direct anode (fuel) flow in order to heat up the main furnace from ambient up to operating temperature with both air and fuel on the cathode and anode sides of the test stand, respectively. This allowed for leak checks to be completed prior to operating a stack; a critical safety measure. Preparation for the cross-over plate initially involved polishing the surfaces to a mirror finish in order for the C-Ring seals to properly seal the bottom flange plate to the manifold plate. Cross-over plate enabled testing of the test stand and safety system, solenoid valves, mass flow controllers and hood exhaust system (Figure 4.1-3). A hydrogen specific combustible gas detector was installed and interlocked into the fuel supply at the top of test stand at the hood duct entrance for further safety measures.

The final commissioning activity was the testing of a 45-cell CSA 81 cm² active area solid oxide stack. The voltage leads with alumina sleeves were potted into the flange plate after installation of the C-Ring seals. The CSA stack was then lowered into place. Lastly, the in-stack cathode inlet thermocouples were added and the CSA enclosure cap was bolted on to the flange plate. Initially the enclosure had to be heated to 110°C and held for several hours so that the enclosure cap gasket could properly seat; then the final heat up to operating temperature began. The CSA stack was heated up to 700°C and was subjected to various utilization and polarization curves at varying levels of fuel and oxidant utilization. Performance closely matched that when operated in factory acceptance tests. No anomalies were observed in the test stand and considered a success as reproducible operation. The fuel cell mode operation was completed with use of hydrogen. In order to complete oxidizer testing, as well as studying the effects of stack performance with all transformational enhancements, the use of methane was required.. This also allowed the control of a small amount of methane into simulated anode exhaust gas when first testing the integrated oxidizer manifold with use of a mock stack.

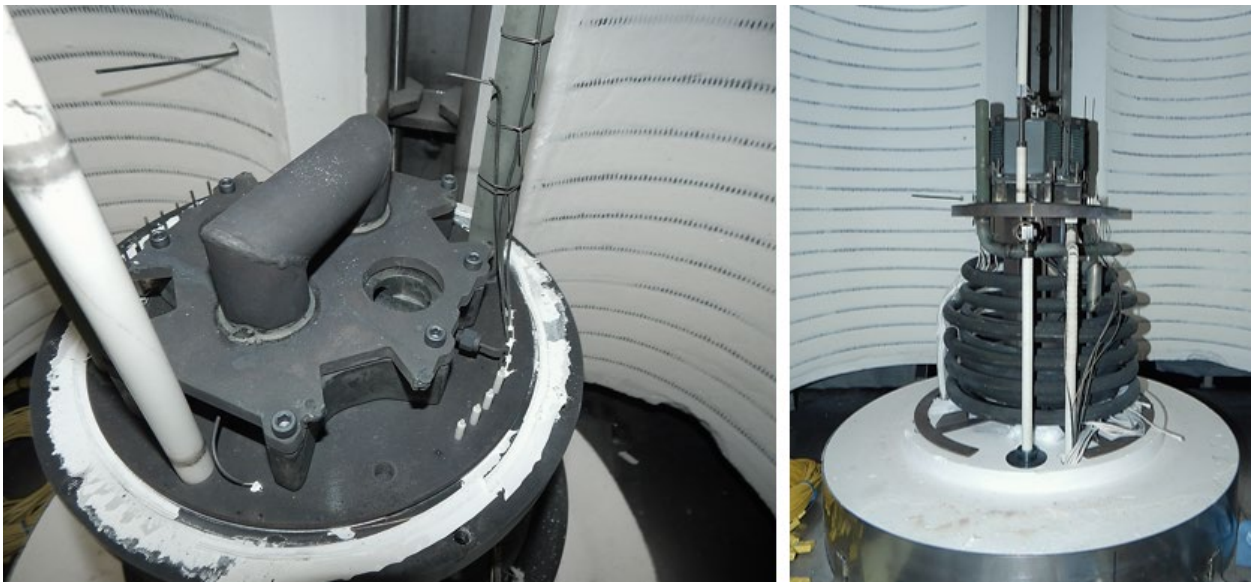

Figure 4.1-3 Test Stand Checkout with Cross-Over Plate and CSA Stack

Initial CSA stack development efforts used a large clamshell furnace to simulate temperatures in proximity of the stack that would be representative of that resulting from use of an insulated vessel – which is eventually how it would be used as a product. A novel stack containment vessel was developed to allow for test of the integrated stack in a more realistic operating environment. The design of this vessel allowed for use of a more compact clam shell heater, sitting below the stack containment vessel, and able to focus and control heating of anode and cathode supply gases independently from the stack (Figure 4.1-4).

A drawing specification of the containment vessel fabrication was completed, and the unit was fabricated. As shown in Figure 4.1-5, there is a removable lid to allow for access to stack test instrumentation such as thermocouples, voltage leads, power take off cables, and sense lines to monitor pressures. The layer-cake construction allowed the upper chamber to be removed to replace the stack without requiring the removal of the critical test stand process connection below it in the lower chamber. A number of access ports and pins around the perimeter of both chambers provided a means to route instrumentation wiring to a cold zone away from the test environment while protecting the individual leads from shorting.

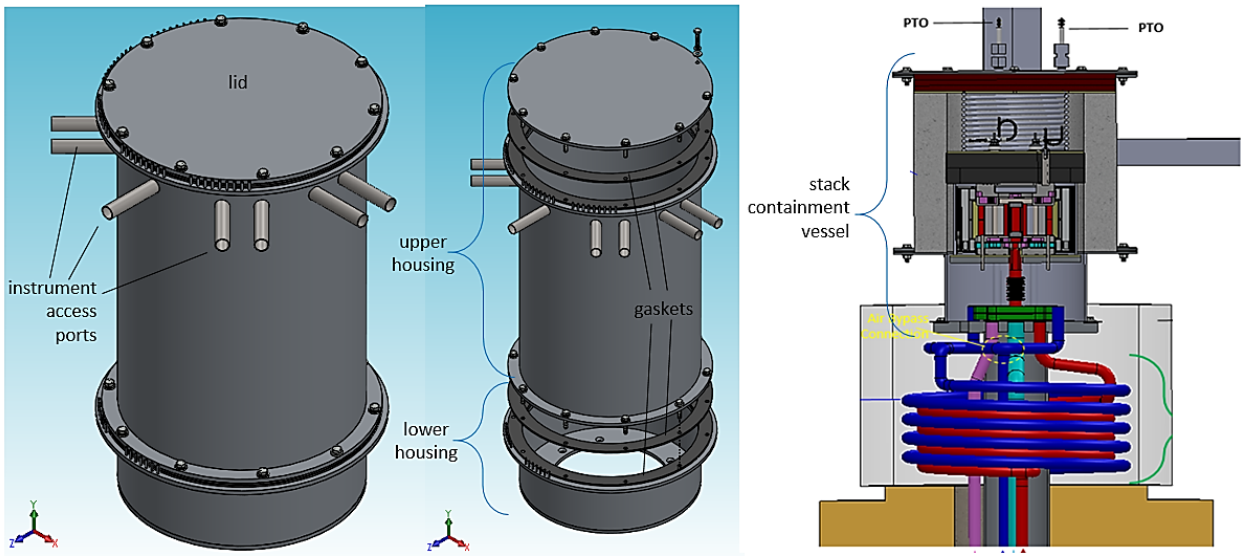

Figure 4.1-4 Stack Containment Vessel Housing Assembly drawing

Figure 4.1-5 Stack Containment Vessel Housing Assembly – as built

A critical component of the integrated CSA stack was the oxidizing manifold, which combined a stream of anode out gas into a chamber within the cathode out manifold. This oxidizing chamber housed a catalyst-coated porous substrate which lowered the activation energy required to oxidize fuel in the mixed fuel-air flow stream. For the application, the energy released during combustion was attempted to be harnessed to heat cathode supply air by way of counterflow heat exchange through the external facing wall of the manifold.

As the SOFC power plants are primarily fueled by Natural gas, methane was used during mock and functional stack testing. By installation of flow control hardware, that capability was added to the test stand used for this project. Images of what the test stand looked like before and after modification are shown Figure 4.1-6.

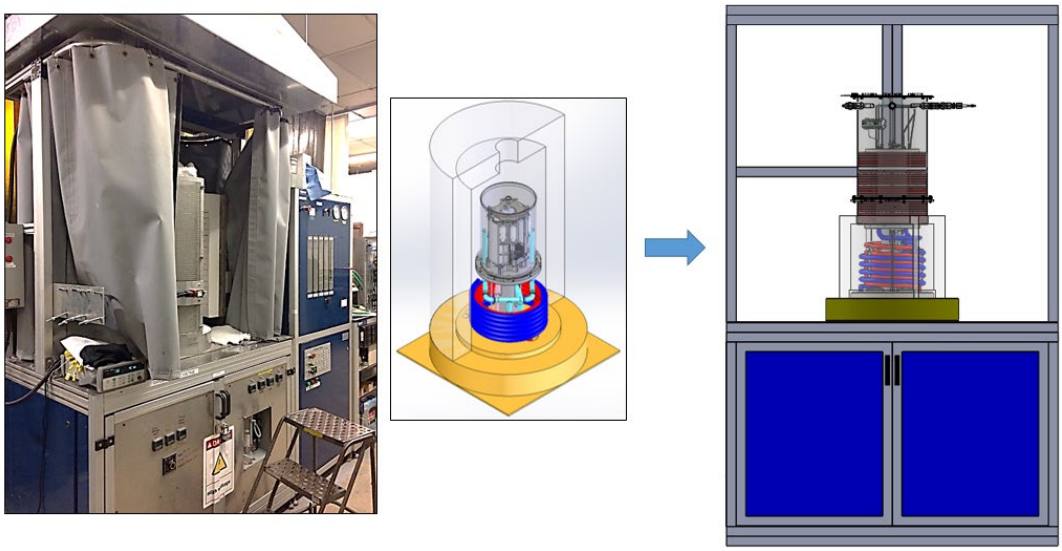

Figure 4.1-6 Test Stand Before and After Modifications

The initial testing was performed with a mock stack within the test stand designated for testing performance of CSA stacks. The planned mock stack was a stack assembled with all non-repeat components (end plates, manifolds, etc.) but with a metal cylinder core replacing the repeating components (fuel cells, interconnects, seals, etc.). The metal cylinder core is shown sandwiched between the two end plates in Figure 4.1-7 below. A photo of the oxidizer manifold is shown as well with the cover removed from the oxidizing chamber.

Figure 4.1-7 Mock Stack Components – Oxidizer Manifold (left); Core and End Plates (right)

Hand calculations using correlations were used to determine pressure drop across the catalyst coated metal substrate. The single cell test stand was used for this purpose. It included test gas supply, a pneumatic ram to compress gaskets to seal the flow path, and instrumentation to characterize the gas and pressure drop Figure 4.1-8. A 4x4 jig was used for installation of the test specimen and interfaced with the pneumatic ram.

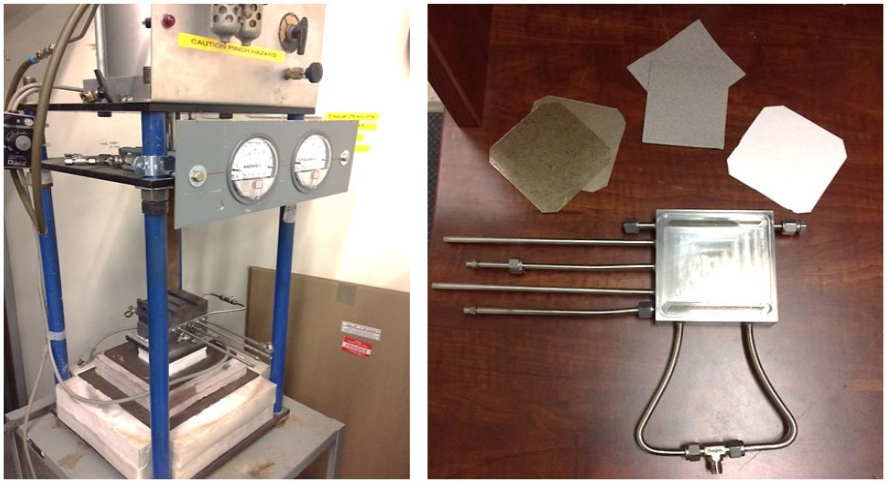

Figure 4.1-8 Pressure Drop Test Equipment, Jig and Shims

Specimens, both coated and uncoated, were tested using the test jig. Nitrogen was supplied to the jig loaded with gaskets and engaged with the pneumatic ram at set flow rates (as measured by rotameter). The gauge pressure was recorded from the upstream side of the substrate. The data was then scaled to highest flow case using numerical techniques; the target gas being that of the combined anode and cathode exhausts, post oxidation. Results showed higher than anticipated pressure drop, the impact of which was assessed for the effects on system efficiencies.

The test stand (Figure 4.1-9) has a majority of the required capabilities to run the baseline CSA stack technology, but required a number of updates to become ready for use with Transformational version of the CSA. Specifically, required updates were comprised of the following items: a bypass airflow stream with separate dedicated heater was required to test the heat duty capabilities of the oxidizer manifold, and a smaller clamshell heater to provide isolated preheating of the anode process, and interface plates for testing thermally activated radial seals.

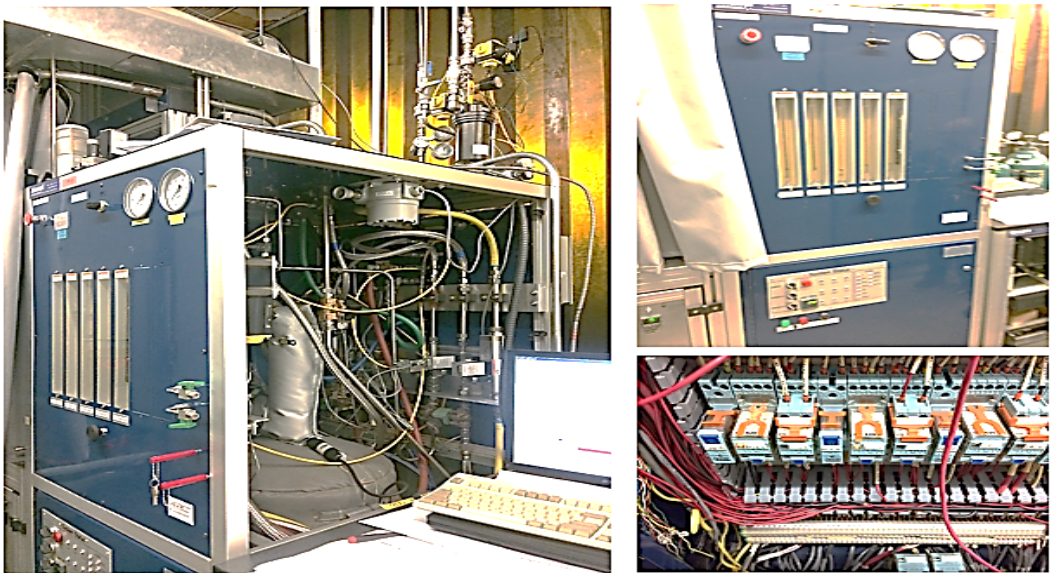

Figure 4.1-9 Repurposed Test Stand

One particular issue of interest occurred during an initial operational checkout of the test stand with a baseline CSA stack which resulted in a beneficial application of new seal design. At the completion of this checkout, it was discovered that chromium oxide had formed on stack and test stand hardware such as air supply tubes and hot compression springs as shown green in Figure 4.1-10. This green coating was a sign that hydrogen, from the fuel gas stream of the stack or test stand, had been leaking into the flush environment around the outside of the stack. This flush zone is where cathode air is supplied. Upon mixing with fuel gas, the hydrogen would oxidize creating steam. And excess steam increases the rate of chrome evaporation from exposed stainless steel and nickel alloy surfaces.

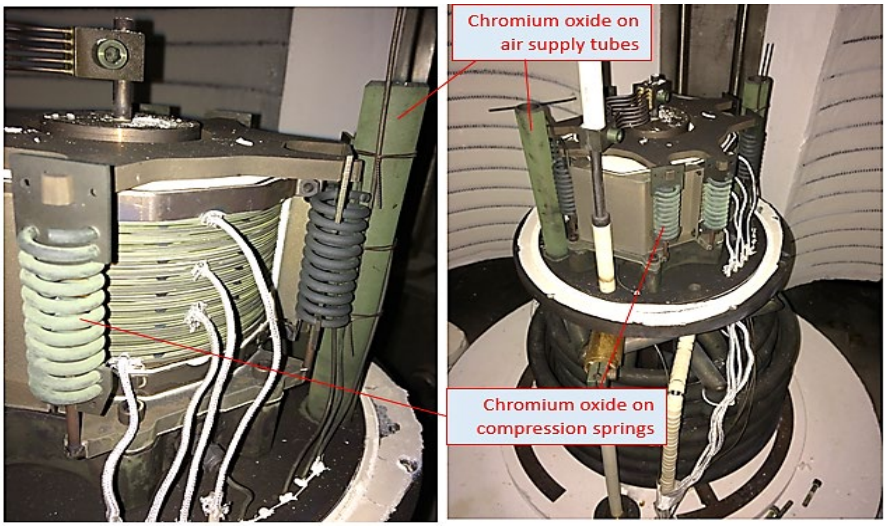

Figure 4.1-10 Chromium Oxide from Fuel Gas Leaking

Leak checks were conducted with the stack still installed and showed a significant leak existing between the mounting plate and adapter plate (Figure 4.1-11). Between these two plates resides compressive metal c-rings that function to seal against leak of inlet and outlet process streams. The stack and adapter plate were removed carefully as not to disturb any physical and visual evidence. Evidence of fuel leaks were shown at locations around the perimeter of the c-ring locations where anode fuel gas is supplied and exhausted (Figure 4.1-11). It was then hypothesized that the mounting plate was warped, resulting in c-rings not being fully seated; allowing fuel gas to leak. A fabrication process step had been missed during the buildup of coiled process tubing to the mounting plate. The plate should have been given a final grinding step after welding of the tubing to it, to address warpage resulting from welding. With use of a straight edge and shims, it was confirmed that the plate was in fact warped (Figure 4.1-12).

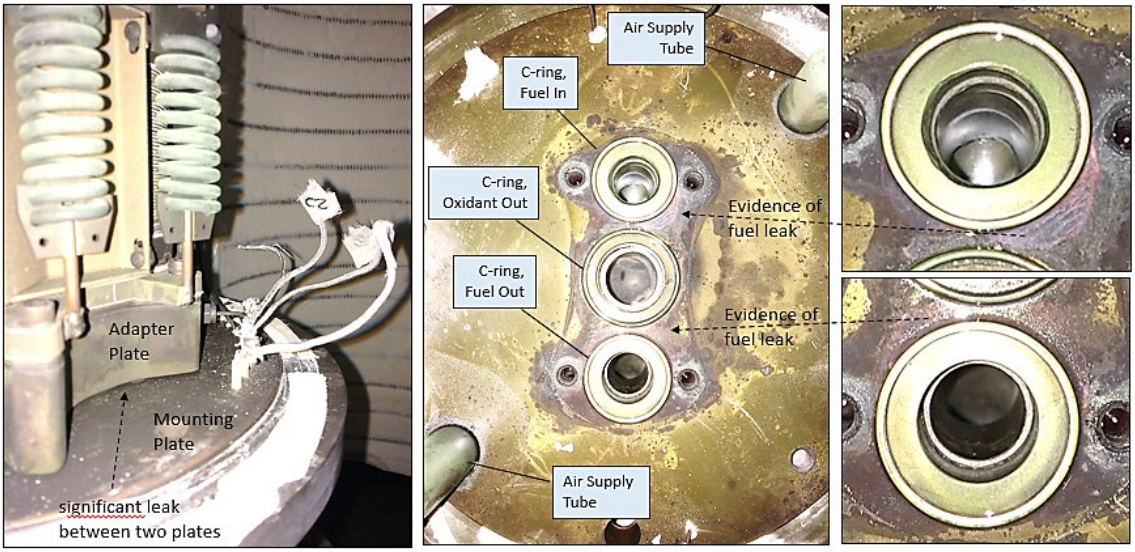

Figure 4.1-11 Images Illustrating Evidence of Location of Leak

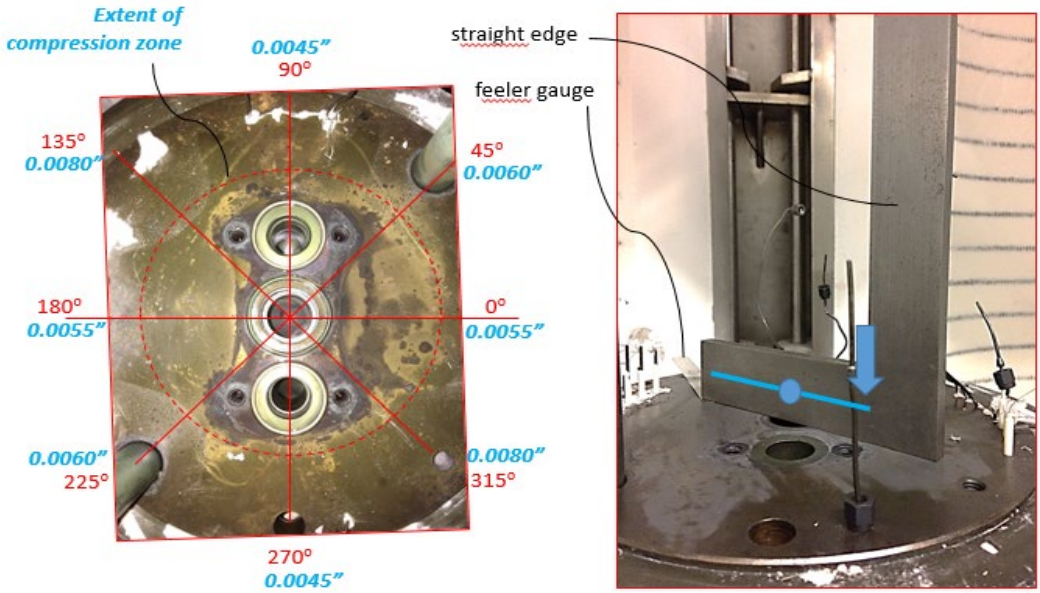

Figure 4.1-12 Surface Assessment with Straight Edge and Feeler Gauges

It was determined that the best pathway to address the warped plate was a new seal. C-ring seals are good to use for high temperature applications due to high strength stability and tight design tolerances. However, this demands mating surfaces to have stringent flatness and surface roughness tolerances. With a warped plate, a more compliant gasket would prevent leaking. Thermiculite gasket material was identified to meet this purpose. Using published data from Flexitallic, the developer and fabricator of the gasket material, along with room temperature weight-deflection tests, an initial gasket size of a flat ring form was chosen to replace the c-ring gaskets. The gaskets, as shown in Figure 4.1-13, were produced. Due to the extent of plate warpage, the design solution required two layers stacked in series. Leak tests were then conducted on the c-rings and thermiculite gaskets. The transformational SOFC adapter plate was bolted onto the mounting plate, with a torque low enough to prevent creep in the bolts at operating temperatures. Air was pressurized in the fuel gas flow streams to 21 IWC and the leak rate was measured. The c-rings leaked at a rate of 176 SCCM, while the Thermiculite gaskets showed no measurable leak. The quantitative measures were backed with visual Snoop checks. These results are quite encouraging.

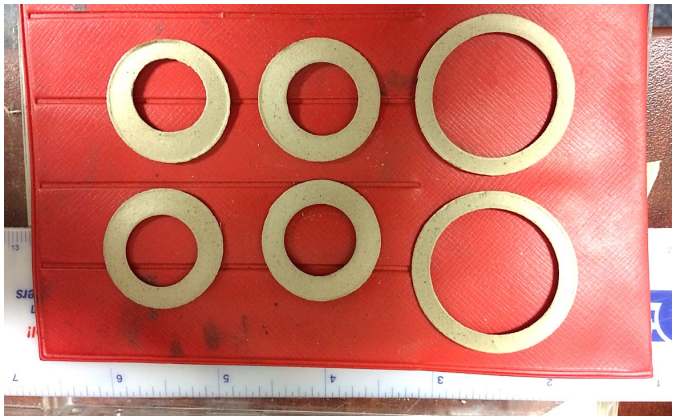

Figure 4.1-13 Thermiculite Flat Ring Gaskets

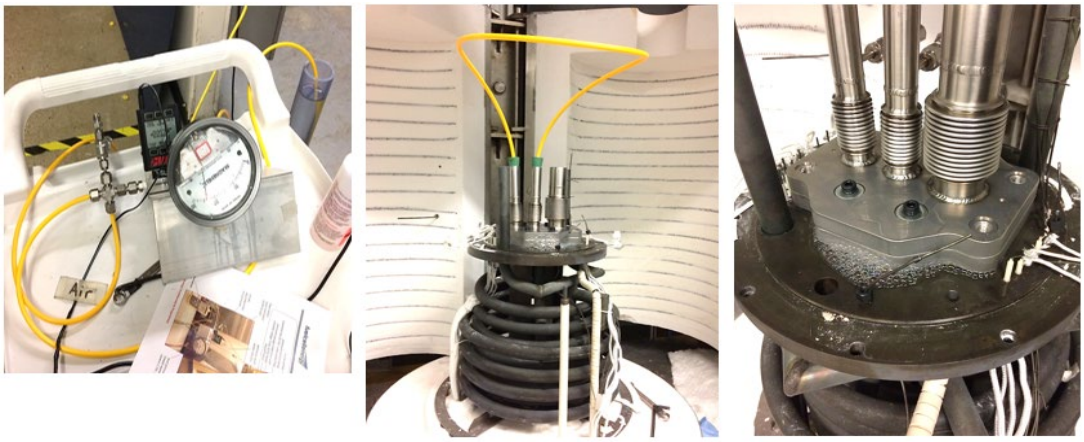

Figure 4.1-14 Cold Test Setup - C-Ring Snoop Check Bubbles Shown

Test stand had two heaters devoted to process streams. One was a porcupine heater used to preheat the air supply stream prior to entering coiled tubing inside the furnace enclosure. The second was a very large heat duty clamshell heater which served as a furnace that heats the process gas via coiled tubes, as well as the stack article itself. This heater arrangement has supported baseline CSA stack development but did not meet the needs for testing the advanced capabilities of the CSA stack developed for this project. The capabilities required were: a smaller clamshell heater isolated to the anode in gas supply stream; a porcupine air preheater connected to a supply line that bypasses the furnace; and cartridge heaters to be installed adjacent to the installed stack. By upgrading the test stand with these heaters, and associated controllers, the features of this project's Transformational design, such as the oxidizer manifold, were more realistically and accurately assessed across many operational states, including heat-up. The baseline heater configuration were preserved for future work, so these new heaters were installed in paralell via transfer switches (Figure 4.1-15). The new clam shell heater is shown in Figure 4.1-16.

Figure 4.1-15 Heater Controllers and Transfer Switches

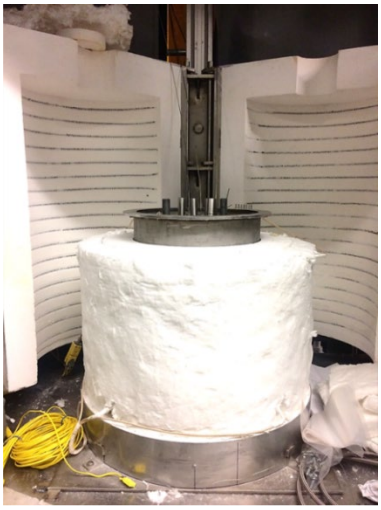

Figure 4.1-16 Insulated Clamshell Shown

The final activities focused on providing the I/O data acquisition capabilities required to complete both the oxidizer manifold and subsequent functional stack tests. The existing DAQ system of the test stand was insufficient to collect data for the expanded stack capabilities, as it was limited in the number of I/O points needed for additional thermocouples and pressure (4-20 mA) measurements. In addition, thermocouple DAQ hardware was ungrounded so live cell temperature readings were not possible. From a high level, the system consisted of voltage and temperature leads connected to a CPU and a rigid I/O user interface software – with limited number of mass flow controller cards. (Figure 4.1-17).

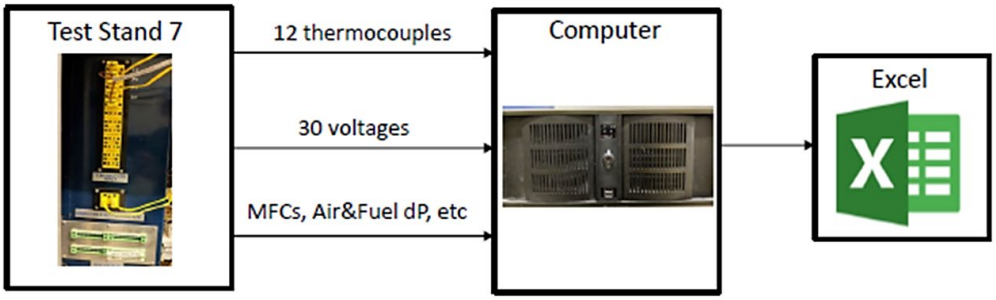

Figure 4.1-17 Baseline DAQ Provided with Test Stand

The I/O data acquisition capabilities for design verification and stack validation tests required additional 20 thermocouples – several of which need DAQ hardware with grounding functionality for cell temperatures. Four grounded thermocouple points were needed for the 45-cell sized stack. The least intrusive and time effective method to add this functionality was to add a couple of portable pieces of DAQ hardware – one Agilent and the other a Watlow F4T – both of which have I/O grounding functionality. The Agilent handled the bulk of the extra thermocouple capacity required for testing while the Watlow F4T handled a mix of both pressure transmitter and thermocouple capacity. The data from the pieces of DAQ hardware – test stand CPU, Agilent, F4T – were merged with use of an R-code script to view data real-time and formatted into a simple csv file for presenting the data (Figure 4.1-18.

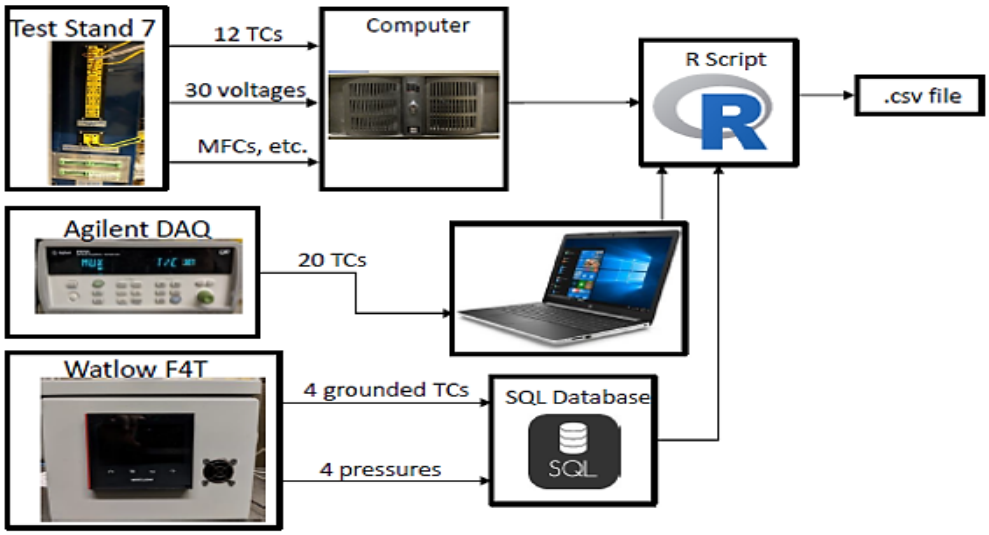

Figure 4.1-18 Upgraded DAQ with Full Testing Capacity

4.2 Validation Stack Fabrication and Testing

Objective:

The objectives were:

- Fabricate a full-height stack (between 2-5 kW) to verify the key design features of the advanced cell materials, new cell component fabrication processes and, above all, the innovative stack architecture design
- Demonstrate stable stack operation over 1000 hours of endurance testing at normal operating conditions with ≤1% degradation per thousand hours.

Approach:

An SOFC stack was tested to evaluate the stack components and incorporated BOP equipment. This is anticipated to be. The stack was integrated into a thermally self-sustaining environment for endurance testing. The results of the (deliverable) stack test and its performance was utilized as input for the Factory Cost Analysis.

Results & Discussion:

Full height stack (350 cells) GT060081-0002 ran to 679 hours with the majority of the cells appreciating over that period (Figure 4.2-1). At 300 hours elapsed some alternate operating point were briefly tested before returning to the baseline conditions of 45% DIR, 68% fuel utilization, 30% air utilization, 0.2 A/cm^2.

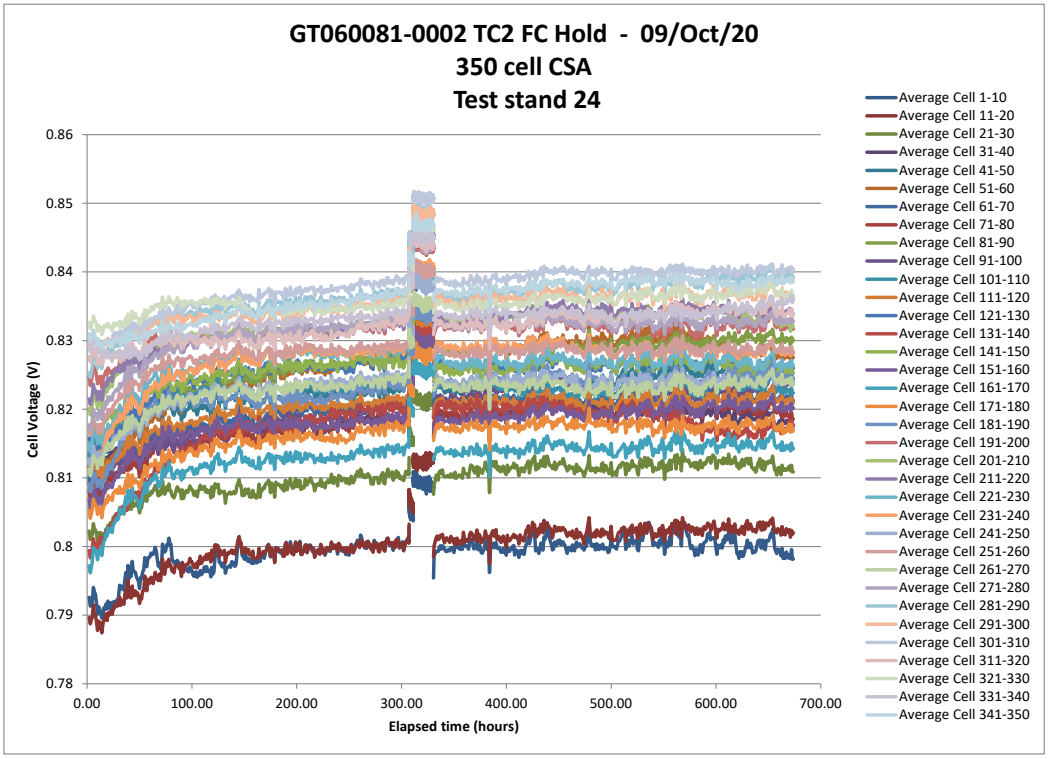

Figure 4.2-1 GT060081-0002 Fuel Cell Hold

At 679 hours the control computer hung and a watchdog timer that was intended to put the test stand into a shutdown condition did not work. Up to that point no test anomalies were recorded. No data was logged after that point. The failure occurred on a Friday night and was not discovered until Monday morning, by which time the stack was damaged beyond repair. We were not able to determine what had gone wrong in what otherwise appeared to be stable operation. The watchdog hardware has been replaced and tested; giving confidence that should a similar case occur in the future the test stand should revert to a safe mode, protecting both the stack and the test stand. With remaining budget in the project, another full height, 350-cell stack is being built in order to attempt to achieve the 1000 hour operating target.

Stack GT060081-0003 was built and placed into the test stand for commissioning and testing. With the next stack, GT060081-0003, a failure occurred with the voltage isolators on the instrumentation channels during the initial conditioning resulting in an electrical short and damage. After repairing the voltage isolators an attempt was made to operate the stack, but the damage was too extensive. The short was found to have melted a hole in an interconnect and the resultant leak precluded stable operation. No useful data was generated on this stack, and therefore another stack was built for the milestone test.

The final stack, GT060081-0004 completed >1800 hours of fuel cell hold at conditions of:

- 45% Direct (in stack) internal reforming
- 68% fuel utilization
- 30% air utilization
- 0.20 A/cm^2
- 750°C (nominal, constant temperature)

Over that period the stack voltage appreciated as shown in Figure 4.2-2. Some cells depreciated during the first 430 hours before changing direction and behaving more similar to the rest of the stack. The cause of this change is not clear, as the conditions were nominally the same for the full test period.

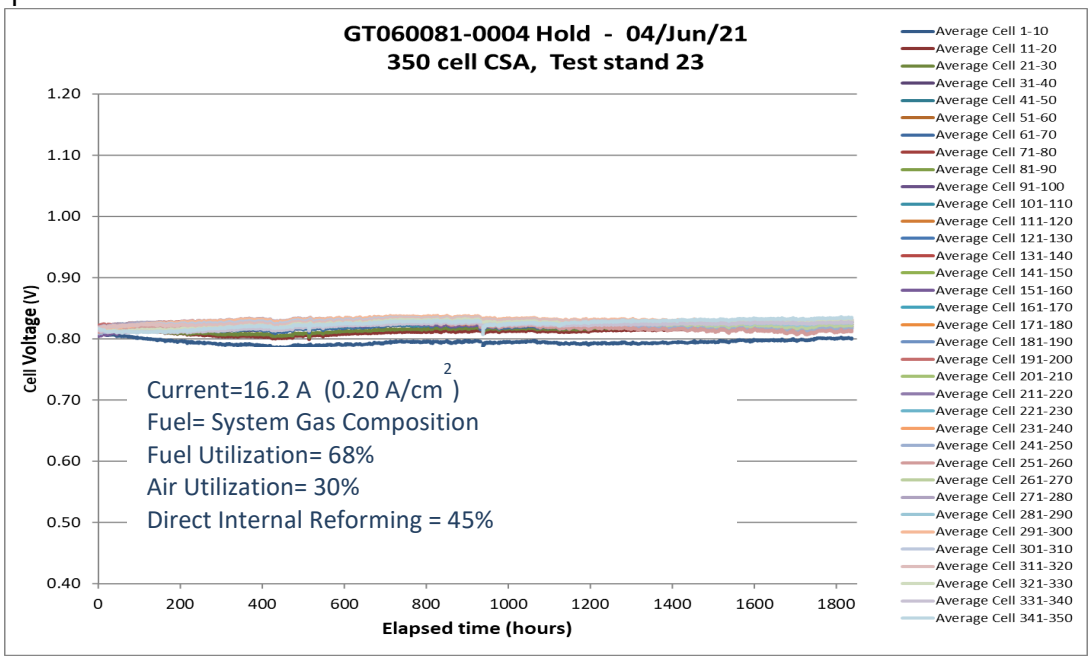

Figure 4.2-2 GT060081-0004 Fuel cell hold on reformate

Figure 4.2-3 shows the same test data, replotted as the best fit linear degradation for each cell grouping (voltage instrumentation was installed in groups of 10 cells). This shows a roughly uniform degradation distribution with an outlier on the first (bottom) cell group which finished with higher degradation and lower voltage than the remainder of the stack. The 4.26 mV/khr degradation slope on this cell grouping equates to a 0.5 %/khr slope. The stack improved over the hold at and average improving slope of 5.1 mV/khr or 0.6 %/khr.

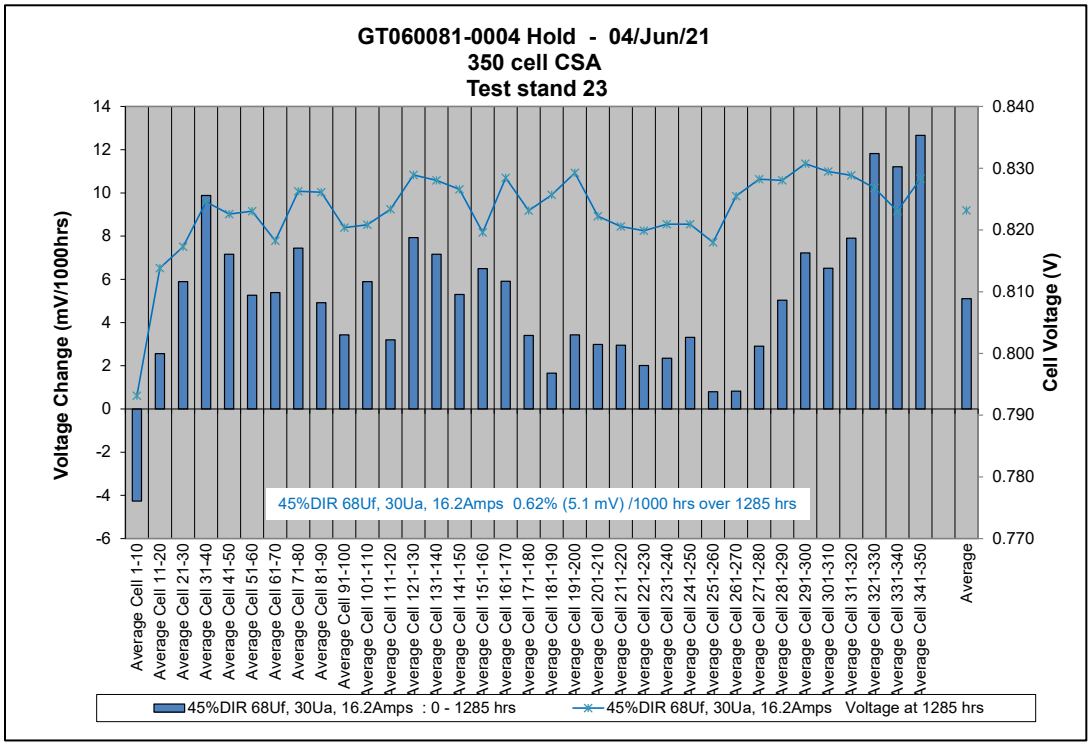

Figure 4.2-3 GT060081-0004 Best fit linear degradation grouped by cell

Although test stand failures interrupted the first two attempts at this milestone test, stack GT060081-0004 ran and demonstrated stable stack operation over 1000 hours of endurance testing at normal operating conditions with ≤1% degradation per thousand hours, exceeding the required test time and all milestone requirements, and did so with performance that appreciated over the test period rather than degrading.

5 Advanced Stack Factory Cost

This activity is focused on validating and verifying the potential of FCE's transformational cell and stack technologies in undercutting the DOE's cost goals for commercial SOFC power plants.

5.1 Cost Analysis

Objective:

The objective of this effort is to estimate the stack factory equipment capital costs for mature market production of the integrated fuel cell stack, in year 2011 U.S. dollars.

Approach:

The denominator for the calculation of cost ($/kWdc) was the experimentally-observed stack performance at Normal Operating Conditions (NOC). The cost estimate established and fully justify a reasonable estimate of the size and number of stacks that must be manufactured per year to support the cost goal. The cost estimate included the following fixed and variable cost elements: Equipment and Plant Depreciation, Tooling Amortization, Equipment Maintenance, Utilities, Indirect Labor, Cost of Capital, Manufactured Materials, Purchased Materials, Fabrication Labor, Assembly Labor, and Indirect Materials. The following costs were not be included: Research and Development, Sales and Marketing, General and Administration, Warranty, and Taxes.

Results & Discussion:

The objective of this study was to provide an updated Factory Cost Estimate for FuelCell Energy's Compact Solid Oxide Architecture (CSA) SOFC stacks. This work served as an update for a 2019 CSA Stack Factory Cost Estimate associated to another Co-Operative Agreement with US DOE, that is, DE-FE0026093 with the title "Innovative SOFC Technologies" project. The main focus of the updated estimate is to follow advancements in the design and manufacturing process adjusting the total number of stack parts, changing input base materials for some stack components, as with as updating component fabrication costs.

Much earlier FuelCell Energy solid oxide technology cost studies pertained to the Large Area Stack (LAS) platform. The Large Area Stack initially utilized 1.0 mm and 0.6 mm (2011 and after) thick planar SOFC-TSC3 cells with an active area of 550 cm^2 active area. The next generation CSA stack minimizes input material content leading to light weight and power dense as key characteristics. The CSA platform uses annular shaped SOFC-TSC3 cells and includes integrated stack manifolds and compression sub-system. Each CSA cell is 0.3 mm in thickness and has a 120 mm outer diameter with 81 cm^2 of active area.

Under DE-FE0026199 (SOFC Prototype System Test), a Large Area Stack cost of $5,316 (Year 2011 USD) was reported, which translates to 270 $/kW DC at a high volume production rate of 1,000 MW per year.

The previous CSA Stack Factory Cost Estimate, under DE-FE0026093 forecasted a CSA stack cost of $889 (Year 2011 USD) which translates to 105 $/kW DC at the same 1,000 MW/year high volume production.

For this updated CSA Stack Factory Cost Estimate, the new CSA stack cost is forecast at $940 (Year 2011 USD) which translates to 111 $/kW DC at the same 1,000 MW/year high volume production.

This significant 59% cost improvement for the CSA stack compared to the Large Area Stack is reported at the same operational power density of 298 mW/cm^2. Additionally, if the Net AC to Gross DC ratio is equal to x1.272, which is the same as that for LAS-SOFC stack, the converted CSA Stack cost at $/kW AC was calculated to be $87/kW AC which is significantly lower than the DOE cost target of $225/kW AC (2011 USD). The reduction of $/kW AC from $/kW DC is due to the presence of a bottoming cycle and thus greater overall power generation within the combined system. This CSA stack achievement is realized via the minimization of stack material content, simplified unit cell design and design for automation and assembly.

Costing efforts and results in this project build off those established under a previous Innovative SOFC project (DE-FE0026093) which is based on a 1,000 MW-AC plant (Giga Factory) and solid oxide annual production level requiring 160,000 stacks per year. Costing focuses on the full-scale CSA-SOFC stack consists of 350 cells and associated repeat parts, a set of non-repeat components and compression system. A repeat unit includes one annular thin (0.30 mm thick) solid oxide fuel cell, annular coated interconnect (with contact paste, glass seal, and metallic support layer), and nickel fuel contact. There are 351 pairs of interconnect assembly (interconnect and nickel fuel contact) as they reside “between” cells.

The overall cell manufacturing and assembly process flows considered in the cost analysis are shown in Figure 5.1-1 and Figure 5.1-2, respectively.

As shown in the stack assembly process flow in Figure 5.1-2, and consistent with previous high volume costing analyses, no stack conditioning and electrochemical testing is planned at the GW/year cell/stack production level. Rather, the stacks would be reduced and conditioning in module at the working system level with this the same basis provided under the Innovative SOFC project factory cost study (DE-FE0026093).

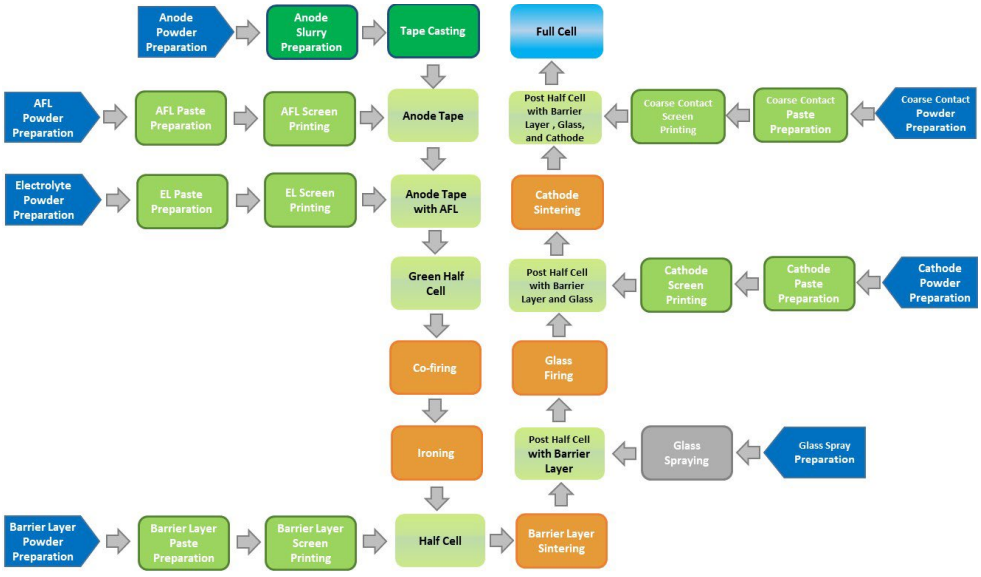

Figure 5.1-1 CSA-SOFC Cell Manufacturing Process Flow

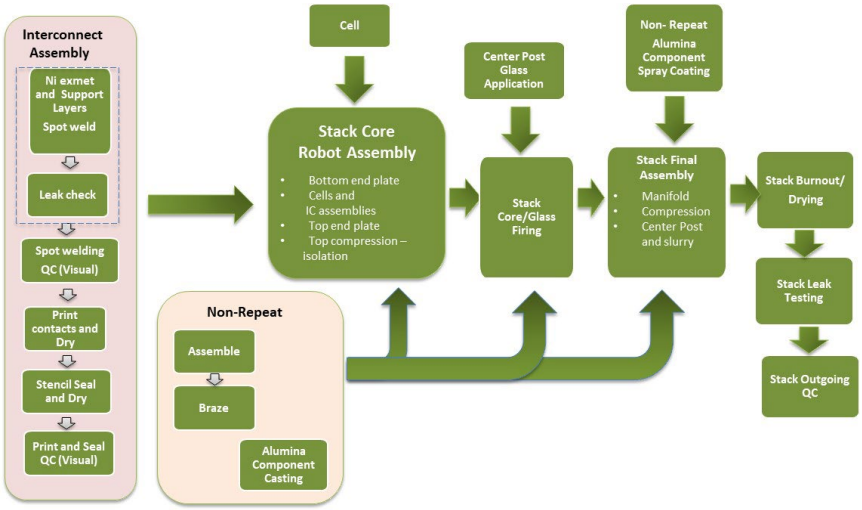

Figure 5.1-2 CSA-SOFC Interconnect Assembly and Stack Assembly Process Flows

As a key input, FCE is using DOE-specified materials cost data based on $2011 unit pricing as shown in Table 5.1-1.

In Table 5.1-1, information is also shown for material price changes between 2011 and 2019 considering production price index (PPI) data of commodities. These were provided for the purpose of material price comparison for 2011 vs 2019 and/or for reference in case stack factory cost report evaluation year would change to 2019 instead of 2011.

For stack cost analysis, the main cost driver is the stack core or repeat units consisting of the cells and interconnect sub-assemblies considering the CSA-SOFC stack composition. A full-scale stack consists of 350 cells, 351 coated interconnects, 1404 inner metallic support layers, 1404 outer metallic support layers, and 351 nickel (expanded metal) fuel contacts. In order to reduce the stack cost, the main focus and effort must be on reducing the costs of the repeat units. The reduction of cell cost can be attained at high volume by:

- Improvement of cell yield. Cell sizing is a current challenge and that there is work to be done. However, for high volume costing, high yield were used (97.7%).
- Increase process capacity through process improvement (e.g., 4-up to 9-up printing)
- Increase process capacity by selecting and purchasing high-capacity and efficient equipment and high-capacity fixture.
- Increasing process capacity through automation of selected process step.
- Minimizing material wastes through process improvement (e.g., disc paste printing instead of square printing for anode functional layer (AFL) and electrolyte.
- Negotiation for discounted material price for high volume purchase.

Table 5.1-1 DOE Materials Cost Data Based on Unit Pricing

Material	Chemical Symbol, Chemical Formula or Other Specification	Best Estimate Unit Price, $/kg (2011)	Projected Estimate Unit Price, $/kg (2019)
Precursors			
Yttrium oxide (yttria)	Y_2O_3	80	Not used by FCE
Lanthanum oxide	La_2O_3	25	26.76
Lanthanum carbonate hydrate (alternative La source)	$La_2(CO_3)_3 . xH_2O$ x ~ 14	20	Not used by FCE
Manganese oxide	MnO_2	2.5	Not used by FCE
Scandium oxide (scandia)	Sc_2O_3	5000	Not used by FCE
Cobalt oxide	Co_3O_4	25	20.22
SOFC Materials			
Yttria stabilized zirconia (3YSZ)	3 mol% yttria	35	13.02
Yttria stabilized zirconia (5YSZ)	5 mol% yttria	37	Not used by FCE
Yttria stabilized zirconia (8YSZ)	8 mol% yttria	45	16.74
Scandia stabilized zirconia (6ScSZ)	6 mol% scandia	470	Not used by FCE
Samarium doped ceria (SDC)		141	Not used by FCE
Gadolinium doped ceria (GDC)		Not priced	Not priced
Lanthanum cobaltite	$LaCoO_3$	60	Not used by FCE
Lanthanum strontium cobalt ferrite	$La_{.6}Sr_{.4}Co_{.2}Fe_{.8}O_3$	50	Not used by FCE
Lanthanum strontium manganite	$La_{.85}Sr_{.15}MnO_3$	50	Not used by FCE
Stainless steel	Grade 4XX	3	2.92
Nickel oxide	NiO	35	25.79
Cerium oxide (ceria)	CeO_2	20	Not used by FCE
Nickel	Ni	18	13.27
Cobalt	Co	29	23.46
Palladium	Pd	22,500	Not used by FCE
Platinum	Pt	52,000	Not used by FCE
Silver	Ag	1100	Not used by FCE

Among the stack repeat components, the needed protective Manganese Cobalt spinel coating is considered a cost driver and important for long term stack operation. For the formed interconnect, cost can be broken down into 3 categories namely: (1) forming cost, (2) coating cost, and (3) base material cost. Figure 5.1-3 shows the % cost contribution for the 3 categories on the part cost at the low volume (1 MW/year production level). It shows 78% for forming cost, 19% for coating cost, and 3% for base material cost. At high volume the base material and coating cost become more important however.

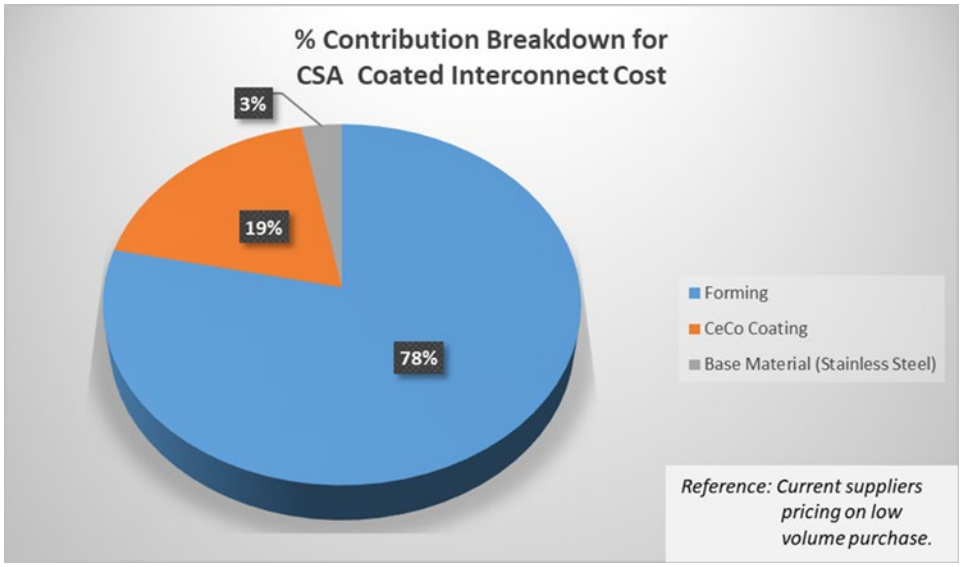

Figure 5.1-3 % Contribution Breakdown for CSA Coated Interconnect Cost (Low Volume)

For high volume requirement (e.g. >10M parts/year), our current interconnect forming is based on *forming + die cutting + tooling cost* while alternatively process is *stamping + 3 cavity progressive die + tooling cost*. For the single side coating on interconnect, this is currently being performed on metal sheet using Physical Vapor Deposition (PVD) coating process before s the coated metal coils are used for interconnect forming. As shown in Figure 5.1-3 and for low volume requirement, 19% of the part cost is due to coating and is 6x the cost of the base material (stainless steel). The importance of having MCO as a protective layer on cathode interconnects is to have protection against Cr evaporation. In FCE's current process, the formation of MCO oxide on the interconnect in the stack is known as in-situ MCO formation as shown in Figure 5.1-4 (left).

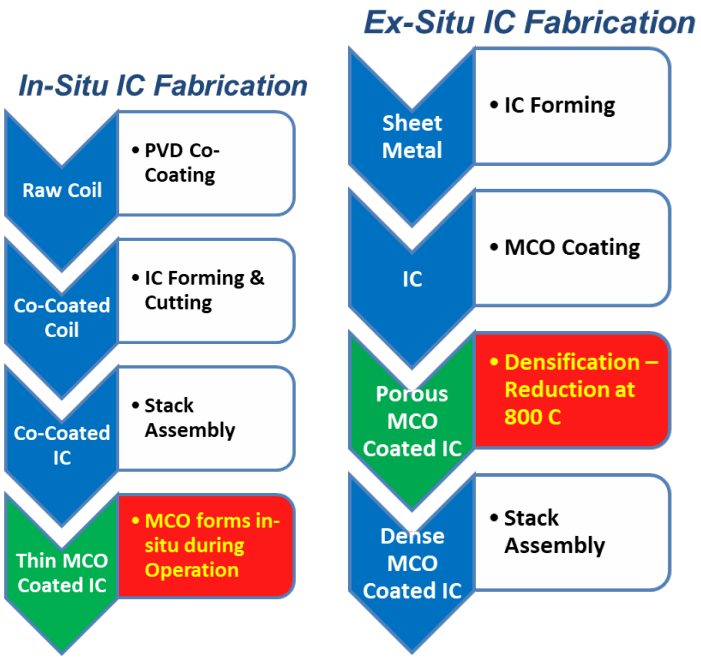

Figure 5.1-4 Interconnect MCO Formation Processes – In-situ formed on left, Ex-situ formed on right

Of interest particularly at commercial scale and for long term solid oxide operation, FCE has also been actively developing and evaluating an alternative in-house ex-situ formed MCO coating (Figure 5.1-4 – right) and is planning to employ this detailed processes into the stack production factory for further efficiencies and cost savings. The ex-situ formed MCO is a thicker (5 to 10 micron coating) versus the thin sub-micron in-situ formed MCO coating. Based on the previous study of our Large Area Stack (LAS) platform, it was found that ex-situ MCO coating has lower initial performance (due to the thicker coating); however, more importantly the stack degradation rate was lower compared to in-situ coating. FCE is now evaluating manufacturing of in-house MCO (Mn0.5Co0.5O3) coating on CSA interconnect following the developed in-house MCO coating IC process flow as shown in Figure 5.1-5**.**

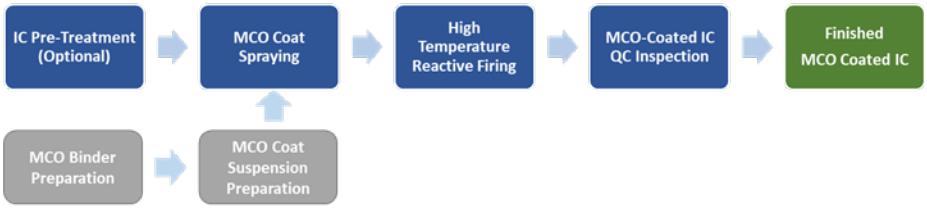

Figure 5.1-5 FCE In-house MCO Coating Interconnect (IC) Process Flow

For this factory stack production cost study, both the in-situ and ex-situ formed processes are projected to the GW-scale production level. The objective is to compare the stack performance and cost when using in-house MCO coated CSA interconnect vs CeCo coated CSA interconnect. If the in-house MCO coating cost is found to be cheaper than supplier CeCo coating cost at high volume and FCE can have a high volume capacity, this option might be considered to lower the coating cost. For the base material cost, the DOE-specified stainless steel cost was used for the costing.

The second stack repeat component that needs investigation and cost reduction is CSA nickel expanded metal fuel contact as shown in Figure 5.1-6.

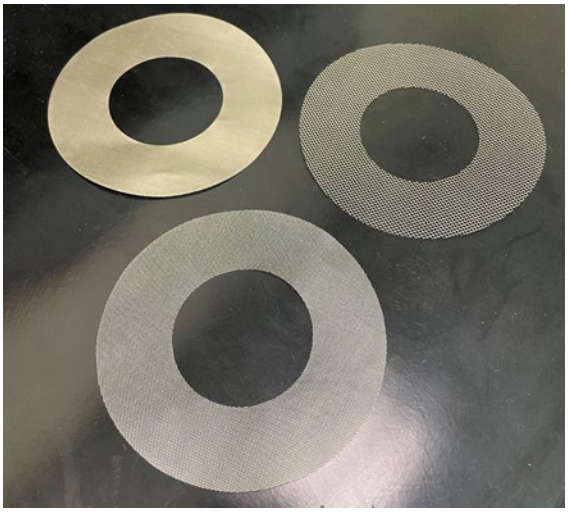

Figure 5.1-6 CSA Nickel Exmet Fuel Contact

Lastly, currently inner and outer metal support layers being welded on the interconnect assembly. The current fabrication process of these parts for low volume is by photo-etching. For very high-volume demand, there is a need to consider lowering the fabrication cost for these parts. There are 2 options that could be considered to lower the cost:

- Check the possibility of converting the fabrication from photoetching to stamping if not affecting the quality of the part for stack build.
- Explore the possibility of including these features in the formed interconnect part. If this is doable without affecting the quality, current welding of separate metal support layers to interconnect assembly can be eliminated.

The tornado chart shown in Figure 5.1-7 presents some sample overall cost sensitivity (in $/kW) for the top 10 contributors to overall stack cost.

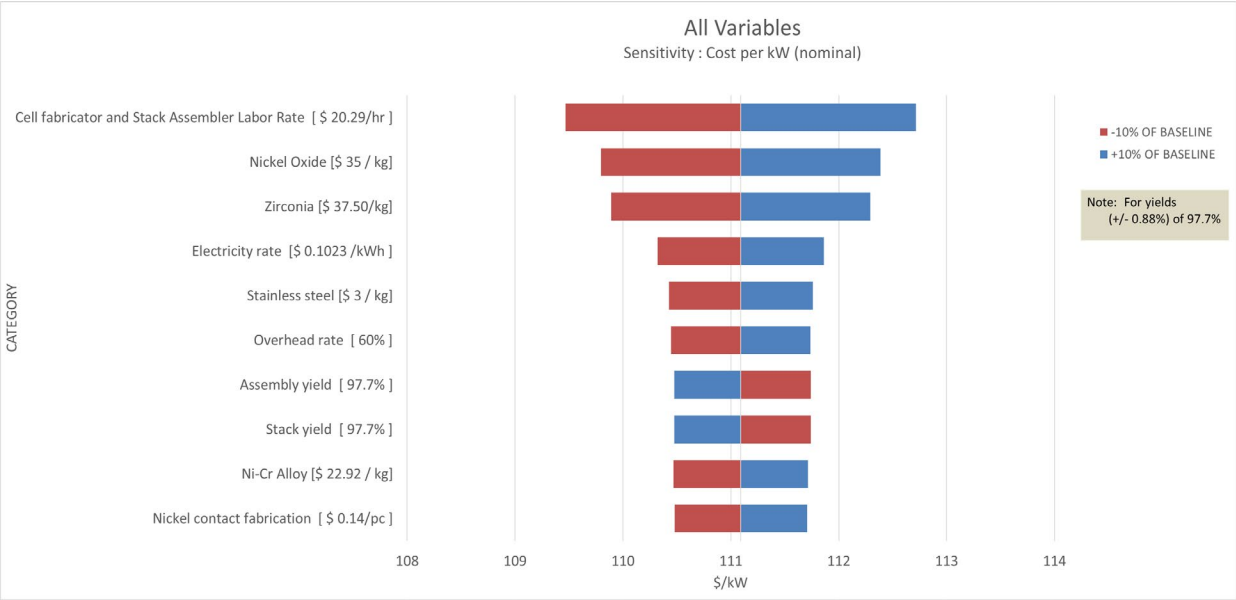

Figure 5.1-7 Simulation Results: Overall Fuel Cell Stack Cost in $/kW (All Variables)

The top 5 contributors to the SOFC CSA stack Factory Cost are:

1) labor rate – 1.46%
2) nickel oxide price - 1.17%
3) zirconia price - 1.08%
4) electricity rate - 0.69%
5) stainless steel price – 0.60%

These results are shown in tabular form in Table 5.1-2. Nickel oxide, Zirconia (YSZ), and stainless steel are DOE-specified materials with target cost.

Table 5.1-2 Stack Cost in $/kW and Percent Variation Summary Data (All Variables)

			Cost per kW ($/kW)					
Input			Minimum	Nominal	Maximum	Range	neg dev	pos dev
Cell fabricator and Stack Assembler Labor Rate [$ 20.29/hr]	**$ 18.26/hr**	**$ 22.32/hr**	**109.47**	**111.09**	**112.72**	**3.25**	**-1.46%**	**1.46%**
Nickel Oxide [$ 35 / kg]	**$ 32 / kg**	**$ 39 / kg**	**109.80**	**111.09**	**112.39**	**2.59**	**-1.17%**	**1.17%**
Zirconia [$ 37.50/kg]	**$ 33.75 / kg**	**$ 41.25 / kg**	**109.89**	**111.09**	**112.29**	**2.40**	**-1.08%**	**1.08%**
Electricity rate [$ 0.1023 /kWh]	**$ 0.0921 /kWh**	**$ 0.1125 /kWh**	**110.32**	**111.09**	**111.86**	**1.54**	**-0.69%**	**0.69%**
Stainless steel [$ 3 / kg]	**$ 2.70 / kg**	**$ 3.30 / kg**	**110.43**	**111.09**	**111.76**	**1.33**	**-0.60%**	**0.60%**
Overhead rate [60%]	54%	66%	110.45	111.09	111.74	1.29	-0.58%	0.58%
Assembly yield [97.7%]	96.8%	98.6%	111.74	111.09	110.48	1.27	0.59%	-0.55%
Stack yield [97.7%]	96.8%	98.6%	111.74	111.09	110.48	1.27	0.59%	-0.55%
Ni-Cr Alloy [$ 22.92 / kg]	$ 22.63 / kg	$ 25.21 / kg	110.47	111.09	111.71	1.24	-0.56%	0.56%
Nickel contact fabrication [$ 0.14/pc]	$ 0.13 / pc	$ 0.15 / pc	110.48	111.09	111.71	1.23	-0.55%	0.55%

CONCLUSION

Significant accomplishments achieved in this project resulted in development of a new generation of high-power density Compact Solid Oxide Architecture (CSA) stack technology with flexibility for integration with balance-of-plant equipment.

The R&D activities were focused on refinement of cell technology and design of new stack integrated BOP components to reduce overall plant cost. Cell technology work investigated alterations to cell microstructure in the anode functional layer to minimize impact of redox events, in addition to consideration of other concepts to improve electrolyte durability. The following summarizes the achievements resulting from the R&D work performed in this project.

- Completed development of redox-tolerant solid oxide cell technology and demonstrated redox tolerance in anode-supported cells for over 10 Testing cycles.
- Demonstrated feasibility of scalable, high-yield manufacturing process for anode-supported cell technology.
- Investigated a variety of design alternatives to incorporate balance of plant functionality within the fuel cell stack in including pre-reforming of the fuel, air pre-heating, and anode exhaust oxidation.
- Completed >1000 hrs. tests of a CSA stack with <1% per 1000 hrs. degradation in performance
- Completed CSA stack Factory Cost estimation indicating a manufactured stack cost of 111 $/kW DC (Year 2011 USD) at 1,000 MW/year volume production (Giga Factory).

REFERENCES

[1] Z. Gao, L.V. Mogni, E.C. Miller, J.G. Railsback and S. Barnett, "A Perspective On Low-Temperature Solid Oxide Fuel Cells," *Energy & Environmental Science* 10.1039/C5EE03858H (2016)

[2] Z.P. Shao and S.M. Haile, "A high-performance cathode for the next generation of solid-oxide fuel cells," *Nature* **431** (2004) 170-173

[3] T.P. Tsai, E. Perry and S. Barnett, "Low-temperature solid-oxide fuel cells utilizing thin bilayer electrolytes," *J. Electrochem. Soc.* **144** (1997) L130-L132

[4] T. Tsai, Perry Murray, E., Barnett, S.A., "Low-Temperature Solid-Oxide Fuel Cells Utilizing Thin Bi-Layer Electrolytes," *J. Electrochem. Soc.* **144** (1997) L130

[5] J.J. Bentzen and H. Schwartzbach, "ELECTRICAL-CONDUCTIVITY, STRUCTURE, AND THERMAL-EXPANSION BEHAVIOR OF ZRO2-CEO2-GD2O3-Y2O3 SOLID-SOLUTIONS," *Solid State Ionics* **40-1** (1990) 942-946

[6] A. Mai, V.a.C. Haanappel, F. Tietz and D. Stover, "Ferrite-based perovskites as cathode materials for anode-supported solid oxide fuel cells - Part II. Influence of the CGO interlayer," *Solid State Ionics* **177** (2006) 2103-2107

[7] N.M. Sammes, G.A. Tompsett and Z.H. Cai, "The chemical reaction between ceria and fully stabilised zirconia," *Solid State Ionics* **121** (1999) 121-125

[8] A. Tsoga, A. Gupta, A. Naoumidis and P. Nikolopoulos, "Gadolinia-doped ceria and yttria stabilized zirconia interfaces: Regarding their application for SOFC technology," *Acta Mater.* **48** (2000) 4709-4714

[9] A. Tsoga, A. Naoumidis and D. Stover, "Total electrical conductivity and defect structure of ZrO2-CeO2-Y2O3-Gd2O3 solid solutions," *Solid State Ionics* **135** (2000) 403-409

[10] Z. Gao, V. Zenou, D. Kennouche, L.D. Marks and S. Barnett, "Characteristics of Solid Oxide Cells with Zirconia/Ceria Bi-Layer Electrolytes Fabricated Utilizing Reduced-Temperature Firing," *J. Mater. Chem. A* 10.1039/c5ta01964h (2015)

[11] Z. Gao, D. Kennouche and S.A. Barnett, "Reduced-temperature firing of solid oxide fuel cells with zirconia/ceria bi-layer electrolytes," *Journal of Power Sources* **260** (2014) 259-263

[12] Z. Gao and S.A. Barnett, "Effects of Reduced Firing Temperature on Anode-Supported Solid Oxide Fuel Cells," *Journal of the Electrochemical Society* **161** (2014) F600-F604

[13] Z. Gao, L.V. Mogni, E.C. Miller, J.G. Railsback and S. Barnett, "A Perspective On Low-Temperature Solid Oxide Fuel Cells," *Energy & Environmental Science* 10.1039/C5EE03858H (2016)

[14] Waldbillig D, Wood A, Ivey DG. Electrochemical and microstructural characterization of the redox tolerance of solid oxide fuel cell anodes. J Power Sources 2005; 145: 206–215

[15] Wood A, Pastula M, Waldbillig D, Ivey DG. Initial testing of solutions to redox problems with anode-supported SOFC. J Electrochem Soc 2006; 153(10): A1929-A1934

[16] Waldbillig D, Wood A, Ivey D. Enhancing the redox tolerance of anode-supported SOFC by microstructural modification, J. Electrochem Soc 2007; 154(2); B133-B138

[17] Waldbillig D, Wood A, Ivey DG. Thermal analysis of the cyclic reduction and oxidation behaviour of SOFC anodes. Solid State Ionics 2005; 176(9–10): 847–859

[18] US DoE SECA Innovative SOFC Technologies Project (DE-FE0026093)